Caracterización Óptica de Lentes Intraoculares

Optical Characterization of Intraocular Lenses

Autor: Francisco Alba Bueno

Dirección María S. Millán García – Varela

Memoria presentada para optar al grado de Doctor por la UPC

Doña María Sagrario Millán y García-Varela, Catedrática de Universidad de la Universidad Politécnica de Cataluña

CERTIFICA

Que Don Francisco Alba Bueno, diplomado en Óptica y Optometría y máster en Optometría y Ciencias de la Visión, ha realizado bajo su dirección y en el Departamento de Óptica y Optometría de la Universidad Politécnica de Cataluña el trabajo "Caracterización Óptica de Lentes Intraoculares", que se recoge en esta memoria para optar al grado de Doctor por la Universidad Politécnica de Cataluña.

Y para que conste de acuerdo con la legislación vigente, firma este certificado.

Prof. María Sagrario Millán y García – Varela.

Terrassa, 23 de abril de 2014.

Resumen

La caracterización óptica de las lentes intraoculares (IOLs del inglés Intraocular Lenses) proporciona una información objetiva y cuantitativa que es necesaria para comprender su funcionamiento como implante que sustituye al cristalino en el sistema visual humano. Además, permite predecir el rendimiento de los nuevos diseños. Dicha caracterización se debe llevar a cabo mediante pruebas *in vivo* en pacientes ya implantados así como con pruebas *in vitro* en banco óptico o mediante simulación teórica. Esta tesis analiza las fuentes de error en el cálculo de la potencia de las lentes intraoculares y la compensación de los errores refractivos residuales mediante el uso de grados de libertad no convencionales. Se centra, fundamentalmente, en la caracterización *in vitro* de una variedad de lentes comercialmente disponibles (monofocales, multifocales, esféricas, asféricas, apodizadas, no-apodizadas, y distintos materiales, potencias y adiciones) en un banco óptico. Para ello se ha diseñado y puesto a punto los métodos de medida, un montaje experimental que reproduzca las condiciones en las que las lentes se implantan en el ojo y de acuerdo con la normativa internacional. Se ha medido la calidad óptica a través de la Función de Transferencia de Modulación o la visibilidad de franjas (contraste). Se ha desarrollado e implementado un método para la cuantificación experimental de la eficiencia energética de los distintos modelos de IOLs. Este método ha servido para explicar algunos resultados clínicos obtenidos al evaluar la visión estereoscópica con dos tests con diferente principio de funcionamiento. Se ha desarrollado e implementado un método para caracterizar el halo que perciben algunos pacientes implantados con IOLs multifocales.

Summary

The optical characterization of an intraocular lens (IOL) provides objective and quantitative information that is essential to fully understand its performance as an implant that replaces the crystalline lens in the human visual system. Additionally, it can be used to predict the performance of the new IOL designs. This thesis analyses the main sources of uncertainty in the calculation of the IOL power and the compensation of the residual refractive errors by using some unconventional degrees of freedom. The thesis focuses on the in vitro characterization of a variety of commercially available IOLs (monofocal, multifocal, spherical, aspherical, apodized, full-aperture, and of different materials, powers and additions) in optical bench. To this end, we have designed and implemented the necessary methods of measurement and an experimental setup that, according to the international standard regulation, reproduces the conditions of such implants in the human eye. We have developed a method to measure the energy efficiency of IOLs. This method has allowed us to explain the clinical results obtained in the evaluation of the stereoscopic acuity when using two tests based on different principles. The optical imaging quality of IOLs has been quantified through the experimental measurement of the modulation transfer function and the fringe visibility (contrast). We have developed and implemented a method to characterize some artifact, named halo, that can be perceived by those patients implanted with multifocal IOLs. Finally, all the experimental results have been used as a basis for the comparison of the IOL performances.

Índice

Capítulo 1: Introducción

1.1 Estado del arte 1.1
1.2 Propósitos y esquema de desarrollo de la memoria 1.2

Capítulo 2: Compensación del desenfoque en el sistema óptico del ojo Pseudofáquico

2.1 Fórmulas de cálculo de la potencia y caracterización de primer orden de la parte anterior del ojo 2.3
2.2 Otros grados de libertad para la compensación del desenfoque 2.9
2.3 Ejemplo de un caso real 2.14
2.4 Conclusiones 2.16

Capítulo 3: Sistema para la caracterización de una lente intraocular en banco óptico

3.1 Descripción del sistema básico 3.2
3.2 Problemas asociados al análisis a lo largo de eje 3.10
3.3 Consideraciones sobre la escala de la imagen desenfocada 3.14
3.4 Conclusiones 3.23

Capítulo 4: Eficiencia energética de lentes intraoculares multifocales

4.1 Marco teórico y descripción de las lentes intraoculares multifocales 4.3
4.2 Medida de la distribución energética con análisis de imagen 4.12
4.3 Resultados experimentales 4.13
4.4 Conclusiones 4.29

Capítulo 5: Influencia de las lentes intraoculares multifocales en la medida de la estéreo-agudeza

5.1 Método 5.3
5.2 Resultados 5.7
5.3 Discusión 5.12
5.4 Conclusiones 5.19

Capítulo 6: Calidad de imagen en lentes intraoculares

6.1 Medidas del contraste para determinadas frecuencias espaciales 6.2
6.2 Función de Transferencia de Modulación 6.9
6.3 Formación y caracterización del halo 6.19

Capítulo 7: Conclusiones

Anexos
Láser de femtosegundo para el tratamiento de la presbica A.1
Resultados funcionales y refractivos tras el implante de LIOs tóricas A.15

Contents

Chapter 1: Introduction

1.1 State of the art 1.1
1.2 Purposes and outline of this thesis 1.2

Chapter 2: Defocus compensation in the optical system of the pseudophakic eye

2.1 IOL power formulae and first-order characterization of anterior eye 2.3
2.2 Other degrees of freedom for defocus compensation 2.9
2.3 Numerical example of a real case 2.14
2.4 Conclusions 2.16

Chapter 3: Intraocular lens characterization optical bench system

3.1 Basic system description 3.2
3.2 Problems related with the through-focus analisys 3.10
3.3 About the magnification of the defocused image 3.14
3.4 Conclusions 3.23

Chapter 4: Energy efficiency in multifocal intraocular lenses

4.1 Theoretical background and description of multifocal IOLs 4.3
4.2 Measurement of the energy distribution by image analysis 4.12
4.3 Experimental results 4.13
4.4 Conclusions 4.29

Chapter 5: Influence of multifocal intraocular lenses in stereo-acuity measurements

5.1 Mehod 5.3
5.2 Results 5.7
5.3 Discussion 5.12
5.4 Conclusions 5.19

Chapter 6: Image quality of intraocular lenses

6.1 Contrast measurement of specific spatial frequencies 6.2
6.2 Modulation Transfer function 6.9
6.3 Halo formation and characterization 6.19

Chapter 7: Conclusions

Annex
Femtosecond laser for presbyopia correction A.1
Functional and refractive results after IOL toric implantation A.15

CAPÍTULO 1

INTRODUCCIÓN

CHAPTER 1

INTRODUCTION

REFERENCE TO THE PUBLICATIONS OF THIS THESIS

Part of the content of this section is included in the publication:

- Millán M.S, Alba-Bueno, F. and Vega, F. *"New trends in intraocular lens imaging."* Proceedings of SPIE 8011, 80119I. 2011.

1.1 Estado del arte

El sentido de la vista comienza en el ojo. Es este órgano el encargado de transformar la energía electromagnética de ciertas longitudes de onda que nos llegan como estímulo visual en impulsos eléctricos, que posteriormente se transmiten a nuestro cerebro generando la sensación de visión. Pero para que estas señales nos aporten el máximo de información es necesario que se formen imágenes correctamente en nuestra retina.

En el sistema óptico del ojo humano la córnea y el cristalino son los componentes ópticos más importantes que se encargan de esta tarea. Por un lado, la córnea es la lente que más poder refractivo aporta al sistema óptico, en torno a unas 43-45D (entre 2/3 del total [Atchison and Smith 2000]) en sujetos sanos. Por otro lado, la lente cristaliniana (o cristalino), es la encargada de aportar el resto de potencia dióptrica para focalizar correctamente las imágenes en la retina (18-24D). Además,

el cristalino, es capaz de cambiar su forma para aumentar o reducir su potencia dióptrica permitiéndonos enfocar a diferentes distancias en un proceso que llamamos acomodación. Ésta lente no deja de crecer a lo largo de la vida y, como consecuencia, va perdiendo flexibilidad originando la vista cansada o presbicia. A la pérdida de capacidad acomodativa inicial se añade, posteriormente, la pérdida de transparencia ocasionando lo que denominamos cataratas. Esta patología es todavía la causa más común de ceguera en el mundo según la Organización Mundial de la Salud.

Para recuperar la visión en los pacientes con cataratas se extrae quirúrgicamente el cristalino opacificado, proceso llamado facoemulsificación, y se implanta una lente intraocular (IOL, por sus siglas en inglés *intraocular lens*) con unas características determinadas (índice de refracción, curvaturas, geometrías, etc.). Se trata de una técnica que ha evolucionado enormemente en las últimas décadas mejorando la calidad y variedad de las IOLs a implantar, la técnica quirúrgica y las medidas biométricas necesarias para un óptimo resultado tanto visual como refractivo. Actualmente, la cirugía de cataratas es tan segura y predecible que se realiza, no sólo con fines funcionales (mejora de la visión por falta de transparencia del cristalino), sino también con fines estéticos o refractivos (eliminar la dependencia de gafas o lentes de contacto corrección óptica) en lo que se denomina "facoemulsificación de cristalino transparente".

Fórmulas de cálculo de la potencia de la IOL

Para obtener un óptimo resultado tras la cirugía de cristalino, el primer paso es poder conocer la potencia refractiva de la lente que se debe implantar. La primera fórmula para el cálculo de la potencia de una IOL fue descrita por Fyodorov et al. en 1967 [Fyodorov and Kolonko 1967; Fyodorov et al. 1975]. Ellos asumieron la IOL como una lente delgada y utilizaron una aproximación de primer orden (óptica de Gauss) para estimar su potencia. En aproximación paraxial, la potencia de la IOL (P_{IOL}) se puede calcular a partir de la diferencia entre las vergencias imagen (X') y la objeto (X), esto es: $P_{IOL} = X' - X$. La vergencia se define como el cociente entre el índice de refracción del medio y la distancia frontal (objeto o imagen) que se considere y se mide en dioptrías. La expresión de la P_{IOL} se puede reescribir en función de la potencia refractiva de la córnea K, la distancia entre el vértice corneal

anterior y la IOL, también llamada posición efectiva de la lente (*ELP*, por sus siglas en inglés *Effective Lens Position*), y la longitud axial del ojo (*ALX*), que es la distancia que existe entre el vértice anterior de la córnea y la retina (figura 1.1), para obtener:

$$P_{IOL} = \frac{n_v}{ALX - ELP} - \frac{n_q}{\frac{n_q}{K} - ELP} \quad , \tag{1.1}$$

donde n_q y n_v son los índices refractivos de los humores acuoso y vítreo, respectivamente. En esta ecuación se asume que *K* y *ALX* se pueden medir, mientras que la *ELP* se puede predecir y estimar con suficiente precisión. A pesar de esta sencilla aproximación paraxial, la ecuación 1.1 presenta muchas dificultades para llevarla a la práctica por varias razones relacionadas con la biometría *in vivo*, el modelo de ojo considerado y la relación entre ambos. Estas dificultades se hacen patentes a la hora de tener que asumir determinadas aproximaciones como, por ejemplo, el modelo de lente (delgada o gruesa) para calcular la potencia de la córnea o de la IOL, los índices de refracción de cada medio, la corrección de los planos principales en un modelo de lente gruesa, la predicción de la posición final de la IOL, la corrección de la medida de la *ALX* en función del grosor retiniano y los diferentes ejes del ojo.

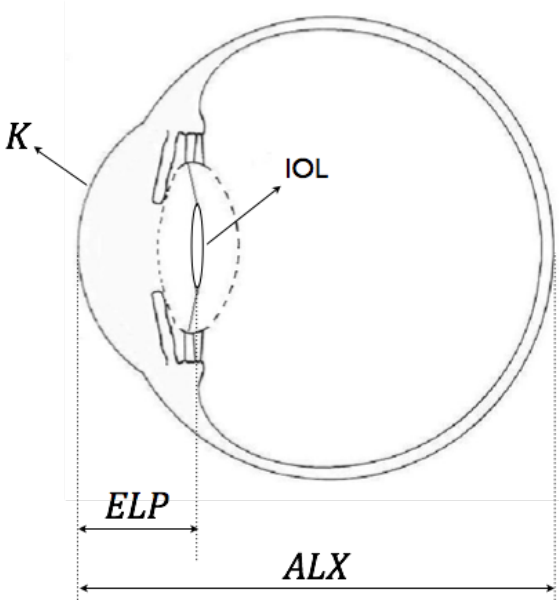

Figura 1.1: Esquema de un ojo implantado con una lente intraocular. Las líneas discontinuas señalan las superficies del cristalino (ya extraído). K es la potencia de la córnea, ELP es la posición efectiva de la lente y ALX es la longitud axial del ojo.

Hoy día existe otro grupo de fórmulas que utilizan una aproximación estadística derivada del análisis de regresión de multitud de casos, como por ejemplo, las fórmulas SRK o SRK-T [Sanders et al. 1990]. Estas fórmulas incorporan constantes que dependen del tipo de IOL y de la media de parámetros biométricos como la *K*, la *ALX*, el diámetro corneal, etc. La fórmula para el cálculo de la potencia de la IOL puede, además, ser sensible a unas determinadas variables específicas en función del tipo de ojo (largo o corto), la técnica quirúrgica, la existencia de una cirugía refractiva corneal previa (como LASIK o PRK), etc. [Holladay 1989; Hoffer 1993; Camellin and Calossi 2006]. Para una mayor información, el lector puede consultar las referencias [Olsen 2007; Holladay 2005; Alba-Bueno and Millán 2011]. A pesar de que la mayoría de los métodos utilizados en la práctica clínica en las últimas décadas se basan en aproximaciones estadísticas, los últimos avances en los equipos de diagnóstico y en la tecnología quirúrgica están dando relevancia de nuevo a las fórmulas basadas en la formación óptica de imágenes, que han demostrado ser más precisas y robustas a los cambios en el entorno clínico.

Los pacientes que han sido intervenidos de cirugía refractiva corneal antes de la intervención de cataratas presentan una dificultad adicional para el cálculo de la potencia de la IOL a implantar. En estas cirugías se modifica la curvatura anterior de la córnea haciendo que la estimación de su potencia (*K*) sea más imprecisa por los métodos habituales de medida y, por tanto, influyendo en el cálculo de la potencia de la IOL. Se han propuesto varios métodos para abordar estos casos considerando que los datos preoperatorios pueden estar o no disponibles en el momento de la elección de la IOL adecuada. Para una información más detallada acerca de estos métodos se recomienda la lectura del trabajo realizado por Savini et al. [Savini et al. 2006].

Compensación de aberraciones de alto orden

Los primeros modelos de ojo únicamente consideraban geometrías esféricas para describir las superficies ópticas oculares utilizando la aproximación paraxial. A pesar de sus limitaciones y simplificaciones, el modelo de ojo de Gullstrand [Atchison and Smith 2000] se ha utilizado mucho para describir la formación de imágenes del ojo y, en este contexto, también se toma como referencia para describir el ojo pseudofáquico (implantado con una IOL en lugar del cristalino). La

córnea ha sido ampliamente estudiada y hoy día se puede hacer una mejor aproximación a su forma utilizando superficies cónicas [Schwiegerling and Greivenkamp 1997]. En general, la córnea introduce ciertas aberraciones en el sistema óptico del ojo; dentro de las aberraciones monocromáticas podemos señalar, principalmente, el astigmatismo, el coma y la aberración esférica (SA, por sus siglas en inglés *Spherical Aberration*). En ojos jóvenes estas aberraciones son parcialmente compensadas por los medios internos del ojo – fundamentalmente por el cristalino – de modo que la cantidad de aberración del sistema óptico ocular en su conjunto es inferior a la que introduce las que la córnea aisladamente [Millodot and Sivak 1979; Navarro et al. 1985; Artal et al. 2001; Kelly et al. 2004; Marcos et al. 2008]. La córnea promedio en ojos sanos tiene una forma prolata que induce una SA en términos del coeficiente de Zernike c[4,0] (o Z[4,0]) de aproximadamente $0.3\mu m$ para un diámetro pupilar de $6mm$ [Norrby et al. 2007]. Las IOLs con geometría esférica biconvexa (generalmente equiconvexa), también presentan SA positiva, que se añade a la SA corneal, deteriorando aún más la imagen en el plano retiniano (a estas lentes las llamaremos IOLs esféricas). Los nuevos diseños de IOLs, tratando de parecerse al cristalino joven y mejorar la calidad óptica de la imagen que se forma en la retina, presentan superficies asféricas que generan una aberración de signo opuesto al de la aberración introducida por la córnea. Las primeras ideas de diseños de IOLs asféricas (reciben este nombre las IOLs que compensan total o parcialmente la SA introducida por la córnea) fueron publicadas a principios de la década de los 90 [Atchison 1991]. Una década después se comenzaron a implantar y, actualmente, existen numerosos estudios que comparan el comportamiento de estas lentes desde el punto de vista teórico, con los resultados obtenidos en modelos de ojo y con los resultados clínicos postoperatorios obtenidos con pacientes implantados [Guirao et al. 2002; Holladay et al. 2002; Marcos et al. 2005; Kasper et al. 2006a; Nanavaty et al. 2009]. Estos trabajos demuestran que las lentes asféricas presentan mejores resultados que las tradicionales esféricas pero la profundidad de foco se puede ver afectada [Marcos et al. 2005]. Actualmente, para la práctica clínica, existen diferentes diseños de IOLs asféricas que compensan total o parcialmente la SA corneal. También existen lentes libres de aberración, es decir que no introducen aberración

esférica en el sistema, pero tampoco compensan la aberración producida por la córnea.

En esta línea de investigación también existen lentes que tratan de compensar el coma generado por el desalineamiento angular que existe entre los diferentes componentes ópticos del ojo, es decir, el que se produce debido a la falta de un eje óptico común [Tabernero et al. 2007], o lentes diseñadas para compensar las aberraciones cromáticas del ojo [Lopez-Gil and Montés-Micó 2007]. Estos diseños, a pesar de estar descritos en la literatura especializada no se fabrican y, por tanto, no se encuentran disponibles actualmente para la práctica clínica.

Modelos de ojo para el análisis y caracterización de IOLs

Los nuevos diseños de IOLs necesitan, por un lado, modelos de ojo teóricos capaces de predecir el comportamiento óptico y, por otro lado, métodos de análisis que permitan la verificación, tanto *in vitro* como *in vivo*, de sus propiedades [Barbero et al. 2003; Norrby 2008b]. En la literatura se puede encontrar una gran variedad de modelos de cada componente óptico del ojo humano (córnea y cristalino-IOL) así como modelos que describen el sistema óptico ocular completo, muchos de ellos revisados en publicaciones ampliamente conocidas [Atchison and Smith 2000; Navarro 2009; Artal and Tabernero 2010].

La Organización Internacional para la Estandarización (ISO, por sus siglas en inglés *International Standarization Organization*) propone un modelo de ojo con una córnea artificial libre de aberraciones [11979-2; 11979-9]. De este modo cualquier deterioro de la imagen sería debido exclusivamente a la IOL. Sin embargo, este modelo de ojo ISO fue establecido antes de la introducción en la práctica clínica de las IOL asféricas. Tal y como se ha descrito en el apartado anterior, actualmente existen IOLs que inducen SA negativa para compensar la SA positiva de la córnea humana promedio. Estos diseños asféricos, cuando se caracterizan en un modelo de ojo basado en la normativa ISO, muestran un comportamiento incluso peor que las IOLs esféricas convencionales (con SA positiva) ya que se tratan de compensar una aberración esférica que la córnea artificial no ha introducido. Por este motivo, entre otros, el modelo de ojo ISO estándar se encuentra actualmente en revisión [Norrby 2008a]. Para obtener una córnea artificial que induzca una SA similar a la

de la córnea humana promedio se pueden utilizar lentes con superficies asféricas – lo que supone un alto coste de fabricación – o bien utilizar una lente de superficies esféricas con el factor de forma adecuado, mucho más fácil de fabricar, como demostraron Vega et al. [Vega et al. 2010]. Además de los cambios concernientes a la córnea artificial, se han planteado algunas modificaciones adicionales al modelo ISO actual para establecer un "modelo de ojo fisiológico", con unas dimensiones más cercanas al ojo natural. Estas modificaciones se han propuesto y analizado en el trabajo de Norrby et al. [Norrby et al. 2007].

Un montaje experimental que reproduce el modelo de ojo en un banco óptico para analizar las imágenes formadas por las IOLs se muestra en la figura 1.2. Básicamente, este dispositivo consta de un sistema formador de imagen, un modelo de ojo y un sistema de captación de imagen. En el capítulo 3 profundizaremos en las características de este modelo de ojo.

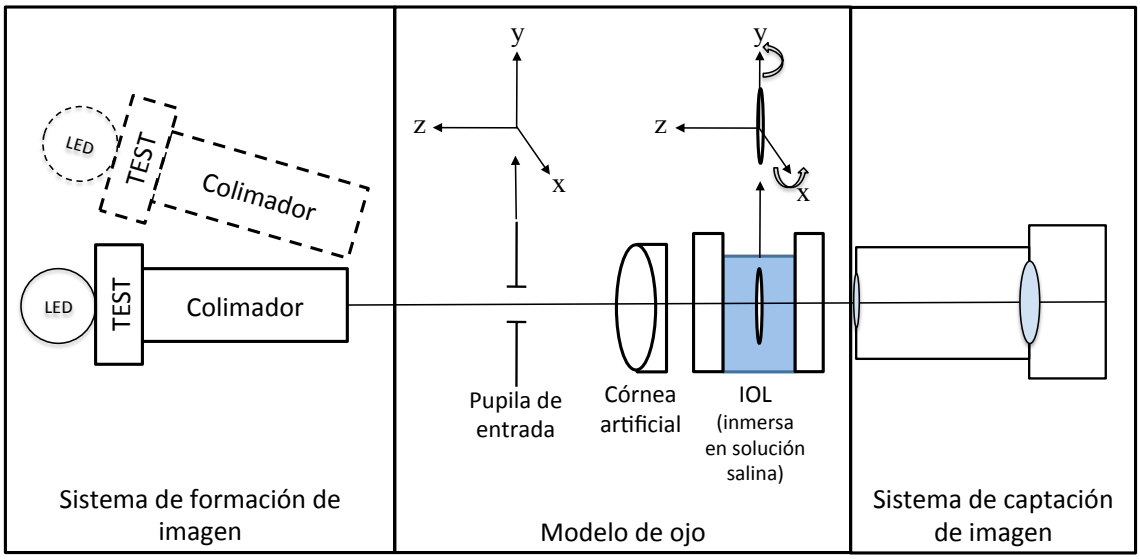

Figura 1.2: Esquema de un dispositivo experimental en banco óptico que contiene el modelo de ojo para el análisis de IOLs.

Lentes intraoculares multifocales para visión lejana y cercana

Como comentábamos al principio de este capítulo, el cristalino es una lente capaz de cambiar de forma gracias a los músculos ciliares que lo rodean dotando al ojo de la capacidad de acomodar. Con la edad esta lente pierde flexibilidad – y por tanto capacidad acomodativa – y transparencia (cataratas). Ante la pérdida de transparencia la única solución es la intervención quirúrgica y el implante de una

IOL. Las lentes monofocales tienen una focal fija, por lo que únicamente pueden proveer visión nítida a una determinada distancia y con una profundidad de campo limitada. Ante esta situación se hace necesario el uso de corrección óptica adicional para el correcto enfoque a diferentes distancias. Teniendo en cuenta que el cálculo de la potencia de la IOL se hace generalmente para proporcionar una correcta visión de lejos, el paciente tras la intervención necesita gafas para visión cercana. Las IOLs multifocales (MIOLs) están diseñadas para disminuir esta dependencia de gafas. Estas lentes operan bajo el principio de visión simultánea, esto es, tienen más de una potencia que focaliza la luz en distintos planos imagen separados. Cada una de las imágenes formadas se perciben sobreimpuestas en la retina, por lo que el cerebro juega un papel importante para seleccionar la "imagen de interés". Lógicamente, este mecanismo de funcionamiento conlleva una reducción de contraste en la imagen que dependerá de diversos factores como el diseño de la lente y el diámetro pupilar entre otros. La superposición de la imagen enfocada con otra u otras imágenes desenfocadas y de diferente escala en la retina puede ocasionar fenómenos incómodos de percepción como halos y deslumbramientos. Estos fenómenos se dan especialmente en condiciones de iluminación mesópica y escotópica. En el capítulo 6 profundizaremos en la caracterización de los halos.

La multifocalidad se puede generar mediante una combinación de elementos ópticos refractivos o difractivos (que llamaremos MIOLs refractivas o difractivas). Las MIOLs refractivas presentan una apertura con zonas de diferente potencia. Estas zonas pueden ser anillos concéntricos (lentes simétricas) o sectores circulares (lentes asimétricas). Las lentes difractivas, en cambio, utilizan una IOL monofocal de base y un perfil difractivo en una de sus superficies para generar uno o más focos utilizando los distintos órdenes de difracción. Generalmente, las MIOLs difractivas utilizan el orden m=0 para contribuir al foco de visión lejana y el orden m=1 para generar el foco de visión cercana. También existen modelos con perfiles difractivos apodizados, limitados a la zona central de la IOL, que ofrecen una mayor contribución al foco lejano para pupilas grandes. Las MIOLs pueden presentar un diseño base esférico o asférico, al igual que las lentes monofocales. Existe un gran interés en determinar, tanto en banco óptico [Pieh et al. 2002; Terwee et al. 2008], como en estudios clínicos [Kohnen et al. 2009a; de Vries et al. 2010], las condiciones y el grado en el que los distintos diseños de MIOLs muestran

beneficio. De hecho, algunos estudios muestran que las ventajas son pequeñas o inexistentes cuando las pupilas son pequeñas [Muñoz et al. 2006; Kasper et al. 2006b].

También hay comercializadas otro tipo de MIOLs que, en lugar de utilizar el principio de visión simultánea, tratan de aportar un cierto rango continuo de poder acomodativo al sistema óptico ocular. Estas lentes se basan en un desplazamiento axial de la lente y/o un aumento de su potencia óptica cuando se contrae el músculo ciliar [Menapace et al. 2006; Sheppard et al. 2010; Migliore et al. 2011] tratando de "emular", de esta manera, el comportamiento del cristalino. El diseño más sencillo de estas lentes es una IOL de potencia fija con un háptico flexible que permite el desplazamiento de la lente cuando se realiza el esfuerzo acomodativo. Otro diseño combina dos lentes en una (doblete acomodativo intraocular [McLeod et al. 2003]). Este implante combina una lente positiva con una negativa unidas por un "resorte". Cuando las lentes están próximas una a la otra, el ojo enfoca correctamente en visión lejana y cuando el cuerpo ciliar se contrae, las lentes se separan aumentando la potencia refractiva y facilitando la visión cercana. La efectividad a largo plazo de este tipo de implantes, sigue estando cuestionada siendo necesarios más estudios y de más larga duración [Migliore et al. 2011].

Nuevas tendencias

Según Olsen [Olsen 2007], a pesar de los esfuerzos por optimizar el cálculo de la potencia de la IOL óptimos, un 90% de los pacientes implantados quedan con una refracción residual postoperatoria que varía entre $\pm 0.50D$ y un 99.9% entre $\pm 2.00D$ con respecto al valor de la refracción deseado. Cuando los ojos presentan una longitud axial fuera de lo común (como los ojos con miopías altas, que suelen ser largos, o con hipermetropías altas, que suelen ser cortos) o han tenido algún tipo de cirugía corneal previa el error es aún mayor. Un error refracción postoperatoria (desenfoque) de entre $0.50D$ a $1.00D$ ha sido clasificado como problemático o desagradable cuando se examina con una pupila efectiva de $5mm$ [Atchison et al. 2009]. Esto hace que algunos errores refractivos tras la cirugía de cataratas puedan necesitar corrección posterior. Con este fin, se puede recurrir a la cirugía refractiva corneal, pero no siempre es recomendable o posible. Por

ejemplo, muchos pacientes que necesitan cirugía de cataratas fueron intervenidos anteriormente de cirugía corneal y tras la intervención no es posible realizar el "retoque" debido a que la paquimetría (grosor corneal) no permitiría otra ablación en condiciones seguras. Una posible solución se puede encontrar en las lentes fabricadas con materiales fotosensibles que, mediante luz ultravioleta, pueden cambiar su geometría – y por tanto su potencia – tras la cirugía [Schwartz et al. 2004].

La modificación de otros parámetros oculares para compensar los posibles errores refractivos se puede analizar como hipótesis a la espera de un futuro desarrollo tecnológico. Este aspecto se tratará con mayor profundidad en el capítulo 2 de esta tesis.

1.2 Propósitos y esquema de desarrollo de la memoria

En este trabajo nos centramos en la caracterización óptica de las IOLs. En particular nos centramos en los aspectos relacionados con el cálculo de la potencia, el diseño de sus superficies, la caracterización y la medida experimental de diferentes parámetros que definen su calidad óptica.

Los objetivos principales de esta tesis son:

1) Realizar una revisión de las fórmulas de cálculo de la potencia de las IOLs. Estudiar las fuentes de error que conllevan errores refractivos postoperatorios. Analizar los distintos grados de libertad no convencionales – más allá de la modificación de la curvatura anterior corneal – que ofrecen los distintos medios oculares para la compensación de estas ametropías. Simular numéricamente cómo afectará la modificación de estos grados de libertad en un ojo real que quedó con refracción residual tras la intervención de cataratas.

2) Aplicar/Implementar las normativas ISO para el análisis de IOLs en banco óptico y detectar sus ventajas e inconvenientes. Diseñar un banco óptico que cumpla con estas normativas y que mejore los inconvenientes detectados en ellas. Además, el dispositivo debe tener suficiente versatilidad para poder realizar modificaciones que hagan que las IOLs se

analicen en condiciones más próximas al ojo humano real. El sistema debe permitir la medida de la eficiencia energética y de la calidad de imagen de una IOL inmersa en el modelo de ojo en función del tamaño pupilar, y la variación de su comportamiento en función de los errores de posicionamiento de la IOL. El banco debe facilitar asimismo el uso de fuentes de luz de diversa longitud de onda, test objeto de diversas características y dispositivos de captación y análisis de señales (espectrofotómetro, sensor de frente de onda, sensor pixelado matricial CCD). El banco y el sistema de captación deben poder adaptarse para evaluar la profundidad de foco.

3) Diseño de un método para cuantificar la eficiencia energética de las IOLs a partir del análisis de la imagen que forman. Aplicar este método a diferentes lentes mono y multifocales y estudiar su comportamiento en función del tamaño pupilar. Además, en el caso de lentes multifocales híbridas (refractivas-difractivas), estudiar la dependencia de la eficiencia en función de la longitud de onda y el orden de difracción.

4) Aplicación a un estudio clínico: realizar un análisis comparativo con los resultados derivados de la actuación quirúrgica. Relacionar la influencia que tiene la eficiencia energética de la IOL multifocal medida *in vitro* con la medida de la estereopsis en pacientes implantados en ambos ojos con lentes del mismo diseño (*in vivo*). Analizar la importancia que tiene la elección del test de estereopsis en la medida de la estereoagudeza en función de su mecanismo de funcionamiento (disociación visual basada en filtros cromáticos o polarizadores).

5) Caracterizar y analizar la calidad óptica de la formación de imágenes de un modelo de ojo con diversos tipos de IOLs. Medir el contraste para la visibilidad de las franjas en frecuencias espaciales relevantes para la función visual. Realizar estas medidas de contraste para distintos diseños de IOLs mono y multifocales y analizar la influencia del diámetro pupilar en los resultados. Comparar las medidas de las Funciones de Transferencia de Modulación (MTF, por sus siglas en inglés) obtenidas para diferentes IOLs analizando, de nuevo, la influencia del diámetro pupilar. Diseño de un

método para caracterizar el halo que se forma en determinadas circunstancias con IOLs mono y multifocales. Aplicar de este método a varios diseños y analizar los resultados obtenidos.

A continuación mostramos un esquema del desarrollo de los contenidos que abarca la investigación llevada a cabo:

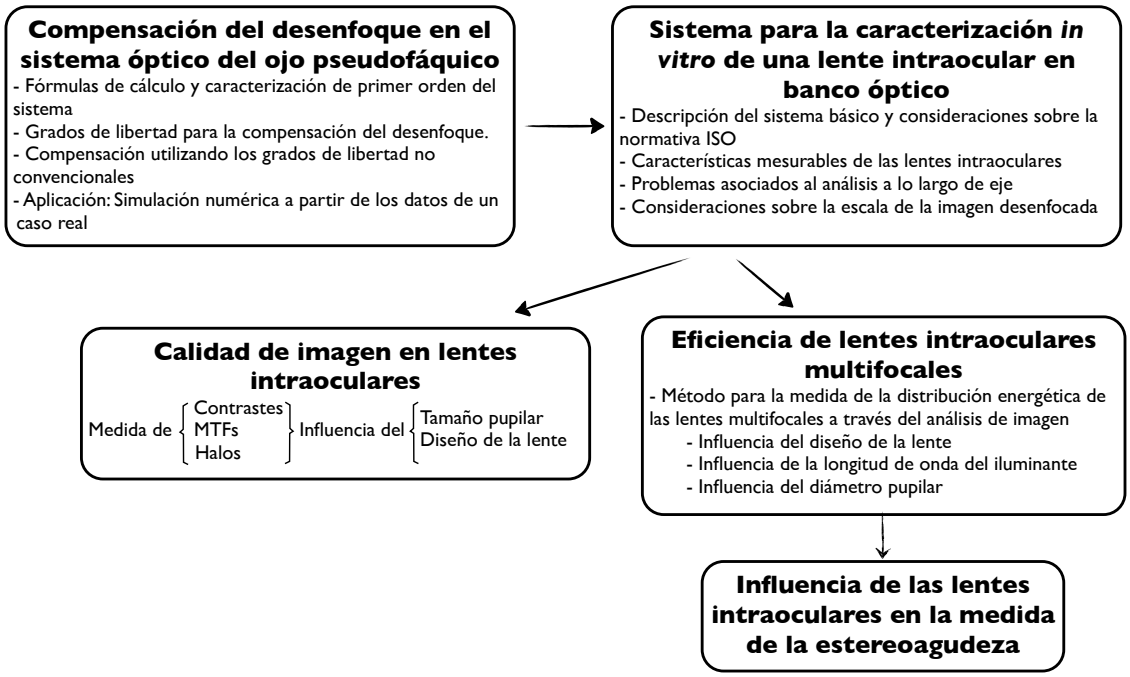

Figura 1.3: Esquema del desarrollo de los contenidos que abarca la investigación llevada a cabo

Esta tesis se presenta en la modalidad de compendio de publicaciones. En este contexto, el esquema de la figura 1.3 ayuda a presentar de forma sintética la organización del trabajo y sirve como referencia para situar en su contexto cada uno de los capítulos incluidos en esta memoria (parte II de la memoria). En cada capítulo se incluyen asimismo referencias a las publicaciones más relevantes del compendio relacionadas con el tema tratado. Finalmente, en la parte III, se anexa una lista de las publicaciones que constituyen el compendio y una selección con la copia impresa en papel de las más relevantes. Por último, en el apartado anexo I, se incluyen dos trabajos clínicos realizados a través un convenio de colaboración con la empresa "Oftalmoplus" en la que se analizan aspectos complementarios que tienen relación directa con los temas tratados en esta tesis. Un dispositivo electrónico con todos los documentos en formato electrónico acompaña la edición de esta tesis.

CAPÍTULO 2

COMPENSACIÓN DEL DESENFOQUE EN EL SISTEMA ÓPTICO DEL OJO PSEUDOFÁQUICO

CHAPTER 2

DEFOCUS COMPENSATION IN THE OPTICAL SYSTEM OF THE PSEUDOPHAKIC EYE

REFERENCE TO THE PUBLICATIONS OF THIS THESIS

The content of this section is included in the publications:

- Alba-Bueno, F., and Millán M.S. *"Defocus correction in the optical system of the eye: Unconventional degrees of freedom".* J Biomed Opt 2011; 16(1) p.016010.
- Alba-Bueno, F., and Millán M.S. "Caracterización Óptica de las Lentes Intraoculares Monofocales: Cálculo de la potencia". Trabajo de Final de Máster 2009.

The most common and important source of image degradation in the visual system is defocus. It is represented by the refractive error (measured in diopters, D), which accounts for the mismatch being between eye power and eye length. Defocus caused by myopia, hyperopia and presbyopia, that are symmetrical, as well as non-symmetrical defocus caused by astigmatism have long been corrected by means of spectacles and/or contact lenses. Nowadays, with the development of new materials, instruments and surgical techniques in ophthalmology it is possible a surgical compensation of defocus, with optical design playing an essential role. Remarkable achievements in the last few decades are based on a permanent

change in some physiological component of the optical system of the eye: corneal refractive surgery (CRS) to modify the corneal curvatures, implantation of intraocular lenses (IOLs), and combined solutions. New advances in IOL designs need, on the one hand, theoretical eye models able to predict optical imaging performance [Atchison and Smith 2000; Navarro 2009] and on the other, testing methods [Norrby et al. 2007; Vega et al. 2010; Alba-Bueno et al. 2011], verification through "in vitro" and "in vivo" measurements [Artal et al. 1995; Barbero et al. 2003], and clinical validation [Norrby 2008b]. The calculation of an IOL implant requires a precise calculation but also an accurate position inside the eye because the effects of IOL misplacements degrade the image very quickly [Atchison 1989].

In this chapter we study the role of an IOL in first order defocus compensation and consider the modification of other ocular parameters for the correction of possible refractive error after the IOL implant. In some problematic cases (i.e. corneal ectasy or corneal transplantation), we consider the possibility of modifying some less conventional ocular parameters than the anterior corneal curvature.

Despite the effort to calculate the IOL power for an absolute error lower than 0.5D, about 90% of postoperative refractive errors fall within ±1.0D and 99.9% within ±2.0D of their targets [Olsen 2007]. Eyes with either large or small axial length and those that have undergone prior CRS usually obtain higher error. Atchison et al. [Atchison et al. 2009] stated that the blur due to defocus establishes the narrowest limits for acceptability. More specifically, a defocus associated with a refractive error ranging in absolute value from 0.5D to 1.0D was classified from troublesome to objectionable (for a 5mm effective pupil and black letter targets). Therefore, some post-surgical refractive errors may require further neutralization by means of corneal ablation that modifies the anterior curvature of the cornea. This is the preferred option in many cases, but it is not always recommendable or even possible. Nowadays the number of patients that underwent prior CRS in their eyes and currently need cataract surgery is increasing. In many cases these patients are not suitable candidates to a second corneal ablation due to the insufficient corneal thickness or the presence of irregularities in the surface that would not admit a second ablation in safe conditions.

Our analysis in this chapter aims to determine which components of the eye would be the most advantageous to modify provided the necessary biocompatible materials were available. Finally, we illustrate all the treated concepts through their application to a real case from the clinical practice.

2.1 IOL power formulae and first-order characterization of anterior eye

One of the most effective ways to compensate for both symmetric defocus and astigmatism is the replacement of the crystalline lens for an IOL. Assuming the thin lens equation in first-order approximation, the IOL power (P_{IOL}) can be computed from the difference between the vergence of the image beam (X') and the vergence of the object beam (X), that is, $P_{IOL} = X' - X$ [Fyodorov and Kolonko 1967; Fyodorov et al. 1975]. These vergences are given by $X = n_q/z$ and $X = n_v/z'$, where n_q, n_v are the refractive indexes of aqueous and vitreous humors, and z and z' are the object and image distances to the IOL plane (thin lens in Figure 2.1), respectively.

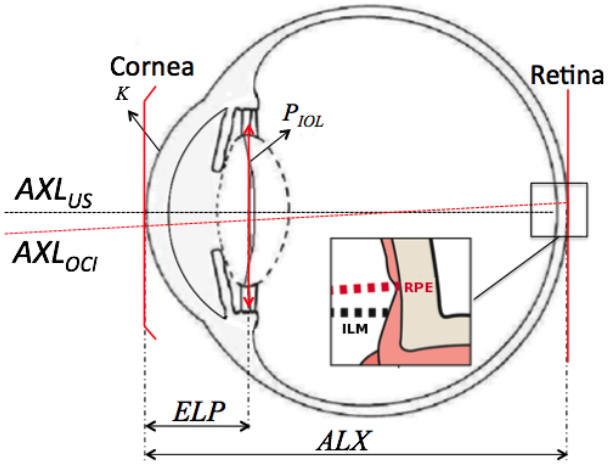

Figure 2.1: Sketch or an eye. See text for abbreviations.

If we assume an object at infinity and a corneal refractive power of K, the cornea images the object at its focal plane (F'), placed at a distance equal to n_q/K from its back principal plane (H') which can be assumed to be very close to the anterior vertex of the cornea (for example, see the Gullstrand eye model (GE) in Ref

[Atchison and Smith 2000]. Provided the distance between the corneal anterior vertex and the IOL, named the effective lens position or plane (*ELP*), can be predicted, then the object distance for the IOL is given by $z=\left(n_q/K\right)-ELP$. The axial length of the eye (*ALX*) is defined as the distance from the anterior vertex of the cornea to the retina. Taking into account these considerations, the first order formula for the calculation of the IOL power is:

$$P_{IOL}=X'-X=\frac{n_v}{ALX-ELP}-\frac{n_q}{\left(\frac{n_q}{K}\right)-ELP}. \qquad (2.1)$$

This simple paraxial approach for the IOL power estimation has encountered many practical difficulties in application due to a number of reasons concerning *in vivo* biometry, eye model-based formulas and their interconnected nuances. These problems are strongly related with any (or some) of these issues: The measurement of the *ALX* , the prediction of the *ELP* , and the optical characterization of the cornea. Lets briefly comment the first two and afterwards we will focus on the third one. For further insight in the field, the reader is addressed to [Olsen 2007; Holladay 2005; Fang et al. 2005].

Axial length of the eye (ALX): This parameter represents an essential measurement in the IOL power calculation because an error of 0.1mm will involves, approximately, a refractive error of 0.27D in the spectacle plane of the eye. The *ALX* can be measured with different techniques and may have a different definition and precision depending of it. Using ultrasound biometry, ALX_{US} is the distance, measured on the optical axis, from the anterior corneal vertex to the internal limiting membrane (ILM in Figure 2.1), the uncertainty of this technique is about 0.15mm. Optical coherence interferometry has been recently introduced as an alternative method to estimate the *ALX* . Using this technique, the ALX_{OCI} is the distance, measured on the visual axis, from the anterior corneal vertex to the retinal pigment epithelium (RPE in Figure 2.1). In this case the uncertainty is about 0.01mm. The clinical advantages and drawbacks of these methods have been

detailed in several works [Olsen 2007; Holladay 2005; Fang et al. 2005; Haigis et al. 2000].

Prediction of the effective lens plane (ELP): This is probably the most critical parameter because it requires an estimation of the postoperative position of the lens with preoperative measurements. From the early formulae, many efforts have been made to improve the IOL power calculation and the accuracy in predicting the postoperative ELP. In this evolution, the formulas derived from a mathematical description of the optical system of the eye have been combined with other formulas based on statistical analysis of a large number of cases. As a result, there are four generations of IOL formulae whose significance and mathematical descriptions are reviewed in [Olsen 2007; Holladay 2005; Fang et al. 2005; Alba-Bueno and Millán 2009].

Optical characterization of the cornea: The corneal power is one of the most important data in the IOL power calculation because it represents 43D of about 60D of the whole eye refractive power. The anterior corneal curvature is easy measurable by topography or keratometry with a precision of about 0.018mm (0.1D) approximately, but the posterior surface has been technically more difficult to characterize. Because of this difficulty, a simplified one-surface model was initially adopted (figure 2.2a), whose refractive power is

$$P_s = \frac{n_s}{f_s} = \frac{(n_s - n_a)}{R_1} \ , \qquad (2.2)$$

where n_a is the refractive index of the air (1.0); n_s is the posterior refractive index, f_s is the focal length measured from the anterior corneal vertex, and R_1 is the anterior radius of the cornea. In keratometry and Placido-disk based topographers the value taken for n_s does not correspond to any real anatomical component; instead, it averages the effects of both the cornea and aqueous humor. In this single-surface cornea model the cornea and aqueous are replaced by one "effective" medium with refractive index of either $n_s = 1.3375$ (e.g. Javal-Schötz keratometers) or $n_s = 1.3315$ (Zeiss intruments). There is a practical reason to take $n_s = 1.3375$ in Eq. 2.2: it relates two round numbers, a corneal curvature of radius

7.50mm for a corneal power of 45.00D [Holladay 1997]. Nevertheless, as we will see later, $n_s = 1.3315$ is the value necessary to obtain, through Eq. 2.2, a refractive power equivalent to that of the cornea in the GE [Olsen 1986]. The value to consider, either 1.3375 or 1.3375, for n_s has been a controversial issue for long. Some authors refer it to an obscure origin [Holladay 1997], while some others try to clarify it [Olsen 1986; Haigis 2003]. The value of n_s is also different depending on the clinical instrument used; for example, Zeiss instruments use $n_s = 1.3315$ whereas Javal-Schötz keratometers use $n_s = 1.3375$. This difference in the value of n_s may lead to an important error in the calculated corneal power for a given curvature radius. For instance, if we change the n_s value, from 1.3315 to 1.3375, in Eq. 2.2 for an anterior cornea radius of R_1=7.7mm, the difference in the corneal power reaches $\Delta P_s = 0.78D$. Thus, when no information about the value of n_s is available, the error in the estimation of the corneal power can be relatively high.

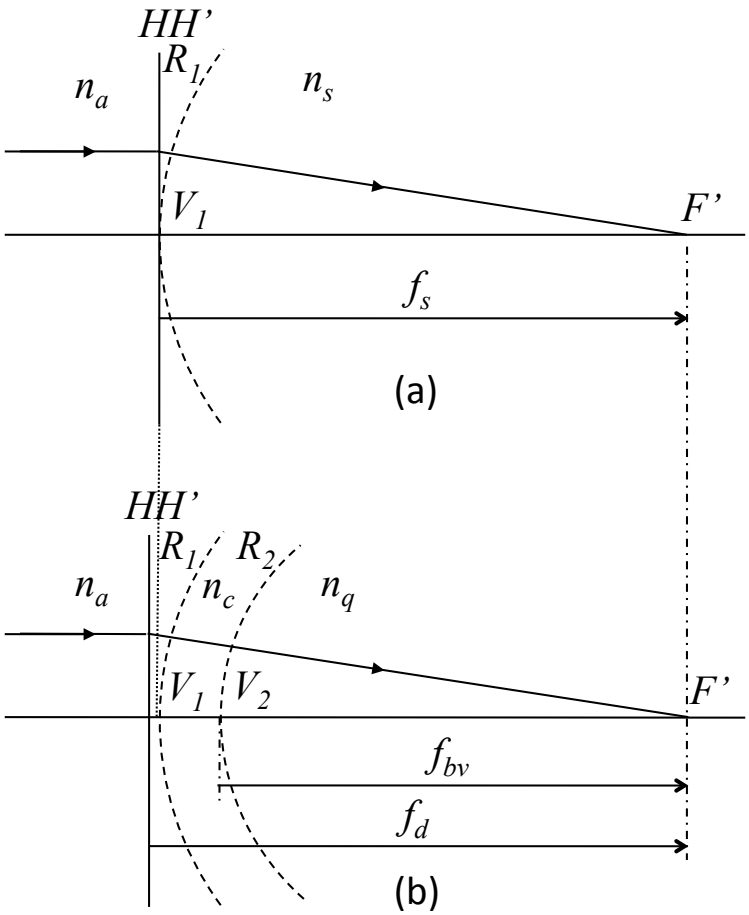

Figure 2.2: Cornea models in first-order optics: a) single surface, b) double surface.

Nowadays, using the slit-scan topography, Scheimpflug topography or optical coherence tomography (OCT), the posterior surface of the cornea can be characterized with a precision of 0.03mm, approximately. Therefore, the calculation can be modified by introducing a thick lens model for the cornea (Figure 2.2b) consisting of three optical materials with their respective refractive indexes (air, n_a; cornea, n_c; and aqueous humor, n_q) and two surfaces of radii R_1 and R_2 separated by a distance e. There are more advanced models that consider the asphericity of the surfaces and its influence in the aberrations of the eye[Liou and Brennan 1997; Kiely et al. 1982; Dubbelman et al. 2002; Navarro 2009], but, since we are currently interested in defocus, a first-order approach and spherical surfaces will suffice in our work. In this situation, the paraxial power of the cornea is given by:

$$P_d = \frac{n_q}{f_d} = P_1 + P_2 - \frac{e}{n_c} P_1 P_2 , \tag{2.3}$$

and the positions of the principal planes (H, H') with respect to the anterior and posterior vertexes (V_1 and V_2 respectively) are given by:

$$V_1 H = -\frac{e n_a P_2}{e P_1 P_2 - n_c \left(P_1 + P_2\right)} , \tag{2.4}$$

$$V_2 H' = \frac{e n_q P_1}{e P_1 P_2 - n_c \left(P_1 + P_2\right)} . \tag{2.5}$$

In these equations, the refractive powers of the corneal surfaces are given by $P_1 = \left(n_c - n_a\right) \big/ R_1$ (anterior) and $P_2 = \left(n_q - n_c\right) \big/ R_2$ (posterior).

The back vertex focal length $f_{bv} = V_2 F'$ differs from the focal length $f_d = H'F'$ in the corneal thickness (Figure 2.2b) and the back vertex corneal power can be expressed as:

$$P_{bv} = \frac{n_q}{f_{bv}} = \frac{n_q}{f_d + V_2 H'} . \tag{2.6}$$

The back vertex power is very used in ophthalmic optics because it is a good approximation to the focal length and is much easier to measure.

All three quantities P_s, P_d and P_{bv}, though different, are commonly used for the value of K in Eq. 2.1 thus affecting the accuracy in calculating the IOL power. Let us further illustrate the use of these quantities. Figure 2.2b shows the results obtained for f_d and f_{bv} when the values of the GE are introduced in Eqs. 2.3-2.6. In such a case, the refractive power of the cornea is 43D. In this situation the principal points H and H' are almost in the same position and very close to V_1, the anterior corneal vertex [Atchison and Smith 2000]. Let us recall that, in the single-surface model (figure 2.2a) the principal points coincide with the surface vertex as well. This fact justifies the simplification of using a single surface model placed at the anterior vertex as a fair approximation to the real double-surface cornea. This explanation must be included wherever the approximation of the single-surface model of the cornea needs to be clarified. It is a good option to keep the same anterior refractive index (air) and the same anterior curvature R_1 in the single-surface model although it is not essential. To complete this approach, it is necessary to calculate a refractive index n_s, equivalent to the joint contribution of cornea and aqueous humor. To this end we can take $P_s = P_d$, that is, making Eq. 2.2 equal to Eq. 2.3. This result was derived for the GE by Haigis [Haigis 2003] who obtained $n_s = 1.3315$.

A similar, but poorer, approach takes $P_s = P_{bv}$, that is, makes Eq. 2.2 equal to Eq. 2.6, which results in $n_s = 1.3375$. Despite it leads to a less accurate result, this value is used in most of the clinical keratometers.

Whilst some investigators have pointed out the confusion regarding the value of n_s, there still exist some ambiguity in the clinical practice and the literature. It is important to emphasize that the refractive index of the aqueous humor n_q is before the lens, not the fictitious and misleading n_s, and there is not any surface between the cornea and the lens as it appears in some eye models (see Table 1 in [Norrby et al. 2007].

When the radii ratio R_1/R_2 or the cornea thickness are different from those values of the GE model, then the approach of the cornea by a single surface must be revised and the values calculated for n_s can be no longer valid. Generally, this ratio is not fulfilled by patients who have undergone corneal ablative refractive surgery (LASIK, PRK…) where the anterior corneal curvature has been modified (see, for instance, the numerical example of a real case in Section 2.3) or in patients with irregular astigmatism (keratoconus or pellucid marginal degeneration). To correctly calculate the IOL power in these cases it is necessary to adopt the more complete double surface model [Haigis 2003].

In conclusion, as a general practice, it is recommendable to replace the traditional single surface model of the cornea for the double surface model because:

- The technological advances allow reliable measurements of the posterior surface.

- The number of patients whose ocular parameters differ significantly from those of the GE is increasing due to the extended application of CRS.

- There is an increasing demand to calculate the IOL power more accurately.

2.2 Other degrees of freedom for defocus compensation

Intraocular lens implantation has proved to be an effective method to compensate for defocus and astigmatism in patients who undergo cataract surgery. Additionally, IOLs are usually proposed as alternative to CRS in cases of high ametropy, corneal pathology or, even, presbyopia. However, it is not always easy to calculate precisely the refractive power of the IOL, its final position in the eye after surgery, and there are still differences between a real human eye and the model used for the calculations. These facts can lead to unexpected postoperative refractive errors (called “refractive surprises” in ophthalmological literature) that may require additional correction or compensation for defocus. In some cases it is recommended to perform a CRS for correction. However, it is not always possible, particularly in patients who have already undergone this kind of surgery before the IOL implant because their corneal thickness may not allow a new ablative process.

In this section we analyze other permanent changes in the ocular optical system, different from reshaping the anterior corneal surface, to compensate for a residual refractive error: changes in the corneal refractive index, its thickness or posterior radius, and changes in the refractive indexes of the aqueous or vitreous humors. Obviously, all of them would require a surgical action and, to the best of our knowledge, they have been neither proposed nor implemented yet in clinical practice. The effectiveness of each change is analyzed here by considering, as an example, the GE with two variants: The GE and an IOL implanted Gullstrand eye (IGE). The latter is described as the Gullstrand eye with an IOL implanted instead of the lens. As for the IOL we consider an optical component with the following parameters: $R_1 = 19.35mm$, $R_2 = -19.35mm$, $d = 1.164mm$, $n = 1.55$, $ELP = V_1L_1 = 5.50mm$, which can be representative of currently available monofocal acrylic IOLs.

We use first-order optical ray-tracing to study the effect of small changes in different parameters in both the GE and the IGE. When the eye is emmetropic the far object point, conjugate to the retina, is at infinity. After slightly changing one of the parameters (±1%, ±2%, ±3%), the refractive error can be computed through the calculation of the new position of the far point. The vergence of the far object point, relative to the anterior vertex of the eye gives the refractive error (Table 2.1 and Figure 2.3). Atchison and Smith [Atchison and Smith 2000] did something similar for the GE, but there is a difference to point out from our study. They computed the refractive error through the vergence of the far object relative to the first principal plane of the eye. In this aspect, since the principal planes change in their positions with the parameter changes, we use the anterior vertex of the eye in order to establish a more stable origin from which distances to the far object point can be referred. In fact, both calculations yield very close values for the refractive errors (differences hardly reach 10^{-3}D). Whenever is possible, we compare their results with ours, as detailed in the next paragraphs.

Table 2.1: Effects of small parameter changes on the variation in refractive error using Gullstrand eye model and first-order optical calculation. Two variants of eye model are considered: Gullstrand eye (GE) and the IOL implanted Gullstrand eye (IGE). Parameters of the IOL are specified in the text. The changes are introduced in the values of the GE parameters, which are taken as reference for the calculation. These results are plotted in Figure 2.3.

		Refractive error in model eyes (D)					
Parameter change		-3%	-2%	-1%	+1%	+2%	+3%
Parameter	*Model eye*						
n_c	GE and IGE	-0,530	-0,351	-0,175	0,173	0,345	0,515
R_2	GE and IGE	0,176	0,116	0,057	-0,056	-0,111	-0,165
n_q	GE	2,424	1,619	0,811	-0,814	-1,630	-2,450
	IGE	4,075	2,718	1,360	-1,361	-2,724	-4,089
n_v	GE	-5,315	-3,501	-1,729	1,689	3,339	4,952
	IGE	-2,738	-1,815	-0,903	0,893	1,775	2,648
Parameter change (μm)		-150	-100	-50	+50	+100	+150
e	GE and IGE	+0,261	+0,174	+0,087	-0,086	-0,173	-0,257

2.2.1 Change of corneal parameters

The ablative CRS procedure changes the anterior corneal surface, that is the element in the ocular optical system with higher influence on the refractive power. But there are still three other degrees of freedom in the cornea lens on which we may think to act: its refractive index, the thickness and the posterior curvature. Figure 2.3 shows the refractive errors induced by a change of ±1%, ±2% and ±3% in the corneal refractive index (blue line with circles, n_c), posterior radius of curvature (red line with squares, R_2) or a change in ±50, ±100 and ±150μm in the corneal thickness (purple line with triangles, e). The numerical data of these plots are contained in table 2.1. We can see how the influence of these modifications is small in terms of refractive error agreeing with Atchison and Smith [Atchison and Smith 2000]. We have also computed the influence of these changes on the position of the principal planes H, H' and the results are plotted in figure 2.4. As we can see, the positions of the principal planes remain close together and slightly shifted away from the anterior corneal vertex (less than $20\mu m$). The effects of such parameter changes remain constant for both the GE and the IGE (table 2.1 and figure 2.3).

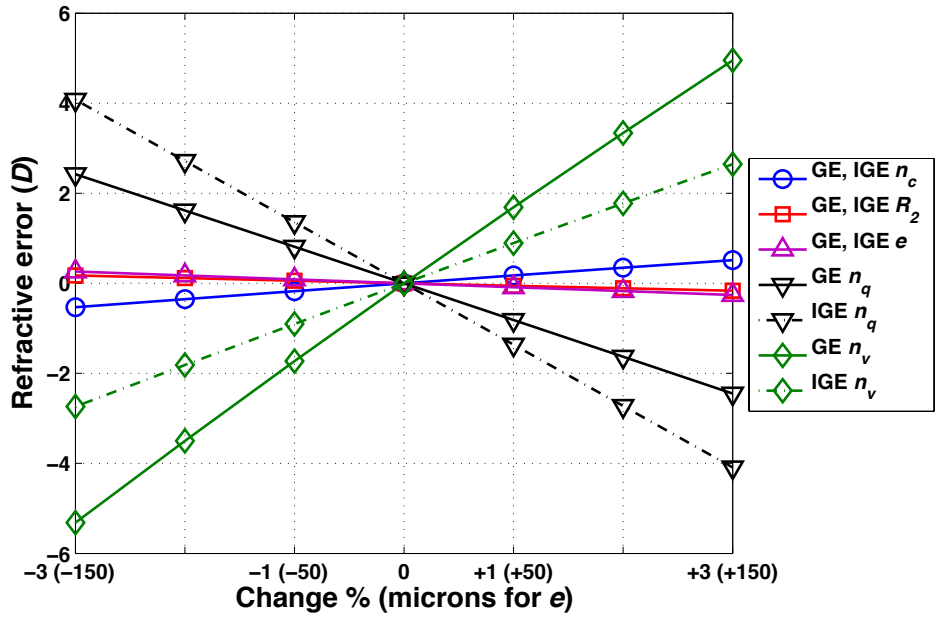

Figure 2.3: Graphs corresponding to data contained in Table 2.1. The refractive error is plotted versus a change in a parameter (n_c, R_2, e, n_q, n_v) for GE and IGE.

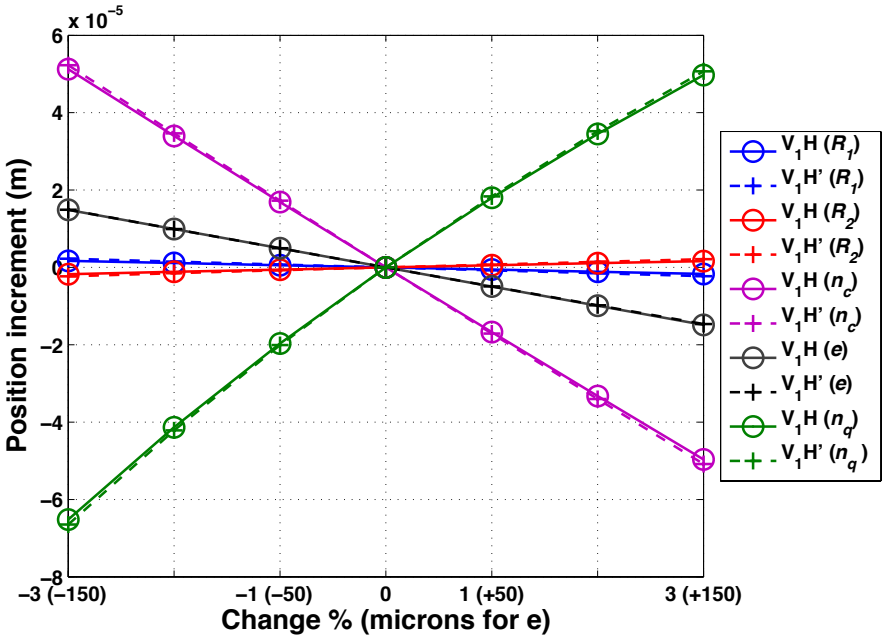

Figure 2.4: Effects of the variation of corneal parameters n_c, R_1, R_2, e, n_q on the position of the corneal principal planes V_1H, V_1H' in the GE eye model.

For defocus compensation, a change in one of the three corneal parameters considered above is of little effectiveness in the GE cornea. According to Atchison and Smith, about three times lesser than a change in the corneal anterior curvature [Atchison and Smith 2000] In addition, an anterior curvature change is compatible with a non-symmetrical shape to compensate for both defocus and astigmatism. These properties clearly justify the anterior CRS. However, as we will see in the next paragraph, changes in other parameters of the eye can even be more effective.

2.2.2 Change of humor refractive indexes

A small change in the crystalline lens has a much more important effect on the refractive error in the GE than a similar variation in any other lens parameter (thickness or curvatures). For instance, Atchison and Smith [Atchison and Smith 2000] computed a refractive error of -2.298D induced by a change of +1% in the refractive index of the lens, whereas it was inferior to +0.05D for the same amount of variation in any of its radius. Nowadays, IOLs are made of a variety of refractive indexes than can go from 1.40 up to 1.55. From a practical point of view, the higher the IOL refractive index, the higher the index difference between the lens and aqueous and vitreous humors, thus allowing lower lens curvatures and thinner thicknesses. This facilitates the folding and, consequently, the insertion of the IOL in the eye. The effects of changing the refractive indexes of aqueous and vitreous humors are also plotted in figure 2.3 and table 2.1 and are very interesting. An increment of +1% in the refractive index of the humors results in a refractive error of opposite sign and different magnitudes (-0.813D for the aqueous and +1.689D for the vitreous). These calculations agree with those computed by Atchison and Smith [Atchison and Smith 2000], which in turn are much higher values than the refractive error they obtained for a similar change in the corneal anterior curvature (+0.483D). It is important to emphasize that, at least theoretically, a change in the refractive index of those humors can be much more effective than a change in the corneal anterior curvature to achieve the targeted refractive result. In eyes that have undergone vitrectomy, the vitreous cavity is filled with silicon oil, whose refractive index is about 1.4034, which represent a change of +5% with respect to the refractive index of natural vitreous (1.336). In these cases, an

additional power must be added to the original IOL calculation as reported and formulated by Meldrum and co-workers [Meldrum et al. 1996].

Clearly, the refraction indexes of the aqueous and vitreous humors constitute two additional and effective degrees of freedom to exploit in the development of new techniques for refraction error compensation and this is a key conclusion of this work. These new techniques, which also entail a challenge to develop biocompatible materials with the requested optical properties, could be applicable to natural eyes and to eyes with some prior surgical action. In the case of GE, small changes in the refractive index of the aqueous humor are less effective than changes in the vitreous humor (table 2.1 and figure 2.3). In the case of IGE, the effectiveness of changes in the refractive indexes of the aqueous and the vitreous humors are strongly dependant on the refractive index of the implanted IOL. If the IOL has a relatively high refraction index, such as in the IGE of table 2.1, changes in the aqueous humor are more efficient than changes in the vitreous humor. This technique of modifying the refractive index of the eye humors would be adequate to compensate for symmetrical defocus, such as that caused by spherical ametropia, but it is not clearly applicable to compensate for astigmatism, unless the material injected had specific non-symmetrical opto-mechanical properties or could be provided with them by means, for instance, of laser radiation. We also think that it would be promising that the material used to replace the aqueous or vitreous humor showed dispersive characteristics that could compensate for the chromatic aberration of the eye in some extent. The results presented in table 2.1 and figure 2.3 would not be the same if gradient index profiles had been considered for the lens (crystalline or IOL) but, at least, they would be useful to show the tendencies.

2.3 Numerical example of a real case

In this section we present a real case of a patient who underwent corneal refractive surgery (LASIK) and some years later required cataract surgery with IOL implantation. The numerical data and the method of measure used to obtain each parameter are shown in table 2.2. As we stated previously, IOL power calculation after any form of CRS is problematic and, consequently, the final refractive result

may still end up with the so-called "refractive surprise". In this case, the postoperative refractive error was measured through the subjective refraction three months after the surgery and it turned out to be -1.25D.

Table 2.2: Data of the eye that underwent CRS prior to IOL implant.

Magnitude		Value	Source
Axial length (*mm*)	ALX	25.57	Partial coherence interferometry
Cornea			
Anterior radius (*mm*)	R_1	8.82	Scheimpflug topography
Posterior radius (*mm*)	R_2	6.38	Scheimpflug topography
Central thickness (*mm*)	e	0.501	Scheimpflug topography
Front principal plane (μm)	V_1H	-62.61	Calculated (-49.65μm in GE)
Back principal plane (μm)	V_1H'	-67.79	Calculated (-50.62μm in GE)
Refractive power (single surface) (*D*)	P_s	37.59 38.27	Calculated taking n_s=1.3315 in Eq.2 Calculated taking n_s=1.3375 in Eq.2
Refractive power (double surface) (*D*)	P_d	36.46	Calculated (43.05*D* in GE)
Back vertex power (double surface) (*D*)	P_{bv}	37.03	Calculated (43.83*D* in GE)
Intra Ocular Lens			
Anterior radius (*mm*)	R_1^{IOL}	8.081	Supplied by manufacturer
Posterior radius (*mm*)	R_2^{IOL}	-15.72	Supplied by manufacturer
Central thickness (*mm*)	e^{IOL}	1.091	Supplied by manufacturer
Refractive index	n^{IOL}	1.47	Supplied by manufacturer
Refractive power (*D*)	P_{IOL}	20,0	Supplied by manufacturer
Effective lens position (mm)	ELP	4.83	Ultrasound
Refractive Error (D)	R_x^S	**-1.25**	Subjective postoperative refraction
	R_x^C	**-1.29**	Calculated

The cornea has been characterized paraxially using Eqs. 2.2 to 2.6 considering the data provided. The principal planes of the cornea are very close to one another, but their distance from the anterior vertex is somewhat longer than in the GE. The corneal powers P_s, P_d, P_{bv} also vary from the GE and the values obtained are

significantly different dependent on whether the single surface or the double surface model is considered. Finally, we found a good agreement between the calculations of the refractive error (-1.29D) and the subjective refraction (-1.25D), assuming that the minimum step for subjective refraction in clinical practice is ±0.25D. This amount of myopia leads to an unacceptable loss of visual acuity [Atchison et al. 2009] and a need for defocus compensation (spectacle or contact lenses). In this study, we have also explored the possibility of targeting emmetropy by modifying some other eye parameters among n_c, R_2, n_q, n_v, e. The resulting refractive errors after introducing slight changes in each parameter are presented in table 2.3. In this case, good options to obtain emmetropy (i.e. with a refractive error lower than $\pm 0.25D$) would be represented by either a -2% change in n_q, or a +1% in n_v, or a +2% in n_c. In the last case, the relative importance in the n_c can be explained because of the flattening of the anterior corneal surface after CRS (R_1=8.82mm).

Table 2.3: Refractive error (D) that results from the introduction of parameter changes in the real case of the numerical example. The best options to obtain emmetropy, with errors lower than ±0.25D appear underlined and boldfaced.

	Refractive error (D)						
Parameter change (%)	-3%	-2%	-1%	0*	+1%	+2%	+3%
n_c	-2,915	-2,371	-1,829	-1,290	-0,753	**-0,217**	+0,316
R_2	-1,102	-1,166	-1,229	-1,290	-1,350	-1,409	-1,467
n_q	+0,888	**+0,170**	-0,557	-1,290	-2,031	-2,778	-3,533
n_v	-4,537	-3,443	-2,360	-1,290	**-0,231**	+0,816	+1,852
Parameter change (μm)	-150	-100	-50	0*	+50	+100	+150
e	-1,103	-1,165	-1,228	-1,290	-1,352	-1,414	-1,475

** When no change is introduced, the relative error is the value obtained after CRS and IOL implant (-1.29D), see also table 2.2.*

2.4 Conclusions

Apart from spectacles and contact lenses, permanent modifications of the anterior eye optical system, either anterior refractive surgery or IOLs or both, are commonly applied to compensate for defocus. Defocus compensation can be dealt with in first-order (Gaussian) optics and this sort of correction is prior to other compensation intended for high order aberrations.

Although there has been an increasing interest in developing new and improved formulas for IOL power calculation, there still are several sources of uncertainty that may well give rise to a residual refractive error. The sources of this uncertainty that are related to the cornea have been reviewed in this chapter. They are particularly important in the case of patients who have undergone CRS. We have explored the possibility of introducing changes in other parameters of the eye to compensate for the refractive error and have illustrated their effectiveness in some cases: GE, IGE, and a clinical case of a real human eye that has undergone anterior refractive surgery and cataract surgery with IOL implant.

The results show that changes in the corneal refractive index, thickness or posterior radius of curvature have relatively little effect on the overall refractive error. However, small changes in the refractive indexes of the aqueous or the vitreous humors are highly effective, much more than a similar amount of change in the anterior curvature of the cornea. This fact opens new and attractive possibilities to compensate for defocus, through the introduction of changes in degrees of freedom that have been considered unconventional up until now. Our results agree with the results formerly obtained by Atchison and Smith for the GE [Atchison and Smith 2000].

Although some questions arise concerning biocompatibility, stability, and drainage, the great progress experienced in the generation of new materials allows us to think positively and consider our proposal as the basis of promising upcoming techniques.

CAPÍTULO 3

SISTEMA PARA LA CARACTERIZACIÓN DE UNA LENTE INTRAOCULAR EN BANCO ÓPTICO

CHAPTER 3

INTRAOCULAR LENS CHARACTERIZATION OPTICAL BENCH SYSTEM

REFERENCE TO THE PUBLICATIONS OF THIS THESIS

The content of this section is included in the publications:

- Alba-Bueno, F., Vega, F. and Millán M.S. *"Design of a test bench for intraocular lens optical characterization".*J Phys: Conf Ser 2011; vol.274, p.012105.
- Millán M.S., Alba-Bueno, F., and Vega F. *"New trends in intraocular lens imaging".* Proc SPIE 2011; vol.8011, p.80119I.

Actualmente existe una normativa estándar ISO [11979-2; 11979-9] que regula cómo se deben medir diferentes parámetros de las IOLs. Esta normativa está diseñada para el control de calidad industrial y en muchos aspectos no refleja las condiciones reales en las que después se encontrarán implantadas estas lentes.

En nuestro caso, se ha realizado el diseño de un montaje específico en banco óptico (del inglés IOL-tester) para ajustarse a la normativa ISO, por un lado, pero también para tener mayor versatilidad y poder ajustarnos en la medida de lo posible a las características fisiológicas oculares.

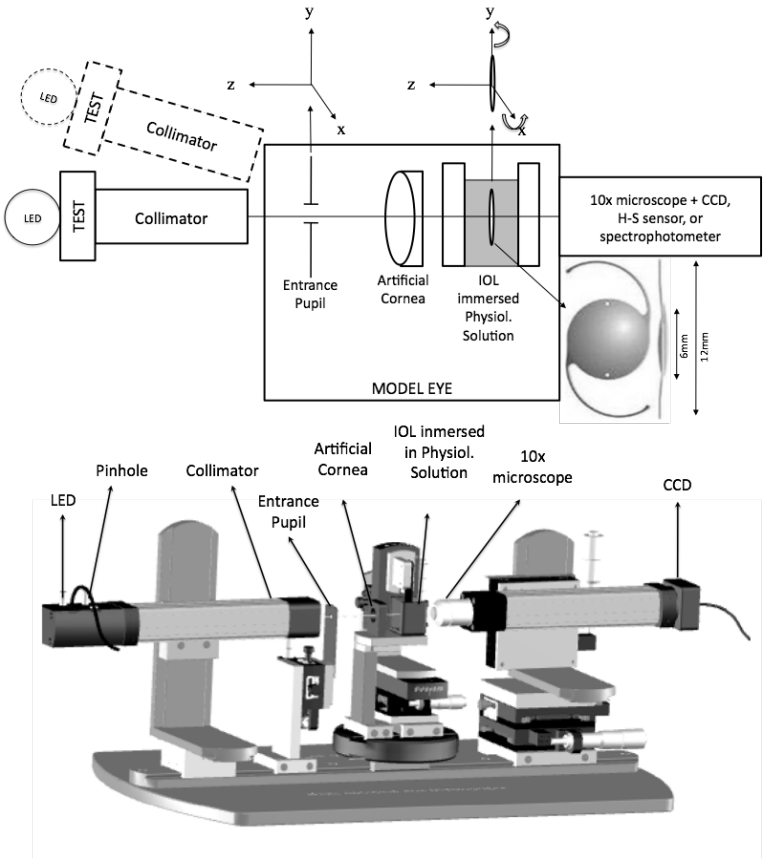

Figura 3.1: Superior: esquema del IOL-tester. Inferior: Imagen del dispositivo.

3.1 Descripción del sistema básico

Las partes principales del IOL-tester son:

- Un sistema de iluminación que consta de una fuente de iluminación, un test objeto y una lente.

- Un modelo de ojo con pupila de entrada, una córnea artificial y una cubeta transparente que contendrá a la IOL inmersa en solución salina.

- Y, por último, un sistema de captación que analice la imagen del objeto formada por el modelo de ojo. Un sensor en el plano de captación haría las funciones de la retina humana. En su lugar, un sistema capta la imagen aérea, real, formada por el modelo de ojo. El sistema incluye generalmente un sistema de aumento (microscopio), pero también puede consistir en un sensor de Hartmann-Shack para la medida del frente de onda, un espectrofotómetro para medir el espectro cromático de la señal, etc.

Un esquema del montaje y una imagen del dispositivo se pueden ver en la figura 3.1. En la mayoría de los casos estudiados, el modelo de ojo opera con objeto en el infinito, por lo que el test se sitúa en el plano focal objeto de la lente del sistema de iluminación (lente colimadora).

3.1.1 Sistema de presentación del objeto al modelo de ojo

Es un sistema de iluminación que consta de tres partes principales que se detallan a continuación:

- Las fuentes de luz: La normativa ISO señala que el iluminante sea de una longitud de onda de 546±10nm. Puesto que, en condiciones reales de visión, la luz no es monocromática, nuestro IOL-tester dispone de cuatro fuentes de luz tipo LED: tres fuentes cuasi-monocromáticas con radiancias centradas en las bandas espectrales roja (λ_r=637nm), verde (λ_g=521nm) y azul (λ_b=459nm) y otra fuente de luz blanca. De todas ellas, la fuente de luz verde es la que mejor satisface los requisitos de la norma ISO. El espectro de emisión de los LEDs está representado en la figura 3.2.

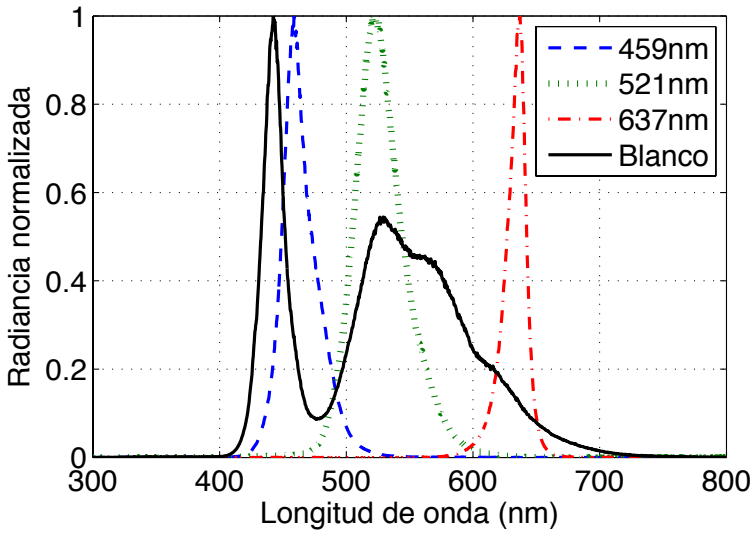

Figura 3.2: Medida experimental de la distribución espectral de los cuatro LEDs utilizados como fuentes de iluminación. Radiancias normalizadas la radiancia de cada LED.

- Tests objeto: Orificios circulares (pinholes) de diferentes diámetros, tests de resolución USAF, tests con cuadrículas, bordes, etc. (ver figura 3.3). A partir de la imagen que forma el modelo de ojo de estos tests se

pueden evaluar diferentes magnitudes para caracterizar ópticamente un sistema óptico. En particular, nos referimos a la distancia focal, la Función de Transferencia de Modulación (MTF, por sus siglas en inglés Modulation Transfer Function), la Razón de Sthrel (SR, del inglés Sthrel Ratio), la Función de Extensión del Punto (del inglés Point Spread Function, PSF), el contraste para una determinada frecuencia espacial, el Error Cuadrático Medio (RMS, del inglés Root Mean Square) etc. El diámetro del pinhole es un parámetro incómodo puesto que tiene que ser lo suficientemente grande para permitir el paso de una cierta cantidad de luz pero, por otro lado, tiene que ser lo suficientemente pequeño para obtener un frente de onda plano (ver figura 3.4). En nuestros montajes consideraremos que un frente de onda plano se obtiene al utilizar diámetros de pinhole por debajo (o iguales) a $200\mu m$.

- Lente: la normativa ISO exige que el objeto se sitúe en el infinito lo que corresponde a una simulación de la visión de lejos. Para ello el test objeto está colocado en el punto focal objeto de una lente colimadora acromática de 200mm de focal. Para estudiar la visión a distancias intermedias y cercanas se puede situar el test objeto a una distancia de la lente inferior a su distancia focal, de manera que la lente formará una imagen virtual del test objeto a la distancia deseada. Otra opción es colocar el test directamente a una distancia determinada, sin la lente colimadora. Alternativamente, se pueden utilizar lentes de potencia negativa delante de la córnea artificial. Para vergencias objeto positivas, se puede poner el test objeto a una distancia de la lente superior a su distancia focal. Otra posibilidad para estudiar la visión a distancias intermedias consiste en actuar en el espacio imagen, desplazando convenientemente el sistema captador de imagen a lo largo del eje óptico (ver apartados 3.2 y 3.3).

Todo el sistema de iluminación está montado en un brazo giratorio que ofrece la posibilidad de utilizar una iluminación fuera de eje en el modelo de ojo.

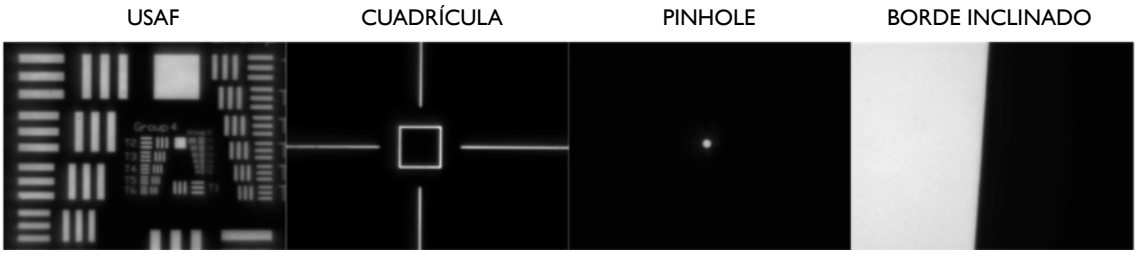

Figura 3.3: Tests utilizados para calcular los parámetros ópticos de las lentes.

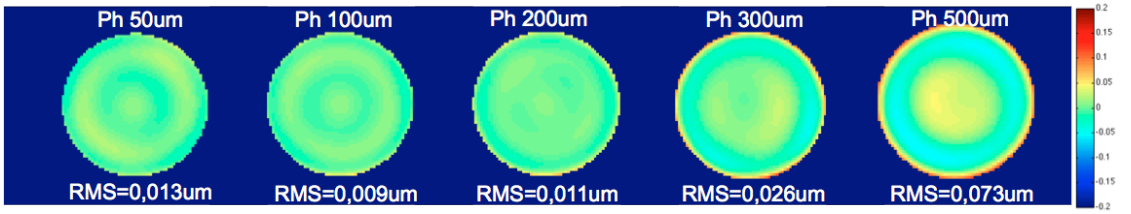

Figura 3.4: Medidas experimentales y representación en pseudocolor de los frentes de onda y sus RMS medidos en haces colimados utilizando una pupila de entrada de 6mm y diferentes diámetros de pinhole.

3.1.2 Modelo de ojo

La normativa ISO recomienda utilizar una córnea libre de aberraciones a pesar de que las córneas humanas no suelen ser así [Artal and Guirao 1998; Guirao et al. 2000; Wang et al. 2003]. Existen IOLs diseñadas para compensar parcial o totalmente la aberración esférica inducida por la córnea humana promedio. Por esta razón, además de disponer de una córnea artificial libre de aberraciones ópticas (LAO), como indica la normativa, disponemos también de córneas (DCX) que inducen una cantidad de aberración esférica (SA, por sus siglas en inglés Spherical Aberration) similar a la de la córnea humana. Se puede encontrar un procedimiento para diseñar córneas con la cantidad de SA deseada en el trabajo de Vega et al. [Vega et al. 2010]. El análisis de los frentes de onda que emergen de las dos córneas – LAO y DCX – muestra, al realizar la expansión en los polinomios de Zernike, que éstas sólo difieren significativamente en el coeficiente correspondiente a la SA de tercer orden, que alcanza el valor de $+0.122\mu m$ para la córnea DCX (tabla 3.1). Los valores de los demás coeficientes son muy pequeños en general, lo cual indica la práctica inexistencia de otras aberraciones en el frente de onda.

En la figura 3.5 se representan las siguientes características medidas experimentalmente con el sensor de Hartmann-Shack para ambas córneas artificiales: la medida de la MTF con referencia al límite de difracción , el frente de

ondas, el coeficiente de Zernike correspondiente a la SA de tercer orden, la PSF y la SR para una pupila de 6*mm*. Las medidas del coeficiente de SA (Z_8, también representado por c[4,0]) en función del diámetro pupilar y del LED utilizado se muestran en la figura 3.6.

Tabla 3.1: Análisis del frente de onda mediante desarrollo en polinomios de Zernike de las córneas artificiales LAO y DCX para una pupila de entrada de 6mm.

Coeficiente de Zernike	LAO(µm)	DCX(µm)
Astigmatismo 0º (Z_4)	+0,014	+0,017
Astigmatismo 45º (Z_5)	+0,003	-0,009
Coma 0º (Z_6)	-0,020	-0,003
Coma 90º (Z_7)	+0,013	+0,011
SA de 3er orden (Z_8)	+0,020	**+0,122**
Trefoil 0º (Z_9)	+0,003	+0,010
Trefoil 90º (Z_{10})	+0,012	+0,001
SA de 5º orden (Z_{15})	+0,009	+0,015
Astigmatismo 0º (Z_4)	+0,014	+0,017

Para simular las condiciones reales de la IOL en el ojo, ésta debe estar inmersa en solución salina. Según la norma ISO, el haz convergente refractado por la córnea debe iluminar los 3.0±0.1mm centrales de la IOL. Para ello, el IOL-tester diseñado en nuestro trabajo dispone de un diafragma situado delante de la córnea artificial que hace las funciones de iris ocular, regulando el diámetro efectivo de la apertura.

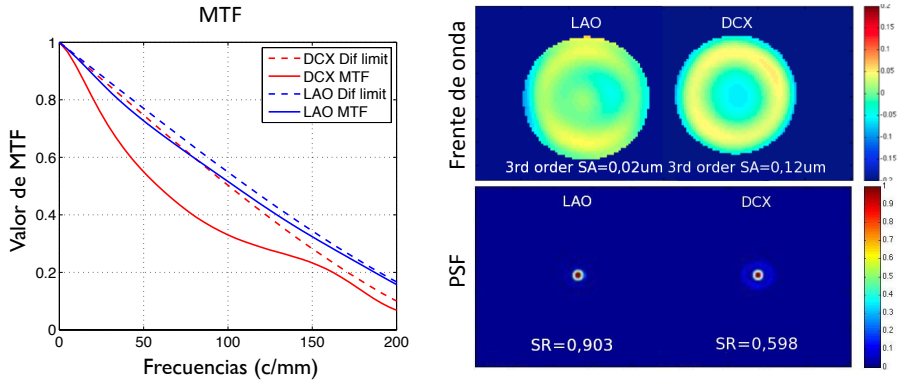

Figura 3.5: Medidas experimentales con pupila de entrada de 6mm. Izquierda: MTFs (líneas continuas) y límite de difracción (líneas discontinuas) de las córneas artificiales (en rojo la DCX, afectada de SA; y en azul la LAO, libre de aberraciones). Derecha superior: Representación en pseudocolor del frente de onda y valor numérico SA de tercer orden, que corresponde al coeficiente de Zernike Z_8. Derecha inferior: PSF y valor de la SR.

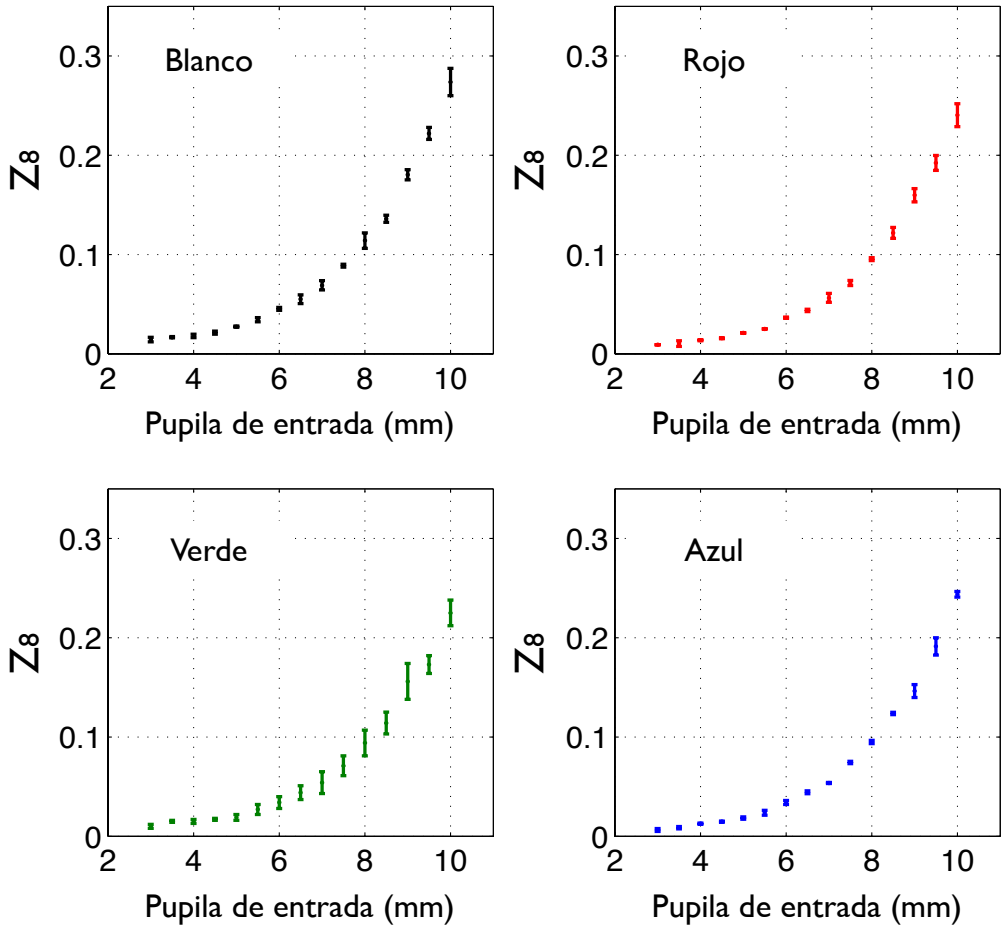

Figura 3.6: Medida experimental de los coeficientes Z_8 (o c[4,0]) de Zernike correspondiente a la aberración esférica para la lente DCX en función del diámetro pupilar (media de tres medidas y desviación estándar).

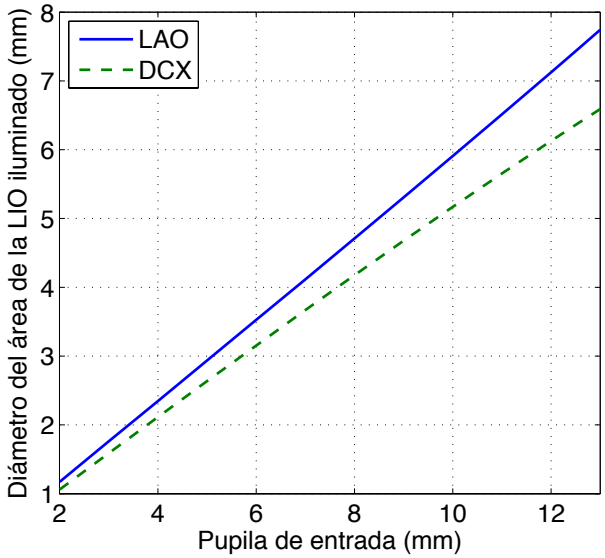

Figura 3.7: Relación existente entre la pupila de entrada (diámetro del diafragma) y el diámetro de la zona iluminada de la IOL para cada córnea artificial.

La relación existente entre el diámetro de la pupila de entrada y el diámetro de la zona iluminada de la IOL se muestra en la figura 3.7 para cada lente (LAO y DCX). El hecho de que la pupila de entrada se encuentre delante de la córnea artificial limita las posibilidades de nuestro montaje de modo que, en la práctica, sólo se puede utilizar iluminación en eje, es decir, hemos de considerar que el haz objeto ha de estar alineado con el eje óptico del modelo de ojo. Para trabajar con haces objeto fuera de eje sería necesario que la pupila de entrada se situara sobre la IOL, pero en nuestro caso es difícil debido a la limitación de espacio dentro de la cubeta.

Para asegurar el correcto centrado de la IOL en el eje óptico se dispone de tornillos micrométricos para el ajuste lineal en los ejes X, Y, Z así como un control de la inclinación en dos ejes.

En la tabla 3.2 se muestra un resumen de las curvaturas y distancias de cada una de las superficies del modelo de ojo.

Tabla 3.2: Características del ojo modelo con la córnea DCX.

Superficie	Radio (mm)	Espesor (mm)	Índice de refracción
Objeto		Infinito	1
Pupila de entrada	-	-	-
Córnea Sup. anterior	35.99	4.29	1.4599
Córnea Sup. porterior	-35.99	8.6	1
Cubeta anterior	Plano	6	1.5185
cubeta posterior	Plano	6.25	1.336
IOL	Plano	10	1.336
Pared anterior	Plano	6	1.5185
Pared posterior	Plano	9.24	1
Imagen	---	---	---

3.1.3 Análisis de la imagen y del frente de onda.

La imagen del test formada por el modelo de ojo con la IOL se capta mediante un microscopio de pocos aumentos (por ejemplo10*x*) acoplado a un sensor pixelado matricial CCD. Mediante el análisis de este tipo de imágenes se pueden calcular los distintos parámetros que caracterizan la calidad óptica del modelo de ojo tales como:

- La MTF: puede ser calculada a partir del análisis de la imagen formada por un test puntual pinhole o por un test de escalón o de borde ligeramente inclinado.
- La PSF: a partir de la imagen de un pinhole.
- Contraste para una frecuencia espacial: a partir del test USAF.
- Resolución del sistema: a partir del test USAF (y a partir de la MTF).
- La distancia focal del sistema: a partir del test USAF y a partir del test cuadrícula.

Un ejemplo de las imágenes captadas de un pinhole y un test USAF formadas por el modelo de ojo con una pupila de entrada de 8*mm* con dos IOLs diferentes se muestra en la figura 3.8 (izquierda). En la figura 3.8 (derecha) se representa la MTF calculada en ambas situaciones.

El frente de onda también puede ser caracterizado utilizando un sensor Hartmann-Shack, con el que además también es posible obtener la MTF, la PSF o la SR mediante una aplicación informática que nos facilita los cálculos.

La transmitancia espectral de las IOLs puede ser medida mediante un espectrofotómetro. La transmitancia de una IOL es de especial interés dada la tendencia a la fabricación de lentes que incorporan un filtro amarillo (figura 3.9).

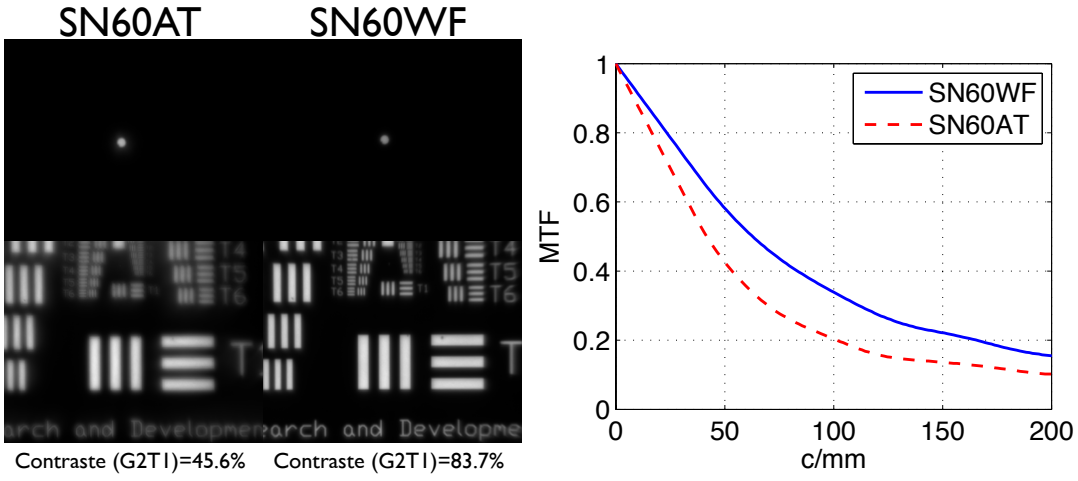

Figura 3.8: Izquierda: Imágenes de un pinhole y un test USAF formadas por el modelo de ojo con dos lentes intraoculares, una esférica (SN60AT) y otra asférica (SN60WF) para una pupila de entrada de 8mm (4mm en el plano de la IOL). También se indica el contraste del test USAF medido en el grupo G2T1. Derecha: MTFs calculadas a partir de estas imágenes.

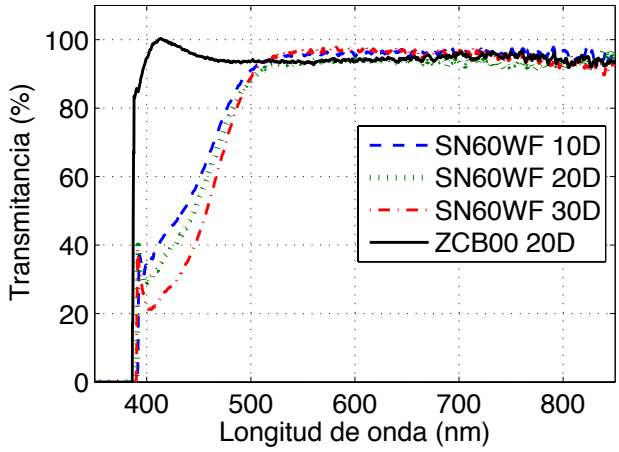

Figura 3.9: Medida experimental de la transmitancia espectral para tres lentes intraoculares con filtro amarillo de diferente potencia (SN60WF) y una lente sin filtro (ZCB00).

3.2 Problemas asociados al análisis a lo largo del eje (trough-focus testing)

REFERENCE TO THE PUBLICATIONS OF THIS THESIS

The content of this section is included in the publications:

- Millán M.S., Alba-Bueno, F., and Vega F. *"Experiment design for through-focus testing of intraocular lenses"*. 8th Ibero American Optics Meeting/11th Latin American Meeting on Optics, Lasers and Applications 2013; vol.8785 p.8785CP.

En la actualidad existen numerosos diseños de IOLs multifocales (MIOLs, por sus siglas en inglés) (refractivas, difractivas, simétricas, asimétricas, apodizadas, no-apodizada, bifocales, trifocales…), que hacen que haya un enorme interés en conocer las propiedades pseudo-acomodativas de estas lentes, es decir, en la caracterización de las propiedades ópticas que presentan en el espacio comprendido entre los diferentes focos (T-F, del inglés *Through-Focus*). Clínicamente, el comportamiento T-F en un paciente con su mejor corrección subjetiva (cilindro y esfera) se suele hacer mediante optotipos de agudeza visual, ya sea utilizando optotipos calibrados para diferentes distancias (lejos, intermedia y cerca) [Alfonso et al. 2007; Kohnen et al. 2009]; o bien, utilizando lentes positivas y negativas en gafa de prueba.

En un banco óptico se puede llevar a cabo un experimento similar utilizando un modelo de ojo [Lang et al. 1993; Lang and Portney 1993]. Mediante las medidas de la PSF y la MTF en distintos planos focales, la profundidad de foco y/o la función de

transferencia de desenfoque [Goodman 2005; Schwiegerling 2007], se puede caracterizar el rendimiento y la calidad óptica de las MIOLs. Dichos parámetros se pueden realizar tanto en los mejores planos imagen de la IOL (lejano, intermedio(s) – si existen – y cercano) como en planos próximos a éstos en los que la imagen está afectada por distintos grados de desenfoque. El estudio del comportamiento T-F se puede realizar considerando dos opciones básicas:

- Cambio de vergencias (VC, del inglés *Vergence Changing*): Generando diferentes vergencias en el espacio objeto del modelo de ojo. Esto se puede realizar cambiando la adición en gafa de prueba (figura 3.10a y b) o bien cambiando la posición del objeto.

- Escaneo posterior (BS, del inglés *Back Scanning*): desplazando el sensor alrededor del plano focal imagen del modelo de ojo para captar la distribución de intensidad en diferentes planos a lo largo del eje óptico (figura 3.10c).

En relación con las MTFs, Lang y colaboradores [Lang et al. 1993; Lang and Portney 1993] demostraron que ambos métodos eran ópticamente equivalentes en el rango de desenfoque entre $0D$ y $-3.0D$ para un ojo humano de $60D$. No obstante, para otros rangos de valores, ellos mismos advierten que no existe una equivalencia general entre las MTFs obtenidas por ambos métodos. Como veremos a continuación, esta afirmación tiene implicaciones adicionales cuando la imagen aérea formada en el plano focal del modelo de ojo con la IOL no es captada directamente por el sensor, sino, como sucede en el banco óptico de la figura 3.1, por un sistema de aumento de la imagen (microscopio) unido al sensor para mejorar la resolución.

Volviendo sobre la figura 3.10, decíamos que la respuesta T-F puede ser evaluada cambiando la vergencia objeto (opción VC), mediante la adición de lentes positivas (figura 3.10a) o negativas (figura 3.10b), o bien cambiando el plano del sensor, que en este caso sería la retina, hacia delante y hacia atrás (opción BS) como se esquematiza en la figura 3.10c. A pesar de que ambas opciones proporcionan imágenes desenfocadas, no son completamente equivalentes en términos de aumento ni desenfoque. Tal y como se muestra en esta figura (figura3.10a-c), una

imagen desenfocada puede ser expresada como la convolución (representada mediante el símbolo *) de una imagen enfocada y un círculo de desenfoque. Con la opción VC, la imagen enfocada se desplaza de la retina a otra posición con un cambio de escala (figuras 3.10a y b). En el plano de la retina, por tanto, se obtiene una versión desenfocada y con distinto tamño de la imagen. Con la opción BS (figura 3.10c), en cambio, la imagen enfocada se mantiene fija en posición y tamaño y es el plano de la retina el que se desplaza hacia detrás y delante para obtener las imágenes desenfocadas. Al igual que otros trabajos [Lang and Portney 1993; Lang et al. 1993; Kim et al. 2011; Remón et al. 2012; Pepose et al. 2012; Gatinel and Houbrechts 2013; Montés-Micó et al. 2013], consideramos que el sistema óptico del ojo es telecéntrico en una primera aproximación (la imagen no cambia de tamaño con el desenfoque), aunque no lo sea estrictamente.

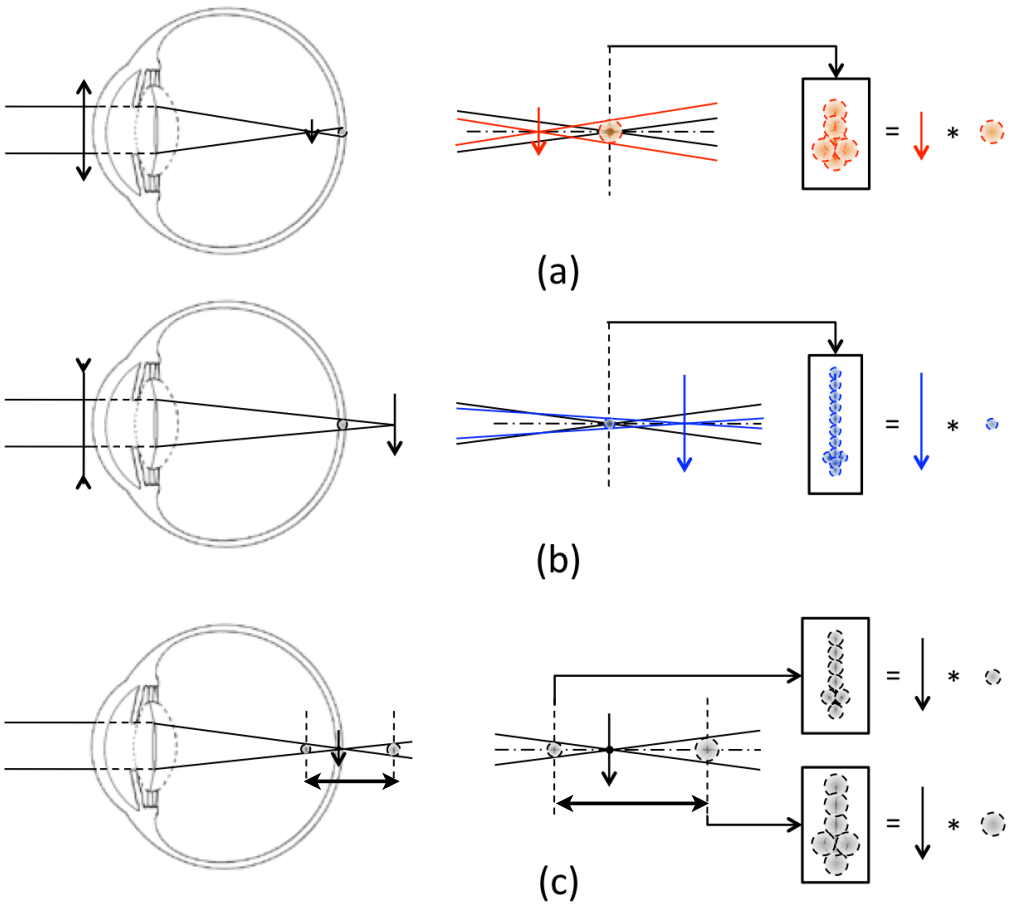

*Figura 3.10: (a), (b) Imágenes desenfocadas mediante la adición de lentes positivas (a) o negativas (b) (opción VC); (c) Imágenes desenfocadas mediante escaneo posterior (opción BS). La imagen desenfocada se representa mediante la convolución (con el símbolo *) de la imagen enfocada con un círculo de desenfoque. Nótese la influencia tanto del tamaño de la imagen como del tamaño del círculo de desenfoque.*

Lang et al. [Lang and Portney 1993; Lang et al. 1993] estudiaron las variaciones de MTF para dos tipos de desenfoque (VC y BS) en un modelo de ojo humano de 60D en banco óptico, con una córnea limitada por difracción y una MIOL con una pupila de 3mm. Para captar la imagen, utilizaron un sensor en el plano imagen del modelo de ojo, sin ningún tipo de óptica adicional.

El cambio de potencia equivalente en gafa (ΔS) para un cambio dado en la posición del plano focal imagen (Δf_b) viene dado por:

$$\Delta f_b = -\frac{\Delta S}{P^2} \quad , \tag{3.1}$$

donde P es la potencia del modelo de ojo. En estos trabajos se aproxima una variación de la potencia en el plano de las gafas por una variación igual en el plano corneal, que es una suposición válida para pequeños cambios de potencia. El desenfoque VC se implementa utilizando adiciones en gafa de -1.2D, -2.4D y -3.0D, mientras que el desenfoque BS fue implementado moviendo hacia atrás el sensor en el espacio imagen a las posiciones equivalentes a las adiciones consideradas. A continuación calcularon las MTFs para los desenfoques efectuados por ambos métodos sin encontrar diferencias significativas, por lo que concluyeron que eran ópticamente equivalentes para ese rango de potencias.

Un problema similar al estudiado por Lang et al. se origina cuando se utiliza un sistema óptico adicional (usualmente un microscopio) para aumentar y adquirir en un sensor CCD, con suficiente resolución, la imagen aérea formada por el modelo de ojo que contiene la IOL, tal y como sugieren las normativas ISO [11979-2; 11979-9] y como se ha descrito anteriormente en este capítulo [Alba-Bueno et al. 2011].

Recientemente se han publicado diversos trabajos utilizando estos métodos para caracterizar el comportamiento a lo largo del eje de varias MIOLs [Kim et al. 2011; Pepose et al. 2012; Remón et al. 2012; Gatinel et al. 2011; Gatinel and Houbrechts 2013; Montés-Micó et al. 2013]. Estos estudios consideran bien una de las dos opciones:

- La opción VC manteniendo la posición del sensor fijo en el mejor foco de visión lejana, es decir, 0*D* de vergencia en el modelo de ojo [Kim et al. 2011; Pepose et al. 2012; Remón et al. 2012],

- Una versión modificada de la opción BS, en la que el microscopio, junto con el sensor, se desplaza a lo largo del eje para captar la imagen de una secuencia de planos entre los focos de lejos y cerca [Gatinel et al. 2011; Gatinel and Houbrechts 2013; Montés-Micó et al. 2013].

Los resultados experimentales obtenidos utilizando tanto uno como otro método les permiten establecer comparaciones entre los comportamientos T-F de un determinado número de MIOLs. Todos estos trabajos, como hemos mencionado anteriormente, asumen que hay una estricta equivalencia entre las imágenes (enfocadas y desenfocadas) captadas por el sensor en el espacio imagen del microscopio y las imágenes (enfocadas y desenfocadas) que se obtendrían si hubiera una pantalla difusora situada en el plano conjugado del sensor, en el espacio objeto del microscopio. Un trazado de rayos de primer orden (figura 3.11) nos muestra una discordancia en el aumento de estas dos imágenes. Por esta razón, la equivalencia mutua no puede ser garantizada en general, sino que necesita ser justificada función de los valores de los parámetros implicados en los experimentos, de un modo similar al que Lang et al. [Lang and Portney 1993; Lang et al. 1993] realizaron en sus trabajos. Es necesario hacer hincapié en que el difusor imaginario no existe realmente y, por lo tanto, la luz que forma la imagen aérea se propaga en el espacio libre y pasa a través del microscopio hasta el sensor.

En este aspecto, desafortunadamente, las normativas ISO [11979-2; 11979-9] no definen con precisión el método experimental a seguir para el análisis T-F de una IOL. Por esta razón se hace necesario estudiar, definir y establecer un método más preciso para realizar medidas T-F antes de establecer alguna equivalencia *a priori* entre las imágenes. En la próxima sección estudiaremos inicialmente el caso de una IOL monfocal y, posteriormente, el caso más complejo de una MIOL.

3.3 Consideraciones sobre la escala de la imagen desenfocada

3.3.1 Análisis T-F (opción VC) para una IOL monofocal

Consideremos una imagen aérea en la posición *O* de tamaño *y* (figura 3.11a) formada por el modelo de ojo con una IOL monofocal (no mostrado en la figura). Esta imagen aérea formada en *O* se convierte en objeto para el microscopio que forma su imagen con aumento m_1 en el sensor situado en la posición *O'*. De este modo, *O* y *O'* son planos conjugados a través del microscopio. Para el análisis T-F vamos a considerar inicialmente la opción VC. Supongamos un desplazamiento *x* de la imagen aérea, desde *O* hasta *A* como se indica en la figura 3.11c, como una consecuencia de un cambio previo en la vergencia objeto del modelo de ojo. Además del cambio de posición con respecto al microscopio, la imagen aérea *A* tendrá diferente tamaño (*y'* en la figura 3.11c). Y, lo que es más importante, su conjugado a través del microscopio se localizará en *A',* - no en el plano del sensor – con un aumento m_2 que vendrá dado por:

$$m_2 = m_1\left(\frac{z_O}{z_A}\right) \ , \qquad (3.2)$$

donde z_O, , z_A representan las distancias desde el punto focal objeto del microscopio (*F*) a las posiciones *O* y *A* respectivamente, y $z_A = z_O - x$. El signo de *x* se considera positivo si la imagen aérea se mueve hacia el microscopio (en dirección contraria a la que se muestra en la figura 3.11c) y negativo cuando la distancia de la imagen aérea al microscopio aumenta (tal y como se muestra en la figura 3.11c). Una versión correctamente escalada de esta imagen desenfocada sólo se podría conseguir si se situara un difusor en el plano *O* (figura 3.11b). De un modo parecido al que se muestra en la figura 3.10, la imagen desenfocada formada en el difusor imaginario podría ser expresada por la convolución de la imagen aérea en la posición *A* con un círculo de desenfoque de radio *r* en la posición *O*. Si el difusor estuviera realmente colocado en el plano *O*, la imagen desenfocada proyectada en él sería correctamente captada con aumento m_1 por el sensor en el plano *O'*. Es necesario enfatizar que, en esta situación, tanto el tamaño de la imagen como el círculo de desenfoque serían captados con el mismo aumento m_1. Idealmente, este procedimiento sería adecuado para el análisis T-F de la imagen de la IOL. Por otra

parte, este método presenta un número considerable de inconvenientes prácticos, como son las pequeñas dimensiones de esta región de interés, los errores producidos por el grosor del difusor, la necesidad de una mecánica precisa para mover el difusor a lo largo del eje óptico y, el peor inconveniente de todos, la imagen estaría afectada enormemente por el ruido causado por el grano del difusor. Todos estos factores contribuirían a una reducción considerable de la precisión en todas las medidas.

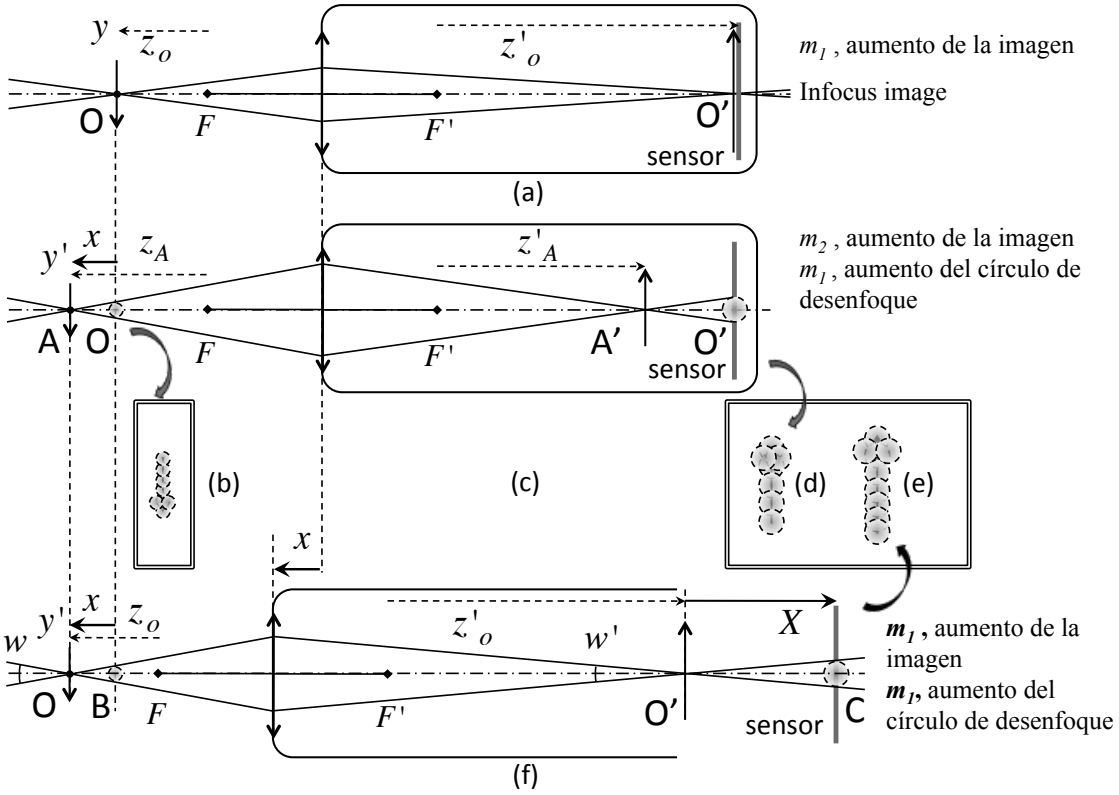

Figura 3.11: Análisis T-F cambiando la vergencia objeto (opción VC). (a) Adquisición de la imagen aérea enfocada en la posición O con aumento m_1. (b) Imagen desenfocada que aparecería en un difusor colocado en la posición O después del cambio de vergencia objeto. (c) Adquisición de la imagen desenfocada con aumento m_2 de la imagen y aumento m_1 del círculo de desenfoque. (d) Apariencia de la imagen desenfocada capturada en (c).(e) Apariencia de la imagen desenfocada con un aumento m_1 común para su tamaño y círculo de desenfoque que se captaría en el sensor del microscopio si en el plano O hubiese el difusor al que se alude en (b). (f) Configuración para la adquisición de la imagen desenfocada que se muestra en (e): El microscopio se mueve una distancia x hacia la posición de la imagen aérea hasta que ésta aparece enfocada de nuevo en el sensor. A continuación, el sensor se separa (sin desplazar el microscopio) una distancia X, hasta llegar al plano C, donde se debe captar la imagen desenfocada (e) que se busca.

En un caso real, donde no hay ningún difusor, la imagen desenfocada en el plano *O* (figura 3.11b) no se puede captar con un aumento m_1 en el sensor. La imagen desenfocada captada de este modo por el sensor (figura 3.11d) es el resultado de la convolución de la imagen localizada en *A'*, escalada por el aumento m_2, con un círculo de desenfoque de radio $r' = m_1 r$. Este círculo de desenfoque es una versión escalada con aumento m_1 de la imagen del círculo de desenfoque *r* que afecta a la imagen desenfocada en la posición objeto *O*. Esta es la imagen que se suele considerar en los estudios T-F que se basan en la opción VC, a pesar de que hay una discordancia de aumentos que afectan a la imagen desenfocada captada por el sensor CCD: m_1 afecta al círculo de desenfoque y m_2 afecta a la escala de la imagen. Puesto que la MTF depende de estos dos factores, esta situación es conceptualmente análoga a la analizada por Lang et al. [Lang and Portney 1993; Lang et al. 1993] para el desenfoque inducido por una adición en gafas y el desenfoque causado por desplazamientos en el plano focal imagen (del modelo de ojo).

Existe otra posibilidad de formar la imagen desenfocada de la figura 3.11b en el sensor con un aumento m_1 común para la imagen y el círculo de desenfoque (figura 3.11e). El procedimiento se representa el la figura 3.11f. Consiste en mover el microscopio una distancia *x* hacia la imagen aérea hasta que aparezca enfocada de nuevo en el plano del sensor situado en la posición *O'*. En estas circunstancias, la nueva imagen enfocada tiene un aumento m_1. A continuación, el sensor (sólo el sensor, el microscopio se queda fijo en esa posición) se mueve una distancia *X* en dirección contraria para hasta alcanzar el plano *C*. Para calcular esta distancia *X*, consideraremos la condición $r' = m_1 r$, que es necesaria para igualar el aumento del círculo de desenfoque, y los ángulos *w, w'* que, en aproximación paraxial, se pueden expresar como $w=2r/x$, y $w'=2r'/X$. Como el aumento angular $\gamma = {w'}/{w}$ es el valor inverso del aumento lateral ($\gamma = m^{-1}$), obtenemos

$$X = m_1^2 x \ . \qquad (3.3)$$

Procediendo de este modo, el sensor captará la imagen representada en la figura 3.11e, que es una versión correctamente escalada de la imagen desenfocada que se obtendría en el plano *B* (figura 3.11f) con un aumento único m_1 para el tamaño de

la imagen y el círculo de desenfoque. Este procedimiento evita los inconvenientes de utilizar un difusor y no añade una complejidad conceptual, ni de realización práctica, al sistema.

Es muy común que el sistema óptico del microscopio no sea una única lente, como se representa en la figura 3.11, sino un sistema compuesto, generalmente en una configuración de Badal, que consiste en un objetivo corregido al infinito combinado con una lente de tubo. En este caso, que llamaremos a partir de ahora microscopio IC (del inglés *Infinity Corrected*), el plano objeto O se hace coincidir con plano focal objeto del objetivo F_O y el plano conjugado imagen O' se forma en el plano focal imagen F'_t de la lente de tubo, donde se sitúa el sensor para captar la imagen. Esta configuración de Badal para el microscopio no modifica esencialmente la discusión hecha hasta el momento para el análisis T-F utilizando la opción VC y todos los comentarios acerca de la discordancia entre aumentos son igualmente válidos.

Resultados experimentales

Para esta experiencia, se utilizó una IOL monofocal asférica (ZA9003) de +10D en el modelo de ojo. En este caso, el microscopio consistió en un objetivo $10x$ IC combinado con una lente de tubo de $200mm$ de focal. Como objeto consideramos el grupo G2T3 del test de resolución USAF. En este caso la configuración del banco óptico se utilizó de acuerdo con las normativas ISO con la excepción de la córnea artificial, que se utilizó la previamente descrita DCX que induce una SA similar a la del ojo humano promedio. El diámetro pupilar se fijó en $3mm$ en el plano de la IOL a lo largo de todo el experimento. Puesto que el colimador utilizado fue de $f_c = 200mm$, el grupo G2T3 representa una frecuencia espacial – expresada en ciclos por grado (*cpd*) – de 17.6 *cpd*, que se corresponde con una AV aproximada de 0.5 decimal (0.3 *logMAR* ó 20/40). Se siguieron las etapas representadas en la figura 3.11 y descritas en esta sección. Los resultados experimentales se muestran en la figura 3.12. Inicialmente, ajustamos el microscopio y el sensor para captar la imagen enfocada de la imagen aérea producida por el modelo de ojo con la IOL (figura 3.12a). Para un determinado cambio en la vergencia objeto, captamos la imagen desenfocada del sensor (figura 3.12b). A pesar de que la imagen desenfocada adquirida de este modo presenta una discordancia de aumentos entre

el tamaño de la imagen (m_2) y el desenfoque (m_1), esta imagen es habitualmente tenida en cuenta en los estudios del comportamiento T-F de las IOLs. Para solventar este problema, desplazamos el microscopio hacia el modelo de ojo la distancia necesaria para reenfocar la imagen en el sensor (figura 3.12c); en nuestro caso, esta distancia fue $x = 228\mu m$. En estas condiciones, medimos el aumento de la imagen formada a través del microscopio ($m_1 = 11.1$) y calculamos $X = 28.01\mu m$ utilizando la ecuación 3.3. Con el microscopio fijado en esa posición desplazamos hacia atrás el sensor la distancia X y captamos la imagen desenfocada en ese plano (plano C en la figura 3.11f). Esta imagen desenfocada (figura 3.12d) tiene el mismo aumento (m_1) tanto para el tamaño de la imagen como para el desenfoque. Para facilitar la visualización de la diferencia entre las imágenes desenfocadas de las figuras 3.12b y d, presentamos una parte del grupo G2T3 de cada figura (marcada con rectángulos en las figuras 3.12b y d) enfrentadas en la figura 3.12e.

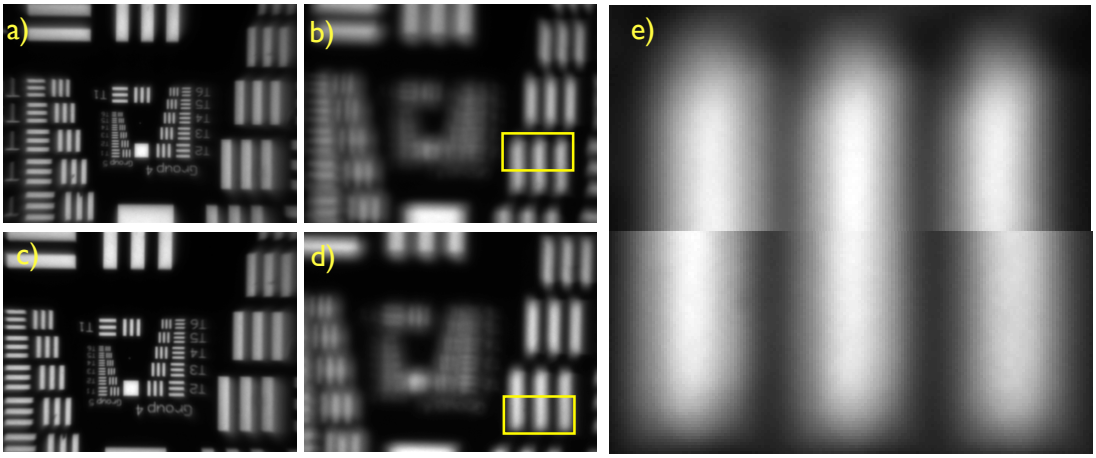

Figura 3.12: Resultados experimentales de las imágenes obtenidas al reproducir los pasos mostrados en la figura 3.11 y descritos en el texto. (a) Imagen enfocada correspondiente al esquema de la figura 3.11a; (b) imagen desenfocada con la discordancia de aumentos de la figura 3.11d. (c) Imagen reenfocada que corresponde al esquema de la figura 3.11f; (d) imagen desenfocada después de mover el sensor una distancia X como en la figura 3.11e. (e) Áreas extraídas del grupo G2T3, marcado en amarillo en las figuras b y d y enfrentadas para facilitar la comparación.

3.3.2 Análisis T-F (opción BS) para una IOL multifocal

Las MIOLs tienen al menos dos focos, uno para visión lejana y otro para visión cercana, representados por D y N (del inglés *Distance* y *Near*) a partir de ahora. Estas lentes producen una visión simultánea, es decir, doble imagen, en diferentes planos y con diferente aumento. Por eso, en cada plano focal, una imagen desenfocada siempre se superpone a la imagen enfocada. La caracterización del

rendimiento de una MIOL es importante tanto en los planos de mejor imagen (D y N) como en los diferentes planos que existen entre ellos. Actualmente se presta especial atención al análisis T-F entre ambos focos porque éste nos da una idea del comportamiento de la lente para distancias de enfoque intermedias. Es obvio que el problema tratado en la sección 3.3.1 se complica cuando el modelo de ojo contiene una MIOL que produce dos imágenes aéreas de un objeto en el infinito (figura 3.13).

Si el análisis T-F se hiciera siguiendo el procedimiento esquematizado en la figura 3.11f, esto es, desplazando el microscopio una distancia *x* y el sensor una distancia *X* para cubrir el segmento Δ = *N D* entre focos (figura 3.13), no habría discordancia de aumentos sólo para una de las series de imágenes, ya fuera la de cerca (en rojo en la figura 3.13) o la de lejos (en negro en la figura 3.13), pero no para ambas simultáneamente. En general, habrá mezclas de aumentos en el espacio imagen del microscopio que harán que la interpretación del escenario en el espacio objeto (que es el espacio imagen del modelo de ojo) sea muy complicada e irreal. En función de las constantes y los parámetros del sistema, la influencia de este error en la precisión de las métricas utilizadas para caracterizar la MIOL pueden ser importantes. Un sistema como el microscopio IC tampoco mejorará esencialmente la situación.

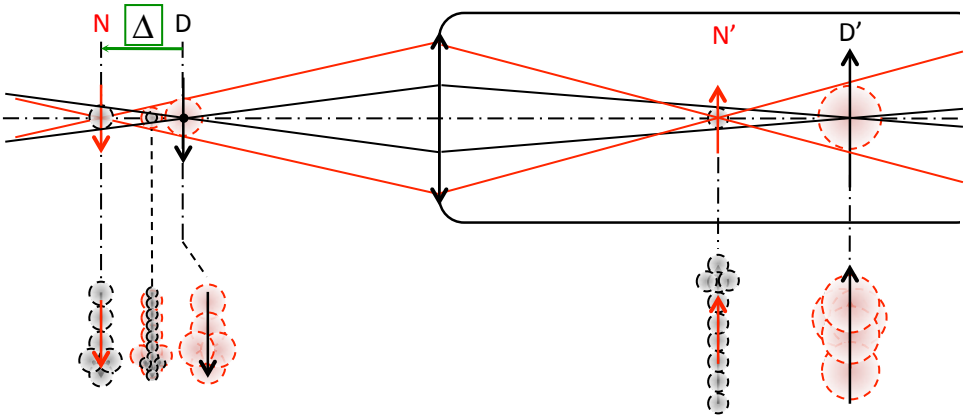

Figura 3.13: Formación de imágenes T-F a través del microscopio en el caso de un modelo de ojo con una MIOL (no mostrado en la figura). N y D representan los focos de cerca y lejos formados por la MIOL.

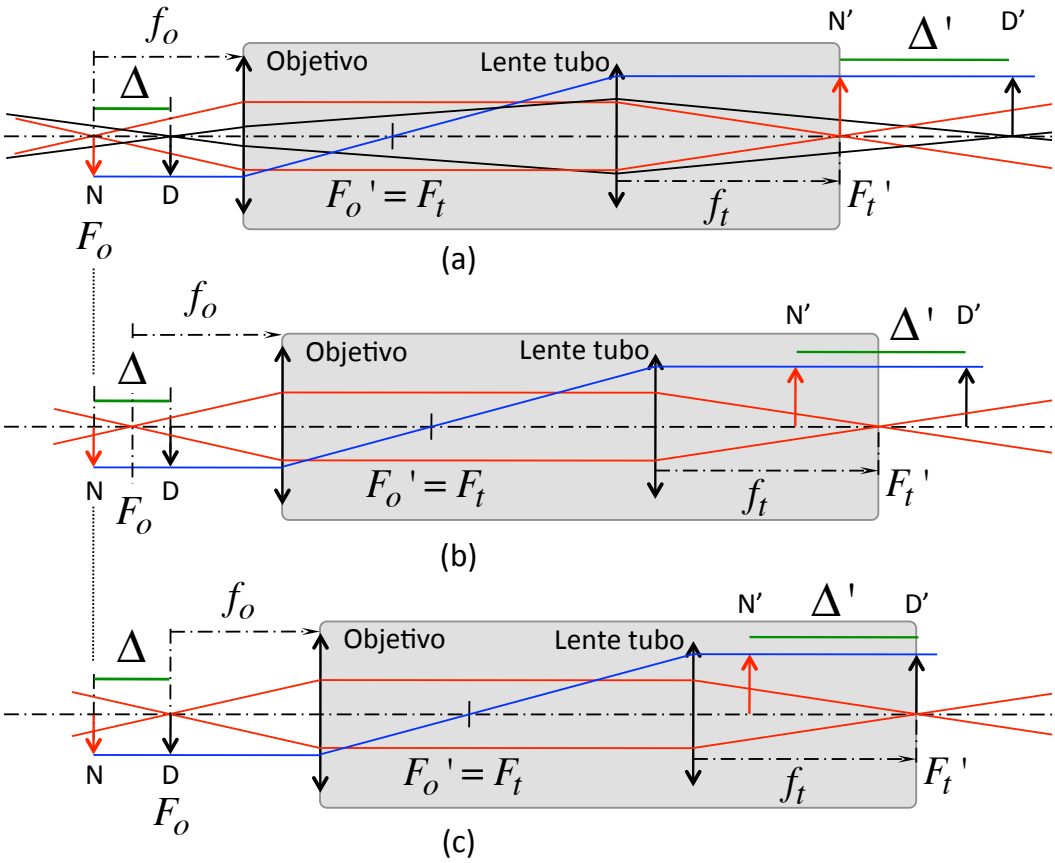

Figura 3.14: Análisis T-F (opción BS) utilizando un microscopio IC-A (afocal). Para cualquier plano objeto situado a distancia finita (N, D, segmento Δ), el sistema afocal del microscopio forma la imagen (N' D', segmento Δ') con aumento lateral m constante. El sensor, situado en el plano focal imagen de la lente de tubo (F'_t) capta la imagen del plano objeto situado en el plano focal objeto del objetivo (F_o). (a) N, N' , (b) posición intermedia. (c) D, D'.

Para salvar este problema a la hora de captar las imágenes, proponemos una nueva configuración para el microscopio y el sensor que evite la discordancia entre aumentos. Consiste en un microscopio compuesto IC con la configuración de sistema afocal (IC-A). Esta combinación (figura 3.14) se obtiene cuando el plano focal imagen del objetivo F_O' coincide con el plano focal objeto de la lente de tubo F_t ($F_O' = F_t$). Un sistema afocal tiene la destacable propiedad de proporcionar aumento constante para todas las distancias objeto finitas. El valor absoluto de este aumento es el cociente entre la distancia focal de la lente de tubo y la distancia focal del objetivo, es decir, $m = -f_t / f_o$ (donde el signo negativo indica la inversión de la imagen). De hecho, el microscopio afocal se puede conseguir a partir de un microscopio IC convencional únicamente separando la distancia apropiada el objetivo y la lente de tubo. El sensor, al igual que en la configuración IC, se debe fijar en el plano focal imagen de la lente de tubo, F'_t. Con este microscopio IC-A, se pueden captar todas las imágenes necesarias para realizar la caracterización T-F

entre los focos N y D, con sus imágenes superpuestas desenfocadas, siempre con un aumento constante para cada plano (figura 3.14). La distancia entre los planos N y D, $\Delta = N\ D$, se transforma en $\Delta' = N'\ D' = m^2\ \Delta$ en el espacio imagen del microscopio IC-A.

Cuando el sistema completo formado por el microscopio IC-A y el sensor se desplazan a lo largo del eje, el conjunto de planos imagen entre N' y D' también lo hace, en dirección opuesta (figura 3.14). No obstante, el aumento m y la distancia Δ' se mantienen sin cambios. En esta disposición, el sensor capta directamente una imagen con aumento m que corresponde al plano conjugado de F_0. En la figura 3.14a, F_0 coincide con el foco cercano N y su conjugado imagen N' a través del microscopio esta focalizado en el sensor. En la figura 3.14b, el sistema formado por el microscopio y el sensor se ha desplazado hacia atrás, de modo que F_0 está en una posición intermedia del segmento. Finalmente, en la figura 3.14c, el sistema entero se ha desplazado nuevamente hacia atrás y F_0 coincide con el foco de lejos D del modelo de ojo y su conjugado imagen D' está focalizado en el sensor. Para completar el análisis T-F se puede continuar desplazando el microscopio IC-A más allá del segmento $\Delta = N\ D$. Como la configuración afocal es un caso particular del sistema Badal considerado inicialmente para el microscopio IC, también se beneficia de la compensación de aberraciones de su diseño original. A pesar de que la figura 3.14 representa la opción BS, el microscopio IC-A también es válido para la opción VC en un análisis T-F.

Resultados experimentales

En esta ocasión hemos considerado dos lentes asféricas con el mismo diseño base: Una IOL monofocal ZA9003 de +10D y una la MIOL ZMA00 de +10D y adición de +4.0D. Como test objeto también utilizamos el test USAF centrándonos, en esta ocasión en el grupo G2T1, que corresponde a una frecuencia espacial de 14cpd en nuestro sistema. El resto de los parámetros de la configuración del banco óptico (colimador, diámetro pupilar, córnea artificial, objetivo de microscopio y sensor CCD) fueron los mismos que en la anterior experiencia con la excepción de la lente de tubo del sistema de observación, que en este caso fue de focal 150mm. El objetivo 10x y la lente de tubo, que producen un aumento m = 8.33, se combinaron para formar dos microscopios con diferentes configuraciones:

- En configuración Badal convencional (microscopio IC)
- y en configuración Badal-afocal (microscopio IC-A).

Se realizaron medidas de contraste T-F de la imagen de las barras del grupo G2T1 del test USAF formada por el ojo artificial con cada IOL utilizando la definición de Michelson para la visibilidad de las franjas. Este procedimiento se describe detalladamente en la sección 6.1. En la figura 3.15a se muestra el resultado del estudio T-F de los contrastes para una IOL monofocal con los sistemas IC (línea roja discontinua) e IC-A (línea azul continua). A pesar de que pueda parecer que ambas curvas están simplemente desplazadas una respecto de la otra, no se trata de desplazamiento, ni de un error experimental, puesto que el criterio de centrado en la posición $0\mu m$ de estas curvas es el punto de máximo contraste. Si observamos atentamente esta figura vemos cómo en el caso del microscopio IC la curva de desenfoque presenta cierta asimetría, que no está presente en la curva IC-A (obsérvense los valores de contraste para las posiciones de $\pm 200\mu m$). En la figura 3.15b se muestran las diferencias absolutas de los valores de ambas curvas. Lógicamente esta diferencia depende de la posición del desenfoque (es mínima en la posición $0\mu m$) y llega a alcanzar valores de ±10 puntos porcentuales en algunas posiciones.

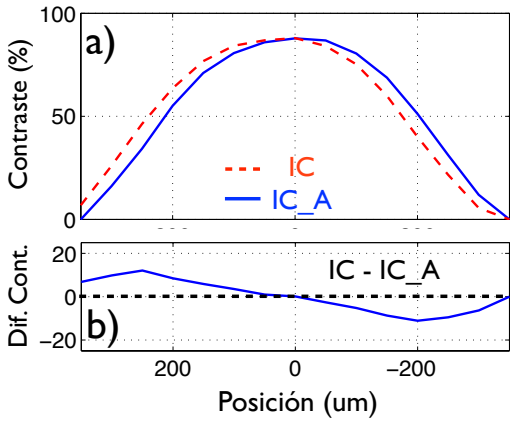

Figura 3.15: Análisis T-F de una IOL monofocal. (a) Medidas de contraste para el grupo G2T1 del test USAF con un microscopio IC convencional (IC, línea discontinua roja) y un microscopio IC afocal (IC_A, línea continua azul). (b) Diferencia absoluta en puntos porcentuales.

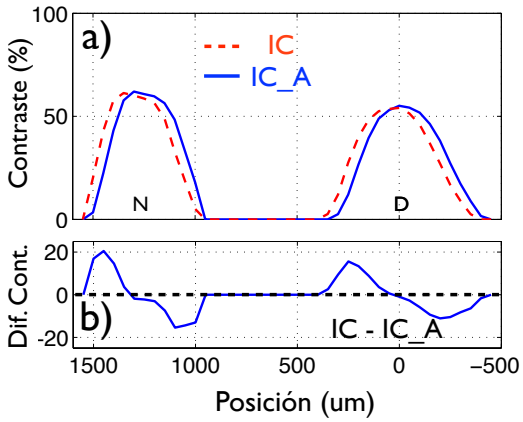

Figura 3.16: Análisis T-F de una MIOL. (a) Medidas de contraste para el grupo G2T1 del test USAF con un microscopio IC convencional (IC, línea discontinua roja) y un microscopio IC afocal (IC_A, línea continua azul). (b) Diferencia absoluta en puntos porcentuales.

En la segunda parte del experimento, hemos repetido el mismo análisis T-F para la MIOL. En la figura 3.16a se muestran las curvas de desenfoque obtenidas para cada configuración de microscopio tal y como se hizo en la figura 3.15a con la IOL monofocal. Nótese cómo en este caso existen dos máximos correspondientes a los focos N y D. Es destacable que los valores de contraste obtenidos con la MIOL son claramente inferiores a los obtenidos con la IOL monofocal debido a la formación simultánea de dos imágenes. Las diferencias absolutas (figura 3.15b) de nuevo dependen de la posición del microscopio y, en este caso, pueden llegar en algunas posiciones a ±20 puntos porcentuales de diferencia (sobre un máximo de 60%) para la frecuencia espacial analizada.

3.4 Conclusiones

Hemos diseñado un banco óptico para la caracterización de las IOLs que sigue la normativa ISO, pero que además, tiene versatilidad para analizar las lentes en condiciones más parecidas a las del ojo humano. El análisis de las lentes se puede realizar mediante la evaluación cuantitativa de diferentes parámetros como la PSF, la MTF, el contraste o el análisis del frente de onda mediante un sensor Hartmann-Shack.

Cuando la calidad de imagen de una IOL se analiza con un modelo de ojo en un banco óptico, normalmente es necesario utilizar un microscopio y una cámara para captar con suficiente resolución tanto la imagen aérea enfocada como otros planos cercanos en el eje óptico. Con este fin, generalmente se utiliza un microscopio IC. Un análisis de rendimiento T-F de una IOL monofocal requiere captar una serie de imágenes desenfocadas alrededor de la imagen aérea con aumento constante tanto para la imagen como para los diferentes círculos de desenfoque. Esto no se cumple cuando la vergencia objeto cambia y el microscopio y el sensor se mantienen en una posición fija. La imagen desenfocada adquirida de esta manera está afectada por una discordancia de aumento entre su escala y su desenfoque.

Una posible solución al problema de la discrepancia de aumento consiste en desplazar la posición del sensor la distancia adecuada (manteniendo el resto del microscopio sin cambiar de posición). Esta distancia es proporcional al desplazamiento del objeto causado por el cambio de vergencia (objeto) y el

cuadrado del aumento de la imagen enfocada. Esta solución sólo es válida para IOLs monofocales y no para MIOLs.

En el caso de las MIOLs la solución radica en la configuración afocal del microscopio, que tiene aumento constante para todos los objetos situados a distancias finitas. Esta solución resuelve el problema sin un aumento de la complejidad de la configuración y permite sacar provecho del diseño optimizado de los objetivos IC.

Los resultados experimentales han permitido corroborar el análisis teórico realizado sobre las diversas configuraciones de captación. Asimismo hemos verificado experimentalmente la validez de las configuraciones propuestas para n análisis T-F que no introduce errores de discordancia de aumentos.

CAPÍTULO 4

EFICIENCIA ENERGÉTICA DE LENTES INTRAOCULARES MULTIFOCALES

CHAPTER 4

ENERGY EFFICIENCY IN MULTIFOCAL INTRAOCULAR LENSES

REFERENCE TO THE PUBLICATIONS OF THIS THESIS

The content of this section is included in the publications:

- Vega, F., Alba-Bueno, F. and Millán M.S. *"Energy distribution between distance and near images in apodized diffractive multifocal intraocular lenses"* Invest Ophthalmol Vis Sci; 2011 vol.52(8) p.5695-5701.
- Alba-Bueno, F. Vega, F. and Millán M.S. *"Energy balance in apodized diffractive multifocal intraocular lenses"* Proc SPIE vol.8011 p.80119G.
- Vega, F., Alba-Bueno, F. and Millán M.S. *"Energy efficiency of a new trifocal intraocular lens"* J Eur Opt Soc-Rap. Public; 2014 vol.9 p.14002

After cataract surgery the eye loses its accommodation capability (ability to focus correctly objects at different distances). An implant of a monofocal IOL implies that the patient will need an optical correction for properly focusing at some distances, usually spectacles for near vision. Nowadays the implant of accommodative or bi- or multifocal IOL (MIOLs) to achieve higher independence from spectacles is very frequent. To achieve multifocality IOLs can incorporate on one of their surfaces either different radii of curvature (refractive MIOLs) or diffractive profiles (diffractive MIOLs). The latter generates two or more foci by using different

diffraction orders [Larsson et al. 1992; Cohen 1992]. Multifocal IOL designs produce two or more foci (named the distance and near foci) that allow the pseudophakic eye to correctly focus at least at two different distances at the same time but, on the other hand, the simultaneous perception of different images has an inherent drawback: the focused retinal image, provided by one of the lens powers, is always overlaid by out-of-focus images from the other powers. This side effect may be visually disturbing and as a matter of fact, quite a few patients typically complain of perceiving halos and/or glares that appear under some illumination conditions. This side effect also depends on the lens powers, the pupil diameter and the relative energy distribution among the foci [Vingolo et al. 2007]. For these reasons, the contrast sensitivity in eyes implanted with MIOLs may be worse than in those implanted with monofocal IOLs [Schmidinger et al. 2005; Gil et al. 2014]. To fully understand the nature of these effects it is interesting to characterize the optical performance of these IOLs in a test bench [Alba-Bueno et al. 2011]. The Point Spread Function (PSF) and the Modulation Transfer Function (MTF) are metrics widely used to characterize the optical quality of different IOLs [Eppig et al. 2008; Pieh et al. 2009]. However, it is less common to analyze the energy distribution between the distance and near images (or intermediate, if any) and its variation with the pupil diameter. The energy distribution is an optical quality feature that is especially important in the case of the apodized diffractive MIOLs, which are specifically designed with a twofold purpose: to reduce the glare and halo phenomena and, in addition to this, to have an increasing distance-dominant behavior for large pupil sizes. The latter implies to make the energy distribution between the distance and near images dependent on the eye pupil. Furthermore, some of these IOLs have aspheric surfaces, and there is a great interest to determine, both in a test bench [Pieh et al. 2002; Terwee et al. 2008] and in clinical studies [Alfonso et al. 2009; Kohnen et al. 2009b; Alió et al. 2008; Alfonso et al. 2007; de Vries et al. 2010; Petermeier and Szurman 2007], the advantages of these aspheric designs versus the spherical ones.

In this chapter we propose a method that measures, for an object at infinity, the energy that contributes to the image formed by an IOL at the focus plane as a function of the pupil diameter. The method requires the IOL tester described in chapter 3 [Alba-Bueno et al. 2011] and can be applied to either monofocal or

multifocal IOLs. When it is applied to multifocal IOLs, the method will allow us to determine the energy distribution among the images corresponding to the different foci of the lens as a function of the aperture. In this chapter, the method is applied to different MIOLs and the results obtained experimentally are compared with the theoretical predictions.

4.1 Theoretical background and description of multifocal IOLs

4.1.1 Diffractive multifocal IOLs

Diffractive multifocal (bifocal) IOLs typically divert light simultaneously into the zero ($m=0$) and first ($m=1$) diffraction orders that correspond to the distance and near foci, respectively. The radii of the diffractive rings measured from the optical axis ($r=0$) are determined by the design wavelength and add power through the equation [Lee and Simpson 1997]:

$$r_i^2 = (2i-1)\lambda \frac{1000}{D_{add}} \quad , \qquad (4.1)$$

where i is the zone number $\{i=1...n\}$, λ is the design wavelength and D_{add} is the addition power (in Diopters). Thus, for $\lambda = 550nm$ and $D_{add} = +3.0D$, the radius of the central disk is $r_1 = 0.428mm$ whereas it reduces to $r_1 = 0.371mm$ for $D_{add} = +4.0D$.

The height h_i of the diffractive step is determined by:

$$h_i = \alpha_i \frac{\lambda}{n_{IOL} - n_q} \quad , \qquad (4.2)$$

where α_i is the phase shift (in wavelength units), n_{IOL} is the refractive index of the IOL and n_q is the refractive index of the aqueous medium (usually $n_q = 1.336$) where the lens is immersed. The diffractive profile of the lens acts as an optical interface between the IOL material and the aqueous medium. The phase shift (and consequently the step height) determines the proportion of energy that contributes to the $m=0$ (distance power) and $m=1$ (near power) diffraction orders.

If α_i were constant for all the rings, the diffraction throughput efficiency (TE) of the $m=0$ and $m=1$ orders would be given by [Cohen 1993]:

$$TE_{m=0,1} = \mathrm{sinc}^2(m-\alpha_i) \tag{4.3}$$

An example of a bifocal IOL with this characteristic is shown in figure 4.1. Since the diffractive profile covers the full aperture of the IOL, this kind of MIOLs are named "full-aperture MIOLs" herein.

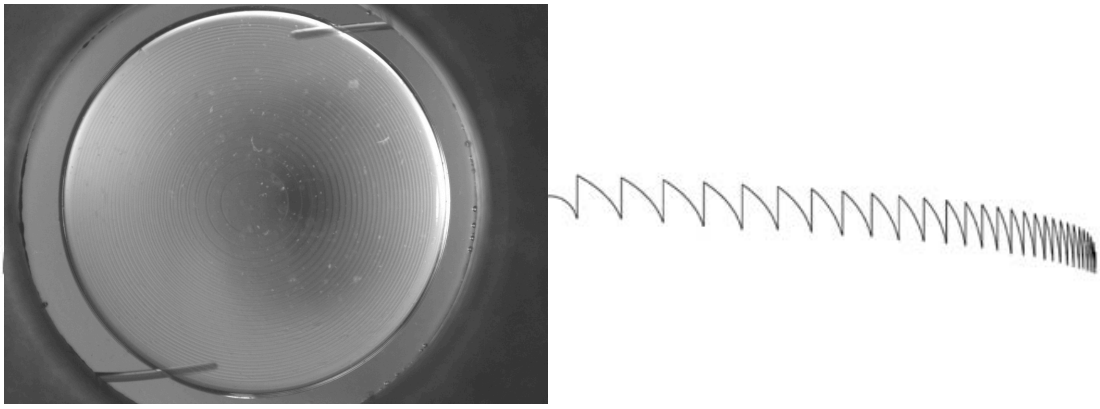

Figure 4.1: Lef: Image of a Tecnis multifocal IOL (ZMA00). Right: Profile that shows the constant height step from the center to the periphery.

In order to alleviate from reduce the halo and glare perceptions in distance vision with large pupils, there are "apodized" multifocal IOLs (ADMIOLs) such as the AcrySof ReSTOR (Alcon). In the design of apodized MIOLs h_i diminish with the radius, and, consequently, the phase shift α_i varies in the central zone of the IOL. In the periphery, the lens presents a purely refractive ring sector (figure 4.2). The apodization factor, f^{ap} in the design of the AcrySof ResSTOR is given by Lee et al. [Lee and Simpson 1997]as:

$$f_i^{ap} = 1 - \left(\frac{r_i}{r_n}\right)^3 \text{ for } r = 0, r_1, r_2, \ldots r_n, \tag{4.4}$$

for which the step height reduction is given by:

$$h_i = f^{ap} \cdot h_0 \tag{4.5}$$

where h_0 is the maximum height at the optical axis ($r = 0$). The AcrySof Restor with +4.0D of addition presents twelve diffractive rings, i.e. $r_i\{1,2,...12\}$ while the design with +3.0D of addition present nine rings, i.e. $r_i\{1,2,...9\}$.

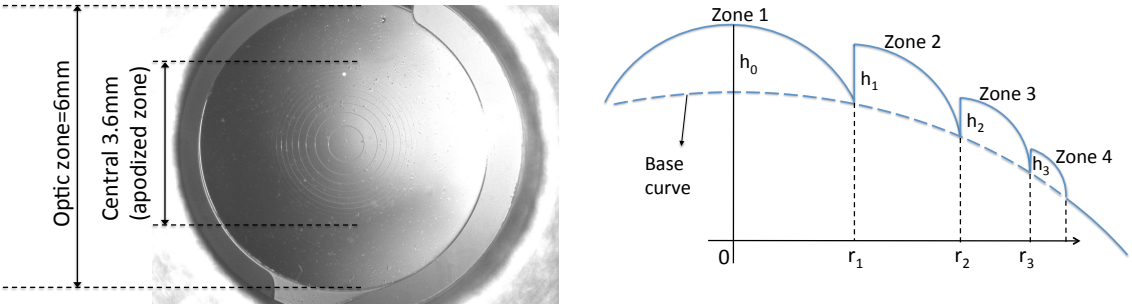

Figure 4.2: Left: Image and dimensions of an AcrySof ReSTOR. Right: Sketch of the apodization profile of the central zone.

In this situation, the TE for each $\alpha_i\left(TE^i_{m=0,1}\right)$ has to be weighted by a factor that corresponds to the *ith*-diffractive ring area. Therefore, the energy that the diffractive part of the IOL would divert from an incident plane wave into the $m = 0$ and $m = 1$ diffraction orders is calculated by means of linear combination of the weighted contributions of the rings:

$$I^{dif}_{m=0} = c_{te}\sum_{i=1}^{n} A^i \cdot TE^i_{m=0} \ , \qquad (4.6)$$

$$I^{dif}_{m=1} = c_{te}\sum_{i=1}^{n} A^i \cdot TE^i_{m=1} \ , \qquad (4.7)$$

where c_{te} is a proportionality constant and n is the number of diffractive rings of area A^i that are illuminated and thus are taking part in the diffraction process.

With a reduced pupil aperture, for which the IOL only operates with the first diffractive zone (i.e. α_i = α_0), there is nearly equal diffraction throughput efficiencies for the distance ($TE^0_{m=0} = 0.38$) and near ($TE^0_{m=1} = 0.43$) powers. With larger pupils, more diffractive rings are illuminated but the progressive reduction of the phase shift α_i of the waves as they pass through the outer diffractive rings implies that $TE^i_{m=0} > TE^i_{m=1}$ and, according to Equations 4.6 and 4.7, the energy sent

to the distance power ($m=0$) is reinforced at the expense of the energy of the near power ($m=1$).

In the purely refractive region of the ADMIOL periphery, the light goes exclusively to the distance power i.e. $TE_{m=0}^{ref}=1$, and therefore the energy is simply:

$$I_{m=0}^{ref} = c_{te} \cdot A^{ref} \cdot TE_{m=0}^{ref} \quad , \tag{4.8}$$

where A^{ref} is the area of the illuminated refractive region of the IOL.

Then, the amount of energy sent to either the distance or near powers strongly depend on the size of the pupil or, equivalently, on the size of the illuminated area of the IOL (referred from now on as to IOL-pupil) and can be calculated through:

$$I_{m=0} = I_{m=0}^{dif} + I_{m=0}^{ref} \ , \tag{4.9}$$

$$I_{m=1} = I_{m=1}^{dif} \ , \tag{4.10}$$

which can be expressed in terms of energy efficiency as:

$$\eta_{dist} = \frac{I_{m=0}}{I_{IOL}^{total}} \ , \tag{4.11}$$

$$\eta = \frac{I_{m=1}}{I_{IOL}^{total}} \ , \tag{4.12}$$

where I_{IOL}^{total} the total energy transmitted through the whole IOL aperture. This energy is proportional to the area of the IOL aperture A_{IOL}, provided that any loss of energy (for instance, caused by scattering in the diffractive steps [de Vries et al. 2008] is neglected:

$$I_{IOL}^{total} = c_{te} \cdot A_{IOL} \tag{4.13}$$

We have calculated the energy efficiencies according to Equations 4.11 and 4.12, as a function of the IOL-pupil diameter in the case of two AcrySof ReSTOR IOLs. The results, plotted in figure 4.3, are in excellent agreement with those reported elsewhere [Davison and Simpson 2006].

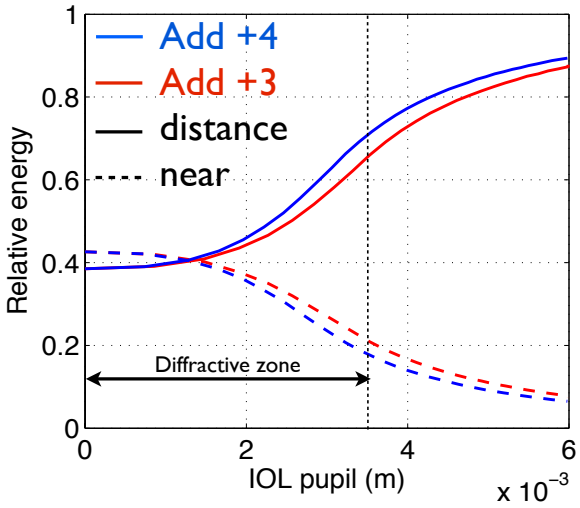

Figure 4.3: Theoretical energy efficiencies calculated for the distance and near powers (η_{dist} and η_{near}) of two AcrySof ReSTOR lenses with +3.0D (red lines) and +4.0D (blue lines) of addition.

Clinical tests have shown that patients implanted with any of these bifocal diffractive MIOLs, either full aperture or apodized, achieve good distance and near VAs [Blaylock et al. 2006; Alió et al. 2008] but with a significant reduction of VA at intermediate distances [Alfonso et al. 2007; Petermeier and Szurman 2007]. This reduction was smaller in patients with aspheric MIOLs of lower add power [Alfonso et al. 2010].

In order to achieve a better intermediate VAs, Swanson [Swanson 1994] disclosed a trifocal IOL based on a binary phase profile that used the m=-1, m=0 and m=1 diffraction orders to obtain the distance, intermediate and near foci respectively, each of them having a theoretical diffraction efficiency of 28.8% while the rest of the light energy (approximately 14%) was wasted in higher diffraction orders. Lately, Valle et al. [Valle et al. 2005] showed that the add power of the intermediate and near foci, as well as the diffraction efficiency of each of the three foci, could be modified in a controlled way if the trifocal IOL had a phase profile of the form $b \cdot \cos(2\pi a r^2)$, being r the radial coordinate and a and b two independent design parameters.

A different approach in the design of trifocal IOLs relies on the combination of two kinoform diffractive profiles with different step heights in the surface of the lens [Cohen 2012]. The first profile provides focus for distance (order m=0) and near (order m=1) vision, while the second one splits the light into distance (m'=0) and

intermediate (order *m'*=1) foci. Moreover, the order *m'*=2 of this profile coincides with the order *m*=1 of the first one and thus also contributes to the near focus. The Finevision trifocal IOL (Physiol) features an apodized diffractive profile (i.e. pupil dependent) with add powers of +1.75*D* for intermediate and +3.50*D* for near foci [Gatinel et al. 2011] uses such design and the first visual outcomes after implantation of this trifocal IOL are now available [Cochener et al. 2012].

A third trifocal diffractive IOL, the AT Lisa 839MP from Carl Zeiss Meditec has been recently launched (2012). This lens features an aspheric optic to compensate for SA as much as 0.18μm (c[4,0] (or Z_8) Zernike coefficient). The light distribution among the foci is intended to be independent from the pupil size. This lens presents an addition of +1.66*D* for intermediate and +3.33*D* for near vision. Multifocality is achieved by means of a diffractive anterior surface of 6*mm* with the trifocal zone having a diameter of 4.34mm (figure 4.4). The outer region of the lens to the 6*mm* edge sends light to the distance and near foci exclusively. In contrast with other trifocal IOL whose diffractive profile features are currently available [Voskresenskaya et al. 2010; Gatinel et al. 2011], to the best of our knowledge, no details about the characteristics of the diffractive profile of the AT LISA 839MP have been disclosed yet by the manufacturer. The theoretical light distribution between the three foci, as provided by the manufacturer, is shown in figure 4.5.

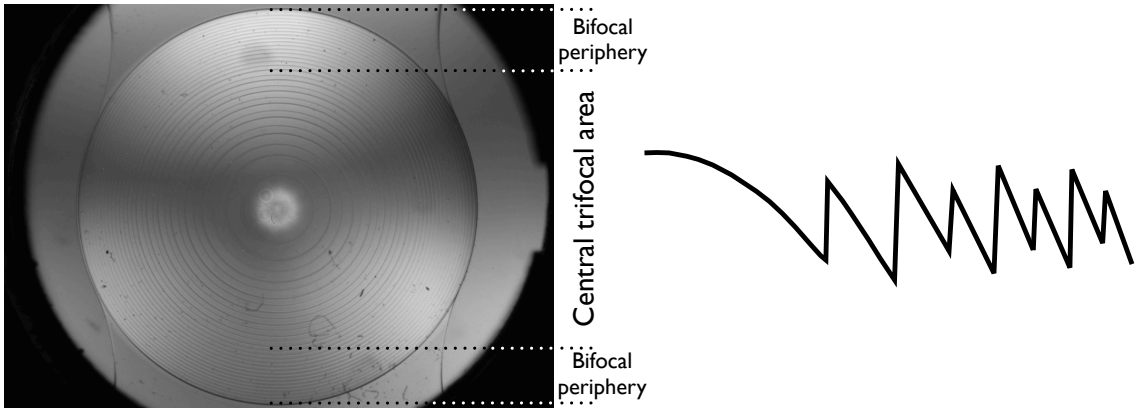

Figure 4.4: Left: Image of the front surface of the AT LISA 839MP IOL. The central area of the lens has the diffractive profile responsible for the formation of the near, intermediate and distance foci. The bifocal periphery sends light just to the near and distance foci. Right: Sketch of a possible trifocal-diffractive lens profile.

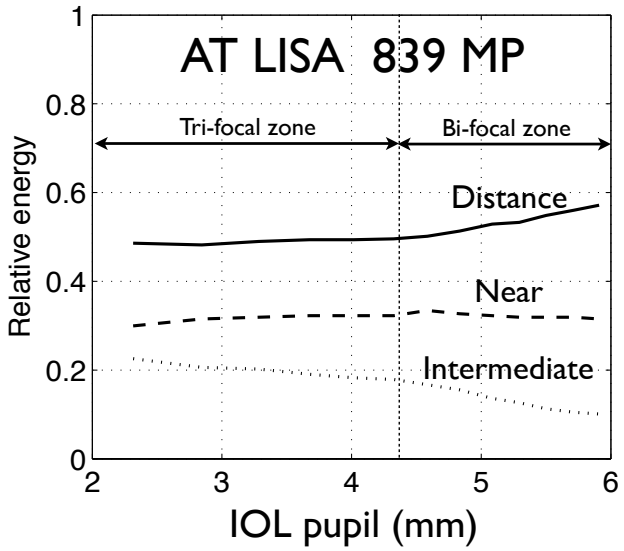

Figure 4.5: Energy efficiency provided by the manufacturer for the distance (continous line), intermediate (dotted line) and near (dashed line) powers of the AT LISA 938MP.

Since the amount of the energy transmitted by diffractive MIOLs and sent to each focus is proportional to the diffraction efficiency, it is generally assumed that the theoretical light distribution showed in figures 4.3 and 4.5 will correspond to the energy correctly focused onto the respective image planes. However, in addition to the diffraction efficiency there are other factors that determine how much of the diffracted energy really ends up correctly focused on the image. Thus, it has been pointed out [Tabernero et al. 2007] the importance of the shape factor and aspheric design of the base lenses of the IOL to properly tackle with the converging and aberrated wavefront [Pieh et al. 2009; Marcos et al. 2007] that comes from the cornea and impinges upon the IOL in order to obtain a high quality retinal image. Additional issues such as the contribution to higher diffraction orders (i.e., others than the ones that create the multiple foci) [Cohen 2012] scattering in the diffractive steps [de Vries et al. 2008; Meyers and Albrecht 1998], and the dependence of the depth of focus on the pupil size, also make that a significant fraction of the diffracted energy, which otherwise would be sent to a particular focus, gets out of focus at the image plane. This out of focus energy increases the background noise of the image and reduces the efficiency of the foci below the theoretical prediction. [Vega et al. 2011]. For this reason, the performance of the MIOL is better characterized by measuring experimentally the energy correctly focused on each image plane, that is, in terms of its energy efficiency distribution

because it accounts not only for the diffraction efficiency but also for all the aforementioned remaining factors.

4.1.2 Refractive multifocal IOLs

A refractive multifocal IOL is a compound lens that has different optical powers in different parts of the lens aperture. These lenses present different curvatures on one of their surfaces to produce multifocality.

There are two basic refractive MIOLs designs: One shows concentric rings and the other shows sectorial zones (also called asymmetric).

Refractive MIOLs (such as the AMO-ReZoom NXG1) with concentric rings have a surface with a curvature map that shows rotational symmetry. The rings are distributed in the lens aperture so that they contribute to either the distance or the near focus (figure 4.6).

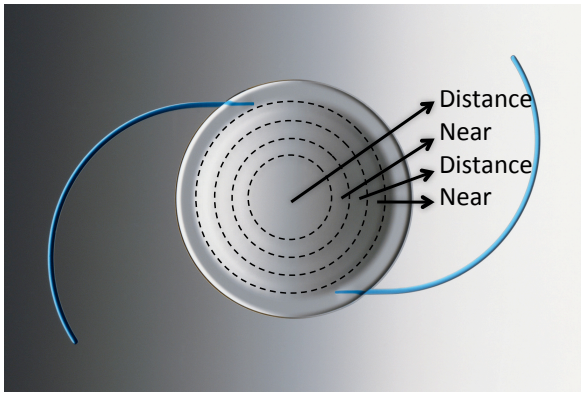

Figure 4.6: Sketch of a refractive MIOL (AMO-ReZoom NXG1) with concentric design.

In this lenses the amount of energy sent to each foci will depend on the pupil size. For very small pupils, only the central disk of the MIOL is illuminated and the lens behaves as a monofocal IOL. As the pupil size increases, the second and other rings are illuminated, thus producing the distance and the near foci.

The other types of refractive MIOLs are the asymmetric models. These lenses present one of their surfaces with a non-rotational design; a zone of its aperture contributes to the distance focus whether another zone, with a different curvature, generates the near focus. Figure 4.7 shows the LS-313 IOL that is to be studied in this work. It has a central disk that corresponds exclusively to the distance power. The rest of the aperture is distributed in two sectors. The largest corresponds to

the distance power whereas the smallest to the near power. Therefore, the relative amount of energy sent to the foci depend basically on the ratio of their respective sector areas.

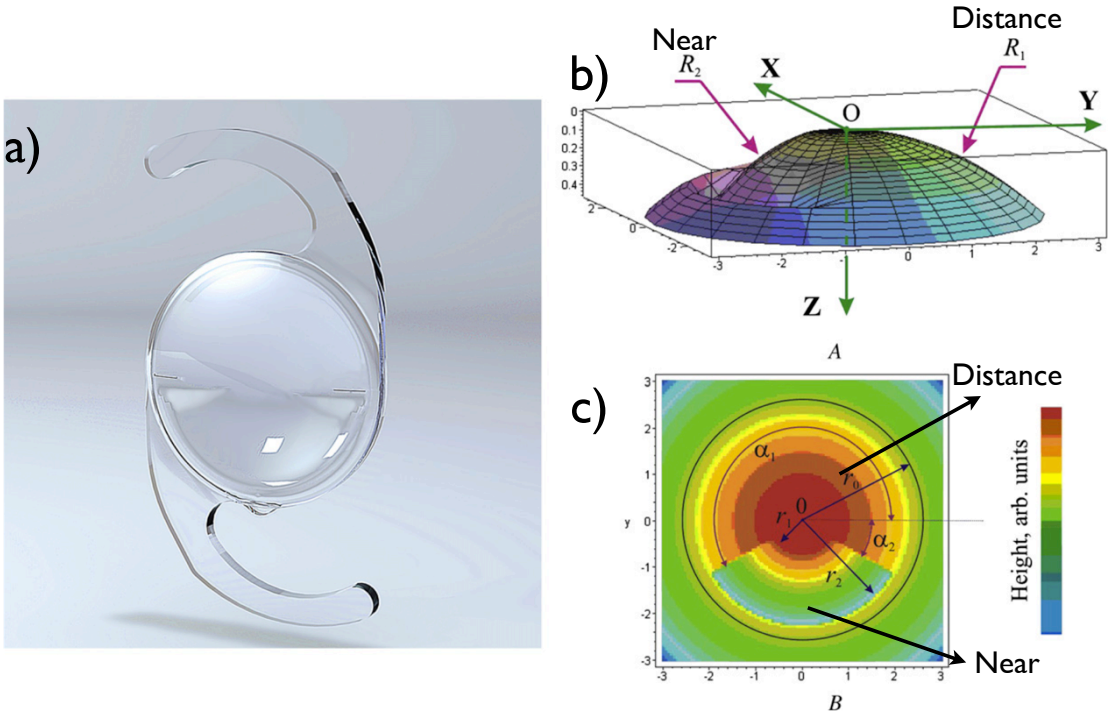

Figure 4.7: a) Illustration of the LS-313 IOL; b) Sketch of the radii of curvatures of the front surface; c) Height in arbitrary units of the front surface of the IOL.

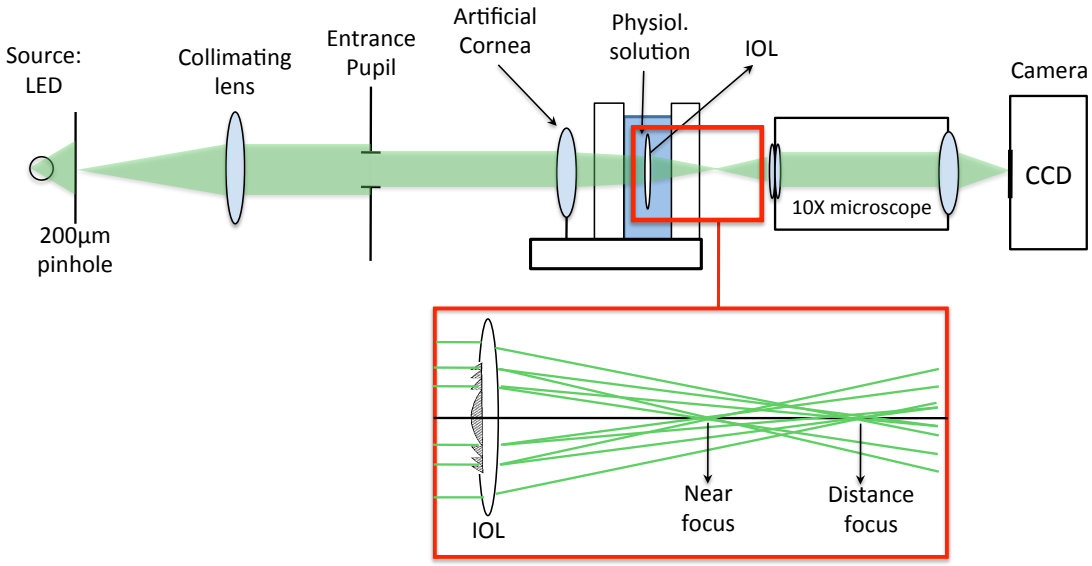

Figure 4.8: Setup used to obtain the distance and near images of a pinhole object. The inset shows how an ADMIOL works: The diffractive part of the lens (in gray) sends light to both foci, whereas the outer purely refractive part sends light to the distance focus exclusively.

4.2 Measurement of the energy distribution by image analysis

The in-focus images formed by different monofocal and multifocal IOLs of a 200μm pinhole have been obtained with different LEDs in the optical bench system described in chapter 3. Different IOL pupil values within the range 1.5mm to 5.5mm approximately have been considered. As we want to analyze the performance of lenses designed to correct different amounts of corneal SA, we used a lens for the artificial cornea that induces an amount of SA at the IOL plane similar to that naturally induced by the human cornea [Guirao et al. 2000; Wang et al. 2003; Vega et al. 2010]. A sketch of the setup used to obtain the images is shown in figure 4.8.

All the images were acquired with the same integration time by a CCD camera working in linear regime and optimized for the largest IOL pupil in the most intense focus. Thus, their energy content and features can be directly compared. Examples of the near and distance images of the pinhole obtained with an ADMIOL are shown in figure 4.9. Both images basically consist of the focused image of the pinhole (labeled I_{pinh}) surrounded by blurred background or halo (labeled I_{backg}). This background corresponds primarily to the overlaying defocused image. In the case of the distance image (figure 4.9(b)), however, there is an additional contribution that strongly depends on the level of SA upon the IOL, as it will be shown in the following sections. The energy of the image just in the focused pinhole region (I_{pinh}), and the energy of the total image that comprises the pinhole image plus the light in the background regions ($I_{total} = I_{pinh} + I_{backg}$), are obtained by integration of the pixel grey level in the corresponding areas:

$$I_R = \sum_{n_{pixel}}^{n \in R} g(n) \quad , \tag{4.14}$$

where R stands for either the pinhole region or the total image (*R=pinh, total*), *n* is a pixel contained in the *R* region, and *g(n)* is the pixel grey level. Since the images are blurred, it is not straightforward to segment the region of the focused pinhole from the background. An edge detection algorithm was used to crop the image of the pinhole, that is, to remove all the background around the pinhole (figures

4.9(c) and 4.9(d)). Then I_{pinh} was calculated from the filtered images according to equation 4.14 and the energy efficiency η of each focus (i) was obtained from:

$$\eta_i = \frac{\left(I_{pinh}\right)_i}{\left(I_{total}\right)_i} \text{ , with } i = \{\text{near, intermediate, distance}\} \text{ .} \qquad (4.15)$$

Then, this experimental energy efficiency of each focus can be compared to the theoretical ones calculated according to equations 4.11 and 4.12.

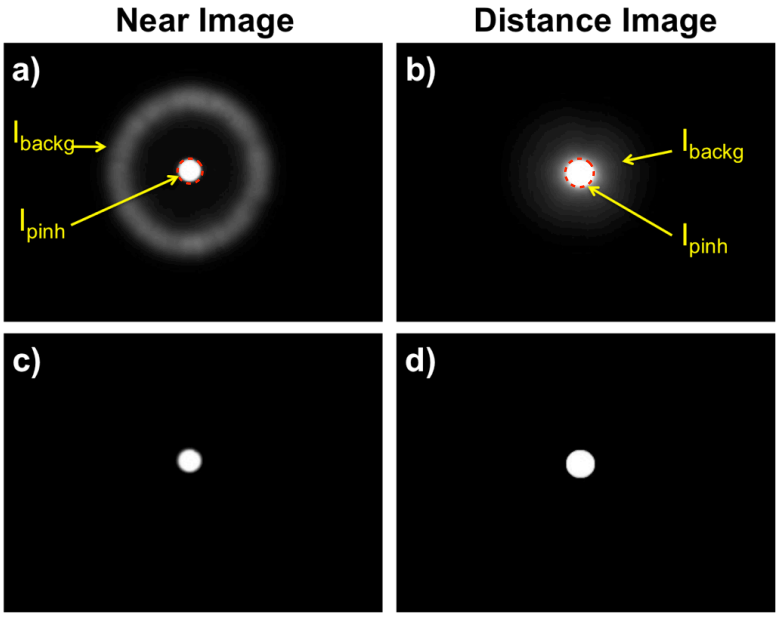

Figure 4.9: a) near and b) distance images experimentally obtained with an ADMIOL in the model eye. The dotted red line indicates the edge of the pinhole image. The arrows point to the region named pinhole (pinh) and background (backg). c) and d) idem after removing the background.

4.3 Experimental results

The energy efficiency of monofocal and multifocal IOLs has been measured under different conditions along the experimental stages of this thesis. The main technical characteristics of these lenses are contained in table 4.1.

In sections 4.3.1 and 4.3.2 the light source used was a quasi-monochromatic green LED. Section 4.3.3 is focused on analyzing the behavior of a multifocal-refractive IOL and a multifocal-diffractive IOL under different illuminating wavelengths. The analysis was performed with four different LEDs with spectral distributions centered in: the red band of the spectrum (R); the green band (G); the blue band (B); and finally, another one with wider spectral distribution that we will call white

(W). The spectral distribution of the radiance measured for these four LEDs is plotted in figure 3.2 (chapter 3).

Table 4.1: Main characteristics of the tested IOLs. Note that they all have the same base power.

Optical design	Reference (commercial name)	Corneal SA correction	Base power (D)	Addition (D)
Monofocal	SN60AT	No	20	-
	SN60WF (AcrySof IQ)	Partial	20	-
	ZA9003 (Tecnis)	Total	20	-
Diffractive (full aperture) -**Bifocal**	ZMA00 (Tecnis multifocal)	Total	20	4
Apodized – Diffractive **- Bifocal**	SN60D3 (AcrySof ReSTOR)	No	20	4
	SN6AD3 (AcrySof ReSTOR)	Partial	20	4
	SN6AD1 (AcrySof ReSTOR)	Partial	20	3
Central **trifocal** – Bifocal periphery	AT.lisa 389 MP	Partial	20	3.33 / 1.66
Refractive – Bifocal Sectorial Asymmetric	LS-313 (MPlus)	*	20	3

** Information not supplied by the manufacturer.*

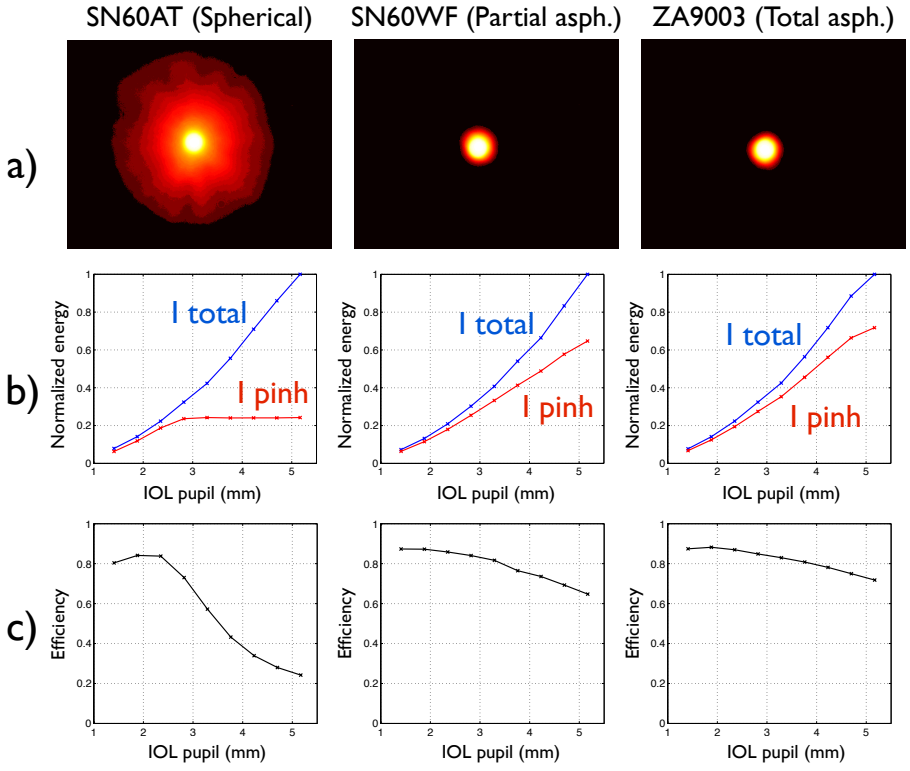

Figure 4.10: a) Images of a 200µm pinhole formed by three different monofocal IOLs with large IOL-pupil of 4.7mm. The images are displayed using a pseudocolour logarithmic scale. b) Normalized I_{total} and I_{pinh}. c) Relative energies (I_{pinh}/I_{total})

4.3.1 Spherical and Aspheric monofocal IOLs

In order to show the impact of the SA upon the IOL and to know how the lens design may help to tackle it, the first comparisons were made between the spherical and aspheric designs of monofocal intraocular lenses. In this section we present the study of the variation of the energies I_{total} and I_{pinh} with the IOL pupil for monofocal spherical IOL (SN60AT in figure 4.10), an aspheric IOL with partial compensation of the corneal SA (SN60WF in figure 4.10) and another aspheric design with total compensation of the corneal SA (ZA900 in figure 4.10). The relative energies or efficiency, defined as I_{pinh}/I_{total} are also plotted for each IOL (figure 4.10c). To make the comparison of results easier, I_{total} and I_{pinh} are normalized to the value of I_{total} obtained with the largest pupil diameter.

The images formed by the three IOLs in pseudocolour logarithmic scale (figures 4.10a) for a large pupil show the impact of the high amount of SA at the image plane of the spherical lens while both aspheric designs present sharper images.

The results of the normalized energy are plotted for I_{pinh} and I_{total} in figure 4.10b. As can be seen in this figure, the energy I_{total} scales cuadratically with the pupil diameter. Additionally, for small IOL pupil diameters up to 3mm (when the level of SA upon the IOL is small), the energy I_{pinh} is close to I_{total} for all three IOLs, which means that the background contribution is negligible in this condition, no matter the design of the monofocal IOL. As a consequence, images of high efficiency - of the order of 80% - are obtained with small apertures for all three IOLs as can be seen in figure 4.10c.

For larger pupil diameters, a different behavior between the spherical and aspheric monofocal IOLs can be observed. In the case of the SN60AT, the energy I_{pinh} remains constant, even though the measured I_{total} increases (figure 4.10b). This result implies that, when opening the entrance pupil, most of the additional avaliable energy is not sent to the pinhole image but “spoiled” in the background, and consequently, a dramatic reduction of the image efficiency occurs (figure 4.10c). For aspheric IOLs (SN60WF and ZA9003), the larger the entrance pupil the larger the value of $I_{pinh,}$ but the increase occurs with a slope less steep than the increase of I_{total} (figure 4.10b). This implies a moderate reduction in its relative

energy for larger pupil diameters as shown in figure 4.10c. The aspheric design with partial compensation of the corneal SA (SN60WF) present just slightly lower values of efficiency decrease than the aspheric design with total compensation (ZA9003). This difference in the efficiency decrease is only manifested for very large pupils.

4.3.2 Multifocal Intraocular lenses

Figures of the images of a pinhole formed by the tested MIOLs are shown in pseudo-color logarithmic scale in figure 4.11. The normalized energy values for I_{pinh} and I_{total} are plotted in figure 4.12 and their relative energy in figure 4.13. For all the MIOLs, the energy contained in the whole image (I_{total}) shows a quadratic dependence on the pupil diameter and is the same, within the experimental uncertainty, for each focus. This fact further confirms that there is no loss of energy when recording the images formed by the three MIOLs in the image space and guarantees that the normalization of the results by the maximum of I_{total} is correct.

In addition to the I_{total} (blue lines) and I_{pinh} (red lines), the sums $\left(I_{pinh}\right)_{distance}+\left(I_{pinh}\right)_{near}$ for bifocal IOLs and $\left(I_{pinh}\right)_{distance}+\left(I_{pinh}\right)_{intermediate}+\left(I_{pinh}\right)_{near}$ for the trifocal IOL in figure 4.12 in black continuous line are also plotted. In these plots we see that for small pupils up to $3mm$ the sum of the correctly focused energy of the multiple foci agrees pretty well with the value of the total energy contained in the images I_{total}, but for larger pupils this sum is clearly lower than I_{total}. This means that for small pupils, the background noise in the images is basically due to the contribution of the non-focused powers of the multifocal IOLs, which are out of focus in that plane but correctly focused in their respective image planes. On the contrary, for large IOL-pupils the background energy presents an additional contribution that does not come uniquely from the out of focus IOL powers. As a consequence, there is a reduction of the efficiency (shown through the relative energy in figure 4.13) well below the values computed in the theoretical estimation. To explain these results we must consider the different increasing values of the SA upon each IOL as a function of the IOL pupil, as well as the larger number of diffractive steps taking part in the process (and the

associated light scattering), and the transitions between the near and distance focus in the case of the refractive-based multifocal IOL. All these circumstances affect negatively the capacity of the lenses to correctly focus the energy onto the image plane.

Full-aperture diffractive design

The full-aperture diffractive design (ZMA00) MIOL has an aspheric surface to totally compensate the corneal induced SA to the optical system. Its diffractive surface, designed for an addition power of +4.0*D*, has the same step height in the entire aperture to theoretically split the incident beam energy equally between the distance and near powers. This characteristic is manifested in the images of a 200μm pinhole for a large pupil in the distance and near foci shown in figure 4.11. In this figure we see how the background occupies approximately the same area for both the distance and near focus.

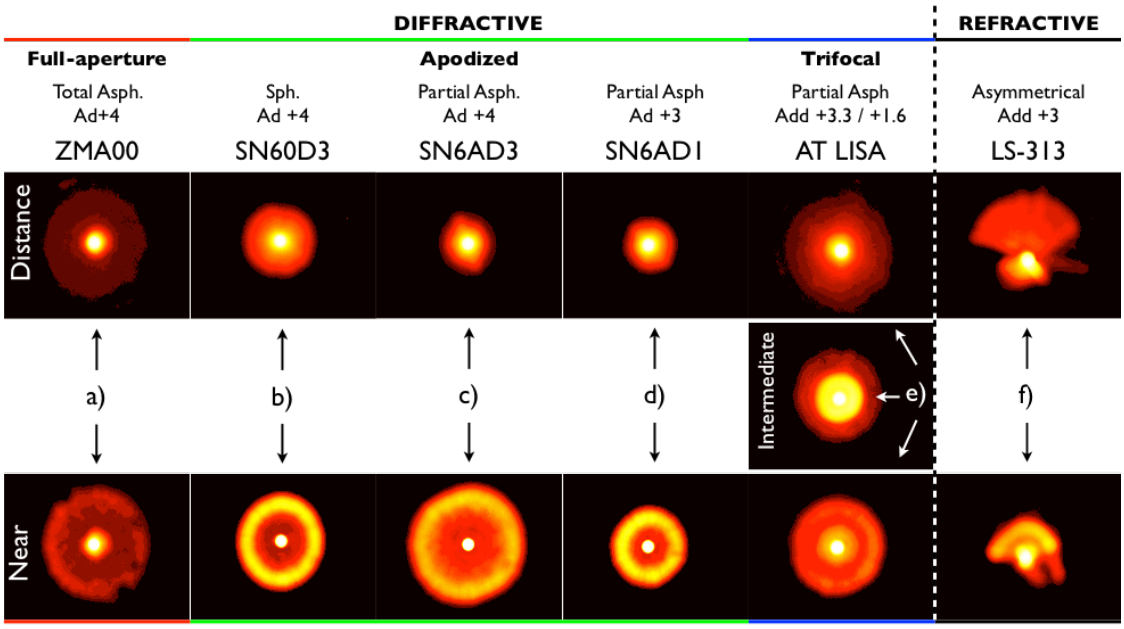

Figure 4.11: Images of a 200µm pinhole formed by various MIOLs with large IOL-pupil of 4.7mm. The images are displayed using a pseudocolour logarithmic scale. Note that the AT-LISA presents 3 images because is a trifocal-diffractive IOL.

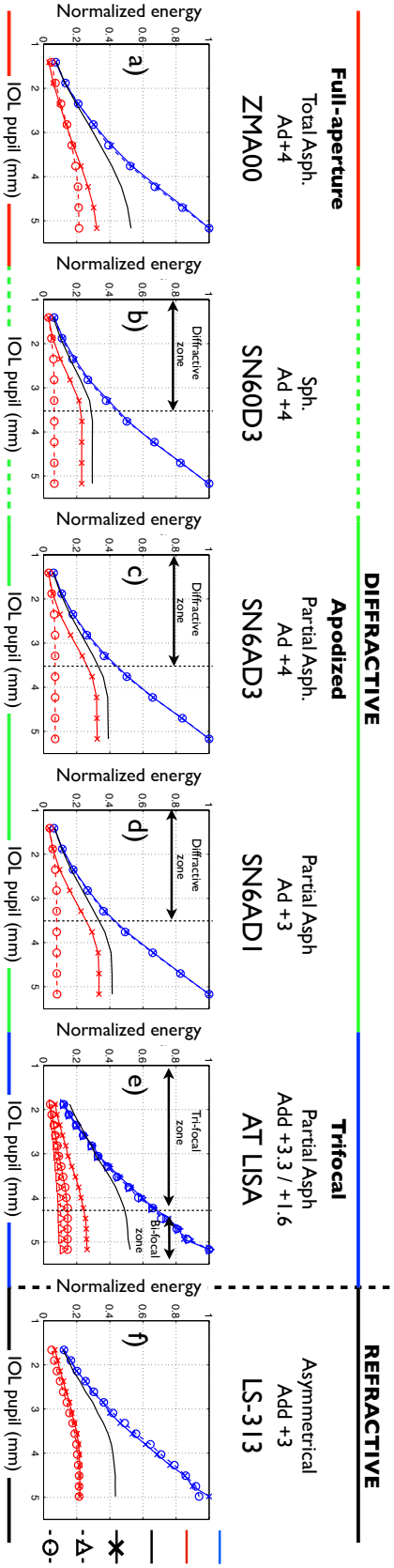

Figure 4.12: Normalized I_{total} and I_{pinh} at distance, intermediate (only for the AT-LISA) and near image planes for each MIOL.

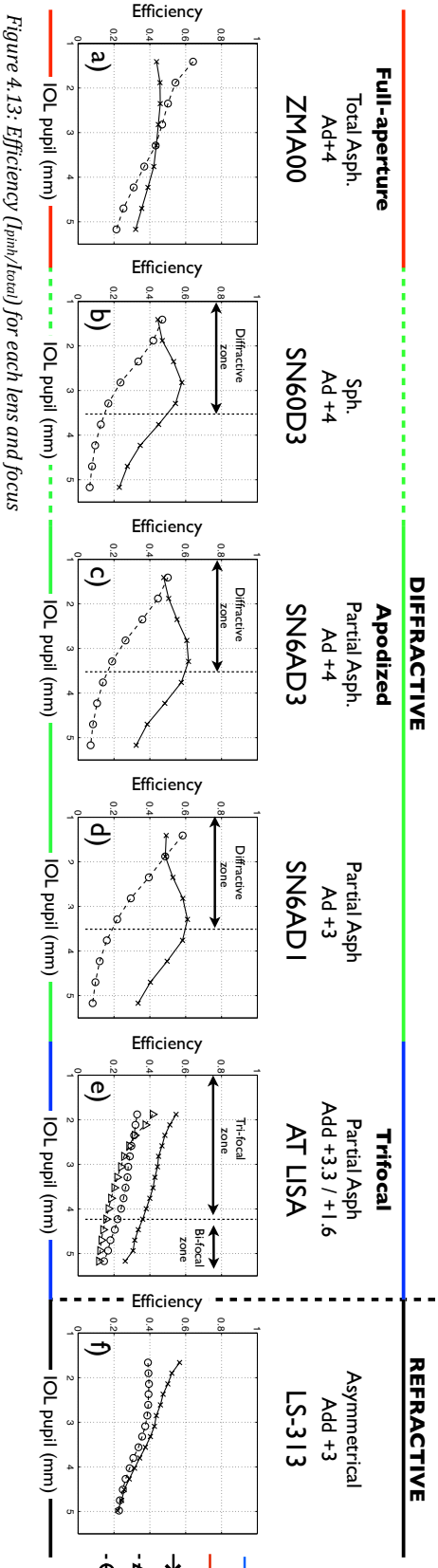

Figure 4.13: Efficiency (I_{pinh}/I_{total}) for each lens and focus

In figure 4.12a the normalized energies I_{total} and I_{pinh} of the distance and near image planes are plotted. As the energy I_{total} increases for the distance focus, the I_{pinh} also increases but at a lower rate. Consequently, the ratio I_{pinh}/I_{total}, represented in figure 4.13a is almost horizontal (declining slightly for large pupils). On the contrary, in the near focus, the energy I_{pinh} increases for IOL-pupil diameters up to $\approx 4.0mm$ and then keeps constant at a value of 20% for larger pupils (figure 4.12a) while the I_{total} continues increasing quadratically with the entrance pupil diameter. Therefore, the energy efficiency I_{pinh}/I_{total} (figure 4.13a) of the near power diminishes constantly as the IOL-pupil increases. This result for the near focus may have several explanations, one of them is that the error in the step manufacturing could be higher in the periphery of the IOL aperture, where the diffractive rings are closer to each other, than in the center thus resulting in higher scattering and loss of diffractive efficiency [Meyers "techniques to eliminate…"]. Another possible explanation is that the asphericity of this lens would be optimized for the distance power but not for the near one, thus resulting in a reduction of the efficiency as the level of SA increases for large pupils.

Apodized-diffractive designs

These lenses present a common characteristic: all three have the same apodization factor in the central 3.6mm zone of the diffractive profile. But they differ in the spherical (SN60D3) and aspheric (SN6AD3 and SN6AD1) base designs and in the addition power (+4.0D in SN60D3 and SN6AD3 and +3.0D in SN6AD1).

The images of a $200\mu m$ pinhole formed by these lenses with a large pupil in the model eye are represented in pseudocolor logarithmic scale in figures 4.11b-d. Because of the apodized design, the background energy in the near focus is greater and occupies a larger zone than in the distance focus in all three MIOLs. We can see how, in the distance focus, the spherical lens (SN60D3) present a larger size of the background energy due to the presence of SA. Both aspheric designs, however, have a better and similarly small distance image. The apodization benefits the distance focus, with a lower influence of the defocused near focus. In the near focus, the background energy of the lens with +3.0D of addition (SN6AD1) occupies less area than in the other lenses with +4.0D of addition due to the closer proximity between their distance and near foci. Other interesting results can be

seen in the near images of the spherical (SN60D3) aspheric (SN6AD3) MIOLs with +4.0D. Even though they have the same addition, so the distance along the axis between their respective foci are the same in both designs, the smaller amount of SA of the SN60D3 in the near focus leads to a more concentrated distribution of the background energy (produced by the unfocused image of the distance power) than in the SN6AD3. In the section 6.3 we will come back to these issues and deal with the characterization of the halo produced by the simultaneous imaging in MIOLs.

The normalized energies as a function of the IOL-pupil size of these lenses are plotted in figures 4.12b-d and show that in the case of the near images there is almost no difference between the energy I_{pinh} measured in the three apodized-diffractive MIOLs: it increases slightly with the IOL pupil diameter up to ≈3.6mm, which corresponds to the limit of the diffrative zone of the IOLs and then, keeps this low constant value for larger IOL-pupils. Since, on the other hand, the energy I_{total} of the near image increases with the entrance pupil (figures 4.12b-d), the energy efficiency I_{pinh}/I_{total} of the near image strongly decreases for large pupils as it is shown in figures 4.13b-d.

These results are not unexpected taking into account that for these apodized-diffractive MIOLs the maximum aperture involved in the formation of the near image corresponds to the diffractive zone of the IOL, which is relatively small (≈*3.6mm* diameter), and so is the level of SA of the system. Once the diffractive zone of the lens is fully illuminated, there is no way to send more energy to the near image and, as a consequence, I_{pinh} in the near image remains constant (figures 4.12b-c) for larger IOL apertures independently of the particular design (spherical or aspheric) or add power (+4.0D or +3.0D) of the IOL. In these conditions, the aspheric design of the SN6AD3 and the SN6AD1 proves not to be advantageous, with respect to the near image energy efficiency, in comparison with the spherical design of the SN60D3.

The influence of the surface asphericity produces some differences in the experimental results. With the spherical SN60D3, as it is plotted in figure 4.12b, the value of I_{pinh} first increases with the IOL-pupil diameter (up to 3-4mm) and then keeps a constant value of the order of ≈20% for larger pupils. The results of the aspheric SN6AD3 IOL follow a similar tendency, but the measured values of

I_{pinh} for large pupils are above 30%, higher than the values measured for the spherical SN60D3 IOL. On the other hand, there are no significant differences in the results obtained for both the distance and near foci in the apodized-diffractive MIOLs of aspheric design but different add power (SN6AD3 vs SN6AD1).

Expressing these results in terms of the relative energy or efficiency of the images (figure 4.13b-d), it can be seen that for the distance image both IOLs (spherical and aspheric) behave very similarly - and these results are in agreement with theoretical calculations - only up to moderate pupil diameters (IOL-pupils of $\approx 3.6mm$ for the spherical and $\approx 4.2mm$ for the aspheric). In these conditions, which correspond to reduced levels of SA upon the IOL, the maximum energy efficiency achieved is around the same value of 60%. However, for larger pupils, when the contribution of the refractive part of the IOLs to the distance image is gaining importance, there is a clear reduction of the energy efficiency for both IOLs, in contrast with the increasing distance dominant behavior predicted theoretically and plotted in figure 4.3. Once again, the results obtained with the aspheric designs of $+4.0D$ and $+3.0D$ turn out to be quite similar due to the same apodization factor in the diffractive profile of these lenses.

As for the distance image and large pupils, the significant differences that we have found between the experimental results and the theoretical ones put into question the theoretical distance dominant behavior of the apodized-diffractive MIOLs in the presence of SA. These results show that most of the additional energy available for the distance image when the entrance pupil diameter increases, does not actually end up in the pinhole image but spoiled in the background. This adverse effect is even worse in the case of the spherical multifocal IOL that cannot compensate properly for the SA produced by the model eye.

Trifocal

Figure 4.11e shows the experimental images of the $200\mu m$ pinhole object obtained in the near, intermediate and distance image planes for a large IOL pupil. These images again evidence that there is a non-negligible fraction of the energy that is out of focus, thus contributing to the background halo-shaped energy.

As can be seen in figure 4.12e the distance focus achieves the highest energy I_{pinh} for all pupil sizes. Near and intermediate foci have similar energy for small pupils while for larger pupils the near focus is slightly more intense. The intensities I_{pinh} for distance, intermediate and near foci increases as a function of the IOL-pupil, but their increase is slow and has not the steep slope of the total energy of the images I_{total}. This fact implies a reduction of the energy efficiency for larger pupil diameters as shown below.

The experimental image energy efficiency for each focus is plotted in figure 4.13e. In this figure we can see that for pupils up to ≈3.25mm, the energy efficiency of the far and near foci are around 50% and 30% respectively, and these values for small apertures are still close to the values of the diffraction efficiency provided by the manufacturer (figure 4.5). In these conditions, the influence of the corneal SA upon the IOL is relatively small and few diffractive zones of the lens are taking part in the process of diverting light to the foci, so is the light scattering associated with the steps of the diffraction profile [Meyers and Albrecht 1998]. On the other hand, for small IOL pupils the intermediate focus shows slightly larger efficiencies than expected.

As for pupils larger than 3.0mm, and consequently higher levels of SA upon the IOL and more diffractive zones involved in the process, there is a significant reduction in the experimental efficiencies for the far and near foci in comparison to the provided values. In the case of the intermediate focus, the experimental efficiency as a function of the pupil size is in good agreement with the curves provided by the manufacturer (figure 4.5).

The lens performance concerning the intermediate focus deserves further explanation. We have found that for pupils up to 3.0mm approximately, the experimental energy efficiency for this focus is, somehow surprising, larger than the provided values (figure 4.5), the smaller the pupil the larger the difference. To explain this fact we refer to figure 4.14. The intermediate focus is between the distance and near foci and for such small pupils (2.0 to 3.0*mm*, where the effects of the SA and scattering have proved to play a minor role) it is well known that depth of focus (DoF) increases [Zalevsky 2010]. Thus, the smaller the pupil the more extended the depth of focus of the distance and near foci and, as a consequence,

the smaller the fraction of the energies $\left(I_{pinh}\right)_{near}$ and $\left(I_{pinh}\right)_{distance}$ that are out of focus at the intermediate plane (see figures 4.14b and 4.14c). This fact becomes more evident when the focal segment corresponding to the depth of focus of both the near and distance foci reach one another or even overlap at the intermediate focus plane (figure 4.14c). The result is a reduction of the background energy in the intermediate image plane and, consequently, an increase in the relative energy of this focus as was experimentally observed. Obviously, this effect related to the distance and near extended DoF is absent in the results provided by the manufacturer who possibly only considered the diffraction efficiency for the intermediate focus in their estimation.

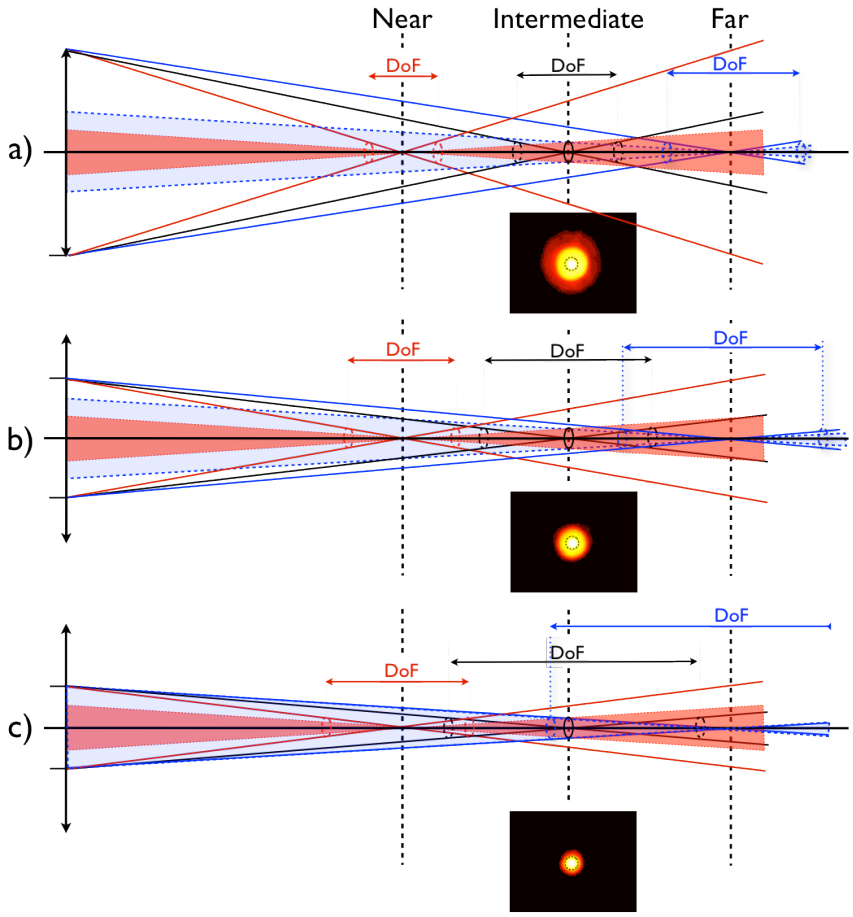

Figure 4.14: Sketch of the increasing depth of focus as the pupil size is reduced (from (a) to (c)). The images at the intermediate plane are shown in a pseudocolor logarithmic scale for the sake of visualization.

For pupils larger than 3.0*mm* the measured energy efficiency for the intermediate focus shows a reduction that is in good agreement with the provided values of theoretical diffraction efficiency. This is not unexpected taking into account that the maximum aperture involved in the formation of the intermediate image is relatively small (4.3*mm*) and so is the maximum level of SA that the trifocal IOL has to compensate. Moreover, once that this zone of the trifocal IOL is fully illuminated, there no way to diffract more energy to the intermediate image I_{pinh}, and this fact produces the observed reduction of the efficiency (figure 4.13e).

Refractive

In figure 4.11f the images of a pinhole formed by the LS-313 IOL with a large IOL-pupil is shown. These images present clear asymmetry that was not noticeable in the images formed by any other multifocal IOL so far because this is the only design in our study with a non-rotational surface profile (figure 4.6). Anyway, this lack of symmetry will not affect to our calculations because we compute the total energy outside the region I_{pinh} independently of its spatial distribution.

The normalized energies of the distance and near images, plotted in figure 4.12f, show similar behavior as a function of the IOL pupil. The curves corresponding to I_{pinh} for distance and near foci are very close to each other and this is the main difference in comparison with the diffractive-based multifocal IOLs. Consequently, the efficiency (I_{pinh} / I_{total}) of distance and near foci plotted in figure 4.13f are also very close to each other. Anyway, as we have seen with all the diffractive-based IOLs already studied, for small pupils as the energy I_{total} in figure 4.3.3f increases, the I_{pinh} also increases but at lower rate. For pupils larger than ≈4.0*mm* the increase of I_{pinh} ceases and both the near and distance curves remain almost constant value, meaning that the extra light incoming due to a larger aperture does not contribute to the near or distance I_{pinh} but to increase the I_{backg}.

An interesting result found in figure 4.13f is that the efficiency corresponding to the near focus (dashed with circles) for IOL-pupils smaller than 2.5mm is constant (horizontal zone of the curve). This is not unexpected because the design of the refractive multifocal surface of this IOL model presents the central region with the curvature of the distance power (see figure 4.6c).

4.3.4 Wavelength dependence

The dependence of diffractive-based optical systems on the wavelength is well known [Turunen and Wyrowski 2000]. The objective of this section is to show how the energy efficiency depends on the wavelength for two MIOLs: a MIOL with a diffractive based design and a MIOL with a refractive design (SN6AD1 versus LS-313)[García-Martínez and Millán 2012].

Taking into account the parameters provided by the manufacturer [Lee and Simpson 1997] and applying the equation 4.1 we obtain that the addition is given by:

$$D_{add} = (2i-1)\lambda \frac{1000}{r_i^2} \ , \qquad (4.15)$$

which means that for a design of IOL with an r_1=0.428mm that correspond to a D_{add}=+3.0D (as in section 4.1) for λ=550nm, the same IOL will present D_{add}=2.4D for λ=440nm and D_{add}=3.5D for λ=640nm.

Additionally, the wavelength has another important influence on the energy efficiency. If we apply the same reasoning of the section 4.1 (equations 4.1 to 4.12), but considering different wavelengths we obtain the theoretical efficiencies as a function of the IOL pupil plotted in figure 4.15.

In contrast to this, the refractive design of the LS-313 lens is not be affected by the wavelength in the same way, that is, beyond the dispersive nature of the material.

To obtain the experimental efficiencies for different wavelengths we followed the same procedure described in previous section but using four LEDs: three quasi-monochromatic LEDs, centered in the red (R), the green (G) and the blue (B) spectral bands, and another one with a broader spectrum called henceforth “white” (W) LED. It is worth mentioning that the images of the 200μm pinhole are captured in the distance and near best image plane positions for each LED to overcome the influence of the chromatic dispersion of the IOL materials.

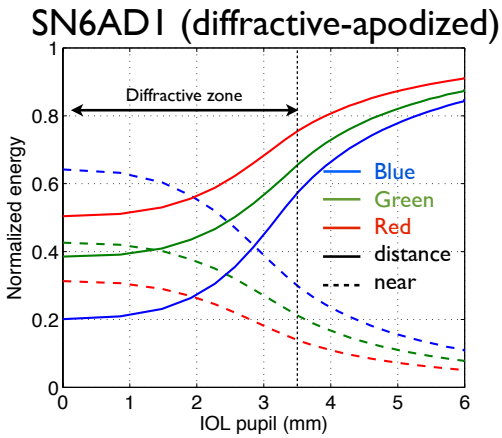

Figure 4.15: Theoretical energy efficiencies of the distance and near foci of the diffractive AcrySof ReSTOR lens of +3.0D addition power for different wavelengths (blue=440nm; green=550nm and red=640nm).

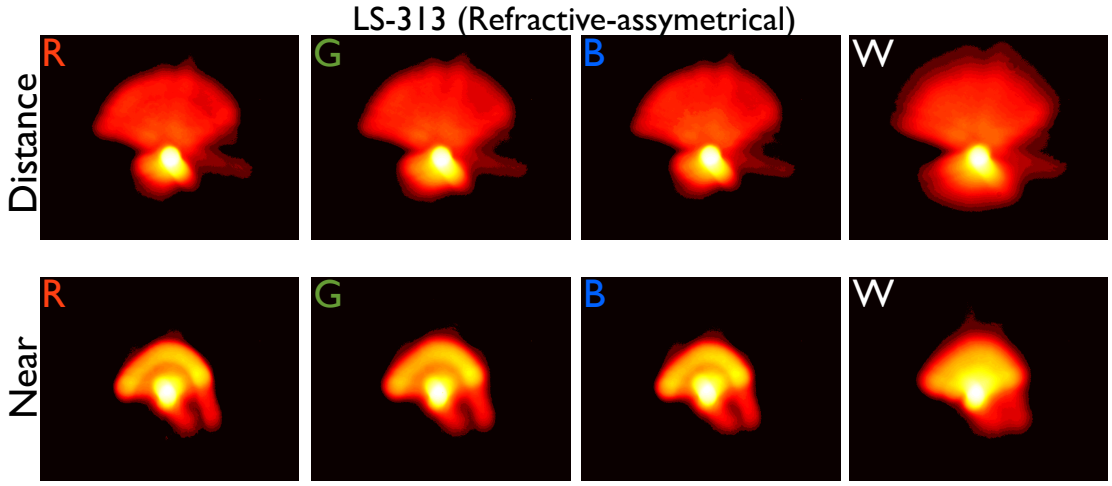

Figure 4.16: Pseudocolored logaritmic image of a 200 µm pinhole formed by the LS-313 MIOL with an IOL pupil of 4.7mm. Red (R), green (G), blue (B) and white (W) LEDs have been used for illumination.

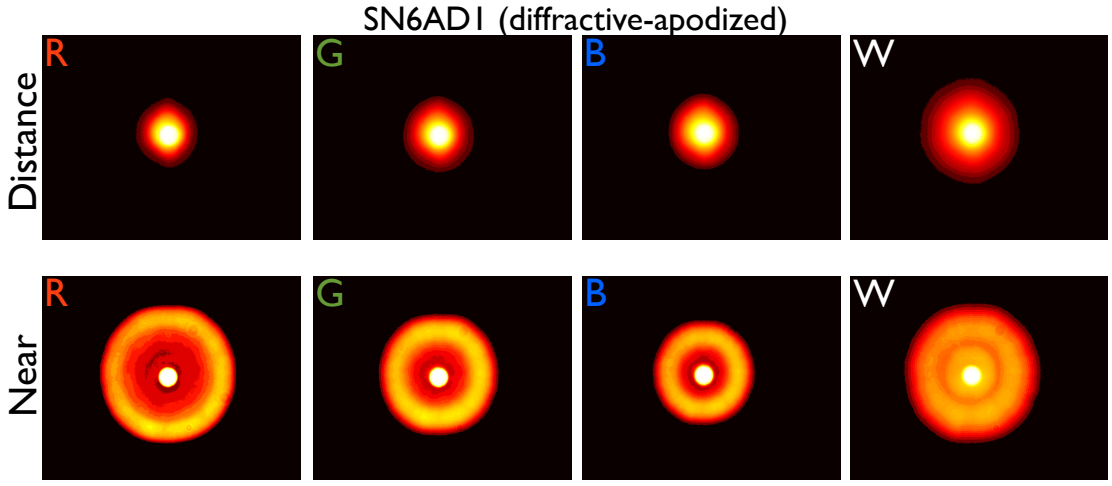

Figure 4.17: Pseudocolored logaritmic image of a 200 µm pinhole formed by the SN6AD1 MIOL with an IOL pupil of 4.7mm. Red (R), green (G), blue (B) and white (W) LEDs have been used for illumination.

From figure 4.16, the images formed by the LS-313 lens with different wavelengths are closely similar. In contrast, the images captured with the SN6AD1 lens (figure 4.17) show noticeable differences in the distribution of the background energy when using LEDs with different spectral distributions especially in the near focus. Althought it is difficult to appreciate from figure 4.17, in the distance focus obtained with the diffractive-based MIOL, the background energy with the red LED is slightly lower than with the other wavelength because for the red one the efficiency of the diffractive profile benefits the distance focus. On the contrary, the distance image of the blue LED shows higher energy in the background because for this wavelength the efficiency benefits the near focus.

Differences in the distribution of the background energy in the near focus are more notorious and can be explained considering equation 4.15 and figure 4.15. As we have seen before, the longer the wavelength used, the larger the addition of the IOL and, consequently, larger distance between foci. Moreover, the longer the wavelength, the lower amount of energy sent to the near focus. For these two reasons, when this lens is illuminated with red light, the near image has higher amount of background energy distributed in a larger surface. The opposite occurs when using blue light.

In terms of the energy efficiency, the lower dependence of the refractive lens (LS-313) on the wavelength than the diffractive lens (SN6AD1) is also evident in the normalized energy plots (figure 4.18). We can see that the lens LS-313 presents similar behavior for all the three light sources while the SN6AD1 presents different performances. In this lens, the effect of the light source is more noticeable in the distance focus. The apodized design of the diffractive surface makes the near focus obtain lower intensity.

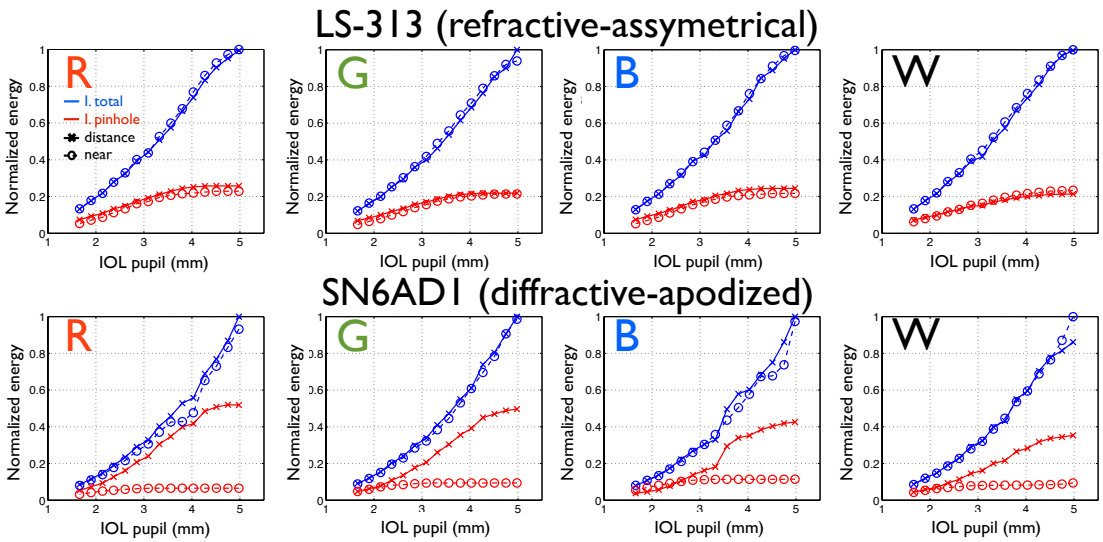

Figure 4.18: Normalized I_{total} and, I_{pinh} for distance and near foci for each light source (R: red, G: green, B: blue and W: white).

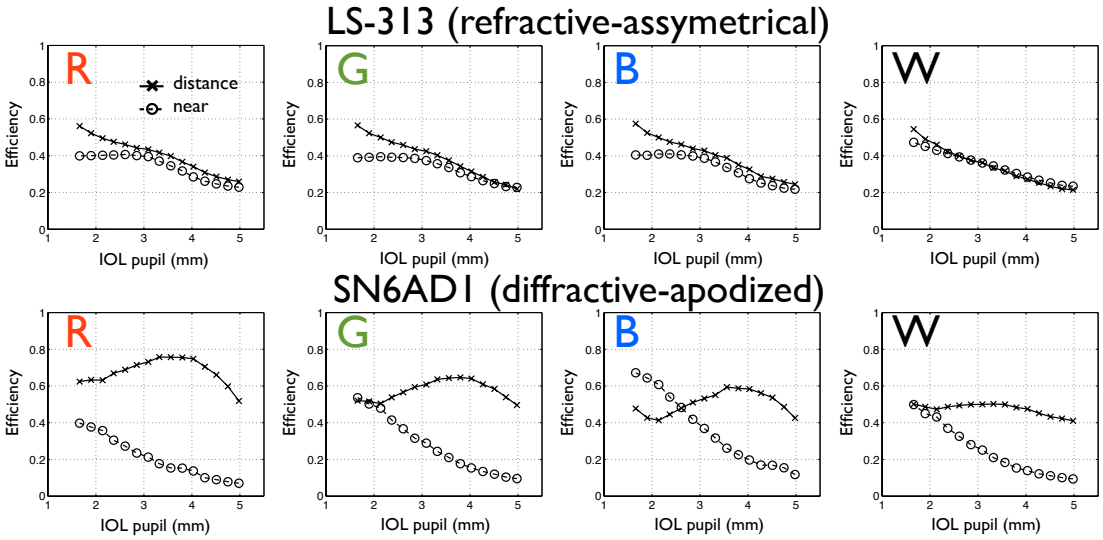

Figure 4.19: Efficiency (I_{pinh}/I_{total}) for each light source (R: red, G: green, B: blue and W: white) and each foci in a refractive MIOL (LS-313) and a diffractive MIOL (SN6AD1).

In figure 4.19 the efficiency curves (I_{pinh}/I_{total}) are plotted as a function of the IOL pupil for each LED. In this figure we see that the refractive LS-313 MIOL presents very similar curves no matter the LED used. On the contrary, the diffractive SN6AD1 present important differences with the wavelength. The relative energy in the distance focus formed by the diffractive SN6AD1 with the red LED is higher than with the other LEDs. On the other hand, the relative energies of the blue LED is lower in the distance focus but the highest in the near one. As it happened in the previous section, the relative efficiency curves measured experimentally for the

distance focus with the SN6AD1 MIOL are lower than the theoretical predictions (figure 4.15) for large pupils no matter the LED used. Again, the presence of unwanted effects such as the SA or scattering in the diffractive steps can be the reason of such decrease. On the other hand, the efficiency of the near focus is in accordance with the theoretical predictions due to the small IOL-pupil that contributes to the *m*=1 diffraction order (only the central 3.6mm).

4.4 Conclusions

An experimental method that measures the energy directed to the focal image, the energy directed to the background, and therefore, the energy efficiency as a function of the pupil diameter has been developed. It has been applied to the single focus of several monofocal IOLs as well as to the different foci of several MIOLs.

Monofocal aspheric IOLs present higher efficiency than other lenses especially in the case of large pupils. The effect of the SA on the IOL performance is evident in the spherical mono and multifocal IOLs.

The energy distribution of the diffractive MIOLs differs from the theoretical predictions because they only consider the diffractive profile but not other factors such as the spherical aberrations and/or scattering that can degrade the image decreasing the energy efficiency.

The wavelength dependence of the performance diffractive based MIOLs in terms of light distribution between their foci, must be considered specially when patients implanted with these type of MIOLs are analyzed with red or infrared light system such as clinical aberrometers, auto-refractors, double-pass systems, etc. and when using anaglyphic based observation systems like some stereotest, as we will see in chapter 5. On the other hand, the refractive MIOLs show less variation with wavelength.

CAPÍTULO 5

INFLUENCIA DE LAS LENTES INTRAOCULARES MULTIFOCALES EN LA MEDIDA DE LA ESTERO-AGUDEZA

CHAPTER 5

INFLUENCE OF MULTIFOCAL INTRAOCULAR LENSES IN STEREO-ACUITY MEASUREMENTS

REFERENCE TO THE PUBLICATIONS OF THIS THESIS

The content of this chapter is included in:

- Varón, C., Gil, M.A., Alba-Bueno, F., Cardona, G., Vega, F., Millán, M.S. and Buil, J.A. *"Stereo-Acuity in Patients Implanted with Multifocal Intraocular Lenses: Is the choice of Stereotest Relevant?*. Curr Eye Res. Posted online on January 8, 2014 (doi:10.3109/02713683.2013.865758).

Stereoscopic vision or stereopsis is the capability to judge the relative distances of objects from the observer by means of binocular vision. This capability depends on the tiny disparities existing between the retinal images of the two eyes [Bennett and Rabbetts 2007]. Stereo-acuity is affected by degraded optical quality in one or both eyes and by binocular impairment [Wood 1983; Lovasik and Szymkiw 1985; Legge et al. 1987; Saladin 1995; Simons 1984]. For this reason, stereo-acuity can be considered a good indicator for the binocular visual quality of a patient, once fusion or motor problems have been discarded.

Large differences in stereo-acuity values have been reported depending on the specific test used to assess the stereopsis of patients implanted with either monofocal or multifocal IOLs [Garnham and Sloper 2006]. For instance, Ferrer-Blasco et al. [Ferrer-Blasco et al. 2010] found, with the Titmus and Random dot stereotests, no statistically significant differences in the mean stereo-acuity of patients with bilateral implantation of an aspheric bifocal AcrySof ReSTOR (SN6AD3) IOL, but significant differences were found when using the Howard-Dolman method, leading the authors to consider this method as the most sensitive and accurate to determine stereo-acuity [Madrid-Costa et al. 2010]. However, the Howard-Dolman apparatus is rarely used in clinical practice because its applicability is less convenient than other tests. Instead, stereo-acuity in patients with MIOLs is commonly measured by using vectographic tests such as the Titmus Wirt test, Random-dot tests such as the Lang Stereotest, or anaglyphic tests such as the TNO, which is a highly dissociative stereotest that, in addition to this, does not present monocular cues [Wood 1983]. In general, clinical works rely on just one of the methods mentioned above and do not provide specific reasons to justify the choice of a particular type of stereotest. Very few works compare the results obtained with different kind of tests applied to patients implanted with IOLs and even more rarely, they try to analyze the physical causes of the differences encountered between them, if any.

In this chapter, we analyze the possible influence of MIOL implants in the results of stereo-acuity obtained with two tests of common clinical practice, namely Timus and TNO. These tests are presented to the patient's visual observation at a near distance of 40 cm (i.e., object vergence of -2.5D). Patients are assumed to have been symmetrically implanted, that is, to have both eyes implanted with the same intraocular lens design. Three basic types of MIOLs have been considered in our study: refractive, diffractive and hybrid refractive-diffractive. For the sake of comparison, we have also included in the study a group of patients symmetrically implanted with monofocal IOLs. To the best of our knowledge, the influence of the kind of test on the stereo-acuity assessment of patients implanted with MIOLs, particularly MIOLs of diffractive or hybrid refractive-diffractive designs (commonly referred in this dissertation as to diffractive-based MIOLs), has not

been yet addressed. Unlike the Titmus test, the principle of chromatic disparity used by the TNO test (i.e., the fact that each eye is tested with a different wavelength) may induce in diffractive-based MIOLs significant wavelength-dependent differences in at least two basic aspects: the add power of the lens and the energy efficiency of the near focus. These effects can be explained in terms of physical optics and highlighted from the comparison of the stereo-acuity measurements in patients obtained by the Titmus and the TNO tests. Finally, the clinical implications derived from all these effects are also discussed.

5.1 Method

5.1.1 Stereo-acuity tests

Both the Titmus and the TNO tests have been used in this study and its main characteristics are resumed in table 5.1.

	Titmus	***TNO***
Dissociative spectacles	Polarized	Red/Green filters *(2)*
Images (1)	Edge-based	Colored random dots
Disparity range	400-800 arcsec	15-480 and >480 arc-sec

Table 5.1: Main characteristics of the stereoacuity tests used. (1) See figure 5.1. (2) See figure 5.2.

The Titmus test (Fig. 5.1 top) uses polarized glasses to induce the retinal disparity (dissociation) that is necessary for the perception of depth. The lateral contours and image displacement of the test facilitate stereopsis. The anaglyphic TNO test (Fig. 1 bottom) consists of random dot chromatic stimuli, which require glasses with red-green filters to give rise and convey disparity. Unlike the Titmus test, the TNO test does not present any contour so that monocular cues have not any influence over the stereoscopic perception. It must be noted that each test has a different and discrete range of disparity: between 40 and 800 arc-second for the Titmus test and between 15 and 480 arc-second for the TNO. The TNO test includes an additional set of non-quantitative figures with a disparity higher than 480 arc-seconds. For both tests, the lower values the better capability to depth perception and, therefore, better stereoacuity. Larger values, on the contrary, correspond to poorer stereoacuity. When using the TNO test, the disjoint spectral transmittances of the red-green chromatic filters (Fig. 5.2) make fellow eyes see

patterns of different spectral content. Interestingly, the measured spectral transmittance of the red filter, which is considerably larger than the one of the green filter (Fig. 5.2(a)), would likely compensate for the lower spectral sensitivity of the eye in the red. To confirm this statement, we have multiplied the curves of transmittance given in Fig. 5.2(a) by the CIE luminous efficiency curve of the eye in photopic conditions. The results are plotted in Fig. 5.2(b) and further confirm that the TNO test is intended to produce similar luminous flux efficiency in both eyes or, in other words, the performance of this test is meant to produce the comparison of images of similar luminance, provided the spectral distributions of the white light source and the test picture reflectance are appropriated as well.

I Figure 5.1: Stereotests used in the study: (Top left) Titmus and (Bottom left) TNO. (Top right): double-polarized images of the Titmus test containing monocular cues; and (Bottom right): Red-Green disparity of the TNO test.

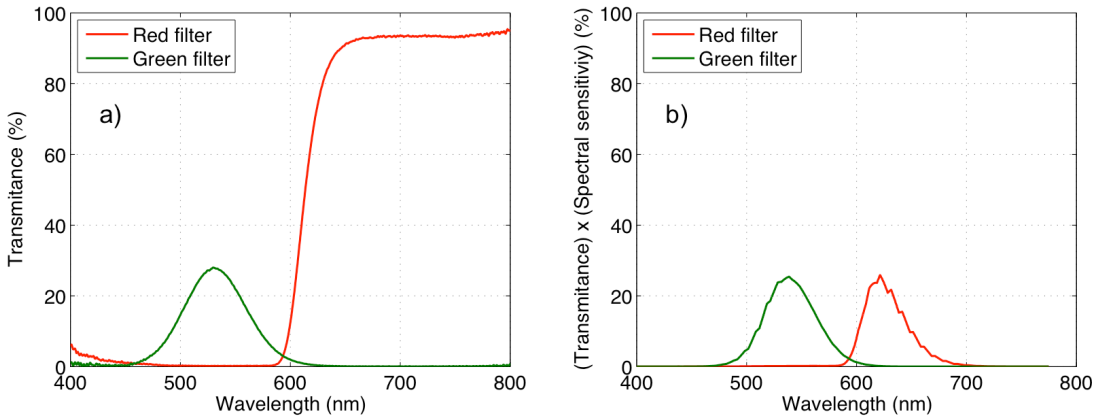

Figure 5.2: Spectral transmittances of the green and red filters used in the pair of glasses of the TNO test. (a) Experimentally measured transmittances. (b) Product of each filter transmittance by the CIE luminous efficiency

n physical optics it is widely known that the performance of any diffractive optical element is strongly dependent on the wavelength[Hecht 2001] and this fact will be crucial to understand the anomalous performance of the TNO test when it is applied to patients symmetrically implanted with diffractive-based MIOLs.

5.1.2 Intraocular lenses, patients, surgical technique and measurements

Intraocular lenses

Four types of MIOLs and one type of monofocal IOL were evaluated in this study. Their main features are summarized below.

Two apodized-diffractive MIOLs (Acrysof ReSTOR, Alcon), the SN60D3 and the SN6AD1. The full-aperture-diffractive Tecnis ZMA00 (AMO), and the refractive ReZoom NXG1 (AMO). All these designs have been described in the previous chapter (chapter 4). The implanted monofocal IOL was the aspheric Tecnis ZA9003.

Patients

This study was designed according to the tenets of the Declaration of Helsinki as revised in Tokyo in 2004, and received the approval of an institutional review board (*Santa Creu and Sant Pau* Hospital in Barcelona, Spain).

This prospective, randomized, double-masked clinical trial was conducted at the Ophthalmology Department of *Santa Creu and Sant Pau* Hospital in Barcelona, Spain. Inclusion criteria were age between 45 and 80 years, potential postoperative visual acuity of each eye of 0.1logMAR or better, preoperative corneal astigmatism lower than 1.5D, symmetrically bilateral MIOL implantation, patient motivation and desire for spectacle correction independence for near and distance vision.

Patients with strabismus, ocular or systemic pathology with potential risk of ocular affection, previous ocular surgery, as well as those reporting critical visual demands (such as night-time drivers), unrealistic expectations or difficulties with the examinations or follow-ups were excluded from the study. Postoperatively,

patients with surgical complications (such as pupil trauma, vitreous loss, extra capsular implant, IOL tilt or decentration) and patients with best distance-corrected near visual acuity (BCNVA) worse than 0.2logMAR, were also excluded as well as those with more than 0.05logMAR difference in BCNVA between both eyes.

Multifocal intraocular lens implantation was randomly determined using a 1:1:1:1 block randomization scheme generated by the statistical software SPSS 17 for Windows. For comparison purposes, an additional group of patients symmetrically implanted with a monofocal IOL was also included in the study with the same inclusion/exclusion criteria than MIOLs except for the BCNVA.

Surgical technique

A single experienced surgeon (M.A.G.) performed all the surgeries. The technique and the medication before and after surgery was the same for all the lens types. A 2.75mm clear corneal incision was performed in the steepest corneal meridian and, for corneal astigmatism over 1.00D; a secondary paired incision was executed at 180º to reduce residual astigmatism. After the phacoemulsification of the crystalline lens, the IOL was inserted in the capsular bag using the injectors recommended by each manufacturer. The target postoperative refraction was always 0D (emmetropy).

Stereopsis measurements

Six months after the surgery, a single optometrist (C.V.) performed all stereopsis measurements under photopic conditions (85cd/m2) at a near distance of 40cm (equivalent to an addition of +2.5D) since these tests are strictly accurate for such a working distance [Madrid-Costa et al. 2010]. Both tests were passed successively in random order. Those implanted with MIOLs passed the tests with their best distance correction (i.e. using the near focus of the MIOL) while those of the monofocal group were provided with an addition of +2.5D to correctly focus the stereo-acuity test.

Aiming to assess the influence of the anaglyphic glasses (red/green) of the TNO test on eyes symmetrically implanted with diffractive-based MIOLs, measurements

were repeated with an "extra-addition" of +2.5D in all groups of patients implanted with MIOLs. The issue that led us to include this experiment in a second part of our study arose from an empirical clinical observation: some patients implanted with MIOLs who showed poor stereo-acuity upon examination with the TNO test, obtained better scores when a +2.5D lens was added over their best distance refraction. It is worth remarking that this "extra-addition" makes the patient observe the test with their distance focus instead of their near focus.

Data analysis

Statistical analysis was performed with the SPSS software 17.0 for Windows. All data were analyzed for normality using the Kolmogorov-Smirnov test, revealing several instances of non-normal distributions, which recommended non-parametric statistical analyses. The Kruskal-Wallis test was employed to examine differences in stereo-acuity values between the lenses (the four MIOLs and the monofocal IOL) and statistically significant differences were then explored pair-wise with the Mann-Whitney test. In addition, the Mann-Whitney test was also employed to examine differences within each type of MIOL, with and without the "extra-addition" over the distance correction. A p value of <0.05 was considered to denote statistical significance throughout the study.

A preliminary analysis revealed no statistically significant differences between groups of patients regarding age or gender distribution, that is, study groups could be considered equivalent.

5.2 Results

A total of 143 patients (46.8% male and 53.2% female) were included in the study: 25 were implanted with SN60D3, 23 with SN6AD1, 28 with ZMA00, 24 with NXG1 and 34 with ZA9003. The age of the patients was 67.64 ± 8.38 years (Mean ± SD). Postoperative BCNVA values for all lens groups are summarized, as median and range in Table 5.2.

5.2.1 Stereo-acuity measurements versus the implanted IOL

Regarding the first part of the study, the number of patients implanted with each lens type and the measured stereoacuities (median and range) are summarized in Table 5.2. Stereo-acuity scores were better with the Titmus test than with the TNO for all lens types, and this result was statistically significant in all cases (SN60D3: Z=-5.958 p<0.001; SN6AD1: Z=-5.628 p<0.001; NXG1: Z=-4.504 p<0.001; ZMA00: Z=-5.744 p<0.001; monofocal ZA9003: Z=-5.362 p<0.001). The results in Table 5.2 also show that, for both stereotests, the type of MIOL has an influence on the value of the measured stereo-acuity (values χ^2 = 18.028; p<0.001 for the TNO and χ^2=11.346; p=0.023 for the Titmus). It is important to highlight that patients implanted with the monofocal lens presented the best stereo-acuity with both tests. The group of patients implanted with diffractive-based MIOLs (SN60D3, SN6AD1 and ZMA00) presented the worst stereo-acuity with the TNO test and the largest differences when compared with the values obtained with the Titmus test.

The distribution of patients in terms of their stereo-acuity scores with each test is shown in Fig. 3. With the TNO test, the majority of patients implanted with MIOLs evidenced poor stereo-acuity, just observing only 'Figures' or having even no measurable stereopsis. In contrast, the majority of patients implanted with the monofocal IOL reached a median value of 60 arc seconds with the TNO test. In fact, statistically significant differences were encountered between the monofocal ZA9003 and all the MIOLs (SN60D3 Z = -6.802; p < 0.001, SN6AD1 Z = -6.194; p < 0.001, NXG1 Z = -5.390; p < 0.001 and ZMA00 Z = -5.703; p < 0.001).

Table 5.2: Best distance corrected near visual acuity (BCNVA) (in logMAR units) for all intraocular lens (IOL) groups. Results are displayed as median (range).

Optical design	**Monofocal**	Diffractive (full aperture) - **Bifocal**	Apodized – Diffractive - **Bifocal**		**Refractive**
Reference (commercial name)	**ZA9003** (Tecnis)	**ZMA00** (Tecnis multifocal)	**SN60D3** (AcrySof ReSTOR)	**SN6AD1** (AcrySof ReSTOR)	**NXG1** (Rezoom)
Corneal SA correction	Total	Total	No	Partial	*
Addition (D)	-	4	4	3	3.5
BCNVA	0.04** (0-0.18)	0.12 (0-0.19)	0.09 (0-0.19)	0.12 (0.15)	0.17 (0.05-0.19)

** Non reliable info.*

*** Fort he patients implanted with monofocal IOL BCNVA (Best Corrected Near Visual Acuity) indicates the use of +2.5D of addition power.*

Table 5.3: Number of patients (n), Median and Range of stereo-acuities (in arc seconds) obtained with the TNO and Titmus tests for each lens type.

Optical design		**Monofocal**	Diffractive (full aperture) - **Bifocal**	Apodized – Diffractive - **Bifocal**		**Refractive**
Reference (commercial name)		**ZA9003** (Tecnis)	**ZMA00** (Tecnis multifocal)	**SN60D3** (AcrySof ReSTOR)	**SN6AD1** (AcrySof ReSTOR)	**NXG1** (Rezoom)
Corneal SA correction		Total	Total	No	Partial	?
Addition (D)		-	4	4	3	3.5
TNO	**n**	34	28	25	23	24
	Median*	60	480-Figures	Figures	Figures	240
	Range	60-240	60-none	120-none	60-none	60-none
Titmus	**n**	23	23	18	19	16
	Median	40	50	50	60	55
	Range	40-80	40-200	40-140	40-200	40-400

**: The term "Figures" of the TNO test indicate values greater than 480 arc-second*

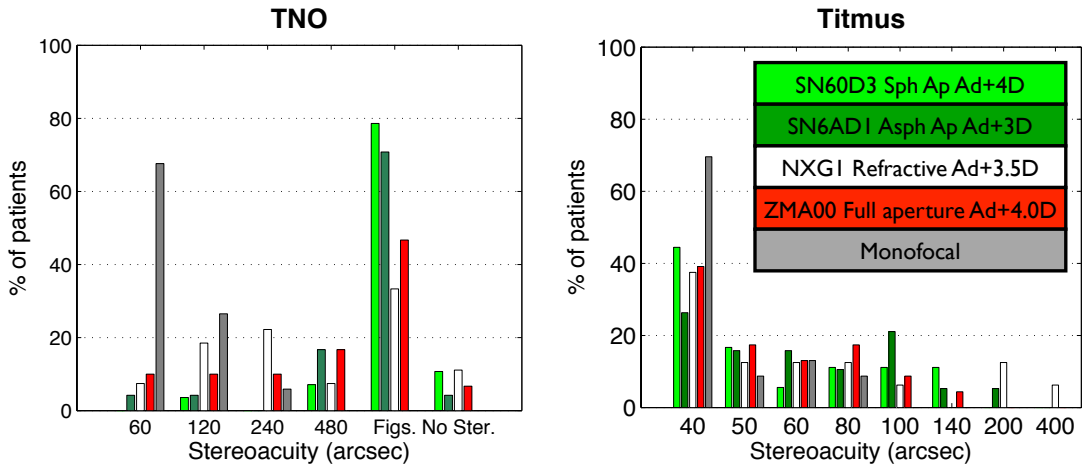

Figure 5.3: Distribution of patients (in percentage) as a function of the measured stereo-acuity. Results obtained with the TNO (a) and Titmus (b) stereotests.

Within the MIOLs, statistically significant differences were encountered between the refractive NXG1 and the hybrids SN60D3 ($Z = -3.748$; $p < 0.001$) and SN6AD1 ($Z = -2.722$; $p = 0.006$); and between the diffractive ZMA00 and the hybrid SN60D3 ($Z = -3.006$; $p = 0.003$).

Interestingly, Fig. 5.3 shows that, when assessed with the Titmus test, patients implanted with MIOLs present a shift in the outcome towards better stereo-acuities, with a higher percentage of patients corresponding now to those reaching the best possible stereo-acuity value that can be measured with this test (40 arc sec). This score also corresponds to the value obtained by the majority of those

implanted with monofocal IOL and, with the exception of the spherical hybrid SN60D3, there were statistically significant differences between the monofocal ZA9003 and all the MIOLs (SN6AD1: Z = -3.185; p = 0.001; NXG1: Z = -2.442; p = 0.015; and ZMA00: Z = -2.353; p = 0.019). It is worth emphasizing that with the Titmus test, we did not found statistically significant differences between the different MIOLs.

5.2.2 Stereo-acuity measurements versus the stereo-test

During the second part of the study, patients implanted with MIOLs had an "extra-addition" of +2.5D over their best distance refraction for the assessment of stereopsis with the TNO test, that is, they used the distance focus of the MIOL instead of the near focus for the visualization of the test. Stereoacuities measured in these conditions are presented in Table 5.4 that, for comparison purposes, also includes the results of the monofocal group already reported in Table 5.3.

The results measured with TNO test show that, with the "extra-addition", the stereoacuity of patients with diffractive MIOLs was better than without this addition (Table 5.4), but still the monofocal lens group exhibited the best stereo-acuity scores, with a majority of these patients reaching 60 arc seconds (see Fig. 5.4)..

The Mann-Whitney test was used to investigate the statistical significance of the differences in stereo-acuity within each type of MIOL, with and without the "extra-addition". The outcome of this analysis revealed that, whereas statistically significant better stereo-acuity scores were obtained with the "extra-addition" in patients implanted with the diffractive-based MIOLs (SN60D3: Z= -4.388; p < 0.001; SN6AD1: Z = -3.747; p < 0.001; ZMA00: Z = -3.314; p = 0.001), patients implanted with the refractive-based MIOL (NGX1) had similar stereo-acuity results with and without the "extra-addition".

Table 5.4: Number of patients (n), Median and Range of stereo-acuities (in arc seconds) obtained with the TNO test with and without the "extra addition" of +2.50 D for each MIOL type. The results of the monofocal group are included for sake of comparison.

Optical design		**Monofocal**	Diffractive (full aperture) - **Bifocal**	Apodized – Diffractive - **Bifocal**		**Refractive**
Reference (commercial name)		**ZA9003** (Tecnis)	**ZMA00** (Tecnis multifocal)	**SN60D3** (AcrySof ReSTOR)	**SN6AD1** (AcrySof ReSTOR)	**NXG1** (Rezoom)
Corneal SA correction		Total	Total	No	Partial	?
Addition (D)		-	4	4	3	3.5
Without +2.50D	**n** **Median** **Range**	-	28 480-Figures 60-Figures	25 Figures 120-figures	23 Figures 60-Figures	24 240 60-Figures
With +2.50D	**n** **Median** **Range**	34 60 60-240	24 120 60-Figures	22 240 60-Figures	2 180 60-Figures	19 240 60-Figures

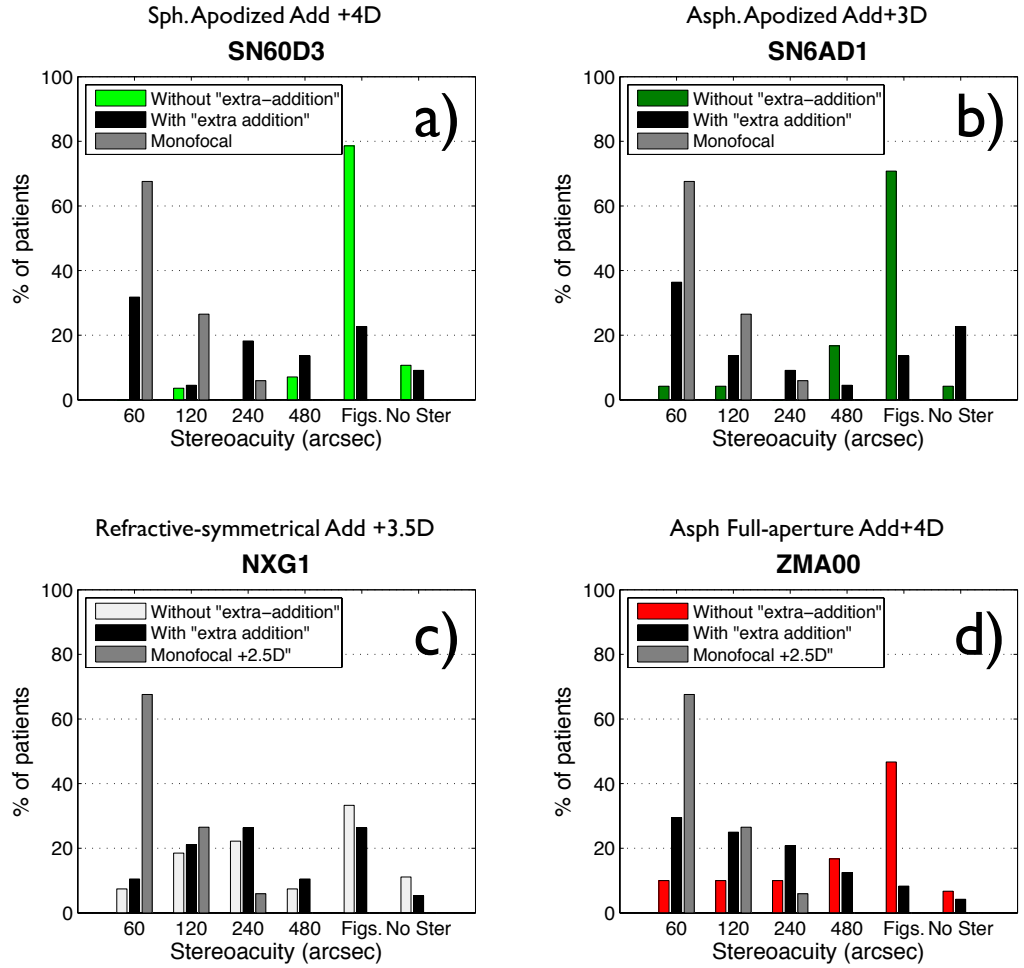

Figure 5.4: Distribution of patients (in percentage) as a function of the stereo-acuity measured with the TNO test, without and with the "extra-addition" of +2.50 D. (a) Patients implanted with the SN60D3. (b) Patients with the SN6AD1. (c) Patients with the NXG1. (d) Patients with the ZMA00. For comparison purposes, the results obtained with the monofocal group are included in all cases

5.3 Discussion

5.3.1 Clinical findings

Our results show that with the Titmus test (Table 5.3), patients implanted with the monofocal lens presented statistically significant better stereo-acuity scores than those patients implanted with three types of MIOLs (SN6AD1, ZMA00, and NXG1) but not better than those patients implanted with the SN60D3 MIOL. The latter is in agreement with the work of Cionni et al. [Cionni et al. 2009] who did not find differences between the stereopsis in patients bilaterally implanted with SN60D3 and patients with bilateral AcrySof monofocal IOLs (SA60AT, SN60AT or SN60WF).

Souza and co-workers [Souza et al. 2006] used the Titmus test to compare stereopsis between 25 patients implanted with the SN60D3 MIOL and 15 patients implanted with the monofocal SA60AT IOL. Although contrast sensitivity was significantly better in the monofocal group at 6 cpd and 18 cpd, they did not find differences in their stereoacuity between the two groups. Additionally, Ferrer-Blasco and co-workers [Ferrer-Blasco et al. 2009] studied the stereopsis in 15 non-cataractous hyperopic patients before and after refractive lens exchange with SN60D3 MIOL and found that the stereoacuity did not change after the surgery. More recently [Ferrer-Blasco et al. 2010], they used the Titmus and Random dot stereotest and the Howard Dolman apparatus in bilaterally multifocal pseudophakic patients implanted with the SN6AD3, which is a lens similar to the SN6AD1 used in our study, but with an addition of +4.0D (approximately +3.2D at the spectacle plane, i.e. optimized for a working distance of 31 cm) instead of +3.0D. With the Titmus test set at a fixed observation distance of 40 cm, they found a stereo-acuity of 44.55 ± 1.08 arc-sec, which is similar to that reported in separate studies [Hayashi and Hayashi 2004] for patients implanted with monofocal IOLs. They hypothesized “the reduction of contrast of the in-focus image at near resulting from

by the defocused image of the distance focus does not seem to affect stereoacuity” [Ferrer-Blasco et al. 2010].

Unlike the conclusion reached in Refs [Ferrer-Blasco et al. 2010; Souza et al. 2006], we have shown in this work that differences in stereo-acuity between monofocal and multifocal groups do exist. They have been particularly evidenced with the TNO test, because in this case the stereo-acuity in the monofocal group was significantly better than in any other group among the four MIOL groups. Let us examine the possible reasons that may explain this fact. It is well known, for instance, that after surgery, stereopsis degrades as a consequence of any possible residual refractive error, unequal blur between the two eyes, and decreased retinal image contrast [Wood 1983; Simons 1984; Lovasik and Szymkiw 1985; Legge et al. 1987]. Actually, Hayashi et al. [Hayashi and Hayashi 2004] showed in bilaterally patients implanted with monofocal IOL that the main factor affecting the stereopsis was a large difference in the spherical equivalent between fellow eyes followed by old age and large pupil diameter. However, since all the patients included in our study had a BCNVA better than 0.2logMAR and differences between both eyes in any of the groups was smaller than 0.05logMAR, any residual refractive error and/or refractive-induced unequal blur between the eyes after surgery have to be discarded as a possible explanation of their worse stereo-acuity.

On the other hand, Martínez-Palmer and co-workers [Martínez Palmer et al. 2008] found that the contrast sensitivity was better on average in patients implanted bilaterally with monofocal IOL (Tecnis Z9000) than in patients implanted with three types of MIOLs (Tecnis ZM900, ReZoom and TwinSet). This result was further confirmed by the Cochrane survey [Calladine et al. 2012]. It has been reported [Heckmann and Schor 1989] that stereoacuity depends on contrast and, as a consequence, the loss of stereopsis with age would be strongly related to the loss of contrast sensitivity [Garnham and Sloper 2006]. It is important to highlight that the four MIOLs in our study have different designs but all of them share the feature of multifocality, which is obviously absent in the monofocal IOL. Thus, the worse stereo-acuity found in patients with MIOLs in comparison to the monofocal group is likely due to the simultaneous presence of a focused image and an out of focus image. This fact unavoidably leads to a reduction in the retinal image contrast thus affecting stereopsis [Wood 1983; Lovasik and Szymkiw 1985; Legge

et al. 1987]. Further investigation is necessary to determine the lack of statistically significant differences found between the monofocal group and the group with the SN60D3 MIOL when stereopsis was assessed with the Titmus test.

Another important issue is the large difference of stereo-acuity found in patients with MIOLs as a function of the particular stereotest. Our results (Table 5.3) show that stereo-acuity scores were significant better with the Titmus test than with the TNO for all the MIOLs types. This fact suggests that the particular characteristics of the TNO test (specifically its chromatic principle) are strongly significant and deserves further discussion.

With the TNO test, there is a statistically significant better stereo-acuity with the refractive NXG1 MIOL than with any other of the hybrid MIOLs (SN60D3 and SN6AD1). This result is in agreement with the work of Chang [Chang 2008], who reported statistically significant differences in stereo-acuity between the NXG1 and the SN60D3 lenses. Moreover, as it was shown in the second part of our study, statistically significant better results were obtained with the TNO test when patients implanted with diffractive-based MIOLs (SN60D3, SN6AD1 and ZMA00) observed the test with an extra addition of +2.50D (i.e., using the distance focus instead of the near focus). Interestingly, this improvement of the stereo-acuity was not evidenced in the group with the refractive NXG1 MIOL (Table 5.4 and Fig.5.4).

5.3.2 Optical explanation

To explain these findings, it is necessary to consider the important differences in the mechanisms involved in distance and near image focusing between refractive and diffractive-based MIOLs. As we have seen in the previous chapter (chapter 4), with diffractive-based MIOLs both the add power and the diffraction efficiency of the near focus are strongly dependent on the wavelength [Castignoles et al. 2010], which is particularly relevant when using a chromatic-based test like the anaglyphic TNO stereotest. To the best of our knowledge, this point has not yet been addressed in previous publications dealing with TNO-based stereo-acuity measurements carried-out in patients implanted with diffractive MIOLs.

Differences of the dioptric powers due to wavelength

For any type of IOL, especially when they work with different wavelengths, the variation of the refractive index of the lens material with wavelength (referred to as the material chromatic dispersion) has to be taken into account. As a consequence of this phenomenon, different wavelengths are focused at different axial positions causing longitudinal chromatic aberration (LCA), or in other words, inducing chromatic differences in the dioptric power of the lens. The strength of this effect depends on the Abbe number of the lens material: the lower the Abbe number the larger the chromatic differences in the dioptric power of the lens. Thus, for an IOL with refractive index $n(\lambda_1)$ and dioptric power $P(\lambda_1)$ in aqueous, if the wavelength is changed to λ_2 there is a dioptric power variation $\Delta P_{dioptric} = P(\lambda_2) - P(\lambda_1)$, given by:

$$\frac{\Delta P_{dioptric}}{P(\lambda_1)} = \frac{n(\lambda_2) - n(\lambda_1)}{n(\lambda_1) - n_{aqueous}} \quad , \qquad (5.1)$$

where $n(\lambda_2)$ is the refractive index of the lens at wavelength λ_2. In the case of a MIOL, Eq (1) applies to both the near and distance focus and obviously it can be also used to obtain the dioptric power difference for a given focus (either the distance or the near one) between two identical MIOLs when each of them is illuminated with a different wavelength. Note that this is the case when stereopsis measurements are carried-out with the TNO test in patients symmetrically implanted with MIOLs.

We have calculated the dioptric power difference between two identical MIOLs in the worst scenario of maximum chromatic dispersion, which occurs for the material with the lower Abbe number, a situation that corresponds in our case to the acrylic material of the hybrid apodized-diffractive Restor MIOLs[Siedlecki and Ginis 2007]. The wavelengths were λ_1=550 nm and λ_2=625 nm, i.e. the wavelengths of maximum transmittance of the filters of the TNO glasses (see Fig. 2). The refractive indices $n(\lambda_1)$=1.5500 and $n(\lambda_2)$=1.5426 were obtained from the dispersion formula provided in Ref. [Siedlecki and Ginis 2007]. Thus, by using a dioptric power $P(\lambda_1)$ of 21.2 D that corresponds to the mean value of the lenses in our study, Eq. (1) leads to $\Delta P_{dioptric}$= -0.73 D. To put this number in a meaningful

context, we have calculated the dioptric power variation in the case of the unaccomodated healthy crystalline lens of the LeGrand eye model, for which $P(\lambda_1)$= 21.8 D. Incidentally, this would correspond to a person capable of obtaining the best stereo-acuity score possible with the TNO test. By using the chromatic dispersion data of the crystalline lens provided by Atchison and references herein [Atchison and Smith 2004], we found $\Delta P_{dioptric}$=-0.85 D. We then conclude that with the TNO test, because of the chromatic dispersion of the material of the MIOLs, there is a real test-induced unequal refraction between the eye with the green filter and the fellow eye with the red filter, but this effect is even somewhat smaller than the one that would occur in healthy eyes that do not experience any problem to achieve good stereopsis scores with the TNO test. Thus, we conclude that the chromatic test-induced dioptric power variations between fellow eyes implanted with MIOLs have a negligible impact in the scores of stereopsis.

Bearing in mind that with the TNO test the chromatic dispersion of the material is the only factor involved in the case of purely refractive MIOLs such as the NXG1, we infer that the chromatic nature of this stereotest must not have a noticeable impact in either the distance or the near foci, and this is the reason why the patients implanted with the NXG1 show similar stereo-acuity results with and without the 'extra' +2.50D addition (Table 5.4 and Fig. 5.4).

On the other hand, a diffractive-based MIOL uses the base dioptric power of the lens and the zero (*m=0*) and first (*m=1*) diffraction orders for the distance and near foci, respectively, which means that there is a combination of two wavelength dependent effects: the one explained above about the chromatic dispersion of the material and the dependence of the diffraction orders on the wavelength.

In the case of the *m=0* diffraction order, it does not depend on the wavelength [Castignoles et al. 2010] and thus the distance focus of the MIOL is only affected by the chromatic dispersion of the lens material, which plays a minor role as it has just been shown. We thus conclude that the distance focus of the diffractive-based MIOLs is also barely affected by the chromatic nature of the TNO test.

The case of the near focus of the diffractive-based MIOLs is further more complex. The add power (P_{add}), due to the *m=1* diffraction order, exhibits a linear dependence with the wavelength, as governed by the equation:

$$P_{add}(\lambda) = \lambda \frac{1}{r_0^2} \qquad (5.2)$$

where r_0 is the radius of the first diffractive zone. The MIOLs used in this study have add powers of either +3.0 D or +4.0 D at the design wavelength of λ=550 nm. Using Equation (2), it is straightforward to obtain the variation of add power (ΔP_{add}) that occurs when changing the working wavelength from λ_1 to λ_2 [Languy et al. 2011]: $\frac{\Delta P_{add}}{P_{add}(\lambda_1)} = \left(\frac{\lambda_2}{\lambda_1} - 1 \right)$.

Using this equation for $P_{add}(\lambda_1)$=+4.0 D and the wavelengths corresponding to the maximum transmittance of the filters of the TNO glasses (i.e. λ_1=550 nm and λ_2=625 nm), a positive relative variation of add power is found, being ΔP_{add}= + 0.54D. Remembering that this focus is also affected by the negative chromatic power difference produced by the chromatic dispersion of the material ($\Delta P_{dioptric}$, -0.73D in the worst case), the total power variation would be $\Delta P_{total} = \Delta P_{add} + \Delta P_{dioptric.}$ Both effects tend to compensate each other (ΔP_{total} =0.54-0.73= -0.19D), and somehow surprisingly, the TNO-induced chromatic differences in the near focus of diffractive-based MIOLs are actually smaller than in the case of the distance focus. It is then necessary to look for another explanation to account for the poor stereopsis scores with the TNO test in the group of patients with diffractive-based MIOLs when they observed the test using the near focus of the lenses and closely related, the improvement found when they used the distance focus instead (i.e., with the 'extra addition' of +2.5 D) (Table 3 and Fig. 4).

Differences in the energy efficiency due to the wavelength

In addition to the power variation, the wavelength also has a significant influence on the diffraction efficiency of any diffractive-based MIOL [Castignoles et al. 2010; Languy et al. 2011]. Let us consider the case of a patient with this type of lens and passing the TNO test using the near focus of the lens. The focused image of the test

formed by the near focus (order *m=1*) is overlaid by a blurred image produced by the distance focus (order *m=0*). The more the energy of the blurred image in relation to the energy of the focused one, a fact intimately related to the diffraction efficiency of the orders, the worst the contrast sensitivity and as a consequence, a degraded stereo-acuity can be expected [Wood 1983; Legge et al. 1987]. By using the expressions given in the chapter 4 (also in references [Castignoles et al. 2010] and [Cohen 1993]) it is straightforward to demonstrate that the longer the wavelength, the lower the diffraction efficiency of the *m*=1 order (i.e., the focused image) and the larger the diffraction efficiency of the *m*=0 order (i.e., the out of focus image). In particular, taking into account the design parameters of the diffractive-based Restor and Tecnis MIOLs [Lee and Simpson 1997; Piers et al. 2008] we have calculated in the case of λ_1=550 nm, a maximum efficiency of 0.41 for the *m= 1* order (with 0.41 for *m=0*), while in the case of λ_2=625 nm it only reaches a value of 0.29 (with 0.53 for *m=0*). Thus, in the case of patients symmetrically implanted with diffractive-based MIOLs that observe the TNO test by using the near focus (*m=1* diffraction order), with a green filter in front of one eye and a red filter in the fellow eye, there is an image with an acceptable contrast (the one corresponding to the eye with the green filter) but the image formed by the fellow eye (the one with the red filter) has considerably lower contrast. According to Simons [Simons 1984], such a large difference in the contrast of the two images that should merge in the stereopsis process, leads to a reduction of the stereo-acuity as experimentally observed in these conditions. Furthermore, since these wavelength-induced differences of diffraction efficiency are obviously absent with the refractive NXG1 MIOL, a better stereo-acuity is expected with this lens design when using the TNO test and near vision, as confirmed by our results.

A similar reasoning applies to the improvement obtained in the stereo-acuity measured in patients implanted with diffractive-based MIOLs when observing the TNO test with the extra-addition of +2.50 D. In these conditions, these patients observed the test with their distance focus, that is, the *m=0* diffraction order, for which the two red and green images have similar contrast and, as a consequence, the stereo-acuity scores were better (Table 5.4, Fig. 5.4).

Finally, as for the patients implanted with the refractive NXG1 MIOL, no statistically significant differences were found with the +2.50 D 'extra addition' when compared with the stereo-acuity obtained without the extra addition, further confirming that the use of TNO test does not alter, *per se*, the outcome of the stereo-acuity evaluation in the case of this lens design. However, it is worth emphasizing that even in these relatively more favorable conditions, patients with this type of MIOL design still have worse stereo-acuity than those implanted with monofocal lenses.

5.4 Conclusions

In this study, we have conducted a randomized, double-mask clinical trial to assess and compare the stereo-acuity in a significant number of patients bilaterally and symmetrically implanted with four different types of MIOLs. In the same clinical trial, a reference group was implanted with a monofocal IOL. Stereo-acuity was measured with the TNO and the Titmus stereotests.

In comparison to the monofocal group and no matter the stereotest used, the results evidence a worsening of the stereo-acuity in patients implanted with MIOLs (refractive, diffractive and hybrid refractive-diffractive) most likely due to a decrease in retinal image contrast originated from the simultaneous presence on the retina of a focused image and a defocused one formed by the near and distance foci of the MIOL.

When stereo-acuity was tested with the Titmus test, there were no statistically significant differences between the stereo-acuities tested in patients implanted with different MIOLs. Additionally, it has been shown that a stereotest based on chromatic dissociation such as the TNO may induce large differences of image contrast between fellow eyes implanted with diffractive-based MIOLs, with the global effect of affecting stereo-acuity results. The experimental results reported here have been supported by a post hoc analysis and a detailed explanation based on the physics of the optical imaging properties of refractive and diffractive lenses.

CAPÍTULO 6

CALIDAD DE IMAGEN EN LENTES INTRAOCULARES

CHAPTER 6

IMAGE QUALITY OF INTRAOCULAR LENSES

En los capítulos anteriores hemos descrito el sistema óptico necesario para evaluar lentes intraoculares *in vitro*.

Para valorar la calidad óptica de un sistema generalmente se utilizan diversas métricas y/o funciones tales como el contraste para una determinada frecuencia, la Función de Transferencia de Modulación (MTF, por sus siglas en inglés: Modulation Transfer Function), la Función de extenSión de un Punto (PSF, del inglés), la razón de Strehl (SR), la diferencia pico-valle (PV), etc. [Marsack et al. 2004]. En este capítulo describiremos cómo podemos medir en el banco óptico algunas de estas métricas para diferentes modelos de IOLs.

En concreto en la primera sección nos centraremos en el contraste de las imágenes formadas por las IOLs monofocales y bifocales para determinadas frecuencias espaciales y los cambios que se producen en función de la pupila.

En la segunda sección nos centraremos en la medida de la MTF de varias IOLs monofocales y bifocales considerando dos diámetros pupilares de 2.4 y 4.2*mm*, que son representativos de pupilas pequeñas y grandes en el ojo humano, respectivamente.

Por último, en la tercera sección, describiremos un método para estimar el tamaño e intensidad relativa del halo que puede inducir diferentes diseños de IOLs mono y multifocales.

6.1 Medidas del contraste para determinadas frecuencias espaciales

REFERENCE TO THE PUBLICATIONS OF THIS THESIS

The content of this section is included in the publications:

- Alba-Bueno, F. Vega, F. and Millán M.S. *"Assessment of the quality of multifocal intraocular lenses through contrast measurements."* Engineering the Eye III, 2011. Benasque (Huesca).

Una de las múltiples maneras de evaluar la calidad óptica de un sistema óptico consiste en medir el contraste de la imagen que forma de barras binarias con diferentes frecuencias espaciales. Para caracterizar las imágenes formadas por diferentes IOLs hemos utilizado el banco óptico descrito en el capítulo 2 [Alba-Bueno et al. 2011b] con la córnea artificial que induce una aberración esférica (SA, por sus siglas en inglés) similar a la de una córnea humana promedio [Wang et al. 2003; Guirao et al. 2000]. En la figura 6.1 hay un esquema de la configuración utilizada para estas medidas.

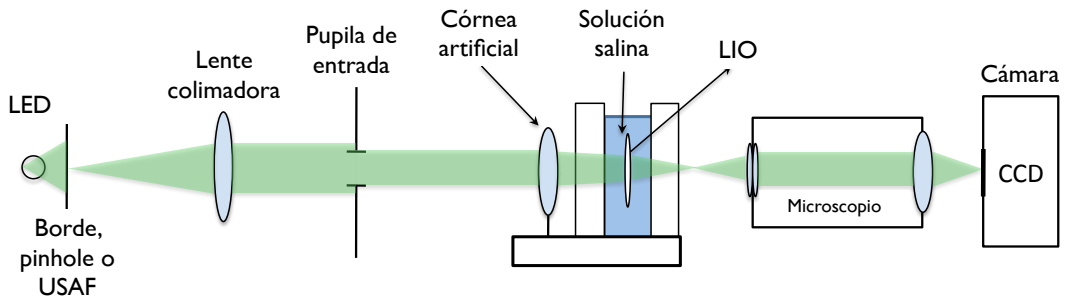

Figura 6.1: Esquema de la configuración del banco óptico

6.1.1 Método

La medida del contraste de la imagen de las barras formada por el ojo artificial se realizó mediante la definición de Michelson para la visibilidad de las franjas:

$$C = \frac{I_{\max} - I_{\min}}{I_{\max} + I_{\min}} , \qquad (6.1)$$

donde I_{max} es la intensidad máxima e I_{min} es la intensidad mínima del perfil de los grupos de barras. Consideraremos dos grupos del test USAF, G2T2 y G3T2 que, en la configuración del banco óptico utilizado, corresponden aproximadamente a agudezas visuales decimales respectivas de 0.5 (0.3logMAR) y 1.0 (0.0logMAR). Estas agudezas visuales corresponden a una pérdida de visión moderada según la Organización Visual de la Salud (0.3logMAR) y una agudeza visual normal (0.0logMAR). En la figura 6.2 se muestra la imagen del test USAF obtenida experimentalmente con una lente intraocular monofocal y los respectivos contrastes en ambos grupos.

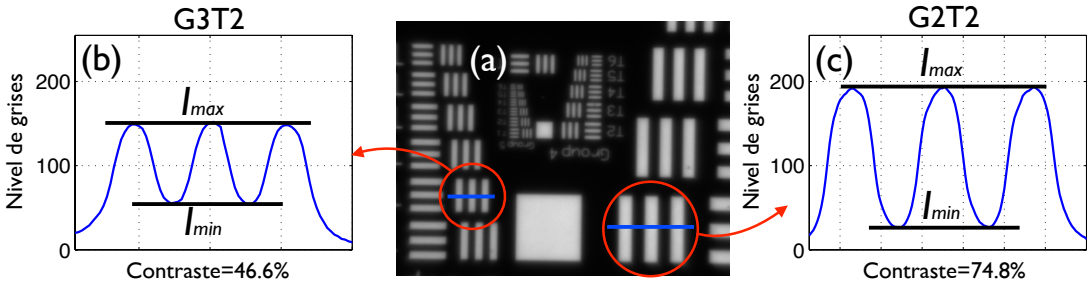

Figura 6.2: (a) Imagen del USAF formada por el modelo de ojo con una IOL asférica (SN60WF) para un diámetro de pupila de 3.5mm (plano IOL). (b) Perfil de intensidad y contraste para el grupo G3T2; (c) ídem para el grupo G2T2.

Tabla 6.1: Características principales de las lentes analizadas mediante la medida del contraste para los grupos G3T2 y G2T2 del test USAF.

Diseño óptico	Referencia (nombre commercial)	Compensación SA corneal	Potencia base (D)	Adición (D)
Monofocal	SN60AT	No	20	-
	SN60WF (AcrySof IQ)	Parcial	20	-
	ZA9003 (Tecnis)	Total	20	-
Bifocal - **Difractiva** (no-apodizada)	ZMA00 (Tecnis multifocal)	Total	20	4
Bifocal - **Difractiva**-apodizada	SN60D3 (AcrySof ReSTOR)	No	20	4
	SN6AD3 (AcrySof ReSTOR)	Parcial	20	4
	SN6AD1 (AcrySof ReSTOR)	Parcial	20	3

Una vez alineada correctamente la IOL, el plano de mejor imagen para una pupila intermedia (3mm en el plano de la IOL) se determinó utilizando el criterio del máximo contraste para el grupo G2T2. Para evaluar el impacto de la SA del sistema córnea-IOL la medida del contraste se realizó con diferentes diámetros pupilares.

Este protocolo de medida se repitió en los diferentes planos imagen de varias IOLs mono- y multifocales, cuyas principales características se resumen en la tabla 6.1.

6.1.2 Resultados

Las imágenes del test USAF obtenidas para pupilas grandes, medianas y pequeñas (5mm, 3.5mm y 2mm en el plano de la IOL respectivamente) con cada lente se muestran en las figuras 6.3 y 6.4 para las lentes monofocales y multifocales, respectivamente.

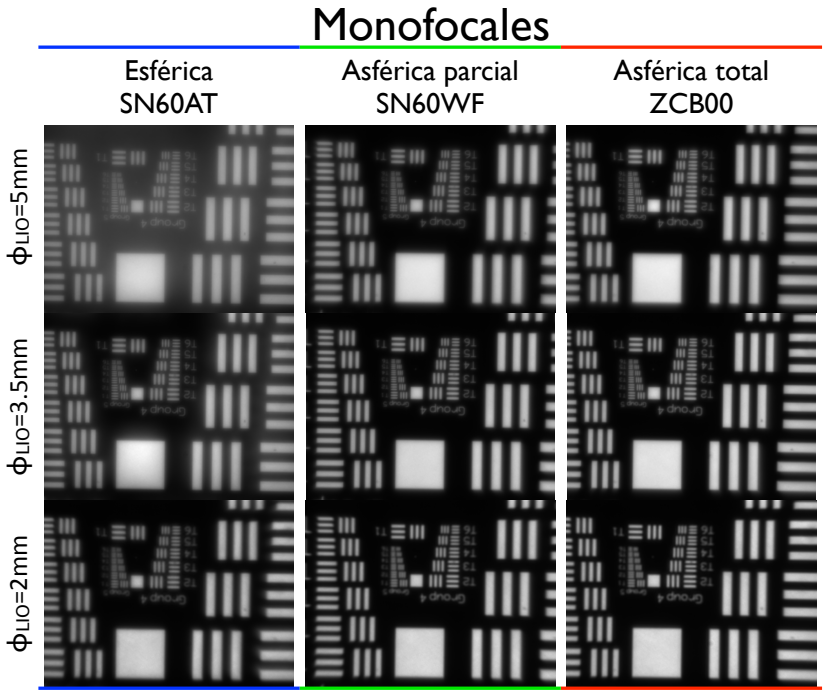

Figura 6.3: Imágenes del test USAF obtenidas experimentalmente con las IOLs monofocales para diferentes diámetros pupilares.

En estas imágenes podemos ver cómo se deteriora la imagen de la lente monofocal esférica (SN60AT) para pupilas grandes mientras que ambas lentes asféricas (SN60WF y ZCB00) apenas presentan diferencias entre ellas (figura 6.3). Asimismo, para pupilas pequeñas podemos ver cómo las tres lentes son equivalentes debido a la poca influencia de la SA en estas condiciones. En cuanto a las lentes multifocales (figura 6.4), podemos observar cómo las diferencias lejos-cerca son relativamente pequeñas en el caso de la lente no-apodizada (ZMA00) y son independientes del tamaño pupilar. Las lentes apodizadas (SN60D3, SN6AD3 y SN6AD1), en cambio, presentan mejor calidad de imagen en el foco lejano que en el de cerca, especialmente cuando se trata de pupilas grandes. Esto es debido a que la

distribución de energía de estas lentes [Vega et al. 2011; Alba-Bueno et al. 2011a] favorece al foco lejano.

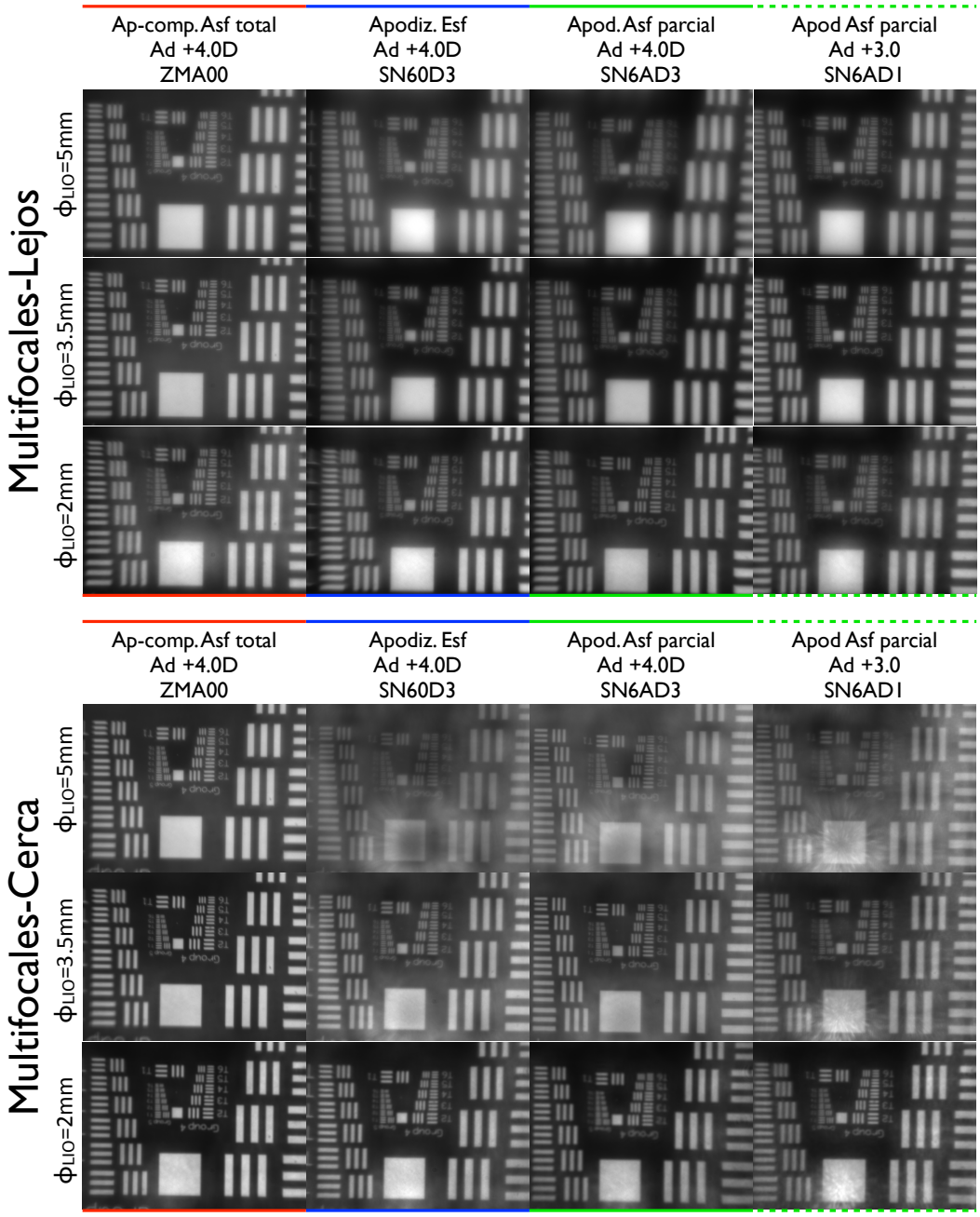

Figura 6.4: Imágenes del test USAF obtenidas con las lentes multifocales (tanto en el foco lejano como en el cercano) para diferentes diámetros pupilares.

Cuantitativamente, los valores de contraste de Michelson encontrados para cada grupo del USAF en función de la pupila y para cada IOL se muestran en la figura 6.5. Tal y como se podía predecir, se puede ver cómo el contraste para las frecuencias altas (G3T2) es siempre inferior al de las frecuencias bajas (G2T2). También podemos ver que las diferencias de contraste entre las diferentes lentes

son más significativas en el caso de las frecuencias bajas, por lo que nos centraremos, principalmente, en analizar las diferencias en el grupo G2T2.

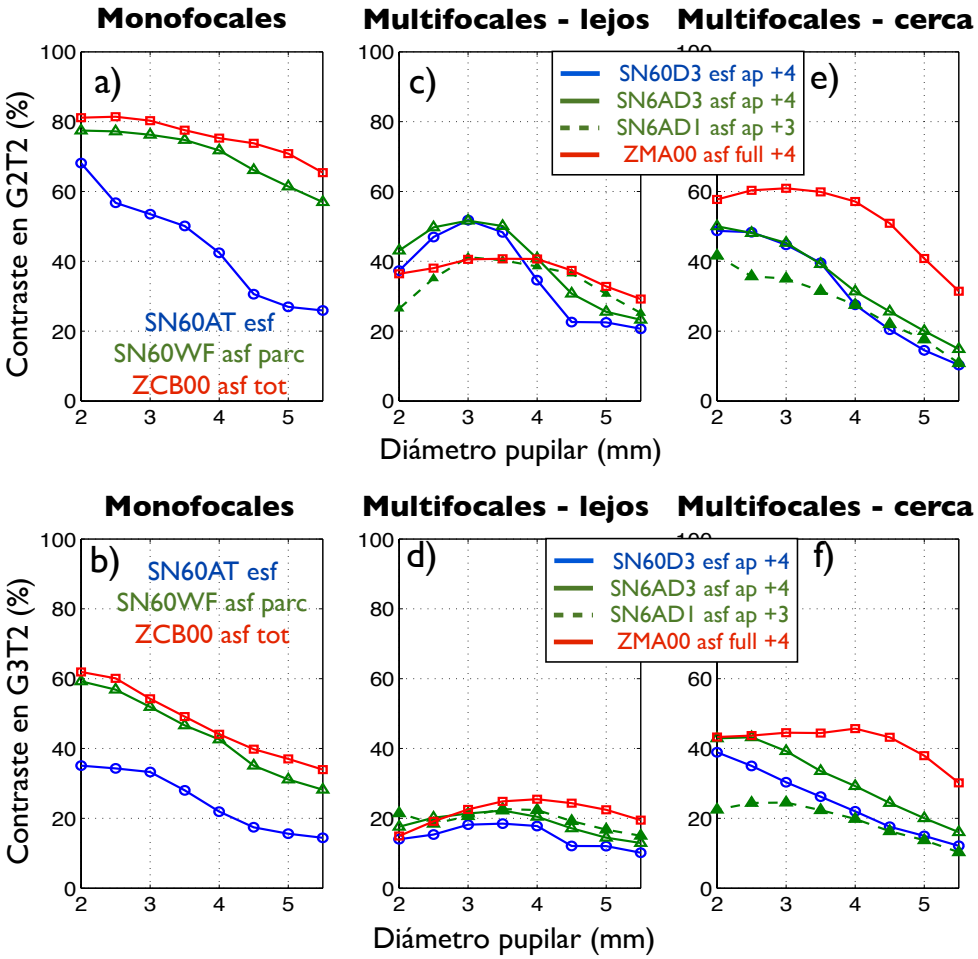

Figura 6.5: Contrastes medidos para los grupos G3T2 y G2T3 en función del diámetro pupilar para cada IOL.

Analizando con detenimiento estos gráficos vemos que con IOLs monofocales la presencia de mayor SA en el sistema óptico causa una importante reducción de los valores de contraste (lente SN60AT en las figuras 6.5a y 6.5b) especialmente con pupilas grandes. Las dos IOLs asféricas (SN60WF y ZCB00) presentan valores de contraste superiores a la lente esférica (SN60AT) para todas las pupilas y para ambos grupos del USAF, si bien se puede observar que la lente con corrección de la SA corneal total (ZCB00) presenta valores ligeramente superiores a los de la lente con corrección parcial (SN60WF).

Si comparamos ahora los resultados de las IOLs monofocales (figuras 6.5a y 6.5b) con el foco lejano de las IOLMs (figuras 6.5c y 6.5d), se puede observar que el contraste medido con las lentes monofocales asféricas (SN60WF y ZCB00) es

mayor que el medido con cualquier IOLM y con cualquier pupila. La IOL monofocal esférica (SN60AT), en cambio, presenta contrastes iguales o ligeramente inferiores que algunas IOLMs cuando se utilizan pupilas grandes.

En el foco lejano, todas las LIOMs analizadas presentan valores de contraste para las altas frecuencias muy bajos (figura 6.5d). En cambio, en el grupo del USAF con menor frecuencia espacial (G2T2, figura 6.5c) vemos claras diferencias entre los comportamientos de estas lentes. En el gráfico de la figura 6.5c se puede observar cómo la IOLM no apodizada (ZMA00) es más pupilo-independiente (curva más horizontal) que las lentes apodizadas. Esto es debido a que la proporción de energía que esta lente destina a cada uno de sus dos focos es independiente de la pupila. Las lentes apodizadas de adición +4.0*D* (SN60D3 y SN6AD3) presentan curvas de contraste con un máximo valor de 50% para la pupila de 3mm, siendo este valor mayor que el de la lente no-apodizada (ZMA00). Este máximo valor disminuye considerablemente con pupilas mayores, llegando a valores mínimos de 20-25%, y siendo ligeramente inferior en el caso de la lente esférica (SN60D3). En este mismo gráfico (figura 6.5c), se observa que la cercanía de los focos en la lente de adición +3.0*D* (SN6AD1) hace disminuir ligeramente el contraste para las pupilas pequeñas.

En el foco cercano de las IOLMs (figuras 6.5e y 6.5f) vemos que el contraste es siempre mayor con la lente no-apodizada (ZMA00). Las curvas de contraste de esta lente presentan una disminución para pupilas grandes. Dicha disminución puede tener varias explicaciones: por un lado la asfericidad de la lente puede estar optimizada para el foco lejano por lo que la corrección de SA en el foco lejano no sea tan efectiva. Por otro lado la periferia de esta lente presenta los escalones difractivos muy próximos los unos a los otros, siendo éstos más difíciles de fabricar y aumentando el "scattering" de esa zona [Meyers and Albrecht 1998]. Las IOLMs apodizadas presentan menor contraste en el foco cercano (figuras 6.5e y 6.5f) que la lente no-apodizada (ZMA00) debido a que la distribución energética de estas lentes favorecen al foco lejano. Si comparamos los diferentes diseños de lentes apodizadas, vemos cómo las dos lentes de adición +4.0D (SN60D3 y SN6AD3) presentan un comportamiento muy similar debido a que el diseño de anillos difractivos, que son los únicos responsables de enviar energía al foco cercano, es el mismo en ambas lentes. Por otro lado, la lente de menor adición (SN6AD1)

presenta menor contraste para pupilas pequeñas mientras que a partir de los 3.5-4mm el contraste es bastante similar al de las lentes de adición de +4.0*D*. Esto es debido a que la periferia de estas tres lentes es puramente refractiva y sólo contribuye a la formación del foco lejano.

6.1.3 Discusión

En esta parte del trabajo hemos mostrado cómo, en términos de contraste para unos grupos del test USAF que representan unas frecuencias espaciales de particular interés, 0.5 y 1.0 decimal (0.3 y 0.0 logMAR), la calidad óptica de las lentes monofocales asféricas (SN60WF y ZCB00) es mayor que el resto de las lentes. En el caso de la lente esférica monofocal (SN60AT) vemos cómo el efecto de la SA disminuye la calidad de la imagen notablemente cuando el diámetro pupilar es grande.

En lentes multifocales, para pupilas pequeñas y en el foco lejano, el perfil difractivo-apodizado hace que el contraste sea mayor que en las lentes no-apodizadas. En cambio, para pupilas grandes, el efecto de la SA hace que el contraste disminuya en las lentes apodizadas y la lente no-apodizada – pero asférica con compensación total de la SA cornal – presenta valores de contraste mayores.

En el foco cercano, las lentes apodizadas proporcionan peor contraste que la lente no-apodizada (ZMA00) debido a que la distribución energética de los diseños apodizados favorecen al foco lejano [Vega et al. 2011; Alba-Bueno et al. 2011a].

Por último, la proximidad entre focos que existe en las lentes de adición menor (SN6AD1) lleva a una reducción del contraste de Michelson que se hace notable especialmente con pupilas pequeñas, donde la influencia de la SA es menor.

6.2 Función de Transferencia de Modulación

REFERENCE TO THE PUBLICATIONS OF THIS THESIS

Part of the content of this section is included in the publications:

- Alba-Bueno, F. Vega, F.Millán M.S and Navarro R. *"Expected Visual Acuity and Depth of Focus with Spherical and Aspheric Intraocular Lenses".* 6th European Meeting on Visual and Physiological Optics (EMVPO) 2012. Dublin (Ireland).

Probablemente uno de los métodos más utilizados para caracterizar la calidad óptica de un sistema óptico formador de imágenes es mediante la representación de la MTF. En esta sección se medirán las MTFs de diferentes IOLs monofocales y multifocales y se comparará su rendimiento considerando dos diámetros pupilares diferentes, de 2.4*mm* y 4.2*mm*, representativos de una pupila grande y otra pequeña en el ojo humano.

6.2.1 Método

Para calcular la MTF utilizaremos la función de extensión un borde (EFS, del inglés: Edge Spread Function) mediante el procedimiento descrito por Samei et al. [Samei et al. 1998; Boreman 2001]. Este método analiza la respuesta del sistema óptico al formar la imagen de un borde de alto contraste ligeramente inclinado (figura 6.6a). Además de captar las imágenes del test de borde para cada plano de mejor imagen, se captaron también las imágenes del test USAF (figura 6.6c) con dos intenciones:

- Poder calcular la focal efectiva del sistema, necesaria para expresar la MTF en ciclos por grado (cdp).
- Para facilitar la visualización cualitativa de las imágenes.

Nuevamente, se utilizó el banco óptico descrito en el capítulo 2 con la configuración que se muestra en la figura 6.1. Se utilizó la córnea artificial que induce una SA similar a la del ojo humano [Wang et al. 2003; Guirao et al. 2000] y, como fuente de luz, el LED cuyo espectro de emisión está centrado en una longitud de onda verde. Se consideraron dos diámetros pupilares, uno de 2.4mm y otro de 4.2mm, representativos de una pupila grande y otra pequeña en el ojo humano. Las características principales de las lentes incluidas en esta parte del trabajo se encuentran resumidas en la tabla 6.2. Son las mismas lentes que las utilizadas en la sección 6.1.1 más la IOLM refractiva simétrica NXG1(ReZoom).

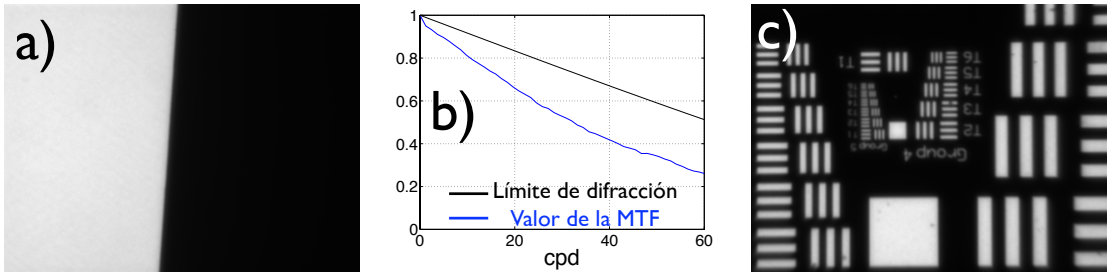

Figura 6.6: a) Imagen del test de borde formada por el modelo de ojo con la IOL asférica (ZCB00) y pupila de 2.4mm; b) MTF calculada a partir del test (a); c) Imagen del test USAF en las mismas condiciones.

Tabla 6.2: Características principales de las lentes caracterizadas mediante la MTF.

Diseño óptico	Referencia (nombre commercial)	Compensación SA corneal	Potencia base (D)	Adición (D)
Monofocal	SN60AT	No	20	-
	SN60WF (AcrySof IQ)	Parcial	20	-
	ZA9003 (Tecnis)	Total	20	-
Refractiva – Simétrica	NXG1 (ReZoom)	*	20	3.5
Difractiva (no-apodizada) Bifocal	ZMA00 (Tecnis multifocal)	Total	20	4
Difractiva-apodizada Bifocal	SN60D3 (AcrySof ReSTOR)	No	20	4
	SN6AD3 (AcrySof ReSTOR)	Parcial	20	4
	SN6AD1 (AcrySof ReSTOR)	Parcial	20	3

** Información no suministrada por el fabricante*

6.2.2 Resultados

Lentes monofocales

En la figura 6.7a podemos ver las imágenes formadas por cada lente monofocal del test USAF y sus correspondientes MTFs en los planos de mejor imagen (mejor MTF). Para una mejor comparación, las MTFs de cada lente han sido representadas en los mismos gráficos - agrupadas por pupilas – en la figura 6.7b. En esta figura se puede observar que, para un diámetro pupilar pequeño (de 2.4*mm*) existen menos diferencias entre ellas, si bien, es la lente esférica (SN60AT) la que presenta la peor MTF. Las diferencias aumentan notablemente al utilizar un diámetro pupilar mayor (de 4.2mm), donde se aprecia claramente cómo la MTF de la lente esférica (SN60AT) es peor que a las de las lentes asféricas. Por otro lado, con esta pupila grande se puede observar que la lente que corrige totalmente la SA inducida por la

córnea (ZMA00) presenta unos valores de la MTF ligeramente superiores a los de la lente que sólo realiza una corrección parcial de esta SA (SN60WF).

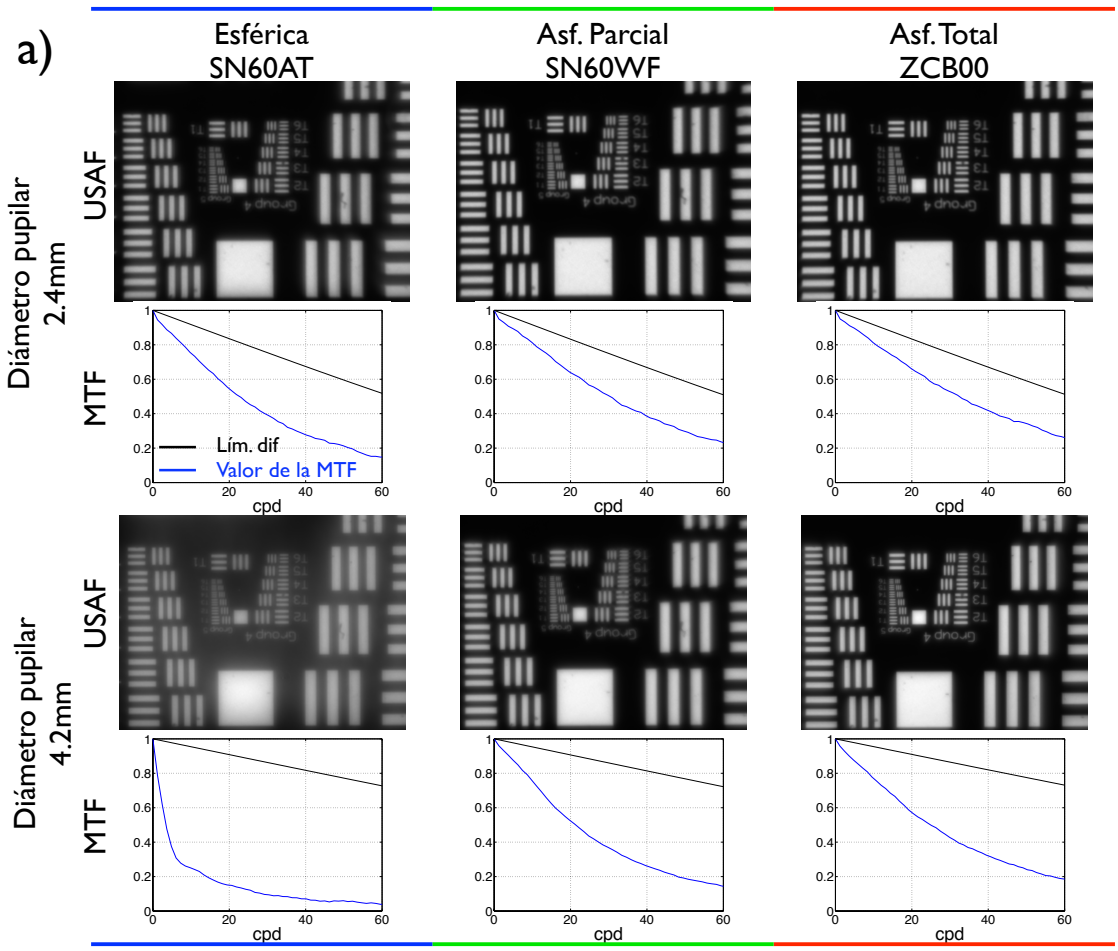

Figura 6.7a: Imágenes del test USAF y MTFs formadas en el plano de mejor imagen por las tres lentes monofocales incluidas en esta parte del trabajo.

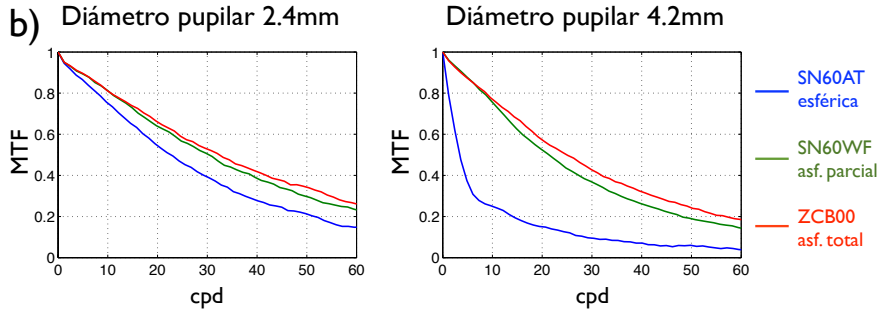

Figura 6.7b: MTFs de las tres lentes agrupadas por diámetro pupilar.

En las figuras 6.8a y 6.8b tenemos los resultados obtenidos para los focos lejano y cercano con las lentes multifocales. Al igual que con las lentes monofocales, en la figura 6.8c se han agrupado las MTFs en función del diámetro pupilar y para cada foco. Analizaremos estos resultados detenidamente.

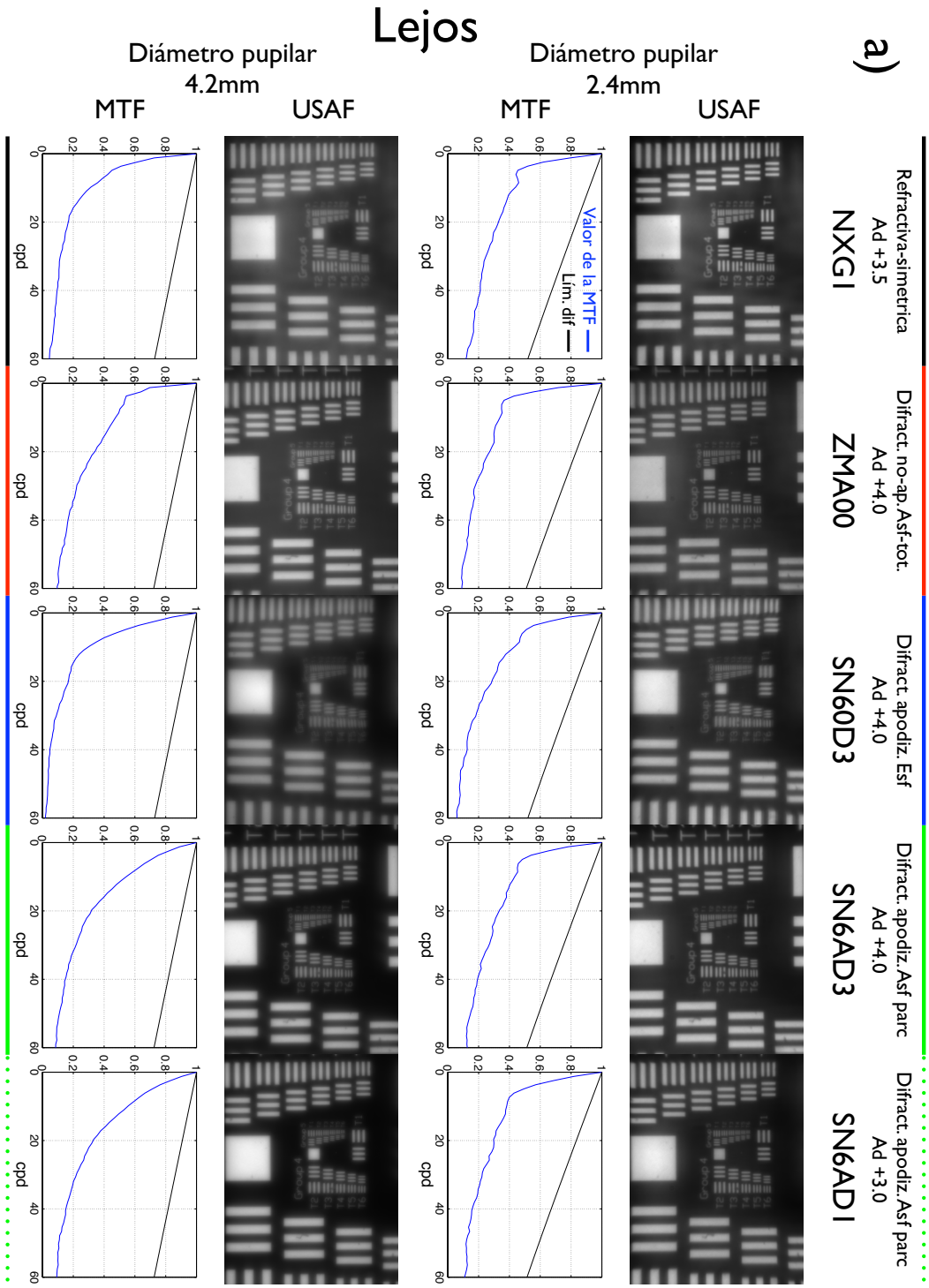

Figura 6.8a: Imágenes del test USAF y MTFs formadas en el foco cercano por un conjunto de lentes multifocales.

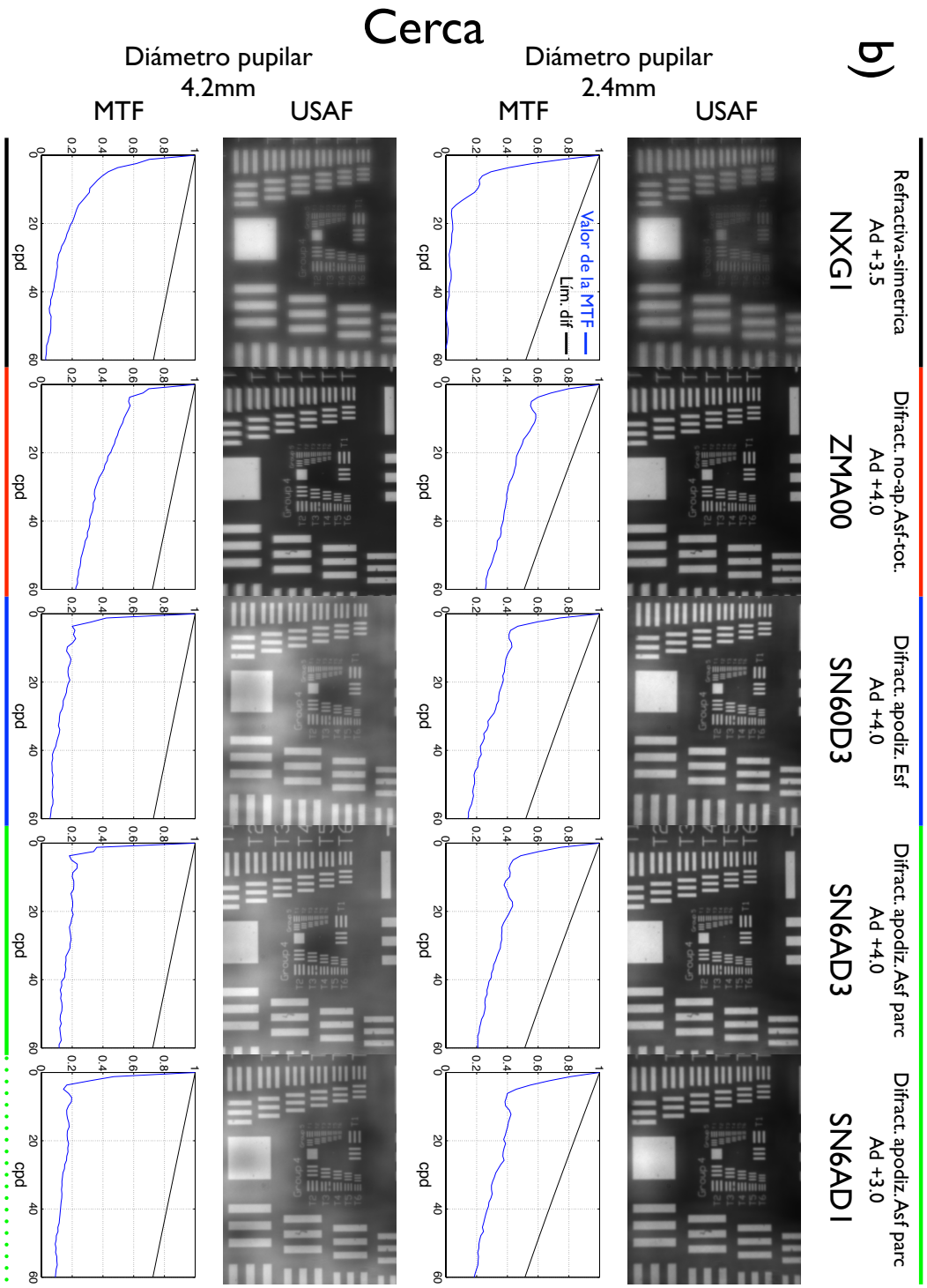

Figura 6.8b: Imágenes del test USAF y MTFs formadas en el foco de cerca por un conjunto de lentes multifocales.

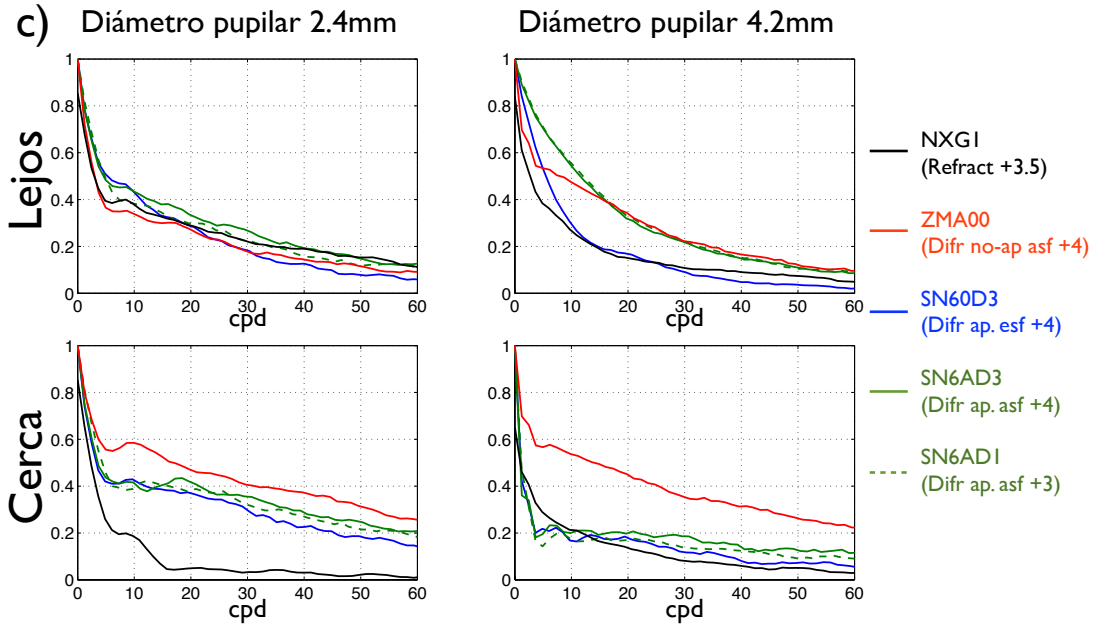

Figura 6.8c: MTFs de las MIOLs agrupadas por diámetro pupilar.

LIOM refractiva NXG1

Vemos cómo para la pupila más pequeña, en el foco lejano, la lente presenta un rendimiento similar a las IOLMs difractivas mientras que en el foco cercano el rendimiento es el peor con diferencia de todas las IOLs multifocales consideradas. Esto se debe a que para esta pupila apenas existe zona iluminada de la IOL que contribuya al foco cercano.

Cuando la pupila es grande, en cambio, tenemos que el rendimiento en visión lejana es peor que el de las IOLMs asféricas-difractivas consideradas (ZMA00, SN6AD3 y SN6AD1), y muy similar al de la esférica apodizada (SN60D3). En visión cercana y para pupila grande, en cambio, obtenemos un rendimiento ligeramente superior que el de las lentes apodizadas (SN60D3, SN6AD3 y SN6AD1) y peor que el de la lente difractiva no-apodizada (ZMA00). Esto se debe a que las lentes apodizadas presentan una contribución al foco cercano muy baja para un diámetro pupilar grande.

LIOMs difractivas asféricas: efectos de la apodización (ZMA00 vs SN6AD3)

La principal diferencia que existe entre estas lentes es que una presenta un diseño difractivo apodizado (SN6AD3) y la otra un diseño difractivo que cubre la apertura completa (no-apodizado, ZMA00). En la figura 6.9 se muestran las MTFs de estas lentes, tanto en el foco lejano como en el cercano y para ambas pupilas, con el fin de facilitar la comparación de resultados.

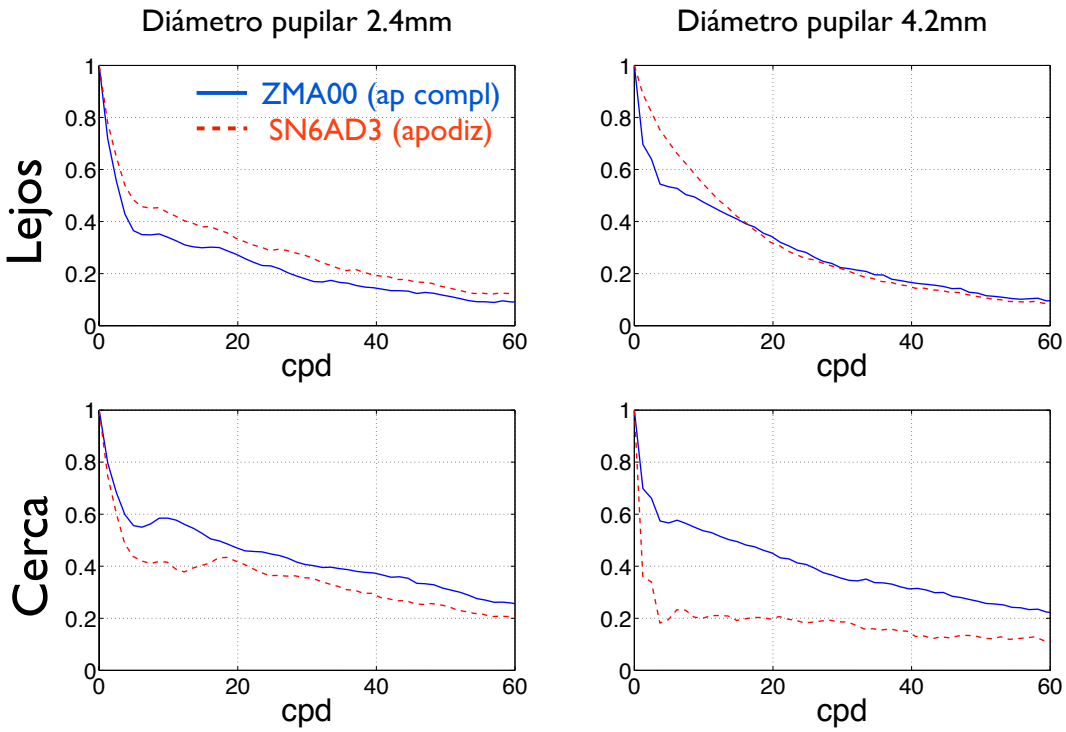

Figura 6.9: Comparación de MTFs entre las lentes ZMA00 (asférica difractiva no-apodizada) y SN6AD3 (asférica difractiva apodizada).

La IOLM no-apodizada (ZMA00) presenta mejor MTF que la apodizada (SN6AD3) en el foco cercano independientemente de su pupila, pero especialmente para la pupila grande. En el foco lejano, en cambio, ambas lentes tienen unas curvas similares, siendo la lente apodizada (SN6AD3) ligeramente mayor que la no-apodizada (ZMA00).

En esta figura se observa también que en el foco lejano, para la pupila pequeña, la apodización favorece el rendimiento de esta lente (SN6AD3). Para pupilas grandes, en cambio, se observa que el rendimiento de ambas lentes es muy parecido a partir de los 20cpd pero para frecuencias inferiores a 20cpd es la lente apodizada (SN6AD3) la que presenta mejores valores de la MTF. Esto es debido a que la energía que viene del foco cercano (que origina el "halo", como veremos en la sección 6.3) está distribuida en una zona mayor debido a que en la lente no-apodizada (ZMA00) la contribución al foco cercano es de toda la superficie, mientras que en la IOL apodizada (SN6AD3) la contribución es únicamente de la parte central de la zona óptica.

En el foco cercano, en cambio, el hecho de que la lente apodizada destine menor cantidad de energía hace que esta lente (SN6AD3) presente valores inferiores de la MTF para ambas pupilas.

LIOMs difractivas apodizadas: efecto de la geometría asférica/esférica (SN60D3 vs SN6AD3)

En este caso ambas lentes presentan idéntico diseño difractivo y su única diferencia es que la lente SN60D3 presenta geometrías de superficies esféricas mientras que la lente SN6AD3 presenta una de sus superficies asférica con objeto de compensar parcialmente la SA corneal. En la figura 6.10 están representadas las MTFs de ambas lentes tanto en el foco lejano como en el cercano con ambas pupilas.

En esta figura vemos como la IOL asférica (SN6AD3) sólo es ligeramente mejor que la esférica (SN60D3), siendo más apreciable dicha ventaja en el foco lejano para pupilas grandes. Se puede observar que en el foco lejano y para pupila pequeña, la MTF de la lente asférica (SN6AD3) es ligeramente superior a la de la lente esférica (SN60D3) y al abrir la pupila estas diferencias aumentan. En el foco cercano, en cambio, ambas MTFs son más parecidas debido a que la zona que contribuye al foco cercano son los 3.6mm centrales y para esta apertura la presencia de SA es baja. No obstante se puede observar cómo los valores de la MTF para frecuencias altas de la lente asférica (SN6AD3) con la pupila grande son mayores.

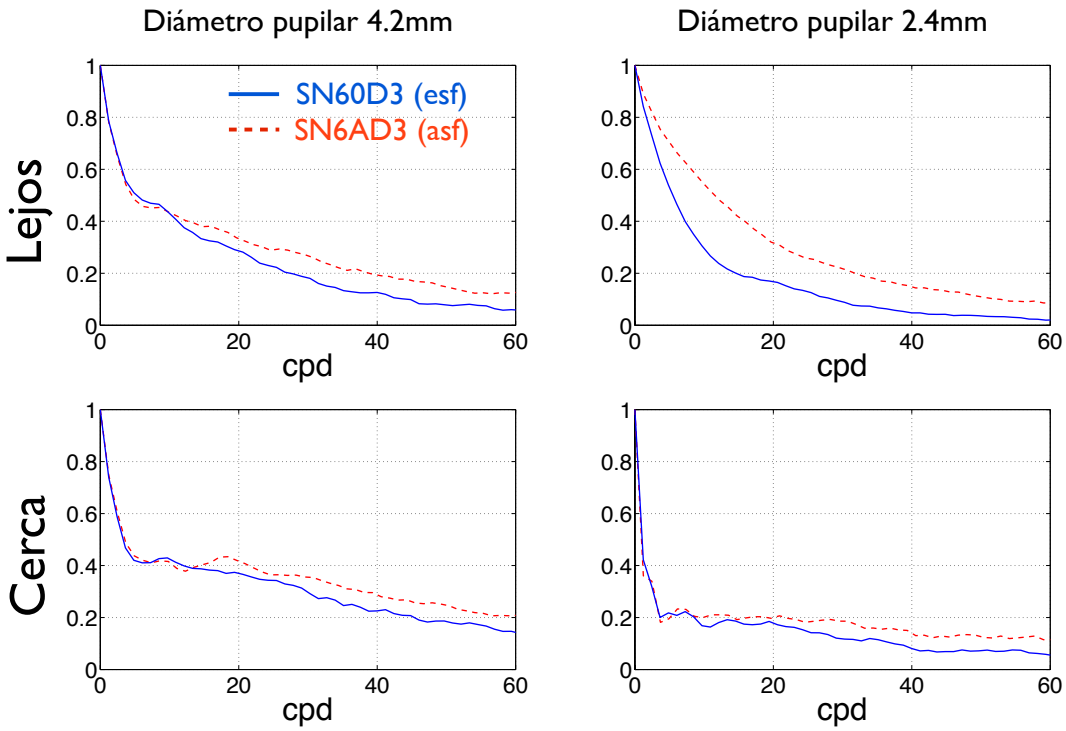

Figura 6.10: Comparación de MTFs entre las lentes SN60D3 (esférica difractiva apodizada) y la SN6AD3 (asférica difractiva apodizada).

LIOMs difractivas apodizadas: efecto de la adición (SN6AD3 vs SN6AD1)

Estas dos lentes únicamente se diferencian en la adición, la IOL SN6AD3 presenta una adición de +4.0D, mientras que la SN6AD1 tiene una adición de +3.0D. Las MTFs para cada pupila y en cada plano focal imagen de estas lentes están representadas en la figura 6.11.

En este caso podemos ver que las MTFs son muy parecidas entre ambas lentes contrastando que su calidad en la formación de imágenes es prácticamente la misma.

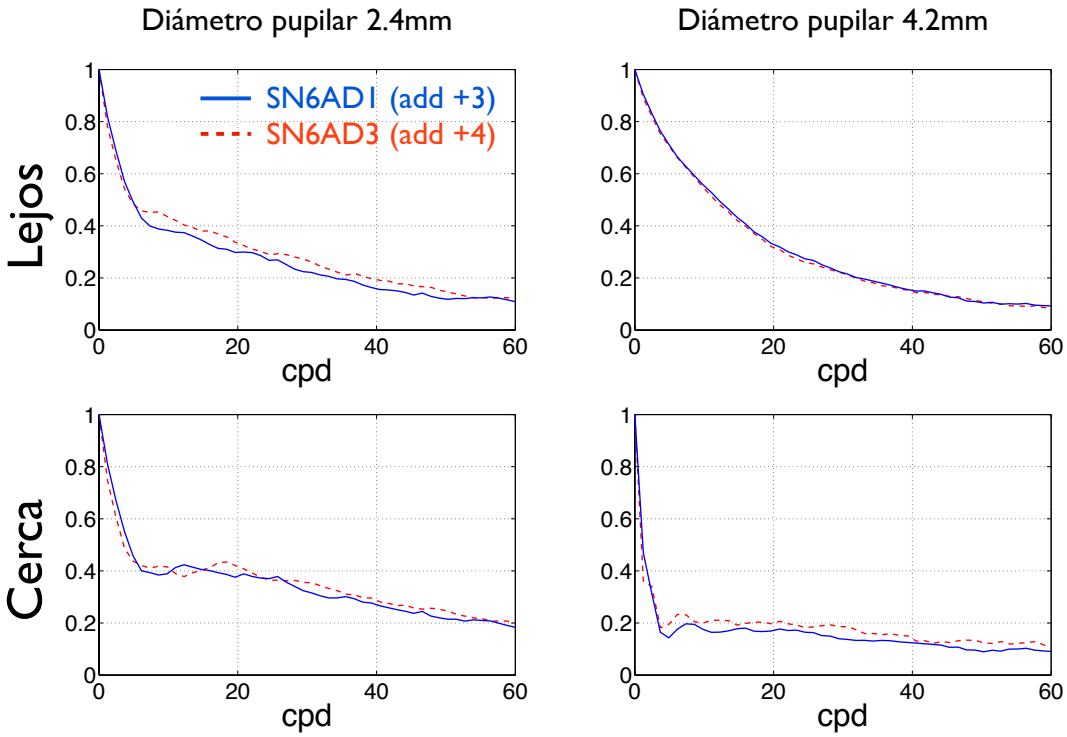

Figura 6.11: Comparación de MTFs entre las lentes SN6AD1 (asférica difractiva apodizada de adición +3.0D) y la SN6AD3 (asférica difractiva apodizada de adición +4.0D).

6.2.3 Discusión

Teniendo en cuenta todas las lentes analizadas, se puede concluir que las lentes con mejor MTF son las lentes monofocales asféricas (SN60WF y ZCB00) independientemente de su pupila. La MTF como parámetro de calidad y al igual que otras métricas, es altamente dependiente del diámetro pupilar. Un resultado sorprendente y que puede tener relevancia en pacientes implantados con estas lentes, es que la MTF con la lente monofocal esférica (SN60AT) con pupila grande puede presentar valores iguales o ligeramente inferiores a algunas lentes multifocales en visión de lejos.

Con las lentes multifocales hemos visto que no existe un diseño que sea claramente ventajoso a los demás cuando valoramos la MTF. Las lentes apodizadas, especialmente las asféricas (SN6AD3 y SN6AD1) presentan mejores MTFs en visión lejana que el resto de las IOLs multifocales mientras que en visión cercana son inferiores.

La lente refractiva (NXG1) puede presentar muy buen rendimiento de lejos cuando la pupila es muy pequeña debido a que en esas condiciones no hay ninguna zona de la lente que contribuya al foco cercano, por lo que su comportamiento puede ser similar al de una IOL monofocal.

Existen multitud de trabajos que caracterizan IOLs mediante el cálculo de su MTF utilizando bancos ópticos y/o simulaciones obteniendo resultados similares a los obtenidos en esta sección. Véanse por ejemplo las referencias: [Holladay et al. 1990; Larsson et al. 1992; Simpson 1992; Pieh et al. 2002; Eppig et al. 2009; Remón et al. 2012].

6.3 Formación y caracterización del halo

REFERENCE TO THE PUBLICATIONS OF THIS THESIS

The content of this section is included in the publications:

- Alba-Bueno, F. Vega, F. and Millán M.S. *"Halos y lentes intraoculares multifocales: Origen e interpretación"*. "89 Congreso de la Sociedad Española de Oftalmología". Aceptado para publicación en los Archivos de la Sociedad Española de Oftalmología.

Una de las principales quejas de los pacientes implantados con lentes intraoculares multifocales (IOLMs) es la percepción de halos [Calladine et al. 2012], especialmente en condiciones de baja iluminación (diámetros pupilares grandes), con estímulos luminosos intensos y con un fondo relativamente oscuro. Estas circunstancias se pueden dar con bastante frecuencia, por ejemplo, al conducir de noche. El concepto de halo se utiliza para definir un contorno o forma luminosa borrosa que percibe el paciente alrededor de estos estímulos. Este efecto se puede originar por diversos factores como las aberraciones de alto orden (especialmente la aberración esférica) y, sobre todo, por a la existencia y la percepción de imágenes múltiples, como en el caso de las IOLMs, donde la imagen enfocada está simultáneamente superpuesta a otra (u otras) desenfocada(s). En la mayoría de los estudios publicados sobre este efecto hacen valorar subjetivamente al paciente la percepción de halos (generalmente mediante cuestionarios) y en muy pocas ocasiones se utilizan métodos objetivos para cuantificarlos [Madrid-Costa et al. 2010; de Vries et al. 2011; Gil et al. 2012].

En esta sección proponemos una aproximación teórica en el marco de la óptica geométrica de primer orden (también conocida como óptica paraxial u óptica de Gauss) para caracterizar el diámetro del halo y un método experimental para analizar in vitro su tamaño y su intensidad relativa. El método se aplicará a diferentes diseños de IOLs mono y multifocales.

6.3.1 Aproximación paraxial para la estimación del diámetro del halo

Para una mejor compresión de la formación del halo, consideraremos una aproximación paraxial para ver cómo pueden influir la potencia y la adición de la

IOL así como el diámetro pupilar. La formación del halo en condiciones de visión lejana y cercana estaría esquematizada en la figura 6.12 a) y b) respectivamente. Se asume, en este ejemplo, que el paciente ha sido implantado con una IOLM bifocal, es decir, con dos focos (lejos y cerca), y es pupilodependiente. La parte central contribuye al foco de lejos y también al foco de cerca, mientras que la parte exterior sólo lo hace al foco de lejos. Por eso, en la figura 6.12, aunque se ilumina la IOLM con un haz de diámetro dpd que cubre toda su apertura, sólo la zona central de la IOLM de diámetro dpn, envía luz al foco de cerca.

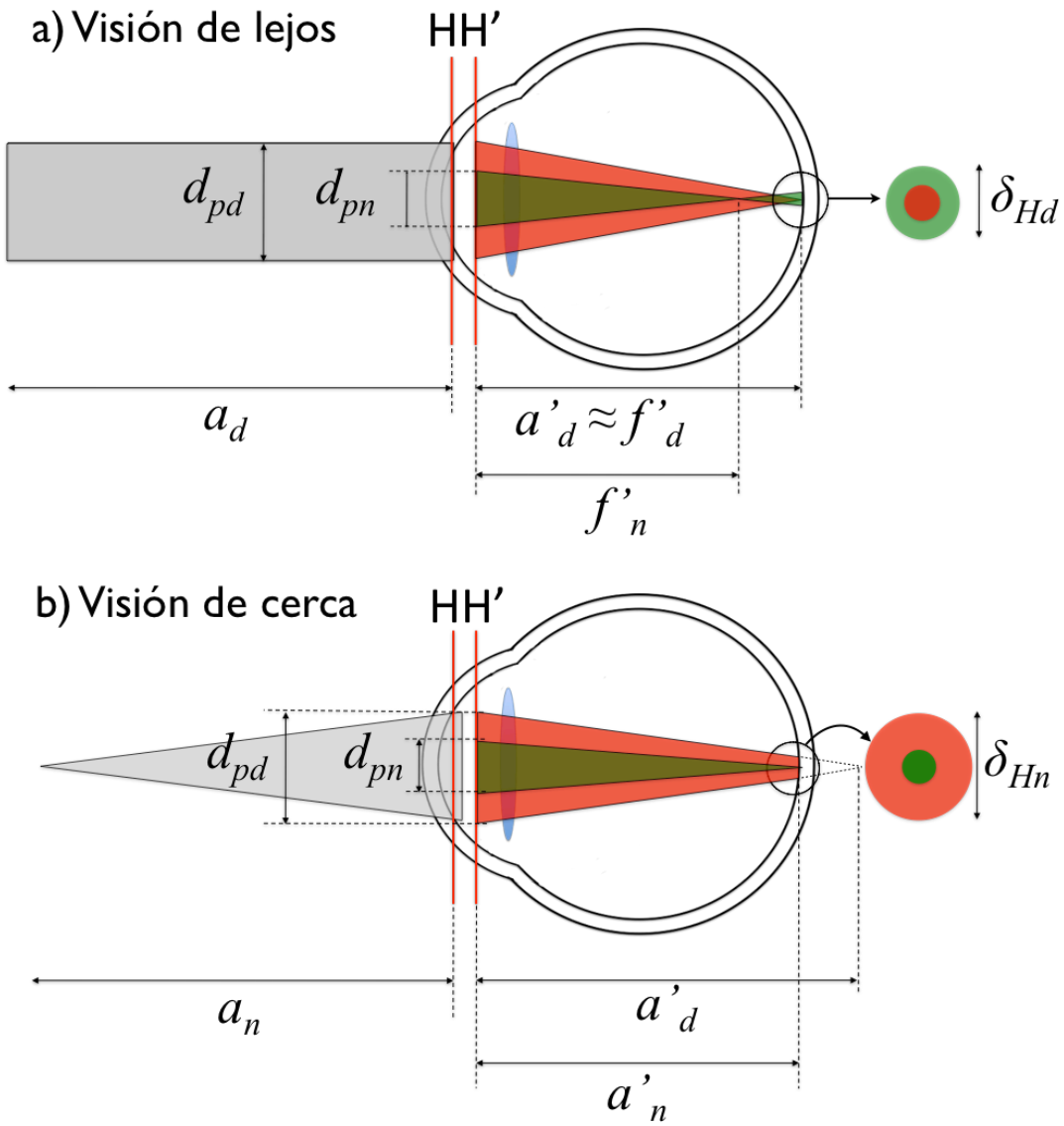

Figura 6.12: Esquema de la formación del halo en visión lejana (a) y cercana (b) en un ojo implantado con una IOLM. Se considera una lente apodizada en la que únicamente la parte central de la IOLM contribuye al foco de cerca.

Para calcular el diámetro del halo empezaremos utilizando la fórmula de correspondencia objeto-imagen a través de un sistema óptico (ojo):

$$\frac{n_v}{f'_i} = \frac{n_a}{a_i} + \frac{n_v}{a'_i} \text{ , con } i = \{n, d\} \tag{6.2}$$

donde n_v es el índice de refracción del vítreo (n_v=1.336), n_a es el índice de refracción del aire (n_a=1), i puede ser "*d*" o "*n*" para el foco de lejos o de cerca, respectivamente, a es la distancia del objeto al plano principal objeto (H) del sistema (ojo), a' es la distancia del plano principal imagen *(H')* a la imagen lejana o cercana y f' es la distancia focal del ojo para el i-foco. Consideramos que los planos H y H' no cambian significativamente en visión cercana y lejana y que:

$$P_d = \frac{n_v}{f'_d} \text{ , } P_n = \frac{n_v}{f'_n} \text{ y } \Delta P = P_n - P_d \text{ , } \tag{6.3}$$

donde P_d y P_n son las potencias refractivas del foco lejano y cercano del ojo, y ΔP es la adición.

En condiciones de visión lejana (figura 6.12a) y desde la aproximación paraxial (no se tiene en cuenta la contribución de las aberraciones de alto orden ni del esparcimiento o "scattering"), el halo se forma debido a la imagen desenfocada del foco cercano. En este caso $a_d=\infty$, así que $f'_d=a'_d$ y $f'_n=a'_n$. De este modo tenemos que:

$$\frac{\delta_{Hd}}{f'_d - f'_n} = \frac{d_{pn}}{f'_n} \text{ , } \tag{6.4}$$

donde δ_{Hd} es el diámetro del halo en condiciones de visión lejana y d_{pn} es el diámetro del sector central iluminado de la IOLM que contribuye al foco cercano. Utilizando las ecuaciones 6.3 en la ecuación 6.4, el diámetro del halo en estas condiciones viene dado por:

$$\delta_{Hd} = d_{pn} \frac{\Delta P}{P_d} \text{ , } \tag{6.5}$$

Por otro lado, cuando el objeto se encuentra a distancia finita del ojo, es decir, en condiciones de visión cercana (figura 6.12b) el halo se forma debido a la imagen desenfocada del foco lejano (de nuevo, en aproximación paraxial que ignora la contribución de las aberraciones de alto orden). El diámetro del halo en visión cercana δ_{Hn} puede ser calculado a partir de:

$$\frac{\delta_{Hn}}{a'_d - a'_n} = \frac{d_{pd}}{a'_d} \text{ , } \tag{6.6}$$

donde d_{pd} es el diámetro de la zona iluminada de la IOL que contribuye al foco lejano.

En condiciones de visión cercana $a'_n \approx f'_d$ ya que la imagen del objeto cercano se forma nítidamente sobre la retina. Particularizando la ecuación 6.2 con la focal de cerca ($i=n$) y después con la focal de lejos ($i=d$), y teniendo en cuenta las ecuaciones 6.3 se obtienen las expresiones de la distancia objeto:

$$a = n_a/\Delta P \text{ ; y } a'_d = n_v/\left(P_d - \Delta P\right) . \qquad (6.7)$$

Nuevamente, utilizando las ecuaciones 6.3 y 6.7 en la ecuación 6.6 se obtiene que:

$$\delta_{Hn} = d_{pd}\frac{\Delta P}{P_d} . \qquad (6.8)$$

Tal y como se muestra en las ecuaciones 6.5 y 6.8, el diámetro de los halos en visión lejana y cercana, depende de la adición ΔP, de la potencia refractiva para el foco lejano P_d, y del diámetro iluminado de la IOL que contribuye a la imagen desenfocada (d_{pn} ó d_{pd} respectivamente). Cuando el diseño de la IOL hace que $d_{pd}=d_{pn}$ como las lentes difractivas no-apodizadas (p.ej. ZMA00), el diámetro del halo debe ser el mismo en condiciones de visión cercana y lejana tal y como publicaron Pieh y colaboradores [Pieh et al. 2001]. Con lentes apodizadas (p.ej. ReSTOR) cuyo diseño difractivo se limita a la zona central de la lente y la periferia es puramente refractiva, el halo puede tener diferente tamaño en condiciones de visión lejana y cercana.

6.3.2 Medidas *in vitro*

En la determinación del diámetro del halo, mediante las ecuaciones 6.5 y 6.8, no hemos tenido en cuenta la posible apodización del perfil difractivo, que tendría un efecto tanto en el tamaño como en la intensidad del halo. Asimismo, tampoco se han considerado los efectos de las aberraciones del sistema. La caracterización *in vitro*, en cambio, nos permite un análisis experimental, que contempla la contribución real de todos estos efectos. Esta caracterización se puede realizar con el sistema óptico descrito en el capítulo 2 de esta tesis. Como se ha hecho a lo largo de todo este capítulo, utilizamos la córnea artificial que induce una aberración esférica sobre la IOL similar a la de la córnea humana promedio [Wang et al. 2003; Guirao et al. 2000; Vega et al. 2010] en la configuración que se esquematiza en la figura 6.1.

El análisis, tanto del diámetro del halo como de su intensidad relativa respecto a la imagen enfocada, se puede realizar mediante la representación del perfil de intensidad de las imágenes captadas. Para facilitar la visualización y el análisis de estas imágenes es conveniente representar tanto los mapas de intensidad de las imágenes como los perfiles en escala logarítmica (figura 6.13).

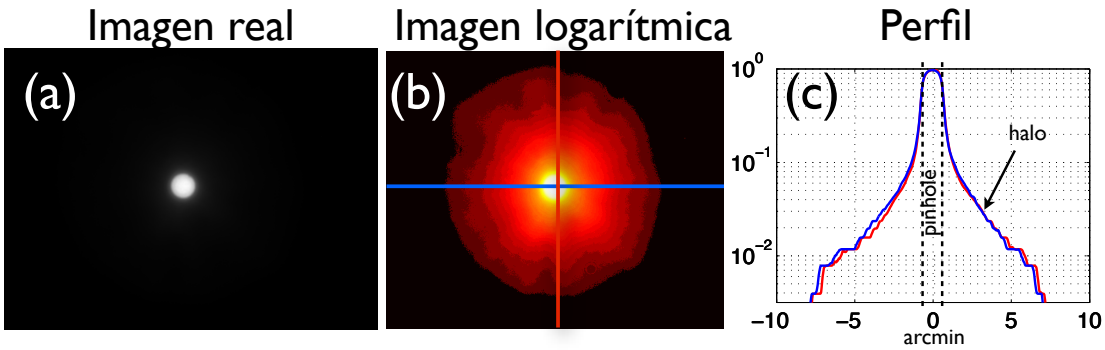

Figura 6.13: (a): Imagen real del orificio (pinhole), con la intensidad representada en escala lineal; (b): representación de la intensidad de la imagen (a) en escala logarítmica y en falso color; (c): perfiles de intensidad verticales (líneas rojas) y horizontales (líneas azules) de la imagen.

6.4 Resultados

El método experimental propuesto para la caracterización del halo se aplicó a diferentes lentes mono y multifocales para dos diámetros pupilares (4.7mm y 2.4mm en el plano de la IOL). Las principales características de las lentes incluidas en este trabajo se resumen en la tabla 6.3. Destacamos la inclusión de lentes refractivas, con y sin simetría de revolución, así como de una lente trifocal, además de las monofocales y bifocales estudiadas en los apartados anteriores de este capítulo.

Tabla 6.3: Características principales de las lentes estudiadas en la caracterización del halo.

Diseño óptico	Referencia (nombre commercial)	Compensación SA corneal	Potencia base (D)	Adición (D)
Monofocal	SN60AT	No	20	-
	SN60WF (AcrySof IQ)	Parcial	20	-
	ZA9003 (Tecnis)	Total	20	-
Refractiva – Simétrica	NXG1 (ReZoom)	*	20	3.5
Refractiva – Asimétrica	LS-313 (MPlus)	*	20	3
Difractiva (no-apodizada) -Bifocal	ZMA00 (Tecnis multifocal)	Total	20	4
Difractiva-apodizada - Bifocal	SN60D3 (AcrySof ReSTOR)	No	20	4
	SN6AD3 (AcrySof ReSTOR)	Parcial	20	4
	SN6AD1 (AcrySof ReSTOR)	Parcial	20	3
Difractiva Trifocal – Bifocal	AT.lisa 389 MP	Parcial *	20	3.33 / 1.66

** Información no suministrada por el fabricante.*

Lentes monofocales

Las imágenes formadas por el modelo de ojo en el banco óptico para tres diseños de IOLs monofocales y sus correspondientes perfiles de intensidad se muestran en la figura 6.14. Como se puede observar, el halo de mayor diámetro lo presenta la lente esférica (SN60AT) para un diámetro pupilar grande. Las lentes asféricas (SN60WF y ZA9003), en cambio, no muestran diferencias apreciables entre ellas en cuanto a diámetro del halo ni a su intensidad, a pesar del diferente grado de compensación de la SA efectuado por cada una. Para pupilas pequeñas, las diferencias entre la lente esférica y las asféricas se reducen notablemente debido a la disminución de la aberración esférica del sistema. Esta misma aberración esférica es la responsable de que la disminución de intensidad máxima para la pupila pequeña que se produce en las lentes asféricas sea mayor que la que se produce en la lente esférica (SN60AT) como se esquematiza en la figura 6.15.

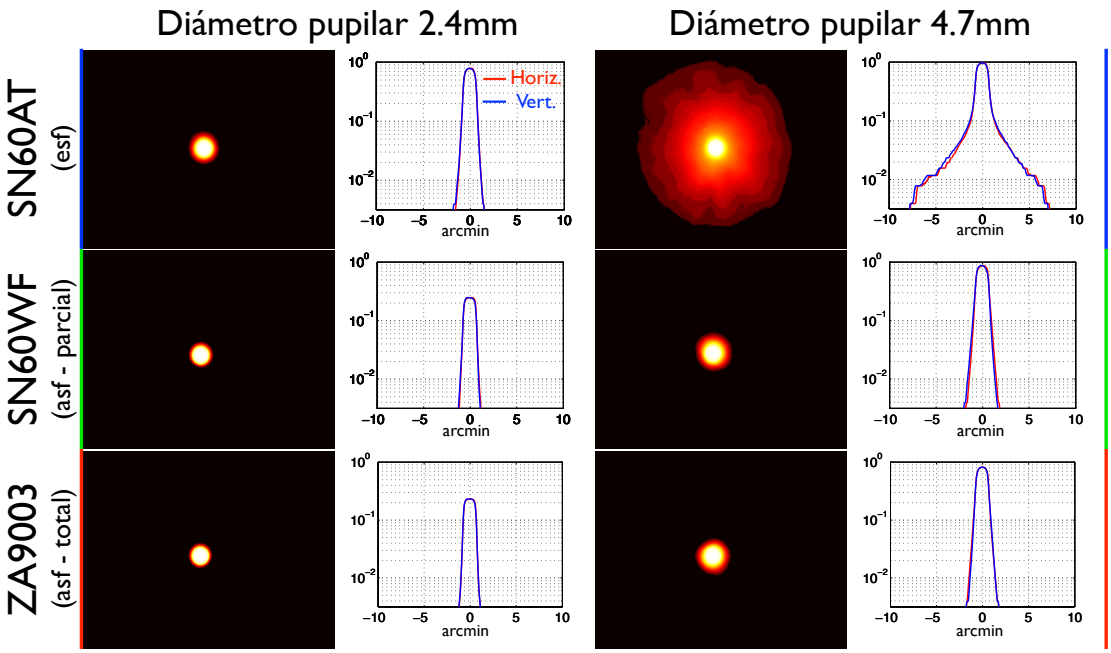

Figura 6.14: Imágenes logarítmicas del plano de mejor imagen de lentes monofocales para un diámetro pupilar (en el plano de la IOL) grande (izquierda) y pequeño (derecha).

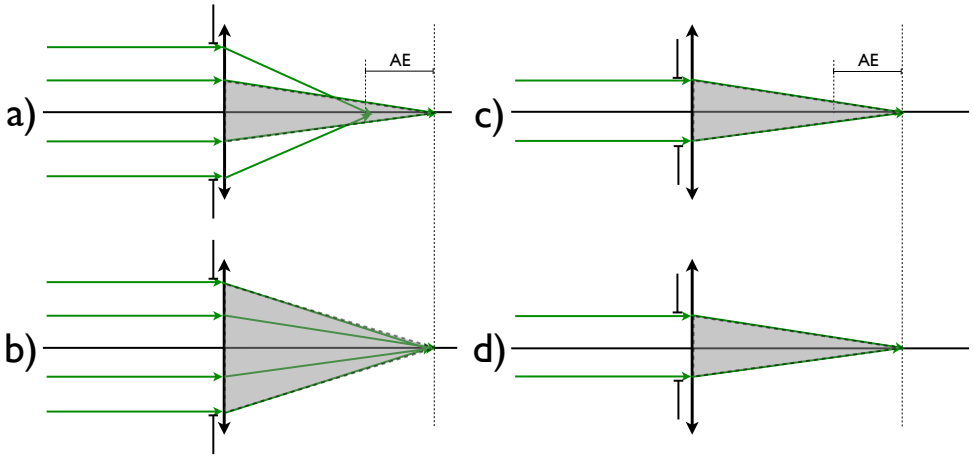

Figura 6.15:

Lentes multifocales

Las imágenes correspondientes a los planos de mejor imagen en el foco lejano, intermedio (en el caso de la lente trifocal) y cercano, así como sus correspondientes perfiles de intensidad, se muestran en escala logarítmica en las figuras 6.16 y 6.17 para los diámetros pupilares en el plano de la IOL de 2.4 y 4.7*mm,* respectivamente. Tal y como se puede deducir de las ecuaciones (6.5) y (6.8), el tamaño del halo es mayor cuanto mayor sea el diámetro pupilar. Puesto

que las diferencias son más notables para diámetros pupilares grandes, analizaremos detenidamente los resultados obtenidos en la figura 6.17 (mayor diámetro pupilar).

Lentes refractivas: NXG1 y LS-313.

En estas lentes podemos observar la influencia del diseño simétrico (NXG1) vs asimétrico (LS-313). Vemos que, mientras la lente NXG1 (figura 6.17a) presenta un halo circular, en la lente LS-313 (figura 6.17b) el halo es asimétrico con un patrón de intensidad que recuerda a una aberración tipo coma.

Lentes difractivas asféricas con adición +4.0D: ZMA00 y SN6AD3

La comparación de estas lentes pone de manifiesto la diferencia en tamaños e intensidades con lentes de similar diseño base y adición (ambas son asféricas y presentan la misma adición) pero con diferente diseño difractivo, una lente con perfil difractivo en toda su superficie (ZMA00) y la otra con perfil difractivo apodizado únicamente en la zona central (SN6AD3).

En la figura 6.36c se puede ver cómo la lente ZMA00 presenta aproximadamente el mismo diámetro de halo tanto de lejos como de cerca. En cambio, en la figura 6e, vemos cómo la lente con perfil difractivo apodizado (SN6AD3) presenta menor diámetro e intensidad de halo en visión lejana que en visión cercana debido al reparto distinto de intensidades entre los focos lejano y cercano para esta pupila. En visión lejana, el tamaño del halo de la lente SN6AD3 es menor que el de la lente ZMA00 mientras que en visión cercana presentan aproximadamente el mismo tamaño, siendo de mayor intensidad en el caso de la lente SN6AD3.

Lentes apodizadas: SN60D3, SN6AD3 y SN6AD1

Estas tres lentes, dado que la zona difractiva es apodizada y ocupa sólo un parte central de la IOL (3.6mm) se cumple que $d_{pn} \leq d_{pd}$ por lo que, de acuerdo con las ecuaciones (6.5) y (6.8), presentan menor tamaño e intensidad de halo en el foco lejano que en el cercano.

Al realizar la comparación entre lentes de igual adición pero con diferentes diseños base (esférico SN60D3 y asférico SN6AD3, figuras 6.17d y 6.17e) vemos cómo la lente esférica (SN60D3) presenta mayor diámetro de halo en el foco lejano que la lente asférica debido a la mayor aberración esférica (SA) total del sistema. En el foco cercano, en cambio, se observa que el halo de la lente esférica (SN60D3) es de menor diámetro que en el caso de la lente asférica (SN6AD3). Para comprender

mejor este resultado podemos referirnos a la figura 6.18. En ella se esquematiza la energía destinada al foco lejano de una lente con SA (figura 6.18a) y sin ella (figura 6.18b). La energía que iría al foco cercano no se ha representado para facilitar la comprensión de la figura. Como podemos ver, en el caso de la lente con SA positiva (figura 6.18a), la energía que proviene de la periferia de la lente converge antes (mayor potencia) por lo que en el plano de cerca (C) esta energía se distribuye en una menor superficie, generando un halo de menor tamaño (segmento rojo) y de mayor intensidad relativa que en el caso de la lente libre de SA (figura 6.18b).

Al comparar las lentes asféricas con diferente adición (SN6AD3, con adición de +4.0D y SN6AD1, con adición de +3.0D; figuras 6.17e y 6.17f) vemos cómo en el foco lejano el tamaño e intensidad del halo es algo mayor con la lente de mayor adición de acuerdo con la ecuación (6.5), si bien la diferencia no es muy grande debido a que ambas lentes presentan la misma superficie difractiva (3.6mm centrales) que destina poca energía relativa al foco cercano. En cambio, el halo que se genera en el foco cercano presenta claramente un mayor diámetro en el caso de la lente de mayor adición (SN6AD3) debido a la mayor adición de esta IOL que origina una distancia más grande entre ambos focos (ecuación (6.8)). Por otra parte la intensidad del halo en esta situación (foco cercano) es mayor en la lente de menor adición (SN6AD1) ya que la energía total destinada al foco lejano es la misma en ambas lentes pero en esta (SN6AD1) se encuentra distribuida en una menor superficie.

Lente AT-LISA trifocal

La periferia de esta lente es puramente bifocal (que origina los focos lejano y cercano) y la zona central es trifocal (que genera los focos lejano, intermedio y cercano). Las imágenes correspondientes a los focos lejano, intermedio y cercano y sus perfiles de intensidad se muestran a escala logarítmica en la figura 6.17g. En el foco lejano el diámetro del halo es similar al de la lente difractiva no-apodizada (ZMA00) y la intensidad es ligeramente superior. En el foco intermedio se aprecia la presencia de dos halos de diferente intensidad generados por las potencias (fuera de foco en el plano intermedio) lejana y cercana. En el foco cercano es donde se observan con más claridad los dos halos generados, en este caso, por las potencias lejana (de mayor diámetro y menor intensidad) e intermedia (de menor diámetro y mayor intensidad), ambas fuera de foco.

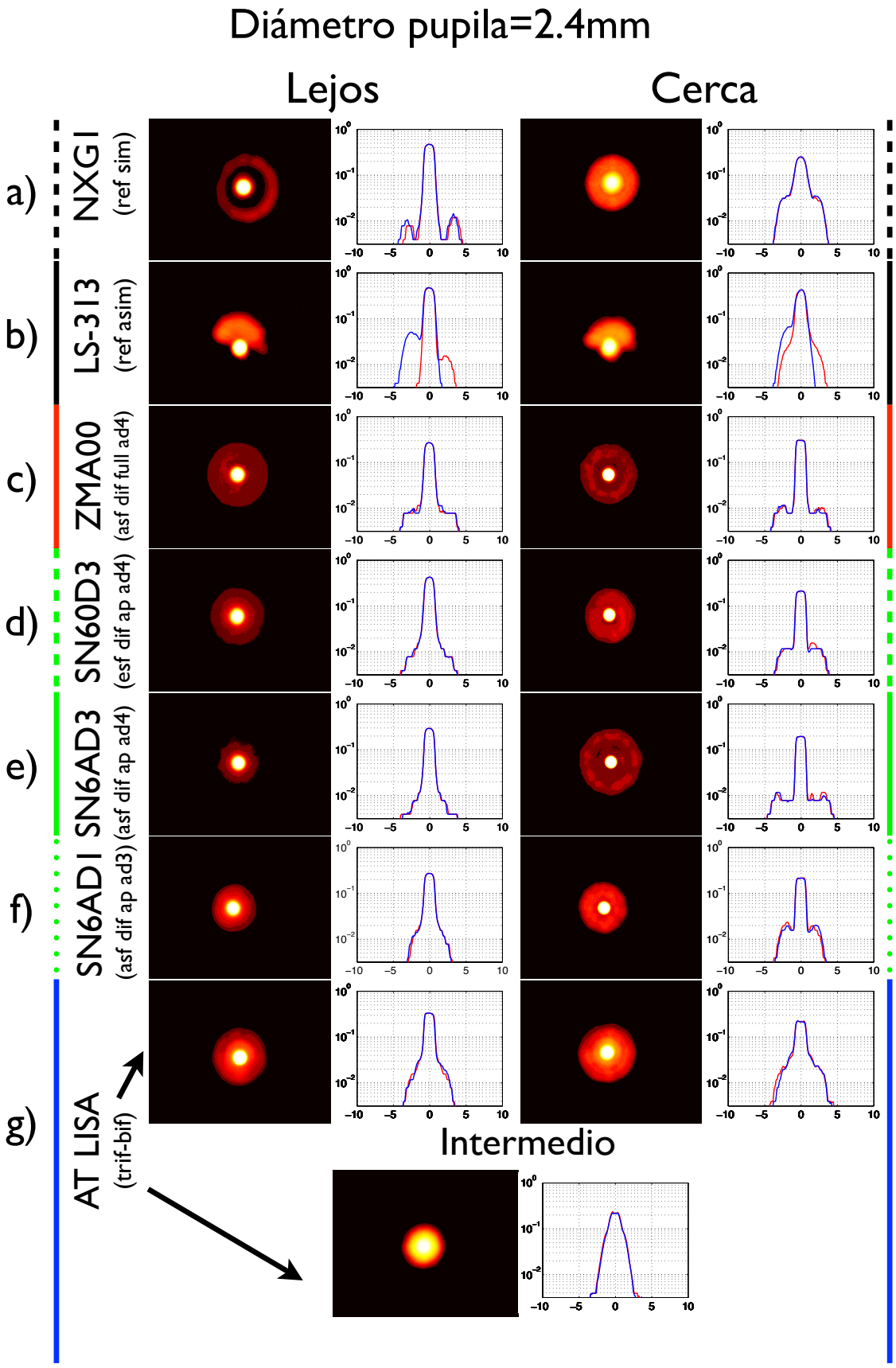

Figura 6.16: Imágenes logarítmicas y perfiles de intensidad en los planos de mejor imagen de cada IOL para un diámetro pupilar de 2.4mm

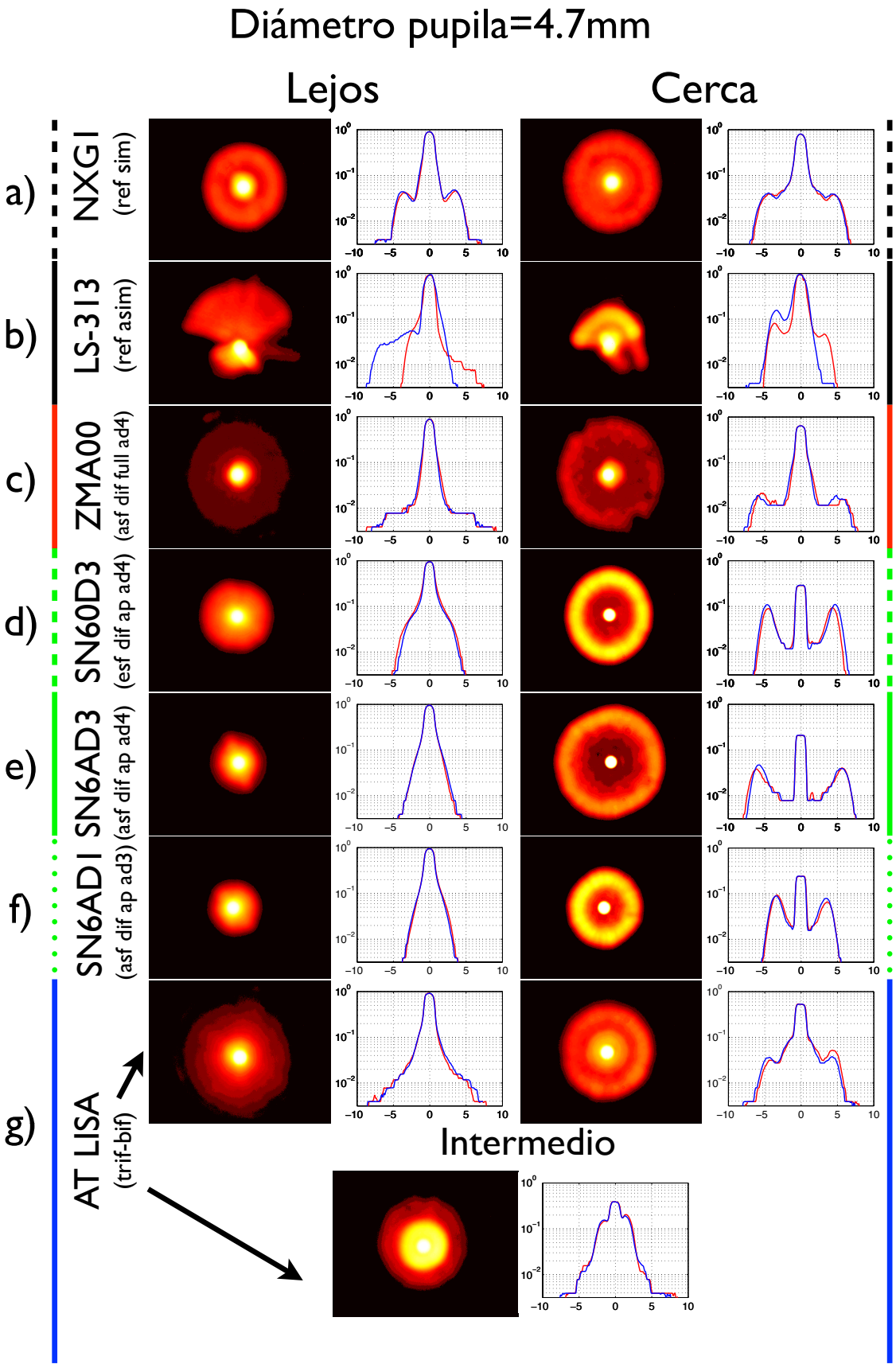

Figura 6.17: Imágenes logarítmicas y perfiles de intensidad en los planos de mejor imagen de cada IOL para un diámetro pupilar de 4.7mm

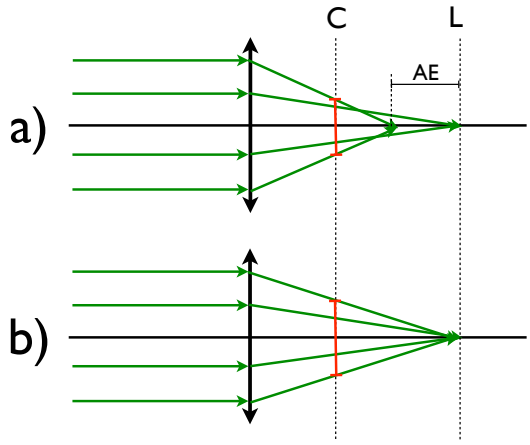

Figura 6.18: Origen del halo en visión cercana de una lente a) con aberración esférica (SA) y b) sin SA. El diámetro del halo en visión cercana está marcado en rojo. Las flechas verdes indican la energía destinada al foco lejano. No se representa la energía destinada al foco cercano.

6.3.4 Discusión

Tal y como predice la óptica geométrica en aproximación paraxial, el diámetro del halo es dependiente del diámetro pupilar que contribuye al foco no-enfocado, de la potencia base de la lente (potencia de lejos) y de la adición. Con diámetros pupilares pequeños las diferencias entre lentes se reducen considerablemente. Para una mejor predicción que la dada por esta aproximación paraxial, se podrían realizar simulaciones de trazado de rayos exacto. Por desgracia, esto no es posible de manera inmediata debido a que los fabricantes no suelen proporcionar los valores de las curvaturas, asfericidades, elevaciones, etc. de las lentes.

Las lentes monofocales asféricas SN60WF y ZA9003 presentan menor tamaño e intensidad de halo que cualquier otra lente multifocal y no se aprecian diferencias significativas entre los dos modelos examinados (SN60WF y ZA9003). El halo producido por la aberración esférica de una lente monofocal esférica (SN60AT) puede ser, para pupilas grandes, del mismo tamaño o superior que los halos que se producen en algunos diseños multifocales.

Las lentes multifocales presentan halos que pueden variar de forma y tamaño en cada uno de sus focos en función del diseño de la lente. De este modo, las lentes multifocales asimétricas generan halos también asimétricos (LS-313); las lentes difractivas no-apodizada (ZMA00) presentan prácticamente el mismo tamaño de halo en visión cercana que en visión lejana; las lentes apodizadas presentan menor tamaño e intensidad de halo en visión lejana pero mayor en cercana; y la lente

trifocal (AT-LISA) en cada plano imagen, presenta dos halos de diferente tamaño e intensidad, uno por cada potencia que está fuera de foco en dicho plano.

Existen numerosos trabajos que caracterizan la calidad óptica de lentes intraoculares in vivo [Montés-Micó et al. 2012; Artigas et al. 2007]; pero, por lo general, no contemplan caracterizar los halos que generan las IOLs y que se forman en la retina de los pacientes implantados con éstas. También existen aparatos llamados "halómetros" que se pueden utilizar para caracterizar la percepción del halo en estos pacientes pero con los que aún no se han realizado mediciones *in vivo* en pacientes implantados con IOLs. La principal diferencia entre estos "halómetros" y el método *in vitro* que proponemos es que en nuestro método únicamente evaluamos el halo inducido por el sistema óptico mientras que mediante el uso de un "halómetro"[Castro et al. 2011] se evalúa la percepción del halo por parte del paciente (es un método subjetivo) que incluye la calidad óptica y el procesado neuronal por parte de la retina-cerebro.

Podemos concluir que en este trabajo se ha diseñado un método *in-vitro* experimental para cuantificar objetivamente las características del halo que se formaría en la retina de pacientes implantados con diferentes IOLs.

CAPÍTULO 7

CONCLUSIONES

CHAPTER 7

CONCLUSIONS

This doctoral dissertation mainly deals with the *in vitro* optical characterization of the imaging properties of intraocular lenses (IOLs). The research conducted was motivated by the need of providing reliable information, both objective and quantitative, of the optical performance of such components in their common use as implants in cataract surgery. Most of the stated objectives share a motivation related to the experimentation with available real IOLs used nowadays in clinical practice.

However, we have also reviewed the theoretical principles involved in all the problems addressed in this research. This task has been essential to fully understand the optical imaging performance of the studied IOLs and to establish a common basis for their objective comparison.

As a general conclusion, this work highlights the importance and need of the *in vitro* optical characterization of IOLs for a correct, objective and complete assessment of their optical imaging quality that complements the clinical assessment and ray-tracing simulations.

We have designed and implemented a variety of experimental methods to measure the following aspects: efficiency, contrasts, MTF, PSF, depth of focus, and halos. From these measurements a set of commercial IOLs have been tested and compared.

From the research work, the following specific conclusions can be derived:

1) Defocus compensation can be dealt with in first-order (Gaussian) optics, and this sort of correction is prior to any other compensation intended for high-order aberrations. In the case power calculation of IOLs, there still are several sources of uncertainty that may well give rise to a residual refractive error. They can be particularly important in the case of patients who have undergone corneal-ablative refractive surgery. We have explored the possibility of introducing changes in other parameters of the eye, different from the anterior corneal surface, to compensate for the refractive error and have shown their theoretical effectiveness in some cases. Small changes in the refractive indices of the aqueous or the vitreous humors are highly effective, much more than a similar amount of change in the anterior or posterior corneal curvature or its refractive index or thickness. This fact opens new and attractive possibilities to compensate for defocus, through the introduction of changes in degrees of freedom that have been considered unconventional up until now.

In the design of the optical bench

2) We have designed an optical bench for IOL characterization following the ISO standards but that allow testing them in closer conditions to a real human eye. In particular we have designed our dispositive able to test using illuminants centered different wavelengths as well as white light. We also can use a Hartmann-Shack sensor to measure the optical aberrations of the model eye or a spectrophotometer to measure the spectral transmittance of the IOLs. Another remarkable feature is the possibility of using of an artificial cornea with values of SA similar to the mean human cornea instead of the aberration-free lens suggested by the ISO. The analysis of the IOLs with our dispositive can be done through different metrics, such as the PSF,

MTF, contrast, wavefront analysis, etc , which are conventional in imaging quality testing.

3) The ISO standard does not provide enough information about the characteristics of the capturing system of the image formed by the model eye. We have detected and analyzed a problem on this issue related with a magnification mismatch between the scaled image formed on the CCD and its defocus circle when using a conventional microscope. This mismatch is particularly relevant when performing a T-F analysis of the performance of the IOLs.

    a. One possible solution to maintain the magnification of the image scale and its defocused circle can be obtained changing the adequate distance of the CCD (without displacing the microscope system). This distance is proportional to the object displacement induced by the object vergence change and the squared magnification of the focused image. This solution is only valid for monofocal IOLs.

    b. For MIOLs the solution relies on an afocal configuration of the microscope, which shows constant magnification for objects at infinite distances. This solution overcomes the problem without increasing the complexity of the setup.

    Anyway, the differences on the T-F performances using the conventional configuration of the microscope and these two solutions can be small depending on the characteristics of each optical system and require further investigation.

In the characterization of efficiency

4) We have developed a new experimental method to measure the energy efficiency as a function of the pupil diameter analyzing the image of a pinhole formed by the model eye.

5) Monofocal aspheric IOLs present higher efficiency than the spherical monofocal design as well as any MIOL tested.

6) The energy distribution of diffractive MIOLs differs from the theoretical predictions that only consider the diffractive profile but not other factors such as spherical aberrations (SAs) and/or scattering that degrade the image decreasing the energy efficiency. However, non-apodized diffractive MIOLs present more pupil-independent efficiencies than apodized ones, which benefit the distance focus for large pupils, as it is intended by the theoretical design.

7) The wavelength dependence of the performance diffractive based MIOLs in terms of light distribution between their foci, must be considered specially when patients implanted with these types of MIOLs are analyzed with red or infrared optical systems (e.g. aberrometers, auto-refractors or double-pass systems). The diffractive profile produces higher efficiency when using red light in the distance focus (*m=0* diffraction order) and a lower with the blue light. On the contrary, in the near focus (*m=1*), the efficiency of the MIOL with blue light is higher than with red. Refractive MIOLs are less wavelength-dependent.

8) We have conducted a clinical trial to assess and compare the stereo-acuity obtained with two types of stereotests (TNO and Titmus) in patients symmetrically implanted with four different types of MIOLs and one monofocal IOL as a reference. Since the stereoacuity test has to be observed at a close distance, patients with monofocal implants were corrected at their best near vision. Patients with monofocal IOL showed better stereo-acuity than those implanted with MIOLs no matter the stereotest used. With the Titmus test (based on polarized filters), there were no differences between stereo-acuities tested in patients implanted with different MIOLs. The test based on chromatic dissociation (TNO) may induce large difference on image contrast between fellow eyes implanted with diffractive-based MIOLs, with the global effect of affecting stereo-acuity results. This effect has been explained taking into account that, with diffractive-based MIOLs, the energy efficiency of the *m=1* diffraction order - that generates the near focus - is quite different when using a red filter than when using the green one.

Regarding the measurement of:

9) Contrast: Monofocal aspheric IOLs form images with higher contrast than the spherical-monofocal IOL, especially with large pupil diameters, due to their compensation for the SA. In the distance focus, the images formed with the apodized designs present higher contrast than the non-apodized one with small pupils. On the contrary, with pupils larger than 4*mm*, the non-apodized MIOL present higher values of contrast because of this lens present asphericity for a total correction of the corneal SA. In the near focus, the apodized design presents poorer contrast images than the non-apodized because the apodization of the diffractive profile benefits the distance focus in detriment of the near one.

10) Modulation Transfer Function: The MTF, as other quality metrics, is highly dependent on the pupil diameter. Monofocal aspheric IOLs presented better MTF than any other monofocal or MIOL. The monofocal spherical IOL with large pupils can present equal or lower values than some MIOLs in the distance focus. Between MIOLs, there is not a clearly advantageous design when evaluating the MTF. Aspheric-apodized MIOLs present better MTFs in the distance focus than the other tested MIOLs. However, the performance in the near focus is poorer. The refractive-symmetrical MIOL presents a high performance with small pupils because, in this conditions, there is not any zone of the MIOL that contributes to the near focus, so its performance in this situation can be similar to a monofocal IOL.

Concerning the measurement of halos:

11) We have designed a new method to characterize the halo formed by IOLs, both in size and intensity, from the analysis of the image(s) formed in the CCD of our optical bench. The diameter of the halo in MIOLs, as predicted by paraxial optics, depends on the pupil diameter that contributes to the non-focused focus, the base power of the lens (distance focus) and the addition.

12) Aspheric monofocal IOLs present lower halo size and intensity than any other IOL. The halo induced by a spherical monofocal kind of IOL can be, for large pupils, of the same size as of those induced by some MIOLs. The halo characteristics of the MIOLs strongly depend on their design. For instance, refractive-asymmetrical MIOL generates asymmetric halos; non-apodized MIOLs presents halos of the same size in distance and near vision; apodized MIOLs show smaller and dimmer halo in distance focus but larger and brighter in the near one; and the trifocal MIOL present two halos in each image plane, of different size and intensity.

Moving foward

Concerning the degrees of freedom we mentioned in conclusion 1 to correct defocus in other parameters of the eye (different from anterior curvature), the biocompability, stability and drainage of new materials to change the refractive index – or substitute - of the aqueous and vitreous humors allow us to consider our proposal as the basis of promising upcoming techniques.

As we shown in chapter 3, the optical bench for IOL assessment suggested by the ISO present several limitations. Future work should be focused on designing a new optical bench with dimensions closer to the real human eye, with the entrance pupil just in front of the IOL, prepared to correctly reproduce the out-of-axis performance and/or able to measure the performance of contact lenses as well.

The T-F characterization of MIOLs using an afocal microscope is also a pending issue using in which we are working in this moment. This kind of analysis will also be applied to different models of MIOLs that are currently being designed or will be commercialized soon. Additionally, the influence of the chromatic aberration in the different foci of MIOLs is an interesting issue. The wavelength dependence of both the refractive nature of the material of the IOL, that affects the distance and near foci, and the diffractive profile that only affects to the near one.

Using an optical bench or optical ray-tracing, the optical quality of the IOL can be measured using optical metrics (MTF, PSF, contrast, etc), but these are purely optical parameters that are not always correlated with the visual function and the

test used to evaluate the visual performance of real patients (usually visual acuity and/or contrast sensitivity). As visual function depends on the one hand, on the optical quality of the image formed by the ocular system, and on the other hand, on the contributions of neural system when processing the image formed in the retina, future work should be oriented to find a better correlation between the optical metrics and the subjective response of the eye when tested clinically.

Referencias

References

[11979-2]

11979-2. *International Organization for Standardization.* Ophthalmic Implants, Intraocular Lenses - Part 2: Optical Properties and Test Methods.

[11979-2]

11979-9. *International Organization for Standardization.* Ophthalmic implants, Intraocular lenses - Part 9: Multifocal intraocular lenses.

[ALBA-BUENO AND MILLÁN 2009]

ALBA-BUENO, F. AND MILLÁN, M.S. 2009. Caracterización Óptica de las Lentes Intraoculares Monofocales. *Trabajo de final de master*, 1–96.

[ALBA-BUENO AND MILLÁN 2011]

ALBA-BUENO, F. AND MILLÁN, M.S. 2011. Defocus correction in the optical system of the eye: unconventional degrees of freedom. *Journal of Biomedical Optics 16*, 1, 016010.

[ALBA-BUENO ET AL. 2011A]

ALBA-BUENO, F., VEGA, F., AND MILLÁN, M.S. 2011a. Energy balance in apodized diffractive multifocal intaocular lenses. *Proc. SPIE*, 80119G–80119G–10.

[ALBA-BUENO ET AL. 2011B]

ALBA-BUENO, F., VEGA, F., AND MILLÁN, M.S. 2011b. Design of a Test Bench for Intraocular Lens Optical Characterization. *Journal of Physics: Conference Series 274*, 012105.

[ALBA-BUENO ET AL. 2014]

ALBA-BUENO, F., VEGA, F., AND MILLÁN, M.S. 2014 Halos en LIOs multifocales: Origen e interpretación. *Archivos de la Sociedad Española de Oftalmología*. (Acepted for publication)

[ALFONSO ET AL. 2007]

ALFONSO, J.F., FERNÁNDEZ-VEGA, L., BAAMONDE, M.B., AND MONTÉS-MICÓ, R. 2007.

Prospective visual evaluation of apodized diffractive intraocular lenses. *Journal of Cataract & Refractive Surgery 33*, 7, 1235–1243.

[ALFONSO ET AL. 2009]

ALFONSO, J.F., FERNÁNDEZ-VEGA, L., AMHAZ, H., MONTÉS-MICÓ, R., VALCÁRCEL, B., AND FERRER-BLASCO, T. 2009. Visual function after implantation of an aspheric bifocal intraocular lens. *Journal of Cataract & Refractive Surgery 35*, 5, 885–892.

[ALFONSO ET AL. 2010]

ALFONSO, J.F., FERNÁNDEZ-VEGA, L., PUCHADES, C., AND MONTÉS-MICÓ, R. 2010. Intermediate visual function with different multifocal intraocular lens models. *Journal of Cataract & Refractive Surgery 36*, 5, 733–739.

[ALIÓ ET AL. 2008]

ALIÓ, J.L., ELKADY, B., ORTIZ, D., AND BERNABEU, G. 2008. Clinical outcomes and intraocular optical quality of a diffractive multifocal intraocular lens with asymmetrical light distribution. *Journal of Cataract & Refractive Surgery 34*, 6, 942–948.

[ARTAL ET AL. 1995]

ARTAL, P., MARCOS, S., NAVARRO, R., MIRANDA, I., AND FERRO, M. 1995. Through focus image quality of eyes implanted with monofocal and multifocal intraocular lenses. *Optical Engineering 34*, 3, 772–779.

[ARTL AND GUIRAO 1998]

ARTAL, P. AND GUIRAO, A. 1998. Contributions of the cornea and the lens to the aberrations of the human eye. *Optics letters 23*, 21, 1713–1715.

[ARTAL ET AL. 2001]

ARTAL, P., GUIRAO, A., BERRIO, E., AND WILLIAMS, D.R. 2001. Compensation of corneal aberrations by the internal optics in the human eye. *Journal of Vision 1*, 1, 1–8.

[ARTAL AND TABERNERO 2010]

ARTAL, P. AND TABERNERO, J. 2010. Optics of human eye: 400 years of exploration from Galileo's time. *Applied optics 49*, 16, D123–30.

[ARTIGAS ET AL. 2007]

ARTIGAS, J.M., MENEZO, J.L., PERIS, C., FELIPE, A., AND DÍAZ-LLOPIS, M. 2007. Image quality with multifocal intraocular lenses and the effect of pupil size. *Journal of Cataract & Refractive Surgery 33*, 12, 2111–2117.

[ATCHISON 1989]

ATCHISON, D.A. 1989. Refractive errors induced by displacement of intraocular lenses within the pseudophakic eye. *Optometry and Vision Science 66*, 3, 146.

[ATCHISON 1991]

ATCHISON, D.A. 1991. Design of aspheric intraocular lenses. *Ophthalmic and Physiological Optics*.

[ATCHISON AND SMITH 2000]

ATCHISON, D.A. AND SMITH, G. 2000. *Optics of the human eye*. Butterworth-Heinemann Medical.

[ATCHISON AND SMITH 2004]

ATCHISON, D.A. AND SMITH, G. 2004. Chromatic dispersions of the ocular media of human eyes. *Journal of the Optical Society of America A 22*, 1, 29–37.

[ATCHISON ET AL. 2009]

ATCHISON, D.A., GUO, H., CHARMAN, W.N., AND FISHER, S.W. 2009. Blur limits for defocus, astigmatism and trefoil. *Vision Research 49*, 19, 2393–2403.

[BARBERO ET AL. 2003]

BARBERO, S., MARCOS, S., AND JIMÉNEZ-ALFARO, I. 2003. Optical aberrations of intraocular lenses measured in vivo and in vitro. *JOSA A*, 1841–1851.

[BENNETT AND RABBETTS 2007]

BENNETT, A.G. AND RABBETTS, R.B. 2007. *Bennett and Rabbetts' clinical visual optics*. Butterworth-Heinemann Medical.

[BLAYLOCK ET AL. 2006]

BLAYLOCK, J.F., SI, Z., AND VICKERS, C. 2006. Visual and refractive status at different focal distances after implantation of the ReSTOR multifocal intraocular lens. *Journal of Cataract & Refractive Surgery 32*, 9, 1464–1473.

[DUBBELMAN ET AL. 2002]

DUBBELMAN, M., WEEBER, H.A., VAN DER HEIJDE, R.G.L., AND VÖLKER-DIEBEN, H.J. 2002. Radius and asphericity of the posterior corneal surface determined by corrected Scheimpflug photography. *Acta Ophthalmologica Scandinavica 80*, 4, 379–383.

[CALLADINE ET AL. 2012]

CALLADINE, D., EVANS, J.R., SHAH, S., AND LEYLAND, M. 2012. Multifocal versus monofocal intraocular lenses after cataract extraction. *Cochrane database of systematic reviews (Online) 9*, 3, CD003169.

[CAMELLIN AND CALOSSI 2006]

CAMELLIN, M.M. AND CALOSSI, A.A. 2006. A new formula for intraocular lens power calculation after refractive corneal surgery. *Journal of Refractive Surgery 22*, 2, 187–199.

[CASTIGNOLES ET AL. 2010]

CASTIGNOLES, F., FLURY, M., AND LEPINE, T. 2010. Comparison of the efficiency, MTF and chromatic properties of four diffractive bifocal intraocular lens designs. *Optics Express 18*, 5, 5245–5256.

[CHANG 2008]

CHANG, D.F. 2008. Prospective functional and clinical comparison of bilateral ReZoom and ReSTOR intraocular lenses in patients 70 years or younger. *Journal of Cataract & Refractive Surgery 34*, 6, 934–941.

[CHARMAN 2005]

CHARMAN, W.N. 2005. Restoring accommodation: a dream or an approaching reality? *Ophthalmic and Physiological Optics*.

[COCHENER ET AL. 2012]

COCHENER, B., VRYGHEM, AND ROZOT. 2012. Visual and refractive outcomes after implantation of a fully diffractive trifocal lens. *Clinical Ophthalmology 6*, 1421–1427.

[COHEN 1992]

COHEN, A.L. 1992. Practical design of a bifocal hologram contact lens or intraocular lens. *Applied optics 31*, 19, 3750–3754.

[COHEN 1993]

COHEN, A.L. 1993. Diffractive bifocal lens designs. *Optometry and Vision Science 70*, 6, 461–468.

[COHEN 2012]

COHEN, A.L. 2012. Diffraction IOL with Micro-modulation. *US Patent 20,120,224,138*.

[DAVISON AND SIMPSON 2004]

DAVISON, J.A. AND SIMPSON, M.J. 2004. How does the ReSTOR lens work? *Review of Refractive Surgery* October 2004.

[DAVISON AND SIMPSON 2006]

DAVISON, J.A. AND SIMPSON, M.J. 2006. History and development of the apodized diffractive intraocular lens. *Journal of Cataract & Refractive Surgery 32*, 5, 849–858.

[DE VRIES ET AL. 2008]

DE VRIES, N.E., FRANSSEN, L., WEBERS, C.A.B., ET AL. 2008. Intraocular straylight after implantation of the multifocal AcrySof ReSTOR SA60D3 diffractive intraocular lens. *Journal of Cataract & Refractive Surgery 34*, 6, 957–962.

[DE VRIES ET AL. 2010]

DE VRIES, N.E., WEBERS, C.A., VERBAKEL, F., ET AL. 2010. Visual outcome and patient satisfaction after multifocal intraocular lens implantation: Aspheric versus spherical design. *Journal of Cataract & Refractive Surgery 36*, 11, 1897–1904.

[EPPIG ET AL. 2008]

EPPIG, T., SCHOLZ, K., AND LANGENBUCHER, A. 2008. Assessing the optical performance of multifocal (diffractive) intraocular lenses. *Ophthalmic and Physiological Optics 28*, 5, 467–474.

[FANG ET AL. 2005]

FANG, J.P., HILL, W., WANG, L., CHANG, V., AND KOCH, D.D. 2005. Advanced intraocular lens power calculations. *Cataract and Refractive Surgery*, 31–46.

[FERRER-BLASCO ET AL. 2009]

FERRER-BLASCO, T., MONTÉS-MICÓ, R., CERVIÑO, A., ALFONSO, J.F., AND GONZÁLEZ-MÉIJOME, J.M. 2009. Stereoacuity After Refractive Lens Exchange with AcrySof ReSTOR Intraocular Lens Implantation. *Journal of Refractive Surgery 25*, 11, 1000–1004.

[FERRER-BLASCO ET AL. 2010]

FERRER-BLASCO, T., MADRID-COSTA, D., GARCÍA-LÁZARO, S., CERVIÑO, A., AND MONTÉS-MICÓ, R. 2010. Stereopsis in bilaterally multifocal pseudophakic patients. *Graefe's Archive for Clinical and Experimental Ophthalmology 249*, 2, 245–251.

[FYODOROV AND KOLONKO 1967]

FYODOROV, S.N. AND KOLONKO, I. 1967. Estimation of Optical Power of the Intraocular Lens. *Vestnik Oftalmologic (Russian) 4*, 27–31.

[FYODOROV ET AL. 1975]

FYODOROV, S.N.S., GALIN, M.A.M., AND LINKSZ, A.A. 1975. Calculation of the optical power of intraocular lenses. *Investigative ophthalmology 14*, 8, 625–628.

[GARCÍA-MARTINEZ AND MILLÁN 2012]

GARCÍA-MARTÍNEZ, E. AND MILLÁN, M.S. 2012. Análisis in vitro de la eficiencia energética de las imágenes formadas por lentes intraoculares multifocales. *Trabajo de final de master*, 1–59.

[GARHAM AND SLOPER 2006]

GARNHAM, L. AND SLOPER, J.J. 2006. Effect of age on adult stereoacuity as measured by different types of stereotest. *British Journal of Ophthalmology 90*, 1, 91–95.

[GATINEL ET AL. 2011]

GATINEL, D., PAGNOULLE, C., YVETTE, H., AND GOBIN, L. 2011. Design and qualification of a diffractive trifocal optical profile for intraocular lenses. *Journal of Cataract &*

Refractive Surgery 37, 11, 2060–2067.

[GATINEL AND HOUBRECHTS 2013]

GATINEL, D. AND HOUBRECHTS, Y. 2013. Comparison of bifocal and trifocal diffractive and refractive intraocular lenses using an optical bench. *Journal of Cataract & Refractive Surgery*, 1–7.

[GIL ET AL. 2012]

GIL, M.A.M., VARON, C.C., ROSELLO, N.N., CARDONA, G.G., AND BUIL, J.A.J. 2012. Visual acuity, contrast sensitivity, subjective quality of vision, and quality of life with 4 different multifocal IOLs. *European Journal of Ophthalmology 22*, 2, 175–187.

[GIL ET AL. 2014]

GIL, M.A., VARÓN, C., CARDONA, G., VEGA, F., AND BUIL, J.A. 2014. Comparison of far and near contrast sensitivity in patients symmetrically implanted with multifocal and monofocal IOLs. *European Journal of Ophthalmology 24*, 1, 44–52.

[GOODMAN 2005]

GOODMAN, J.W. 2005. *Introduction to Fourier Optics*. Roberts and Company Publishers.

[GUIRAO ET AL. 2000]

GUIRAO, A., REDONDO, M., AND ARTAL, P. 2000. Optical aberrations of the human cornea as a function of age. *JOSA A 17*, 10, 1697–1702.

[GUIRAO ET AL. 2002]

GUIRAO, A., REDONDO, M., GERAGHTY, E., PIERS, P.A., NORRBY, S., AND ARTAL, P. 2002. Corneal optical aberrations and retinal image quality in patients in whom monofocal intraocular lenses were implanted. *Archives of ophthalmology 120*, 9, 1143–1151.

[HAIGIS ET AL. 2000]

HAIGIS, W.W., LEGE, B.B., MILLER, N.N., AND SCHNEIDER, B.B. 2000. Comparison of immersion ultrasound biometry and partial coherence interferometry for intraocular lens calculation according to Haigis. *Graefe's Archive for Clinical and Experimental Ophthalmology 238*, 9, 765–773.

[HAIGIS 2003]

HAIGIS, W. 2003. Corneal power after refractive surgery for myopia: contact lens method. *Journal of Cataract & Refractive Surgery 29*, 7, 1397–1411.

[HAYASHI AND HAYASHI 2004]

HAYASHI, K. AND HAYASHI, H. 2004. Stereopsis in bilaterally pseudophakic patients. *Journal of Cataract & Refractive Surgery 30*, 7, 1466–1470.

[HECKMANN AND SCHOR 1989]

HECKMANN, T. AND SCHOR, C.M. 1989. Is edge information for stereoacuity spatially

channeled? *Vision Research 29*, 5, 593–607.

[HOFFER 1993]

HOFFER, K.J.K. 1993. The Hoffer Q formula: a comparison of theoretic and regression formulas. *Journal of Cataract & Refractive Surgery 19*, 6, 700–712.

[HOLLADAY 1989]

HOLLADAY, J.T. 1989. Consultations in refractive surgery. *Refractive & corneal surgery 5*, 3, 202–203.

[HOLLADAY 1997]

HOLLADAY, J.T. 1997. Standardizing constants for ultrasonic biometry, keratometry, and intraocular lens power calculations. *Journal of Cataract & Refractive Surgery 23*, 9, 1356–1370.

[HOLLADAY 2005]

HOLLADAY, J.T. 2005. Intraocular lens power calculations: correction of defocus. In: I. Howard Fine, M. Packer and R.S. Hoffman, eds., *Refractive lens surgery*. Springer, Berlín, 21–38.

[KASPER ET AL. 2006A]

KASPER, T., BÜHREN, J., AND KOHNEN, T. 2006a. Intraindividual comparison of higher-order aberrations after implantation of aspherical and spherical intraocular lenses as a function of pupil diameter. *Journal of Cataract & Refractive Surgery 32*, 1, 78–84.

[KASPER ET AL. 2006B]

KASPER, T., BÜHREN, J., AND KOHNEN, T. 2006b. Visual performance of aspherical and spherical intraocular lenses: Intraindividual comparison of visual acuity, contrast sensitivity, and higher-order aberrations. *Journal of Cataract & Refractive Surgery 32*, 12, 2022–2029.

[KIELY ET AL. 1982]

KIELY, P.M., SMITH, G., AND CARNEY, L.G. 1982. The Mean Shape of the Human Cornea. *Optica Acta: International Journal of Optics 29*, 8, 1027–1040.

[KELLY ET AL. 2004]

KELLY, J.E., MIHASHI, T., AND HOWLAND, H.C. 2004. Compensation of corneal horizontal/vertical astigmatism, lateral coma, and spherical aberration by internal optics of the eye. *Journal of Vision 4*, 4, 262–271.

[KIM ET AL. 2011]

KIM, M.J., ZHELEZNYAK, L., MACRAE, S., TCHAH, H., AND YOON, G. 2011. Objective evaluation of through-focus optical performance of presbyopia-correcting intraocular lenses using an optical bench system. *Journal of Cataract & Refractive Surgery 37*, 7,

1305–1312.

[KOHNEN ET AL. 2009A]

KOHNEN, T., KLAPROTH, O.K., AND BÜHREN, J. 2009. Effect of intraocular lens asphericity on quality of vision after cataract removal: an intraindividual comparison. *Ophthalmology*.

[KOHNEN ET AL. 2009B]

KOHNEN, T., NUIJTS, R., LEVY, P., HAEFLIGER, E., AND ALFONSO, J.F. 2009. Visual function after bilateral implantation of apodized diffractive aspheric multifocal intraocular lenses with a D3.0 D addition. *Journal of Cataract & Refractive Surgery 35*, 12, 2062–2069.

[LANG AND PORTNEY 1993]

LANG, A. AND PORTNEY, V. 1993. Interpreting multifocal intraocular lens modulation transfer functions. *Journal of Cataract & Refractive Surgery 19*, 4, 505–512.

[LANG ET AL. 1993]

LANG, A.J., LAKSHMINARAYANAN, V., AND PORTNEY, V. 1993. Phenomenological model for interpreting the clinical significance of the in vitro optical transfer function. *Journal of the Optical Society of America. A, Optics and image science 10*, 7, 1600–1610.

[LANGUY ET AL. 2011]

LANGUY, F., FLEURY-FRENETTE, K., LENAERTS, C., ET AL. 2011. Flat Fresnel doublets made of PMMA and PC: combining low cost production and very high concentration ratio for CPV. *Optics Express 19*, S3.

[LARSSON ET AL. 1992]

LARSSON, M., BECKMAN, C., NYSTROM, A., HARD, S., AND SJÖSTRAND, J. 1992. Optical properties ofdiffractive, bifocal, intraocular lenses. *Applied optics 31*, 13, 2377–2384.

[LEE AND SIMPSON 1997]

LEE, C.S. AND SIMPSON, M.J. 1997. Diffractive multifocal ophthalmic lens. *US Patent 5,699,142*

[LEGGE ET AL. 1987]

LEGGE, G.E., MULLEN, K.T., WOO, G.C., AND CAMPBELL, F.W. 1987. Tolerance to visual defocus. *JOSA A 4*, 5, 851–863.

[LIU AND BRENNAN 1997]

LIOU, H.L. AND BRENNAN, N.A. 1997. Anatomically accurate, finite model eye for optical modeling. *JOSA A 14*, 8, 1684–1695.

[LOPEZ-GIL AND MONTÉS-MICÓ 2007]

LOPEZ-GIL, N. AND MONTÉS-MICÓ, R. 2007. New intraocular lens for achromatizing the human eye. *Journal of Cataract & Refractive Surgery 33*, 7, 1296–1302.

[LOVASIK AND SZYMKIW 1985]

LOVASIK, J.V.J. AND SZYMKIW, M.M. 1985. Effects of aniseikonia, anisometropia, accommodation, retinal illuminance, and pupil size on stereopsis. *Investigative Ophthalmology & Visual Science 26*, 5, 741–750.

[MADRID-COSTA ET AL. 2010]

MADRID-COSTA, D., CERVIÑO, A., FERRER-BLASCO, T., GARCÍA-LÁZARO, S., AND MONTÉS-MICÓ, R. 2010. Visual and optical performance with hybrid multifocal intraocular lenses. *Clinical and Experimental Optometry 93*, 6, 426–440.

[MARCOS ET AL. 2005]

MARCOS, S., BARBERO, S., AND JIMÉNEZ-ALFARO, I. 2005. Optical quality and depth-of-field of eyes implanted with spherical and aspheric intraocular lenses. *Journal of Refractive Surgery 21*, 3, 223–235.

[MARCOS ET AL. 2007]

MARCOS, S., ROSALES, P., LLORENTE, L., AND JIMÉNEZ-ALFARO, I. 2007. Change in corneal aberrations after cataract surgery with 2 types of aspherical intraocular lenses. *Journal of Cataract & Refractive Surgery 33*, 2, 217–226.

[MARTINEZ PALMER ET AL. 2008]

MARTÍNEZ PALMER, A., GÓMEZ FAIÑA, P., ESPAÑA ALBELDA, A., COMAS SERRANO, M., NAHRA SAAD, D., AND CASTILLA CÉSPEDES, M. 2008. Visual function with bilateral implantation of monofocal and multifocal intraocular lenses: a prospective, randomized, controlled clinical trial. *Journal of Refractive Surgery 24*, 3, 257–264.

[MCLEOD ET AL. 2003]

MCLEOD, S.D., PORTNEY, V., AND TING, A. 2003. A dual optic accommodating foldable intraocular lens. *British Journal of Ophthalmology 87*, 9, 1083–1085.

[MELDRUM ET AL. 1996]

MELDRUM, M.L., AABERG, T.M., AND PATEL, A. 1996. Cataract extraction after silicone oil repair of retinal detachments due to necrotizing retinitis. *Archives of ophthalmology*.

[MENAPACE ET AL. 2006]

MENAPACE, R., FINDL, O., KRIECHBAUM, K., AND LEYDOLT-KOEPPL, C. 2006. Accommodating intraocular lenses: a critical review of present and future concepts. *Graefe's Archive for Clinical and Experimental Ophthalmology 245*, 4, 473–489.

[MEYERS AND ALBRECHT 1998]

MEYERS, M.M. AND ALBRECHT, R.E. 1998. Technique to eliminate scattered light in diffractive optical elements.

[MIGLIORE ET AL. 2011]

MIGLIORE, A., CORIO, M., PAONE, S., CERBO, M., AND JEFFERSON, T. 2011. Accommodating intraocular lenses for patients with cataract: a review. *Expert Review of Ophthalmology 6*, 4, 431–436.

[MILLÁN ET AL. 2004]

MILLÁN, M.S., ESCOFET, J., AND CABRÉ, E.P. 2004. *Óptica geométrica*. Editorial Ariel.

[MILLÁN ET AL. 2011]

MILLÁN, M.S., ALBA-BUENO, F., AND VEGA, F. 2011. New trends in intraocular lens imaging. *Proc. SPIE 8011*, 80119I.

[MILLODOT ET AL. 1979]

MILLODOT, M. AND SIVAK, J. 1979. Contribution of the cornea and lens to the spherical aberration of the eye. *Vision Research 19*, 6, 685–687.

[MONTÉS-MICO ET AL. 2012]

MONTÉS-MICÓ, R., LOPEZ-GIL, N., PEREZ-VIVAS, C., BONASQUE, S., AND FERRER-BLASCO, T. 2012. In vitro optical performance of nonrotational symmetric and refractive. *Journal of Cataract & Refractive Surgery 38*, 9, 1657–1663.

[MONTÉS-MICÓ ET AL. 2013]

MONTÉS-MICÓ, R., MADRID-COSTA, D., RUZ-ALCOVER, J., FERRER-BLASCO, T., AND PONS, Á. 2013. In vitro optical quality differences between multifocal apodized diffractive intraocular lenses. *Journal of Cataract & Refractive Surgery 39*, 6, 928–936.

[MUÑOZ ET AL. 2006]

MUÑOZ, G., ALBARRÁN-DIEGO, C., MONTÉS-MICÓ, R., RODRÍGUEZ-GALIETERO, A., AND ALIÓ, J.L. 2006. Spherical aberration and contrast sensitivity after cataract surgery with the Tecnis Z9000 intraocular lens. *Journal of Cataract & Refractive Surgery 32*, 8, 1320–1327.

[NANAVATY ET AL. 2009]

NANAVATY, M.A., SPALTON, D.J., BOYCE, J., SAHA, S., AND MARSHALL, J. 2009. Wavefront aberrations, depth of focus, and contrast sensitivity with aspheric and spherical intraocular lenses: Fellow-eye study. *Journal of Cataract & Refractive Surgery 35*, 4, 663–671.

[NAVARRO ET AL. 1985]

NAVARRO, R., SANTAMARÍA, J., AND BESCÓS, J. 1985. Accommodation-dependent model of the human eye with aspherics. *Journal of the Optical Society of America. A, Optics and image science 2*, 8, 1273–1281.

[NAVARRO ET AL. 2009]

NAVARRO, R. 2009. The Optical Design of the Human Eye: a Critical Review. *Journal of Optometry 2*, 1, 3–18

[NORRBY 2007]

NORRBY, S., PIERS, P., CAMPBELL, C., AND VAN DER MOOREN, M. 2007. Model eyes for evaluation of intraocular lenses. *Applied optics 46*, 26, 6595–6605.

[NORRBY 2008A]

NORRBY, S. 2008a. Norrby: ISO eye model not valid for assessing aspherical... - Google Scholar. *Journal of Cataract & Refractive Surgery*.

[NORRBY 2008B]

NORRBY, S. 2008. Sources of error in intraocular lens power calculation. *Journal of Cataract & Refractive Surgery 34*, 3, 368–376.

[OLSEN 2007]

OLSEN, T. 2007. Calculation of intraocular lens power: a review. *Acta Ophthalmologica Scandinavica 85*, 5, 472–485.

[OLSEN 1986]

OLSEN, T.T. 1986. On the calculation of power from curvature of the cornea. *British Journal of Ophthalmology 70*, 2, 152–154.

[PEPOSE ET AL. 2012]

PEPOSE, J.S., WANG, D., AND ALTMANN, G.E. 2012. Comparison of Through-Focus Image Sharpness Across Five Presbyopia-Correcting Intraocular Lenses. *American Journal of Ophthalmology 154*, 1, 20–28.e1.

[PETERMEIER AND SZURMAN 2007]

PETERMEIER, K. AND SZURMAN, P. 2007. Subjective and objective outcome following implantation of the apodized diffractive AcrySof ReSTOR. *Der Ophthalmologe : Zeitschrift der Deutschen Ophthalmologischen Gesellschaft*.

[PIEH ET AL. 2001]

PIEH, S., LACKNER, B.B., HANSELMAYER, G.G., ET AL. 2001. Halo size under distance and near conditions in refractive multifocal intraocular lenses. *British Journal of Ophthalmology 85*, 7, 816–821.

[PIEH ET AL. 2002]

PIEH, S., MARVAN, P., LACKNER, B., ET AL. 2002. Quantitative performance of bifocal and multifocal intraocular lenses in a model eye: point spread function in multifocal intraocular lenses. *Archives of Ophthalmology 120*, 1, 23.

[PIEH ET AL. 2009]

PIEH, S., FIALA, W., MALZ, A., AND STORK, W. 2009. In vitro Strehl ratios with spherical, aberration-free, average, and customized spherical aberration-correcting intraocular lenses. *Investigative Ophthalmology & Visual Science 50*, 3, 1264–1270.

[PIERS ET AL. 2008] PIERS, P.A., WEEBER, H.A., AND NORRBY, S. 2008. Multifocal ophthalmic lens.

[REMÓN ET AL. 2012]

REMÓN, L., ARIAS, A., CALATAYUD, A., AND FURLAN, W.D. 2012. Through-focus response of multifocal intraocular lenses evaluated with a spatial light modulator. *Applied optics*.

[SALADIN 1995]

SALADIN, J.J. 1995. Effects of heterophoria on stereopsis. *Optometry and Vision Science 72*, 7, 487–492.

[SAMEI ET AL. 1998]

SAMEI, E., FLYNN, M.J., AND REIMANN, D.A. 1998. A method for measuring the presampled MTF of digital radiographic systems using an edge test device. *Medical Physics*.

[SANDERS ET AL. 1990]

SANDERS, D.R.D., RETZLAFF, J.A.J., KRAFF, M.C.M., GIMBEL, H.V.H., AND RAANAN, M.G.M. 1990. Comparison of the SRK/T formula and other theoretical and regression formulas. *Journal of Cataract & Refractive Surgery 16*, 3, 341–346.

[SAVINI ET AL. 2006]

SAVINI, G., BARBONI, P., AND ZANINI, M. 2006. Intraocular Lens Power Calculation after Myopic Refractive Surgery. *Ophthalmology 113*, 8, 1271–1282.

[SCHMIDINGER ET AL. 2005]

SCHMIDINGER, G., SIMADER, C., DEJACO-RUHSWURM, I., SKORPIK, C., AND PIEH, S. 2005. Contrast sensitivity function in eyes with diffractive bifocal intraocular lenses. *Journal of Cataract & Refractive Surgery 31*, 11, 2076–2083.

[SCHWARTZ ET AL. 2004]

SCHWARTZ, D.M., SANDSTEDT, C.A., CHANG, S.H., KORNFIELD, J.A., AND GRUBBS, R.H. 2004. Light-adjustable lens: development of in vitro nomograms. *Transactions of the American Ophthalmological Society 102*, 67.

[SCHWIEGERLING 2007]

SCHWIEGERLING, J. 2007. Analysis of the optical performance of presbyopia treatments with the defocus transfer function. *Journal of Refractive Surgery 23*, 9, 965–971.

[SHEPPARD ET AL. 2010]

SHEPPARD, A.L., BASHIR, A., AND WOLFFSOHN, J.S. 2010. Accommodating intraocular lenses: a review of design concepts, usage and assessment methods. *Clinical and ….*

[SIMONS ET AL. 1984]

SIMONS, K. 1984. Effects on stereopsis of monocular versus binocular degradation of image contrast. *Investigative Ophthalmology & Visual Science 25*, 8, 987–989.

[SOUZA ET AL. 2006]

SOUZA, C.E., MUCCIOLI, C., SORIANO, E.S., ET AL. 2006. Visual Performance of AcrySof ReSTOR Apodized Diffractive IOL: A Prospective Comparative Trial. *American Journal of Ophthalmology 141*, 5, 827–832.e2.

[SWANSON 1994]

SWANSON, G.J. 1994. Diffractive trifocal intra-ocular lens design. *US. Patent 5,344,447*

[TABERNERO ET AL. 2007]

TABERNERO, J.J., PIERS, P.A., AND ARTAL, P. 2007. Intraocular lens to correct corneal coma. *Optics letters 32*, 4, 406–408.

[TERWEE ET AL. 2008]

TERWEE, T.T., WEEBER, H.H., VAN DER MOOREN, M.M., AND PIERS, P.A. 2008. Visualization of the retinal image in an eye model with spherical and aspheric, diffractive, and refractive multifocal intraocular lenses. *Journal of Refractive Surgery 24*, 3, 223–232.

[TURUNEN AND WYROWSKI 1997]
TURUNEN, J. AND WYROWSKI, F. 1997. *Diffractive Optics*. VCH.

[VALLE ET AL. 2005]

VALLE, P.J., OTI, J.E., CANALES, V.F., AND CAGIGAL, M.P. 2005. Visual axial PSF of diffractive trifocal lenses. *Opt. Express*.

[VEGA ET AL. 2010]
VEGA, F., MILLAN, M.S., AND WELLS, B. 2010. Spherical lens versus aspheric artificial cornea for intraocular lens testing. *Optics letters 35*, 10, 1539–1541.

[VEGA ET AL. 2011]

VEGA, F., ALBA-BUENO, F., AND MILLÁN, M.S. 2011. Energy Distribution between Distance and Near Images in Apodized Diffractive Multifocal Intraocular Lenses. *Investigative Ophthalmology & Visual Science 52*, 8, 5695–5701.

[VEGA ET AL. 2014]

VEGA, F., ALBA-BUENO, F., AND MILLÁN, M.S. 2014. Energy efficiency of a new trifocal intraocular lens. *Journal of the European Optical Society-Rapid publications*.

[VINGOLO ET AL. 2007]

VINGOLO, E.M., GRENGA, P., IACOBELLI, L., AND GRENGA, R. 2007. Visual acuity and contrast sensitivity: AcrySof ReSTOR apodized diffractive versus AcrySof SA60AT monofocal intraocular lenses. *Journal of Cataract & Refractive Surgery 33*, 7, 1244–1247.

[VOSKRESENSKAYA ET AL. 2010]

VOSKRESENSKAYA, A.A., POZDEYEVA, N.N., PASHTAEV, N.N., BATKOV, Y.Y., TREUSHNICOV, V.V., AND CHEREDNIK, V.V. 2010. Initial results of trifocal diffractive IOL implantation. *Graefe's Archive for Clinical and Experimental Ophthalmology 248*, 9, 1299–1306.

[WANG ET AL. 2003]

WANG, L., DAI, E., KOCH, D.D., AND NATHOO, A. 2003. Optical aberrations of the human anterior cornea. *Journal of Cataract & Refractive Surgery 29*, 8, 1514–1521.

[WOOD 1993]

WOOD, I.C. 1983. Stereopsis with spatially-degraded images. *Ophthalmic and Physiological Optics 3*, 3, 337–340.

[ZALEVSKY 2010]

ZALEVSKY, Z. 2010. Extended depth of focus imaging: a review. *Journal of Photonics for Energy*, 018001.

Femtosecond laser treatment for presbyopia: a 6-month follow up study.

F. Alba-Bueno, J. Cabot, S. González-Colás, M. Ralló, M.S. Millán and F. Vega

Presbyopia affects almost everyone older than 45-50 years. Surgical attempts to treat presbyopia include monovision [Garcia-Gonzalez and Teus 2010; Farid and Steinert 2009], blended vision, implantation of diffractive multifocal[de Vries et al. 2010; Alió et al. 2006] or accommodative [Sheppard et al. 2010; Mesci et al. 2010] intraocular lenses, multifocal laser excimer ablations[Epstein and Gurgos 2009], intracorneal pinhole inlays [Yilmaz et al. 2008], scleral implants [Malecaze et al. 2001; Qazi et al. 2002], etc.

In the last few years the femtosecond laser technology has been applied in ophthalmology [Soong and Malta 2009; Binder 2010]. Its major use has been in the cutting of LASIK flaps, keratoplasties, tunnel creation for intracorneal ring segments and astigmatic keratotomies. The TECHNOLAS® femtosecond laser (Technolas Perfect Vision GmbH, Munich, Germany) treatment for presbyopia, INTRACOR®, is a new procedure that received the European Community approval in April 2009. This procedure delivers an intrastromal customized pattern of infrared laser pulses of 5 concentric cylinders (figure 1) to induce a local reorganization of the biomechanical forces and consequently a steepening in the 3mm central cornea (figure 2).

The purpose of this study is to analyze the functional and refractive results after mono and binocular treatment with the INTRACOR® procedure in a private ocular clinic (Institut Oftalmològic de Cirugía Avançada de Barcelona, IOCAB, Spain). There are two previous studies reporting monocular results in far and near vision[Holzer et al. 2009; Ruiz et al. 2009].

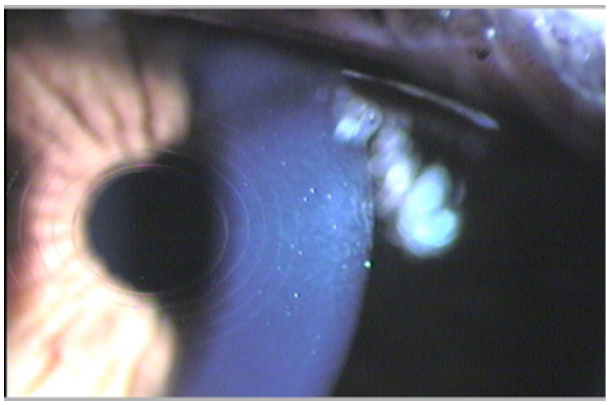

Figure 1: Pattern of corneal intrastromal rings 24h after the procedure.

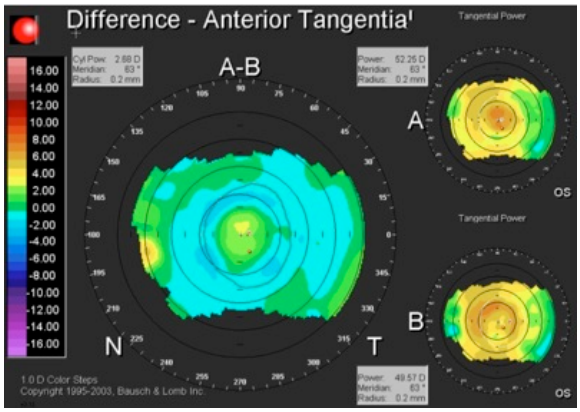

Figure 2: Preoperative and one-month postoperative differential corneal topographies.

Patients and methods

This is a prospective longitudinal study of first consecutive patients treated with INTRACOR® between March and July of 2010 in the "Institut Oftalmològic de Cirugia Avançada de Barcelona" (IOCAB) in Barcelona (Spain).

The inclusion criteria were presbyopic patients older than 45 years old, with spherical equivalent refraction for far vision between 0.00D and +1.50D and refractive astigmatism lower than 1.00D. The mean Orbscan II (Bausch & Lomb) mean simulated keratometries (Km) measured from the apex to the central 3mm had to be between 40 and 46D and thinnest pachymetry higher than 500 microns. The kappa angle had to be lower than 10º to avoid candidates with excessive distance between the visual and the pupillary axis at the anterior corneal plane. Exclusion criteria were previous corneal surgery (LASIK, PRK…) ocular pathology,

corneal ecstasy or topographic irregularities. Pseudophakia was not an exclusion criterion if it was performed by means of microincisional surgery technique.

Mono and binocular visual acuities (VAs) were measured under fixed illumination conditions using previously calibrated (with 4x and 10x microscopy) logarithmic visual acuity ETDRS charts (Precision Vision). We recorded uncorrected and best-distance-corrected visual acuities at far (UDVA and CDVA), intermediate (UIVA and DCIVA at 70cm) and near (UNVA and DCNVA at 40cm) distances. The contrast sensitivity (CS) at 10% and 2.5% were measured with the same ETDRS chart in far vision.

O examination included ocular dominance, Orbscan II topography, wavefront analysis with Zywave (Technolas Perfect Vision GmbH), pupil diameter in scotopic and photopic conditions with Colvard pupillometer (Oasis Medical, Glendora, Calif), intraocular pressure measurement and cycloplegic retinoscopy. In addition, complete ophthalmologic exploration was performed with slit lamp and fundus examination.

All candidates were informed about the nature of the procedure and that the clinical data were recorded for a statistical analysis and further publication of the study in medical journals if relevant results were found. Furthermore, alternative techniques for presbyopia correction were explained and discussed to the patients. Informed consent was obtained following the declaration of Helsinki and International Review Board was obtained (Barcelona Hospital). All the surgeries were performed by the same surgeon (J. C). The evaluations were performed preoperatively and at 1-week, 1-month, 3–months and 6-months after the treatment.

Statistical analysis of the temporal evolution of all variables was performed with SPSS 19.0.0 software (Chicago, IL, USA) using the Friedman test because the values were not normally distributed. It tests whether *k* related samples have been drawn from the same population (there was no significant change). When this overall hypothesis was rejected, we analyzed all pairwise multiple comparisons to investigate where the differences were among the populations. The significance level was set to $\alpha=0.05$. Differences in mean VA measurements were considered of

clinical relevance when they were equal or higher than 0.05 logMAR units (half a line in logMAR charts). A minimum difference of 0.12D was considered clinically significant for Km and SE

Surgical technique

The non-dominant eye was treated first. The repetition of the procedure on the second eye was optional to the patient´s choice and applicable one week after the first treatment.

The surgical procedure started with instillation of Oxybuprocaine 1% drops on the eye that was going to be treated. Under the surgical microscope the visual line was marked monocularly using the patient's visual axis and marking the first Purkinje image while the patient was looking at the fixation spot. Then, a disposable suction-ring was placed on the eye to connect the corneal surface with the specific spherical surface of the disposable cone that connected with the laser device.

The corneal mark has to be aligned with the center of the ring pattern. The treatment time is approximately 18 seconds and afterwards, the suction ring and the connection cone are removed.

After treatment the patient underwent slit-lamp examination. At this time the induced gas bubbles by the laser treatment blurs the eye vision. The gas typically escapes 4 or 5 hours postoperatively, and only thin circular rings are visible after 1-day postoperative time (figure 1). During 1 week patients received Ketorolac Trometamol, Ofloxacin and Dexametason Sodic Phosphate eye drops every four hours.

Results

Twenty patients joined the study, 40% of them were men and 60% were women, with a mean age of 53±4.2 years (range(R)=[46, 61]). A total of 34 eyes were treated, so 14 patients were treated binocularly. The mean preoperative spherical equivalent (SE) of the eyes was +0.71±0.38D (R=[0, 1.50]).

Detailed descriptive information about VAs, CS, medium simulated keratometry (Km) and SE obtained in each visit is shown in table 1. The statistically significant changes among the 6-months period studied are reported in table 2. Four eyes failed to attend the 3-months follow-up evaluation and seven to the 6-months follow-up. As the number of binocular patients was lower, statistical analysis was performed only with the monocular results. Anyway, the binocular results are also shown in table 1 for the reader information.

Six of the 34 treated eyes were pseudophakic implanted with the Alcon Acrysof SN60WF intraocular lens. There were not statistically significant differences between the pseudophakic and the non-pseudophakic eyes.

Functional results

Figures 3, 4 and 5 show the far, intermediate and near vision results, respectively, and standard deviations through the 6-months of follow-up. Red lines represent CDVA and the blue ones, UDVA. The green and black plots of figure 3 (far vision) correspond to the 10% CS and 2.5% CS values, respectively.

In far vision (figure 3) UDVA showed an improvement between the one-week and the one-month examination of -0.09logMAR units (p=0.009). Other changes of the UDVA that are displayed, including an improvement between the preoperative and the 1-month postoperative values, were not statistically significant.

The CDVA experienced a decrease of +0.03logMAR (p=0.045) units between the preoperative and the six-month examinations. The safety index (postoperative CDVA / preoperative CDVA) was of 0.92%. Five eyes lost one logMAR line of CDVA (eight lost half line, figure 6).

The CS analysis (figure 3) shown that, in the 10% contrast chart there were a decrease between the preoperative and the 1-week, 3-months and 6-months examinations. The 2.5% contrast chart did not show statistically significant changes among the study.

In intermediate vision (figure 4), UIVA improved between the preoperative and all the postoperative examinations (-0.32logMAR lines; $p<0.001$; between preoperative and 6-months follow-up). For DCIVA, there was an improvement between the preoperative and the 1-month examination of -0.06logMAR ($p=0.022$).

In near vision (figure 5) UNVA and DCNVA improved since the 1-week examination. Statistically significant differences were found between the preoperative and all the postoperative examinations. Difference between the preoperative and the 6-months follow-ups were of -0.43logMAR ($p<0.001$) for UNVA and -0.25logMAR ($p<0.001$) for DCNVA.

Structural results

The mean corneal keratometry at 3mm (figure 8) increased in 0.63D ($p=0.001$) between the preoperative and the 1-week examinations and no statistically significant changes were observed between the rest of the follow-ups.

The spherical equivalent, represented in figure 9, experienced a myopic shift of -0.78 ($p<0.001$) between the preoperative and the 6-months examinations. Statistically significant differences were found between the preoperative and all the postoperative examinations.

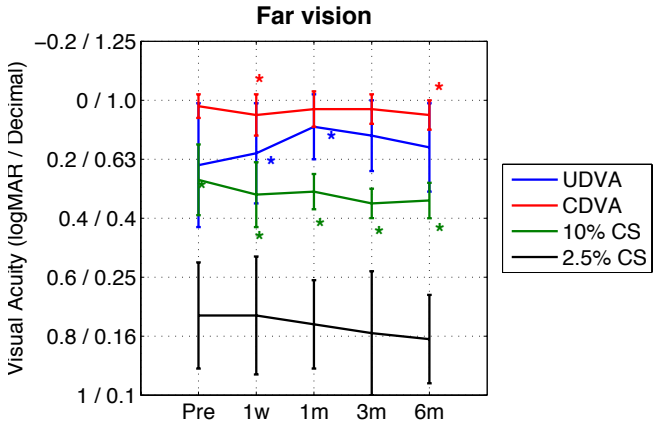

Figure 3: Far monocular and binocular mean visual acuities and contrast sensitivity evolution. Error bars represent the standard deviations and asterisks statistically significant differences.

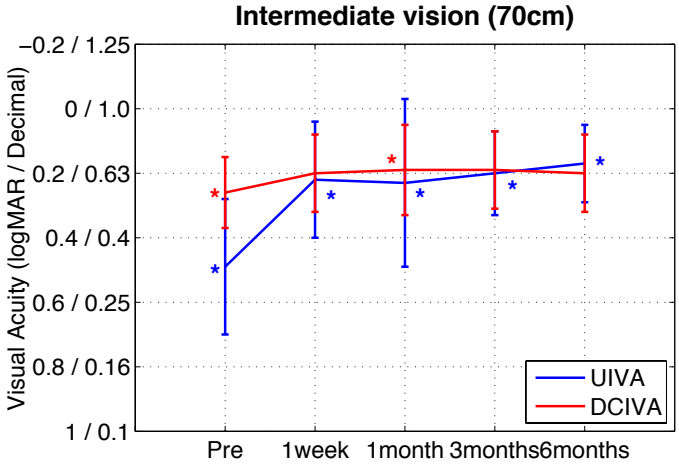

Figure 4: Intermediate monocular and binocular mean visual acuities. Error bars represent the standard deviations.

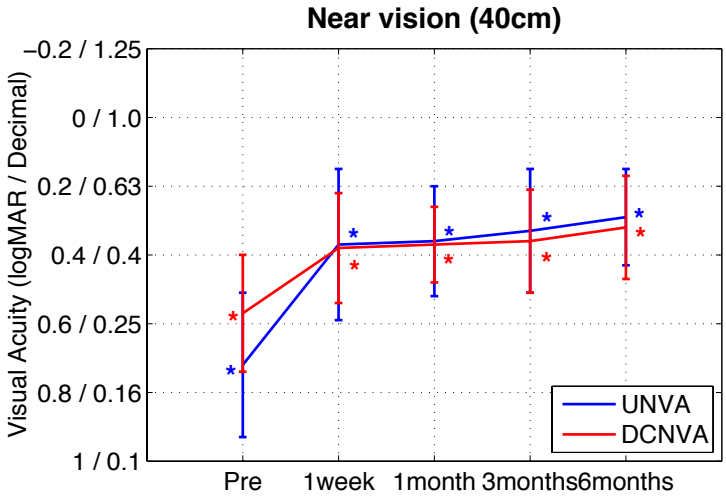

Figure 5: Near monocular and binocular mean visual acuities. Error bars represent the standard deviations and asterisks statistically significant differences.

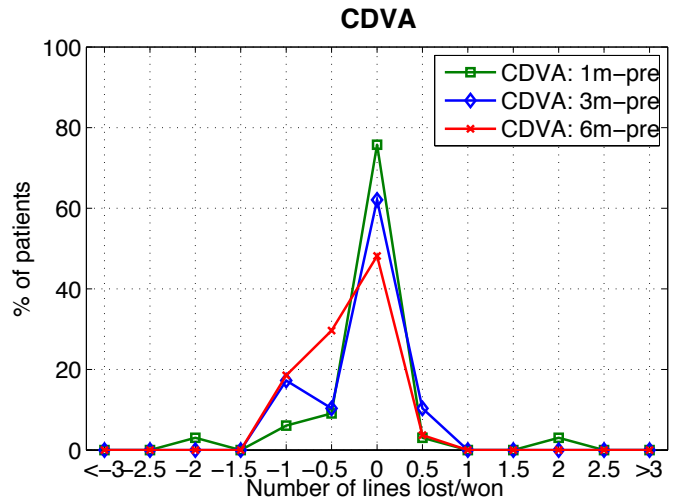

Figure 6: Number of lines of BCVA gained and lost in monocular far vision (safety).

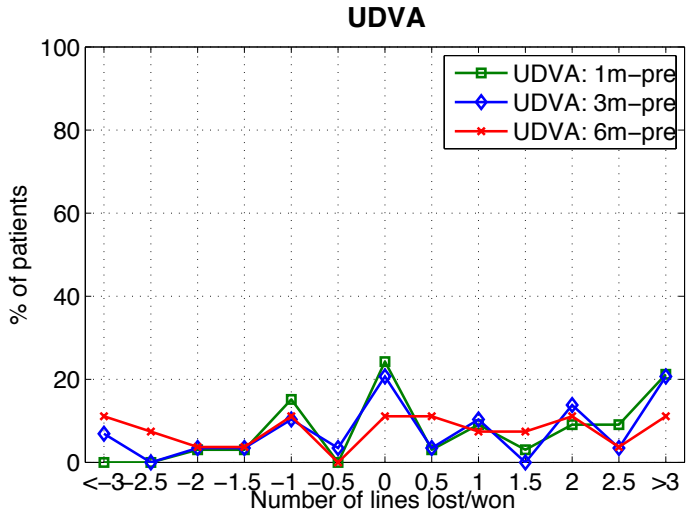

Figure 7: Lines gained and lost of UCVA in far vision.

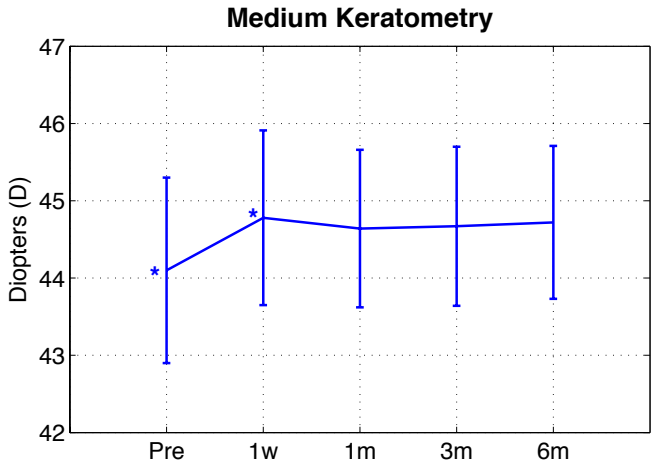

Figure 8: Medium keratometry and standard deviations evolution. Asterisks represents statistically significant differences.

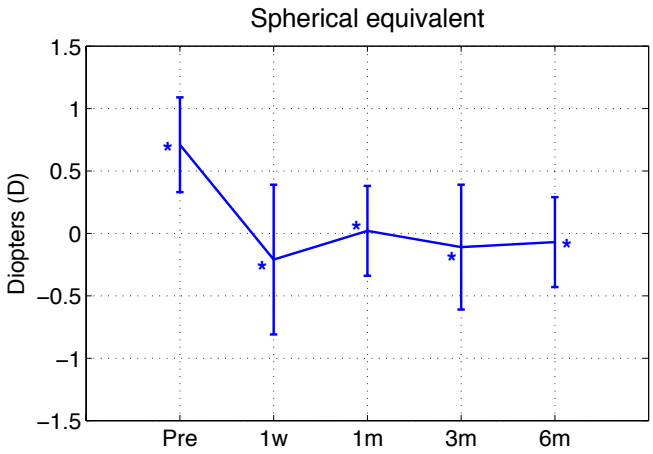

Figure 9: Mean spherical equivalent and standard deviation evolution. Asterisks represents statistically significant differences.

Discussion

Visual outcomes

INTRACOR® treatment for presbyopia improves the UIVA and UNVA, achieving values of 0.17 and 0.29 logMAR units respectively, and DCIVA and DCNVA, with values of 0.20 and 0.32 logMAR. In near vision our results in the 1-month follow-up are very similar that those shown in Holzer et al. [Holzer et al. 2009] who obtained 0.36 logMAR for UNVA and 0.33 logMAR for DCNVA. At the 3-months follow-up our results are slightly worse than Holzer's, that obtained 0.26 for UNVA and 0.23 logMAR for DCNVA). Instead Ruiz et al. [Ruiz et al. 2009] reported better near results than our study in all the follow-ups.

The loss we found in far CDVA, has been found as well after the treatment with other hyperprolates corneal procedures [Choi and Wilson 2001; Pinelli et al. 2008]. In our study 18.52% of the eyes lost one line of far CDVA (29.63% lost 0.5lines) at the 6-months follow up, whereas in Holzer et al. [Holzer et al. 2009] work, approximately 42% of the patients lost one line and 8% lost two lines at the three months examination. On the other hand 40.74% of the eyes we treated gained one or more lines of distance UDVA due to the hyperopic refraction of the sample. In figures 6 and 7 we can see the evolution of lines gained/lost of CDVA and UDVA through the 6 months period. The increase of patients loosing CDVA lines through time suggests that stabilization is not achieved and longer follow-ups

are necessary. We decided to stop performing this treatment after realizing this decrease of CDVA.

In comparison with the results reported by Ruiz et al. [Ruiz et al. 2009], CS showed a slight, but statistically and clinically significant, decrease after the treatment in 10%CS.

The procedure induces a myopic shift in the refractive equivalent sphere of 0.78D after six months, so the preoperative selection of low hyperopic patients is mandatory.

Biomechanical changes.

The intrastromal-customized pattern creates 5 concentric cylinders of photodisruptions (figure 1) respecting the anterior and posterior stroma close to the Bowman and Decemet's membranes. These induce a local liberation of the biomechanical corneal forces and, as a consequence, a steepening of the central cornea occurs. In near vision as the pupil constrict, the eye benefits of the higher refractive power of the central cornea.

Topographic observation of treated eyes shows an increase of the corneal central power that smoothes towards the periphery (figure 2). This corneal steepening induces a small change of 0.63D in simulated keratometry readings at 3mm between the preoperative and the 6-months follow-ups and may explain the SE myopic shift of 0.78D. Recently Rabsilber et al [Rabsilber et al. 2011] have published an interesting paper about the accuracy of the intraocular power calculation after this procedure and they conclude that the calculation using standard formulas incorporated in a PCI biometry device after this treatment was reliable, with minimum understimation on average.

Patient selection.

The patient's selection criterion is one of the most important factors in the final results of the treatment. If both eyes of the patients are hyperopic the bilateral procedure is recommended because it will reduce or eliminate the hyperopic refraction. When the patient is emmetropic, then monocular procedure in the non-dominant eye to reach monovision or blended vision is better, because otherwise,

the treated eye will become myopic. The treatment range selected for the inclusion criteria was broader than the recommended range published by the manufactured nowadays. Anyway in the moment we started to perform the treatments they agreed with this broader inclusion criteria.

Although we did not quantify the halo perception, all patients reported having experienced this visual phenomenon in mesopic and scotopic conditions at the first week and 1-month visits, but it was less noticeable in the third and six months follow-ups. It is important to make the patient understand that before the treatment the halo visual effect may appear after the procedure. Patients with jobs or lifestyle with high requirements of vision in mesopic and scotopic conditions (i.e. professional drivers) are bad candidates for the treatment.

Surgical technique.

At surgery time the rings must be centered on the visual axis and misalignments can lead to unexpected outcomes. Marking on the visual axis is not easy, especially in pseudophakic patients, where the intensity of the third Purkinje reflex is very intense. The use of any kind of biomicroscope is recommended to carry out this action. The alignment between the mark of the cornea and the laser system is manual, and this is another source of error in the treatment. Automation of this alignment must be one of the next steps in the technical improvement of the equipment. During the laser procedure the suction is not as high as in other procedures [Hernández-Verdejo et al. 2007]. This is an advantage because the intraocular pressure does not raise so much, but it can be a problem if the patient moves because suction can be lost. In our study, one patient was excluded for this reason.

Environmental conditions of temperature and humidity are important for the laser stability. Fluctuations in them may lead to overcorrections or the impossibility to apply the treatment. In our case, some treatments had to be postponed due to this kind of fluctuations.

Many factors could affect the effectiveness of the treatment. The influence of age, pupil diameter, corneal asphericity and pachymetry, white-to-white distance,

anterior chamber depth, corneal hysteresis and biomechanics, etc. must be studied with a higher number of patients and longer follow-up study.

The pseudophakic treated eyes have similar functional and structural results than the non-pseudophakic eyes. The size of the sample of the pseudophakic eyes was small and all of them were implanted with the same intraocular lens design (SN60WF). In this aspect, the spherical aberration of the intraocular lens can have an important role in the postoperative visual outcomes. Bigger samples sizes and different intraocular lens designs should be analyzed in the future to assess the efficiency of the treatment in these eyes.

As a conclusion, the study shows that INTRACOR treatment is a valid procedure to improve the intermediate and near vision within a 6-months follow up. Some far vision loss is the main complaint of patients after the treatment.. Longer follow-ups and improvement of laser patterns are recommended.

ALIÓ, J.L., CHAUBARD, J.J., CALIZ, A., SALA, E., AND PATEL, S. 2006. Correction of presbyopia by technovision central multifocal LASIK (presbyLASIK). *Journal of Refractive Surgery 22*, 5, 453–460.

BINDER, P.S. 2010. Femtosecond applications for anterior segment surgery. *Eye & contact lens*.

CHOI, R.Y. AND WILSON, S.E. 2001. Hyperopic laser in situ keratomileusis: primary and secondary treatments are safe and effective. *Cornea 20*, 4, 388–393.

DE VRIES, N.E., WEBERS, C.A., VERBAKEL, F., ET AL. 2010. Visual outcome and patient satisfaction after multifocal intraocular lens implantation: Aspheric versus spherical design. *Journal of Cataract & Refractive Surgery 36*, 11, 1897–1904.

EPSTEIN, R.L. AND GURGOS, M.A. 2009. Presbyopia treatment by monocular peripheral presbyLASIK. *Journal of Refractive Surgery*.

FARID, M. AND STEINERT, R.F. 2009. Patient selection for monovision laser refractive surgery : Current Opinion in Ophthalmology. *Current opinion in ophthalmology*.

GARCIA-GONZALEZ, M. AND TEUS, M.A. 2010. Visual outcomes of LASIK-induced monovision in myopic patients with presbyopia. *American journal of …*.

HERNÁNDEZ-VERDEJO, J.L., TEUS, M.A., ROMÁN, J.M., AND BOLÍVAR, G. 2007. Porcine model

to compare real-time intraocular pressure during LASIK with a mechanical microkeratome and femtosecond laser. *Investigative Ophthalmology & Visual Science 48*, 1, 68–72.

HOLZER, M.P., MANNSFELD, A., EHMER, A., AND AUFFARTH, G.U. 2009. Early Outcomes of INTRACOR Femtosecond Laser Treatment for Presbyopia. *Journal of Refractive Surgery 25*, 10, 855–861.

MALECAZE, F.J., GAZAGNE, C.S., TARROUX, M.C., AND GORRAND, J.M. 2001. Scleral expansion bands for presbyopia. *Ophthalmology*.

MESCI, C., ERBIL, H.H., OLGUN, A., AND YAYLALI, S.A. 2010. Visual Performances With Monofocal, Accommodating, and Multifocal Intraocular Lenses in Patients With Unilateral Cataract. *American Journal of Ophthalmology 150*, 5, 609–618.

PINELLI, R., ORTIZ, D., SIMONETTO, A., BACCHI, C., SALA, E., AND ALIÓ, J.L. 2008. Correction of presbyopia in hyperopia with a center-distance, paracentral-near technique using the Technolas 217z platform. *Journal of Refractive Surgery 24*, 5, 494–500.

QAZI, M.A., PEPOSE, J.S., AND SHUSTER, J.J. 2002. Implantation of scleral expansion band segments for the treatment of presbyopia. *American Journal of Ophthalmology*.

RABSILBER, T.M., HAIGIS, W., AND AUFFARTH, G.U. 2011. Intraocular lens power calculation after intrastromal femtosecond laser treatment for presbyopia: Theoretic approach. *Journal of Cataract & ...*.

RUIZ, L.A., CEPEDA, L.M., AND FUENTES, V.C. 2009. Intrastromal Correction of Presbyopia Using a Femtosecond Laser System. *Journal of Refractive Surgery 25*, 10, 847–854.

SHEPPARD, A.L., BASHIR, A., AND WOLFFSOHN, J.S. 2010. Accommodating intraocular lenses: a review of design concepts, usage and assessment methods. *Clinical and ...*.

SOONG, H.K. AND MALTA, J.B. 2009. Femtosecond lasers in ophthalmology. *American Journal of Ophthalmology*.

YILMAZ, O.F., BAYRAKTAR, S., AGCA, A., YILMAZ, B., MCDONALD, M.B., AND VAN DE POL, C. 2008. Intracorneal inlay for the surgical correction of presbyopia. *Journal of Cataract & Refractive Surgery 34*, 11, 1921–1927.

ATENCIÓ : La pàgina A.15 i següents contenen els articles mencionats a continuació, que es pot consultar a la web de l'editors

ATENCIÓN: La página A.15 y siguientes contienen los indicados a continuación, que puede consultarse en el web de los respectivos editores

ATTENTION: Page A.15 and following of the thesis contains these articles, available at the website of the corresponding publishers

1. F. Alba-Bueno, S. González, M. Biarnés, J. Cabot *Functional and refractive results after one month of AcrySof toric intraocular lens implantation* Journal of Optomety 2011, 4(2) 63-68. DOI 10.1016/S1888-4296(11)70043-7
   http://www.sciencedirect.com/science/article/pii/S1888429611700437

2. M.S. Millán, F. Alba-Bueno, F. Vega. *New trends in intraocular lens imaging.* 22nd Congress of the International Commission for Optics: Light for the Development of the World. En Proceedings of SPIE Vol. 8 1, 8011
   DOI: 10.1117/12.903389
   http://spie.org/Publications/Proceedings/Paper/10.1117/12.903389

3. F. Alba-Bueno, M. S. Millán. *Defocus correction in the optical system of the eye: unconventional degrees of freedom.* Journal of Biomedical Optics 16(1), 016010 (January 2011). DOI 10.1117/1.3528619
   http://biomedicaloptics.spiedigitallibrary.org/article.aspx?articleid=1166605

4. F. Alba-Bueno, F. Vega, M.S. Millán. *Design of a Test Bench for Intraocular Lens Optical Characterization.* XVII Reunión Iberoamericana de Óptica; X Encuentro de Óptica, Láseres y Aplicaciones. En Journal of Physics: Conference Series 274 (2011) 012105 DOI:10.1088/1742-6596/274/1/012105
   http://iopscience.iop.org/1742-6596/274/1/012105

5. M.S. Millán, F. Alba-Bueno, F. Vega. *Experiment design for through-focus testing of intraocular lenses*. 8th Iberoamerican Optics Meeting and 11th Latin American Meeting on Optics, Lasers, and Applications. En Proceedings. of SPIE Vol. 8785. DOI: 10.1117/12.2025474
   http://proceedings.spiedigitallibrary.org/proceeding.aspx?articleid=1782408

6. F. Vega, F. Alba-Bueno, M.S. Millán. *Energy distribution between distance and near Images in apodized diffractive multifocal intraocular lenses*. Investigative Ophthalmology & Visual Science, July 2011, Vol. 52, No. 8 p. 5695-5701. http://www.iovs.org/content/52/8/5695.full.pdf

7. F. Vega, F. Alba-Bueno, M.S. Millán. *Energy efficiency of a new trifocal intraocular lens* Journal of the European Optical Society Rapid Publications 9-14002, 2014
   DOI: 10.2971/jeos.2014.14002
   http://www.jeos.org/index.php/jeos_rp/article/view/14002

8. C. Varón, M.A. Gil, F. Alba-Bueno, G. Cardona, F. Vega, M.S. Millán, J.A. Buil *Stereo-acuity in patients implanted with multifocal intraocular lenses: is the choice of stereotest relevant?* Current Eye Research, Early Online, 1–9, 2014 DOI: 10.3109/02713683.2013.865758
   http://informahealthcare.com/doi/abs/10.3109/02713683.2013.865758

9. F. Alba-Bueno, F. Vega, M.S. Millán *Halos y lentes intraoculares multifocales: origen e interpretación* Archivos de la Sociedad Española de Oftalmología Vol. 89, Issue 10, 2014, p. 397–404 DOI: 10.1016/j.oftal.2014.01.002
   http://zl.elsevier.es/es/revista/archivos-sociedad-espanola-oftalmologia-296/articulo/halos-lentes-intraoculares-multifocales-origen-90349657